Doctoral Dissertation
博士論文

Topological properties of magnon excitation in magnetic skyrmion systems

(磁性スカーミオン系のマグノン励起とそのトポロジカルな性質)

A Dissertation Submitted for the Degree of Doctor of Philosophy

December 2020
令和2年12月博士（理学）申請

Department of Physics, Graduate School of Science,
The University of Tokyo
東京大学大学院理学系研究科
物理学専攻

Tomoki Hirosawa
廣澤　智紀

Abstract

Magnetic skyrmion is a topological soliton characterized by an integer topological charge, which is realized in non-centrosymmetric magnetic systems. Since the first discovery in chiral magnets, they have attracted considerable attention for future spintronic applications. As an isolated single object, they are stable due to the topological protection. In addition, they can be nucleated, annihilated, and driven by external fields. This property makes them an attractive candidate for future information carriers.

They also form a periodic structure with hexagonal rotational symmetry, known as skyrmion crystals. Since the noncoplanar spin textures of skyrmions induces an emergent gauge field on magnons, which are quanta of spin waves, they provide a rich platform for topological magnonics. With the bulk-boundary correspondence as a guiding principle, the nontrivial magnon band topology leads to topologically protected chiral edge states. Crucially, the magnonic chiral edge states are robust against impurities due to the absence of backscattering, thus promising for dissipationless spin transports. Furthermore, the recently discovered higher-order topological phases in electronic systems open up a new possibility of magnonic corner states, which could broaden functionalities of topological magnonics.

In this thesis, we investigate the topological properties of magnon excitations in magnetic skyrmion crystals. The central idea of the thesis is to propose an external control over the magnon band topology, which can be experimentally realized. The main result of the thesis is divided into three research projects: (i) Magnetic-field driven topological phase transition; (ii) Laser-driven skyrmion motion and topological phase transition; (iii) Magnonic corner states protected by the magnonic quadrupole moment.

In (i), we study the magnetic field dependence of magnon band structures in skyrmion crystals. We find that the magnonic topological phase transition occurs at the critical magnetic field, which is associated with the band inversion between characteristic magnetic excitations of skyrmions. We also show that the chiral magnetic edge states can be turned on and off by external magnetic fields.

In (ii), we discuss the classical spin dynamics of skyrmion crystals under circularly polarized lasers with terahertz frequencies, focusing on a skyrmion-hosting multiferroic material. We show that skyrmions carrying the in-plane electric polarization are driven by circularly polarized laser, with its direction controlled by the chirality of laser. We also demonstrate the laser driven topological phase transition arising from the effective magnetic field induced by the laser, which is consistent with the Floquet theory applied to magnons.

In (iii), we extend the magnonic topological phases to higher order topology by introducing the magnonic quadrupole moment. We show that skyrmion crystals support a nontrivial magnonic quadrupole moment, whose hallmark signature is the topologically protected magnonic corner states. We demonstrate that the magnonic corner states emerge with edge-localized objects carrying fractional topological charges, which are stabilized at low magnetic fields.

Acknowledgment

I am deeply grateful to Prof. Ogata and Dr. Matsuura for insightful advices and comments on various parts of this thesis. Without their help, it was not possible to write up the thesis in an organized structure. Also, I appreciate that the comfortable environment of laboratory and good computing resources helped me a lot over five years of the Ph.D. course.

The research projects presented in this thesis are collaborations with a research group led by Prof. Loss and Prof. Klinovaja at University of Basel in Switzerland. I thank Prof. Loss and Prof. Klinovaja for their hospitality and stimulating discussions during my stays in Basel for eight months in total. Among their group members at University of Basel, I give many thanks to Sebastian Alejandro Diaz Santiago, as he helped me settle down at Basel and kindly supported me to start a new project on magnetic skyrmions. He was also a great advisor not only for research projects but also for more personal matters such as careers in academia outside Japan. I also thank the MERIT program and the young researchers' exchange program between Japan and Switzerland 2018 for providing a valuable opportunity to visit University of Basel.

Last but not the least, I would like to thank my parents and family members for continuous supports and giving me opportunities to study as much as I want. During the unusual time under COVID-19 calamity, they have provided a shelter to focus on the thesis, which was truly essential under pressures.

List of Publication

1. Sebastián A. Díaz, Tomoki Hirosawa, Daniel Loss, and Christina Psaroudaki
   "Spin Wave Radiation by a Topological Charge Dipole",
   Nano Lett. **20**, 6556 (2020).

2. Sebastián A. Díaz, Tomoki Hirosawa, Jelena Klinovaja, and Daniel Loss,
   "Chiral magnonic edge states in ferromagnetic skyrmion crystals controlled by magnetic fields",
   Phys. Rev. Research **2**, 013231 (2020).

3. Tomoki Hirosawa, Sebastián A. Díaz, Jelena Klinovaja, and Daniel Loss,
   "Magnonic Quadrupole Topological Insulator in Antiskyrmion Crystals",
   Phys. Rev. Lett. **125**, 207204 (2020).

4. Tomoki Hirosawa, Sebastián A. Díaz, Jelena Klinovaja, and Daniel Loss,
   "Laser-controlled real and reciprocal space topology in multiferroic insulators",
   To be submitted in an academic publication.

Contents

Chapter 1

Introduction

In Chapter 1, three important topics of this thesis are reviewed, namely, topological phases of matter, multipole moments and higher-order topological phases, and magnetic skyrmions. In Section 1.1, we introduce the theoretical basis of topological phases of matter and its formulation in magnonic systems, which are quanta of spin waves in magnetic systems. We show that the topological band theory for magnons is almost the same as electronic systems except for the difference arising from the bosonic nature of magnons. In Section 1.2, we introduce higher-order topological phase that were originally proposed in electronic systems. The relationship between multipole moments in classical electromagnetism and higher-order topological phases is illustrated. In Section 1.3, we provide a brief review of magnetic skyrmion, a topological solitonic particle realized in magnetic systems. As an introduction for later chapters, the magnon band spectrum of isolated skyrmions and a periodic array of magnetic skyrmions, called skyrmion crystals, are explained in details. At the end of this chapter, the outline of the thesis is provided in Section 1.4.

1.1 Topological phases of matter

Topological phases of matter has become a central concept in condensed matter physics these days. It provides us a new classification scheme of Bloch wave functions based on the feasibility of smooth deformations between each other. Surprisingly, it was found that two insulating states with the same energy dispersion cannot always be smoothly deformed to each other. This is due to geometric phases of wave functions acquired over a noncontractible loop across the Brillouin zone, which forms a torus in reciprocal space [1].

One example of insulating phases is the vacuum, which is defined to be a "trivial" phase. Over the last decade, enormous research efforts have been put into the search for "nontrivial" phases that are not topologically equivalent to the vacuum. The concept of band topology is far-reaching as it can be applied to any periodic systems including quantum and classical systems, and fermions and bosons. In Section 1.1, we introduce the topological band theory for magnonic systems based on Ref. [2].

1.1.1   Brief history

One of the early examples of topologically nontrivial phases is the quantum Hall state realized in a two-dimensional system under strong magnetic fields [3, 4]. When the Fermi energy lies in the energy gap, the quantization of Landau levels leads to the integer quantized Hall conductivity

$$\sigma_{xy} = Ne^2/h, \tag{1.1}$$

where N is the occupied number of Landau levels [5]. However, this naive picture could not explain the remarkable precision of the integer quantum Hall effect under disorder. The relationship between the Hall conductivity and the topological invariant was first demonstrated in the TKNN formula [6]. They have shown that the integer coefficient of Hall conductivity is equal to the Chern number of occupied bands, given by

$$N = \sum_m \frac{1}{2\pi} \int d^2\mathbf{k}\, \nabla \times \boldsymbol{\mathcal{A}}_m, \tag{1.2}$$

with $\boldsymbol{\mathcal{A}}_m = i \langle u_m | \nabla_k | u_m \rangle$ denoting the Berry connection of an occupied state $|u_m\rangle$ [1, 7]. Mathematically, this is a topological classification of mapping from the torus in reciprocal space to the Hamiltonian $H(k)$, which is characterized by integers [8, 9]. As long as the band gap remains open, the topological invariant does not change, thus protecting the quantization of the Hall conductivity against disorder.

An important consequence of the nontrivial topological invariant is the presence of edge localized states. This is the manifestation of the bulk-boundary correspondence, connecting the bulk topological invariants with gapless boundary states [10, 11]. A physically intuitive argument is that a band gap must close at boundaries between systems with different topological invariants, resulting in gapless states localized at boundaries [12–15]. In the integer quantum Hall state, it was shown that edge state carries the integer quantized current [15]. Furthermore, they propagate in only one direction along sample edges. The chiral propagation of edge states prohibits the backscattering, providing another mechanism for the robustness of the quantized Hall conductivity.

The quantum Hall state is a topological phase in time-reversal symmetry broken systems. It is also possible to realize a topological phase with the time-reversal symmetry. A prominent example is Z_2 topological insulators [16–18]. Here, the spin-orbit coupling plays a crucial role to lift the degeneracy between spin-up and spin-down states without breaking the time-reversal symmetry. This allows electrons with opposite spins to move in opposite directions, first proposed as the mechanism for the intrinsic spin-Hall effect [19–21]. In 2005, the first example of Z_2 topological insulators was proposed by Kane and Mele [22, 23]. They considered the effect of the spin-orbit interaction in graphene and found a novel insulating phase hosting edge states of oppositely moving electrons with opposite spins due to the spin-momentum locking [22]. This model is a spinful counterpart of the Haldane model, which was the first realization of the Chern insulator (quantum Hall state) without external magnetic fields [24]. The main difference from the quantum Hall state is that edge states are not chiral but helical in Z_2 topological insulators as the time-reversal symmetry is conserved. Furthermore, edge states have a

band crossing at time-reversal symmetric points, which cannot be lifted by time-reversal symmetric perturbations. Therefore, helical edge states in Z_2 topological insulators are also robust against disorder as long as the time-reversal symmetry is conserved. The discovery of topological insulators opens up a possibility of controlled and robust transports on boundaries.

1.1.2 Magnonic Topological Phases

Magnons are quanta of spin waves that carries the magnetic dipole moment in magnetic systems. Since magnons are charge neutral particles, they are free from heat dissipations due to Ohmic losses. This property makes them potential candidates for next generation logic devices. In the field of magnon spintronics, spin currents carried by magnons are employed as information carriers [25]. For technological applications, it is important to control the wavelength and resonance frequency of magnons. A traditional approach is to design a magnonic crystal, consisting of a periodically arranged ferromagnetic materials [26]. A major challenge is that magnon dispersion relations are highly sensitive to the geometry and magnetization of devices. Although it provides a possibility of re-programmable devices, it is difficult to prepare a periodic pattern of magnetic systems without any defect and anisotropy in a nanoscale device. In order to overcome this difficulty, the concept of topological magnonics was proposed as an alternative route [2, 27]. Robustness of topologically protected edge states allows a better control of magnons and spin currents regardless of sample geometries, thus offering a great potential for spintronic applications [28].

Early examples of topological phases of magnons was the discovery of the magnon thermal Hall effect [29–33]. Since magnons are collective excitations of localized spins with no electric charge, external magnetic fields would not induce a Lorentz force. Hence, it was an important problem to find a vector potential coupled to magnons that causes its transverse motion. In earlier literatures, it was shown that the emergent gauge field from a scalar spin chirality $\boldsymbol{S}_i \cdot \boldsymbol{S}_j \times \boldsymbol{S}_k$ could result in a finite Berry curvature and a similar expression to the TKNN formula was derived for thermal Hall conductivity κ_{xy} [6, 29, 34]. The magnon thermal Hall effect was first reported in an insulating collinear ferromagnet $Lu_2V_2O_7$ [30], where a non-zero Dzyaloshinskii-Moriya interaction in the pyrochlore lattice acts as a gauge field [35–37]. Furthermore, it was clarified that contributions from chiral magnon edge currents are essential for the magnon thermal Hall effect analogously to edge current contributions in the integer quantum Hall effect [15, 31, 32]. Finally, the first theoretical models of magnonic topological (Chern) insulators were proposed in yttrium iron garnet and $Lu_2V_2O_7$ [2, 27].

The correspondence between topological phases in electronic and magnonic systems does not end here. Many efforts have been made in the search for topological phases of magnons [38–48]. Magnonic analogues of topological semimetal phases, which is described by the Dirac/Weyl Hamiltonian in the low energy limit [49–51], were also introduced [52–60]. In particular, the discovery of two-dimensional honeycomb ferromagnets in van der Waals materials provides experimentally available platforms to realize the

magnonic counterpart of graphene layers [61–65]. The nontrivial topology of magnonic systems is often induced by the Dzyaloshinskii-Moriya interaction originated from the spin-orbit coupling [35, 36]. It is also possible to introduce geometric phases of magnons under electric field due to the Aharonov-Casher effect [66]. Employing this effect, it was shown that magnons form Lanudau levels under large electric field gradient, leading to the magnonic quantum Hall effect [67, 68]. Since the time-reversal symmetry is broken in magnetic systems, topological phases of magnons are usually characterized by the Chern number and support chiral edge states. However, magnonic topological phases characterized by the Z_2 topological invariant can be realized under the pseudo-time-reversal symmetry that guarantees the existence of bosonic Kramers pairs [69, 70]. In this case, helical edge states are obtained with the magnon spin-momentum locking [71].

1.1.3   Magnon Hamiltonian for noncollinear spin structures

Magnons are described as quantum fluctuations about classical ground-state spin textures. For this purpose, we employ the Holstein-Primakoff (HP) transformation generalized for noncollinear spin textures [72, 73]. Let us consider a generic spin lattice Hamiltonian:

$$H \;=\; \tfrac{1}{2} \sum_{\langle \boldsymbol{r},\boldsymbol{r}'\rangle} (-J_{\boldsymbol{r},\boldsymbol{r}'}\boldsymbol{S_r} \cdot \boldsymbol{S_{r'}} + \boldsymbol{D_{r,r'}} \cdot \boldsymbol{S_r} \times \boldsymbol{S_{r'}}) - g\mu_B B_z \sum_{\boldsymbol{r}} \boldsymbol{S_r} \cdot \hat{\boldsymbol{z}} , \qquad (1.3)$$

where $\boldsymbol{S_r}$ is a spin operator at site $\boldsymbol{r}$ on a square lattice with lattice constant a. The nearest-neighbor coupling includes ferromagnetic exchange $J_{\boldsymbol{r},\boldsymbol{r}'} = J > 0$, and the Dzyaloshinskii-Moriya interaction $\boldsymbol{D_{r,r'}}$. The third term corresponds to the Zeeman energy under the external magnetic field $B_z\hat{\boldsymbol{z}}$, where g and μ_B denote the g-factor and Bohr magneton, respectively. We should note that this is a minimal model for skymion-hosting materials with the Dzyaloshinskii-Moriya interaction vector determined by the crystalline symmetries.

Now, we perform the HP transformation to write Eq. (1.3) in terms of bosonic operators. As a first step, we need to define spin operators with respect to the local orthonormal basis $(\boldsymbol{e_r^1}, \boldsymbol{e_r^2}, \boldsymbol{m_r})$, where $\boldsymbol{m_r}$ is a unit vector parallel to the ground-state spin texture and $\boldsymbol{e_r^1} \times \boldsymbol{e_r^2} = \boldsymbol{m_r}$. In this local basis, the spin operators read $\boldsymbol{S_r} = \mathsf{S}_{\boldsymbol{r}}^1 \boldsymbol{e_r^1} + \mathsf{S}_{\boldsymbol{r}}^2 \boldsymbol{e_r^2} + \mathsf{S}_{\boldsymbol{r}}^3 \boldsymbol{m_r}$, which are transformed as

$$\begin{aligned}
\mathsf{S}_{\boldsymbol{r}}^+ &= (2S - a_{\boldsymbol{r}}^\dagger a_{\boldsymbol{r}})^{\frac{1}{2}} a_{\boldsymbol{r}}, \\
\mathsf{S}_{\boldsymbol{r}}^- &= a_{\boldsymbol{r}}^\dagger (2S - a_{\boldsymbol{r}}^\dagger a_{\boldsymbol{r}})^{\frac{1}{2}}, \\
\mathsf{S}_{\boldsymbol{r}}^3 &= S - a_{\boldsymbol{r}}^\dagger a_{\boldsymbol{r}},
\end{aligned} \qquad (1.4)$$

where $\mathsf{S}_{\boldsymbol{r}}^\pm = \mathsf{S}_{\boldsymbol{r}}^1 \pm i\mathsf{S}_{\boldsymbol{r}}^2$, and $a_{\boldsymbol{r}}$, $a_{\boldsymbol{r}}^\dagger$ are the HP bosonic operators. Assuming $S \gg 1$, the Hamiltonian is expanded as a series in $1/S$. Here, we introduce a matrix for bilinear terms in spin operators:

$$\mathsf{S}_{\boldsymbol{r}}^a \mathsf{S}_{\boldsymbol{r}'}^b = \begin{pmatrix} \mathsf{S}_{\boldsymbol{r}}^1 \mathsf{S}_{\boldsymbol{r}'}^1 & \mathsf{S}_{\boldsymbol{r}}^2 \mathsf{S}_{\boldsymbol{r}'}^1 & \mathsf{S}_{\boldsymbol{r}}^3 \mathsf{S}_{\boldsymbol{r}'}^1 \\ \mathsf{S}_{\boldsymbol{r}}^1 \mathsf{S}_{\boldsymbol{r}'}^2 & \mathsf{S}_{\boldsymbol{r}}^2 \mathsf{S}_{\boldsymbol{r}'}^2 & \mathsf{S}_{\boldsymbol{r}}^3 \mathsf{S}_{\boldsymbol{r}'}^2 \\ \mathsf{S}_{\boldsymbol{r}}^1 \mathsf{S}_{\boldsymbol{r}'}^3 & \mathsf{S}_{\boldsymbol{r}}^2 \mathsf{S}_{\boldsymbol{r}'}^3 & \mathsf{S}_{\boldsymbol{r}}^3 \mathsf{S}_{\boldsymbol{r}'}^3 \end{pmatrix}_{ab} , \qquad (1.5)$$

for $a, b = 1, 2, 3$. Using Eq. (1.4), each bilinear term is expanded as

$$
\begin{aligned}
\mathsf{S}_{\boldsymbol{r}}^a \mathsf{S}_{\boldsymbol{r'}}^b &= S^2 \delta_{a3}\delta_{b3} + S^{3/2}
\begin{pmatrix}
0 & 0 & \frac{a_{\boldsymbol{r'}} + a_{\boldsymbol{r'}}^\dagger}{\sqrt{2}} \\
0 & 0 & \frac{i(-a_{\boldsymbol{r'}} + a_{\boldsymbol{r'}}^\dagger)}{\sqrt{2}} \\
\frac{a_{\boldsymbol{r}} + a_{\boldsymbol{r}}^\dagger}{\sqrt{2}} & \frac{i(-a_{\boldsymbol{r}} + a_{\boldsymbol{r}}^\dagger)}{\sqrt{2}} & 0
\end{pmatrix}_{ab} \\
&+ S
\begin{pmatrix}
\frac{1}{2}(a_{\boldsymbol{r}}^\dagger a_{\boldsymbol{r'}}^\dagger + a_{\boldsymbol{r}}^\dagger a_{\boldsymbol{r'}}) + \text{c.c} & \frac{i}{2}(a_{\boldsymbol{r}}^\dagger a_{\boldsymbol{r'}}^\dagger + a_{\boldsymbol{r}}^\dagger a_{\boldsymbol{r'}}) + \text{c.c} & 0 \\
-\frac{i}{2}(-a_{\boldsymbol{r}}^\dagger a_{\boldsymbol{r'}}^\dagger + a_{\boldsymbol{r}}^\dagger a_{\boldsymbol{r'}}) + \text{c.c} & \frac{1}{2}(-a_{\boldsymbol{r}} a_{\boldsymbol{r'}} + a_{\boldsymbol{r}}^\dagger a_{\boldsymbol{r'}}) + \text{c.c} & 0 \\
0 & 0 & -a_{\boldsymbol{r}}^\dagger a_{\boldsymbol{r}} - a_{\boldsymbol{r'}}^\dagger a_{\boldsymbol{r'}}
\end{pmatrix}_{ab} \\
&+ O(S^{\frac{1}{2}}) + \cdots.
\end{aligned}
\tag{1.6}
$$

The constant term proportional to S^2 corresponds to the total energy of classical ground state, while the linear term with respect to bosonic operators vanishes as shown below. Hence, the lowest order contribution in magnon operators are bilinear terms proportional to S, which corresponds to a single-particle picture of magnons (linear spin wave approximation). Throughout this thesis, we treat magnons up to bilinear terms by neglecting higher order contributions. But, the effect of magnon-magnon interactions arising from higher order contributions are discussed in Section 5.5.4.

Here, we show that the linear term with respect to magnon operators vanishes for the classical ground-state spin textures. Considering a two spin system with $H = -J\boldsymbol{S}_{\boldsymbol{r}} \cdot \boldsymbol{S}_{\boldsymbol{r'}}$, the spin wave Hamiltonian up to the linear order term is obtained by HP transformation as

$$
H_{\text{SW}} = -J\Big[S^2 \boldsymbol{m}_{\boldsymbol{r}} \cdot \boldsymbol{m}_{\boldsymbol{r'}} + S^{3/2}\{(\boldsymbol{e}_{\boldsymbol{r}}^+ \cdot \boldsymbol{m}_{\boldsymbol{r'}})a_{\boldsymbol{r}}^\dagger + \text{c.c.} + (\boldsymbol{m}_{\boldsymbol{r}} \cdot \boldsymbol{e}_{\boldsymbol{r'}}^+)a_{\boldsymbol{r'}}^\dagger + \text{c.c.}\} + O(S)\Big],
\tag{1.7}
$$

where $\boldsymbol{e}_{\boldsymbol{r}}^+ = (\boldsymbol{e}_{\boldsymbol{r}}^1 + i\boldsymbol{e}_{\boldsymbol{r}}^2)/\sqrt{2}$ and $\boldsymbol{m}_{\boldsymbol{r}}$ represents a unit vector parallel to the classical ground-state spin texture at site $\boldsymbol{r}$. The first term, which is the zeroth order term in magnon operators, gives the total energy of classical ground-state $E_{\text{cl}} = -JS^2 \boldsymbol{m}_{\boldsymbol{r}} \cdot \boldsymbol{m}_{\boldsymbol{r'}}$. The linear order term proportional to $S^{\frac{3}{2}}$ is then given as

$$
H_{\text{SW}}^{(1)} = \frac{1}{\sqrt{S}}\Big[\frac{\partial E_{\text{cl}}}{\partial \boldsymbol{m}_{\boldsymbol{r}}} \cdot (\boldsymbol{e}_{\boldsymbol{r'}}^+ a_{\boldsymbol{r'}}^\dagger + \text{c.c.}) + \frac{\partial E_{\text{cl}}}{\partial \boldsymbol{m}_{\boldsymbol{r'}}} \cdot (\boldsymbol{e}_{\boldsymbol{r}}^+ a_{\boldsymbol{r}}^\dagger + \text{c.c.})\Big] = 0.
\tag{1.8}
$$

The last equality follows from the fact that $\frac{\partial E_{\text{cl}}}{\partial \boldsymbol{m}_{\boldsymbol{r}}} = \frac{\partial E_{\text{cl}}}{\partial \boldsymbol{m}_{\boldsymbol{r'}}} = 0$ for the classical ground state. The equivalent identity holds for any bilinear terms of spin operators.

From Eq. (1.6), we notice that magnon-number nonconserving terms ($a_{\boldsymbol{r}} a_{\boldsymbol{r'}}$, $a_{\boldsymbol{r}}^\dagger a_{\boldsymbol{r'}}^\dagger$) are obtained from the in-plane component of $\mathsf{S}_{\boldsymbol{r}}$ and $\mathsf{S}_{\boldsymbol{r'}}$. As a result, magnon Hamiltonians for noncollinear spin structures take the form of Bogoliubov-de Gennes (BdG) Hamiltonian, which is known for the mean-field description of superconductors [74].

We derive the BdG form of magnon Hamiltonian from Eq. (1.3). When the classical ground-state spin texture is spatially periodic, crystal momentum $\boldsymbol{k}$ can be introduced. Here, the position vector is partitioned into $\boldsymbol{r} = \boldsymbol{R} + \boldsymbol{r}_i$, with a lattice vector of magnetic unit cells and a position vector inside a unit cell represented by $\boldsymbol{R}$ and $\boldsymbol{r}_i$, respectively.

The Fourier transform is then performed by $a_{\boldsymbol{k},i} = 1/\sqrt{N}\sum_{\boldsymbol{R}}e^{-\boldsymbol{k}\cdot(\boldsymbol{R}+\boldsymbol{r}_i)}a_{\boldsymbol{r}}$, where N is the total number of spins in the magnetic unit cell. The magnon Hamiltonian is derived as [75, 76]

$$H_{\text{sw}} = \frac{S}{2}\sum_{\boldsymbol{k}}\psi_{\boldsymbol{k}i}^{\dagger}H_{ij}(\boldsymbol{k})\psi_{\boldsymbol{k}j} + \mathcal{E}_0 , \tag{1.9}$$

with

$$H_{ij}(\boldsymbol{k}) = \begin{pmatrix} \Omega_{ij}(\boldsymbol{k}) & \Delta_{ij}(\boldsymbol{k}) \\ \Delta_{ij}^{*}(-\boldsymbol{k}) & \Omega_{ij}^{*}(-\boldsymbol{k}) \end{pmatrix} , \tag{1.10}$$

where $\psi_{\boldsymbol{k}i} = (a_{\boldsymbol{k}i}, a_{-\boldsymbol{k}i}^{\dagger})^T$ and $\mathcal{E}_0 = -\frac{1}{2}NS^2\sum_i\Lambda_i$ with $i = 1,\ldots,N$. Each expression is given by

$$\Lambda_i(\boldsymbol{k}) = \sum_{j}[J_{ij}(\boldsymbol{k}=0)\boldsymbol{m}_i\cdot\boldsymbol{m}_j - \boldsymbol{D}_{ij}(\boldsymbol{k}=0)\cdot\boldsymbol{m}_i\times\boldsymbol{m}_j] + bJ\hat{\boldsymbol{z}}\cdot\boldsymbol{m}_i,$$

$$\Omega_{ij}(\boldsymbol{k}) = \delta_{ij}\Lambda_i + \frac{1}{2}[-J_{ij}(\boldsymbol{k})\boldsymbol{e}_i^{+}\cdot\boldsymbol{e}_j^{-} + \boldsymbol{D}_{ij}(\boldsymbol{k})\cdot\boldsymbol{e}_i^{+}\times\boldsymbol{e}_j^{-}], \tag{1.11}$$

$$\Delta_{ij}(\boldsymbol{k}) = \frac{1}{2}[-J_{ij}(\boldsymbol{k})\boldsymbol{e}_i^{+}\cdot\boldsymbol{e}_j^{+} + \boldsymbol{D}_{ij}(\boldsymbol{k})\cdot\boldsymbol{e}_i^{+}\times\boldsymbol{e}_j^{+}],$$

with $J_{ij}(\boldsymbol{k}) = \sum_{\boldsymbol{R}}J_{\boldsymbol{R}+\boldsymbol{r}_i,\boldsymbol{r}_j}e^{-i\boldsymbol{k}\cdot(\boldsymbol{R}+\boldsymbol{r}_i-\boldsymbol{r}_j)}$, $\boldsymbol{D}_{ij}(\boldsymbol{k}) = \sum_{\boldsymbol{R}}\boldsymbol{D}_{\boldsymbol{R}+\boldsymbol{r}_i,\boldsymbol{r}_j}e^{-i\boldsymbol{k}\cdot(\boldsymbol{R}+\boldsymbol{r}_i-\boldsymbol{r}_j)}$, $b = \frac{g\mu_B B_z}{JS}$, and $\boldsymbol{e}_{\boldsymbol{r}}^{\pm} = \boldsymbol{e}_{\boldsymbol{r}}^1 \pm i\boldsymbol{e}_{\boldsymbol{r}}^2$.

The magnon BdG Hamiltonian of Eq. (1.10) can be diagonalized by the Bogoliubov transformation as usual, but we need to account for the bosonic commutation relations. This is carried out by diagonalizing the spin wave Hamiltonian with a paraunitary matrix $T_{\boldsymbol{k}}$. By definition, a paraunitary matrix satisfies $T_{\boldsymbol{k}}^{\dagger}\Sigma T_{\boldsymbol{k}} = T_{\boldsymbol{k}}\Sigma T_{\boldsymbol{k}}^{\dagger} = \Sigma$ with Σ defined as

$$\Sigma = \begin{pmatrix} \mathbb{1}_{N\times N} & 0 \\ 0 & -\mathbb{1}_{N\times N} \end{pmatrix} , \tag{1.12}$$

where $\mathbb{1}_{N\times N}$ is the identity matrix of order N. The diagonalized spin wave Hamiltonian is given by

$$H_{\text{sw}} = S\sum_{\lambda,\boldsymbol{k}}\mathcal{E}_{\lambda}(\boldsymbol{k})\left(\alpha_{\boldsymbol{k}\lambda}^{\dagger}\alpha_{\boldsymbol{k}\lambda} + \tfrac{1}{2}\right) + \mathcal{E}_0 , \tag{1.13}$$

where λ is the index for each magnon mode, $\mathcal{E}_{\lambda}(\boldsymbol{k})$ is the corresponding eigenvalue, and $(a_{\boldsymbol{k}}, a_{-\boldsymbol{k}}^{\dagger})^T = T_{\boldsymbol{k}}(\alpha_{\boldsymbol{k}}, \alpha_{-\boldsymbol{k}}^{\dagger})^T$. We use the numerical diagonalization method described in Ref. [77] to obtain $T_{\boldsymbol{k}}$ and $\mathcal{E}_{\lambda}(\boldsymbol{k})$.

Since the BdG Hamiltonian has a particle-hole symmetry, "particle" and "hole" bands can be defined in the magnon BdG Hamiltonian. Using the paraunitary matrix $T_{\boldsymbol{k}}$, we have [2]

$$H(\boldsymbol{k})T_{\boldsymbol{k}} = \Sigma T_{\boldsymbol{k}}\begin{pmatrix} \mathcal{E}_{\lambda}(\boldsymbol{k}) & 0 \\ 0 & -\mathcal{E}_{\lambda}(-\boldsymbol{k}) \end{pmatrix} . \tag{1.14}$$

In this theis, we refer to the upper subblock as "particle" bands and the lower subblock as "hole" bands. Although there is no physical "hole" bands in magnon spectrum, this convention is convenient for discussions of topological magnon bands in Section 1.1.4.

1.1.4 Berry curvature and Chern number

Analogously to the topological band theory of electrons, topological properties of magnon bands are characterized by the Chern number in reciprocal space. The main difference from electronic systems lies in the bosonic nature of magnons and paraunitary property of $T_{\boldsymbol{k}}$.

The Berry connection of j-th magnon band was defined in Ref. [2] as

$$\mathcal{A}^j_\nu(\boldsymbol{k}) = \mathrm{tr}[iV_j\Sigma T^\dagger_{\boldsymbol{k}}\Sigma\partial_{k_\nu}T_{\boldsymbol{k}}] = \mathrm{tr}[iV_jT^{-1}_{\boldsymbol{k}}\partial_{k_\nu}T_{\boldsymbol{k}}], \tag{1.15}$$

where V_j is a $2N \times 2N$ matrix whose matrix element is unity only at the j-th diagonal element and zero otherwise. The second equality was obtained from the paraunitary identity $\Sigma T^\dagger_{\boldsymbol{k}}\Sigma T_{\boldsymbol{k}} = \Sigma^2 = \mathbb{1}_{2N\times 2N}$. In addition, the imaginary part of the Berry connection is given as

$$\begin{aligned}
\mathrm{Im}[\mathcal{A}^j_\nu(\boldsymbol{k})] &= \mathrm{Re}\left(\mathrm{tr}[V_jT^{-1}_{\boldsymbol{k}}\partial_{k_\nu}T_{\boldsymbol{k}}]\right) = \frac{1}{2}\,\mathrm{tr}\left[V_jT^{-1}_{\boldsymbol{k}}\partial_{k_\nu}T_{\boldsymbol{k}} + (V_jT^{-1}_{\boldsymbol{k}}\partial_{k_\nu}T_{\boldsymbol{k}})^\dagger\right] \\
&= \frac{1}{2}\,\mathrm{tr}[V_jT^{-1}_{\boldsymbol{k}}\partial_{k_\nu}T_{\boldsymbol{k}} + \Sigma\partial_{k_\nu}T^{-1}_{\boldsymbol{k}}T_{\boldsymbol{k}}\Sigma V_j] = \frac{1}{2}\mathrm{tr}[V_j\partial_{k_\nu}(T^{-1}_{\boldsymbol{k}}T_{\boldsymbol{k}})] \\
&= 0. \tag{1.16}
\end{aligned}$$

Hence, the Berry connection is purely real. The Chern number is obtained by integrating the Berry curvature $\Omega_j(\boldsymbol{k})$ over the first Brillouin zone.

$$\begin{aligned}
C_j &= \int_{\mathrm{BZ}}\frac{d\boldsymbol{k}}{2\pi}\Omega_j(\boldsymbol{k}) = \int_{\mathrm{BZ}}\frac{d\boldsymbol{k}}{2\pi}\left[\partial_{k_x}\mathcal{A}^j_y(\boldsymbol{k}) - \partial_{k_y}\mathcal{A}^j_x(\boldsymbol{k})\right] \\
&= \int_{\mathrm{BZ}}\frac{d\boldsymbol{k}}{2\pi}\,i\mathrm{tr}[V_j\partial_{k_x}T^{-1}_{\boldsymbol{k}}\partial_{k_y}T_{\boldsymbol{k}} - V_j\partial_{k_y}T^{-1}_{\boldsymbol{k}}\partial_{k_x}T_{\boldsymbol{k}}]. \tag{1.17}
\end{aligned}$$

Here, we should note that the Berry curvature takes the equivalent form to electronic systems but adapted to the paraunitary nature of bosons. Denoting $|t_j(\boldsymbol{k})\rangle$ and $\langle t_j(\boldsymbol{k})|$ is the j-th Bloch wave function in $T_{\boldsymbol{k}}$ and $T^{-1}_{\boldsymbol{k}}$, respectively, it is rewritten as

$$\Omega_j(\boldsymbol{k}) = i\epsilon_{\mu\nu}\left(\frac{\partial}{\partial k_\mu}\langle t_j(\boldsymbol{k})|\right)\left(\frac{\partial}{\partial k_\nu}|t_j(\boldsymbol{k})\rangle\right), \tag{1.18}$$

where $\epsilon_{\mu\nu}$ is the antisymmetric operator.

Following arguments in Ref. [78], we show the quantization of the Chern number of Eq. (1.17). Firstly, it vanishes if the Berry connection $\mathcal{A}^j_\nu(\boldsymbol{k})$ is defined uniquely over the entire Brillouin zone. This is understood from the fact that the torus has no boundary. From the Stokes theorem, $\int_S \nabla \times \boldsymbol{\mathcal{A}} \cdot d\mathbf{S} = \oint_C \boldsymbol{\mathcal{A}} \cdot d\boldsymbol{\ell} = 0$ where $C = \partial S$ is the boundary of surface S. The uniquely defined Berry connection $\mathcal{A}^j_\nu(\boldsymbol{k})$ over the whole Brillouin zone implies that the phase of j-th wave function is fixed globally. For example, we could choose $[T_{\boldsymbol{k}}]_{m,j}$ to be real by multiplying $[T_{\boldsymbol{k}}]^*_{m,j}/|[T_{\boldsymbol{k}}]_{m,j}|$ for some $m = 1,\ldots,2N$. However, this is not possible if $[T_{\boldsymbol{k}}]_{m,j} = 0$ at some $\boldsymbol{k}$. Hence, the Berry connection cannot be defined uniquely when $[T_{\boldsymbol{k}}]_{m,j}$ has a zero in the Brillouin zone for any $m = 1,\ldots,2N$.

In this case, we need to choose different gauges for two subregions of the Brillouin zone so that $[T_{\boldsymbol{k}}]_{m,j}$ has no singular point in each region. At the boundary between these regions, the j-th wave function is related by a unitary transformation

$$T_{\boldsymbol{k}}^{(2)} V_j = T_{\boldsymbol{k}}^{(1)} V_j e^{i\theta_{\boldsymbol{k}}}, \tag{1.19}$$

where the superscript indicates subregions. Similarly, the gauge transformation is given by

$$\boldsymbol{\mathcal{A}}^{j,(2)} = \boldsymbol{\mathcal{A}}^{j,(1)} - \nabla_{\boldsymbol{k}}\theta_{\boldsymbol{k}}. \tag{1.20}$$

Applying the Stokes theorem, the Chern number is obtained as

$$C_j \;\; = \;\; \frac{1}{2\pi} \oint_{\mathrm{C}} d\boldsymbol{k} \cdot (\boldsymbol{\mathcal{A}}^{j,(1)} - \boldsymbol{\mathcal{A}}^{j,(2)}) = \frac{1}{2\pi} \oint_{\mathrm{C}} d\boldsymbol{k} \cdot \nabla_{\boldsymbol{k}}\theta_{\boldsymbol{k}}, \tag{1.21}$$

with C denoting the boundary between two subregions. Since the integration over a closed loop C accumulates a $2\pi n$ phase winding, the Chern number is guaranteed to be integers.

The relationship between the Chern number and the number of chiral edge states is known as the bulk-edge correspondence [10, 11]. It states that the difference between the number of left-moving edge states and right-moving edge states inside the i-th band gap is equal to the total Chern number below it:

$$\sum_{j<i} C_j = N_L - N_R, \tag{1.22}$$

where $N_{L/R}$ is the number of left/right-moving edge states inside the i-th band gap. Since the bulk-edge correspondence does not depend on the fermionic/bosonic nature, Eq. (1.22) also holds in magnonic systems [2].

We also note the sum rule of Chern number [2]:

$$\sum_{n=1}^{N} C_n = \sum_{n=N+1}^{2N} C_n = 0. \tag{1.23}$$

Here, the summation is taken over "particle" bands and "hole" bands, respectively (see Eq. (1.14)). The proof for the sum rule is provided in Appendix A.1. The sum rule is only well-defined if there is no gapless modes at zero energy such as Goldstone modes, so that there is no band touching between "particle" and "hole" bands at $\mathcal{E}(\boldsymbol{k}) = 0$. From the bulk-boundary correspondence, Eq. (1.23) implies that there is no chiral edge states between "particle" and "hole" bands. Therefore, chiral magnonic edge modes can only appear at a positive energy but not at zero energy. A simple explanation is that there is no magnon states with negative energy, as it induces instability of the underlying magnetic structure. Hence, the lowest possible energies of chiral edge states lies between the first and second magnon bands, which are positive values.
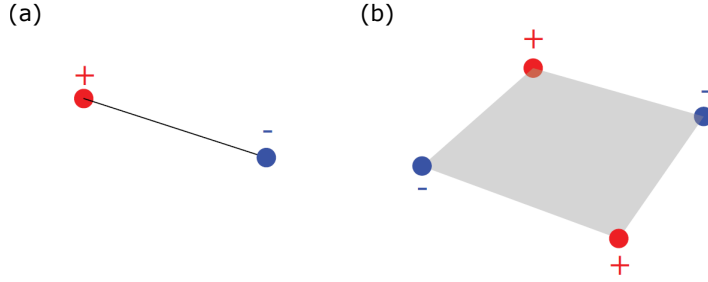
Figure 1.1: **Schematic picture of multipole moments.** Charge distribution for (a) dipole moment and (b) quadrupole moment. Adapted from [80].

1.2 Multipole moments and higher-order topological phases

In Section 1.2, we extend the concept of topological phases of matter to higher orders [79–81]. higher-order topological phases in d-dimensional systems are characterized by boundary localized states in $(d-n)$-dimensional space with $n > 1$. For example, second order topological insulators in two-dimensional systems host corner states instead of edge states.

In the seminal work by W. A. Benalcazar, *et al.* [79, 80], the first model of higher-order topological insulators was proposed, which is characterized by higher multipole moments such as quadrupole moment in 2D and octupole moment in 3D. In this section, we review Ref. [80] to introduce the multipole moment in periodic systems, which is generalization of the modern theory of polarization [82–86]. For interested readers, the modern theory of polarization is reviewed in Appendix D. We also show that bulk multipole moments generate lower order multipole moments on boundaries, leading to fractional boundary signatures of higher-order topological phases. This is illustrated by the minimal model realization of quadrupole topological insulator.

1.2.1 Multipole expansion in classical electromagnetism

Following Ref [80], we introduce multipole moments in the classical theory of electromagnetism. Considering the electric potential generated by multipole moments under the open boundary conditions, we derive the equality between the bulk multipole moment and boundary localized multipole moments.

Let us consider a finite system with local electric charge density $\rho(\boldsymbol{r})$. By dividing the system into small volume elements, the multipole moment densities can be defined. The electric potential at $\boldsymbol{r}$ is given by

$$\phi(\boldsymbol{r}) = \frac{1}{4\pi\epsilon} \sum_{\boldsymbol{R}} \int_{v(\boldsymbol{R})} d\boldsymbol{r}' \, \frac{\rho(\boldsymbol{r}' + \boldsymbol{R})}{|\boldsymbol{r} - \boldsymbol{R} - \boldsymbol{r}'|}, \tag{1.24}$$

where ϵ is the dielectric constant and $\boldsymbol{R}$ is the labeling for each volume element with volume $v(\boldsymbol{R})$. Assuming that $v(\boldsymbol{R})$ is much smaller than the whole volume of system, we

have $|\boldsymbol{r}'| \ll |\boldsymbol{r} - \boldsymbol{R}|$ given that $\boldsymbol{r}$ is outside and sufficiently away from the system. The multipole expansion is then performed by expanding the electric potential in powers of $1/|\boldsymbol{r} - \boldsymbol{R}|$ [87]. The multipole moment densities up to quadrupole moments are given as

$$\rho(\boldsymbol{R}) = \frac{1}{v(\boldsymbol{R})} \int_{v(\boldsymbol{R})} d\boldsymbol{r}' \, \rho(\boldsymbol{r}' + \boldsymbol{R}), \tag{1.25}$$

$$p_i(\boldsymbol{R}) = \frac{1}{v(\boldsymbol{R})} \int_{v(\boldsymbol{R})} d\boldsymbol{r}' \, \rho(\boldsymbol{r}' + \boldsymbol{R}) r_i', \tag{1.26}$$

$$q_{ij}(\boldsymbol{R}) = \frac{1}{v(\boldsymbol{R})} \int_{v(\boldsymbol{R})} d\boldsymbol{r}' \, \rho(\boldsymbol{r}' + \boldsymbol{R}) r_i' r_j', \tag{1.27}$$

where p_i and q_{ij} are the dipole and quadrupole moment, which are shown schematically in Fig. 1.1(a) and (b). The electric potential is expanded in terms of multipole moment densities:

$$\phi(\boldsymbol{r}) = \sum_{\ell=0}^{\infty} \phi^\ell(\boldsymbol{r}), \tag{1.28}$$

where the expressions up to the second order are

$$\phi^0(\boldsymbol{r}) = \frac{1}{4\pi\epsilon} \int_V d\boldsymbol{R} \, \rho(\boldsymbol{R}) \frac{1}{|\mathbf{d}|}, \tag{1.29}$$

$$\phi^1(\boldsymbol{r}) = \frac{1}{4\pi\epsilon} \int_V d\boldsymbol{R} \, p_i(\boldsymbol{R}) \frac{d_i}{|\mathbf{d}|^3}, \tag{1.30}$$

$$\phi^2(\boldsymbol{r}) = \frac{1}{4\pi\epsilon} \int_V d\boldsymbol{R} \, q_{ij}(\boldsymbol{R}) \frac{3d_i d_j - |\mathbf{d}|^2 \delta_{ij}}{2|\mathbf{d}|^5}, \tag{1.31}$$

with $\mathbf{d} = \boldsymbol{r} - \boldsymbol{R}$ and summation taken over repeated indices. Here, the position vector to each volume element $\boldsymbol{R}$ is treated as a continuous variable, justified for a small volume element $v(\boldsymbol{R})$ compared to the system volume V.

We should note that the multipole moment is uniquely defined only if all of the lower order moments vanish. For example, the dipole moment cannot be defined uniquely unless a system is charge neutral. If there is a net charge Q, arbitrary shifts in the coordinate axes by $\boldsymbol{r}' = \boldsymbol{r} + \mathbf{D}$ would result in an additional dipole moment

$$\mathbf{p'} = \frac{1}{V_{\text{cell}}} \int_{\text{cell}} dr'^3 \, \boldsymbol{r}' \rho(\boldsymbol{r}') = \mathbf{p} + Q\mathbf{D}. \tag{1.32}$$

So the dipole moment is uniquely defined irrespective of the reference frame only if $Q = 0$. Similarly, the quadruple moment has a physical meaning only if $Q = \mathbf{p} = 0$.

Now, we consider the electric potential in the presence of bulk quadrupole moment with $Q = \mathbf{p} = 0$. In Appendix A.2, the electric potential due to the quadrupole moment $\phi^2(\boldsymbol{r})$ is rewritten as [80]

$$\phi^2(\boldsymbol{r}) = \frac{1}{4\pi\epsilon} \sum_{a,b} \int_{L_{ab}} dR \left(\frac{1}{2} n_i^{(a)} n_j^{(b)} q_{ij} \right) \frac{1}{|\mathbf{d}|} - \frac{1}{4\pi\epsilon} \sum_a \int_{S_a} dR^2 \left(n_i^{(a)} \partial_j q_{ij} \right) \frac{1}{|\mathbf{d}|}$$

$$+ \frac{1}{4\pi\epsilon} \int_V dR^3 \left(\frac{1}{2} \partial_i \partial_j q_{ij} \right) \frac{1}{|\mathbf{d}|}. \tag{1.33}$$
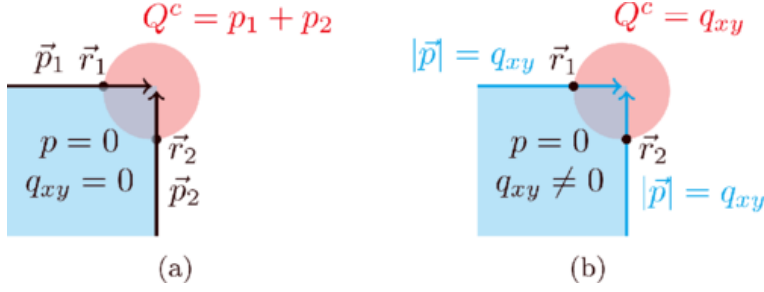
Figure 1.2: **Corner charge induced by higher multipole moments.** In a two-dimensional system with no overall charge and dipole moment, charge accumulation occurs at corners due to (a) a pair of dipole moments localized on edges and (b) bulk quadrupole moment. Adapted from [80].

This expression was derived by assuming a cubic geometry, where S_a represent a surface of cube normal to a unit vector $\hat{n}^{(a)}$ and L_{ab} represent a hinge at the intersections of surfaces S_a and S_b (see Fig. A.1).

From Eqs. (1.29) and (1.33), $\phi^2(\boldsymbol{r})$ can be interpreted as contributions of boundary localized lower multipole moments, which are given as

$$
\begin{aligned}
\lambda_{\text{hinge}}^{a,b} &= \frac{1}{2} n_i^{(a)} n_j^{(b)} q_{ij}, \\
\sigma_{\text{face}}^{a} &= -\partial_j (n_i^{(a)} q_{ij}) = -\partial_j (p_{\text{face},j}^a), \\
\rho_{\text{v}} &= \frac{1}{2} \partial_i \partial_j q_{ij},
\end{aligned}
\tag{1.34}
$$

with $\lambda_{\text{hinge}}^{a,b}$ denoting a charge density per unit length along the hinge where surfaces $S^{(a)}$ and $S^{(b)}$ intersect, σ_{face}^a denoting a bound charge induced by the dipole moment density per unit area $p_{\text{face},j}^a = n_i^{(a)} q_{ij}$ on the surface $S^{(a)}$ perpendicular to $\hat{n}^{(a)}$, and ρ_{v} denoting the volume charge density. Assuming the open boundary condition of a cubic system, the symmetric property of q_{ij} leads to

$$
|\lambda_{\text{hinge}}| = |p_{\text{face},j}| = |q_{ij}|.
\tag{1.35}
$$

As shown in Eqs. (1.33) and (1.34), a quadrupole moment induces a charge on one-dimensional boundaries and a dipole moment on two-dimensional boundaries. By projecting the cubic system to a two-dimensional system within the xy-plane, we get a corner accumulated charge Q^c and an edge localized dipole moment density $\vec{p}$ as shown in Fig. 1.2(b). From Eq. (1.35), we have

$$
|Q^c| = |\vec{p}| = |q_{xy}|.
\tag{1.36}
$$

This is the key equation relating the bulk quadrupole moment to boundary signatures of the corner charge and edge dipole moment. If electrons in crystals support a nonzero

quadrupole moment, we expect the emergence of corner charge and edge dipole moment when the boundary is introduced, leading to the idea of higher-order topological phases.

In contrast, it is also possible to have corner charges without bulk quadrupole moments. Assuming that there is no contributions from higher multipole moments in the bulk of system, Fig. 1.2(a) shows that a corner charge is obtained by the summation of convergent dipole moments from both edges meeting at the corner

$$Q^c = p_1 + p_2. \tag{1.37}$$

Here, edge dipole moments p_1 and p_2 are independent from bulk quadrupole moments. They are simply resulted from the local charge density distribution. The difference from Eq. (1.36) is that both edge dipole moments contributes to the corner charge in Eq. (1.37).

1.2.2   Wannier centers and bulk multipole moments

In the previous section, we have defined multipole moments based on a local charge density. However, the definition of multipole moments needs to be modified in spatially periodic systems. The important point is that the average position of electrons in crystals are only defined up to modulo lattice constant as discussed in Appendix D.1. As a result, bulk multipole moments in crystals have a multivalued property.

In this section, we introduce Wannier functions by following Ref. [86]. They are defined as the Fourier transform of Bloch functions. Crucially, they are eigenstates of position operators in the real space, so the physical meaning of bulk multipole moment in crystals is clarified using the Wannier representation. For example, the bulk polarization can be interpreted as the overall displacement of localized Wannier functions from the center of unit cell. Here, we consider a single band representation of Wannier functions. A multiband formulation of Wanneir functions is explained in Appendix D.2.

Let us consider a n-th band Bloch function $|\psi_{n,\boldsymbol{k}}(\boldsymbol{r})\rangle$ in the periodic gauge

$$|\psi_{n,\boldsymbol{k}+\vec{G}}(\boldsymbol{r})\rangle = |\psi_{n,\boldsymbol{k}}(\boldsymbol{r})\rangle, \tag{1.38}$$

where $\vec{G}$ is the reciprocal lattice vector. Assuming that it is smoothly defined over the entire Brillouin zone, the Wannier function is written as

$$|w_{n,\boldsymbol{R}}\rangle = \frac{V_{\text{cell}}}{(2\pi)^3} \int_{\text{BZ}} dk^3 \, e^{-i\boldsymbol{k}\cdot\boldsymbol{R}} |\psi_{n,\boldsymbol{k}}\rangle, \tag{1.39}$$

$$|\psi_{n,\boldsymbol{k}}\rangle = \sum_{\boldsymbol{R}} e^{i\boldsymbol{k}\cdot\boldsymbol{R}} |w_{n,\boldsymbol{R}}\rangle, \tag{1.40}$$

where $\boldsymbol{R}$ is the lattice vector and V_{cell} is the unit cell volume. While Bloch functions infinitely extend over periodic systems, Wannier functions are exponentially localized within the single unit cell labeled by $\boldsymbol{R}$.

There are several important properties of Wannier functions. Firstly, the Wannier functions are equivalent by translation $w_{n,\boldsymbol{R}}(\boldsymbol{r}) = w_{n,0}(\boldsymbol{r} - \boldsymbol{R})$. Secondly, they form an

orthonormal basis and span the same subspace of the Hilbert space as Bloch functions. Thus, they provide a convenient basis for constructing the tight-binding Hamiltonian in terms of local interactions.

Another important property is that they are eigenstates of position operators. Furthermore, their eigenvalues are the Fourier transform of the Berry connection. In order to derive this property, we apply the position operator to a Wannier function. Noting that $|\psi_{n,\boldsymbol{k}}(\boldsymbol{r})\rangle = e^{i\boldsymbol{k}\cdot\boldsymbol{r}}|u_{n,\boldsymbol{k}}\rangle$, we obtain

$$
\begin{aligned}
(\boldsymbol{r} - \boldsymbol{R})|w_{n,\boldsymbol{R}}\rangle &= \frac{V_{\text{cell}}}{(2\pi)^3}\int_{\text{BZ}} dk^3\,(\boldsymbol{r} - \boldsymbol{R})\,e^{i\boldsymbol{k}\cdot(\boldsymbol{r}-\boldsymbol{R})}|u_{n,\boldsymbol{k}}\rangle \\
&= \frac{V_{\text{cell}}}{(2\pi)^3}\int_{\text{BZ}} dk^3\,(-i\nabla_{\boldsymbol{k}}e^{i\boldsymbol{k}\cdot(\boldsymbol{r}-\boldsymbol{R})})|u_{n,\boldsymbol{k}}\rangle \\
&= \frac{V_{\text{cell}}}{(2\pi)^3}\int_{\text{BZ}} dk^3\,e^{i\boldsymbol{k}\cdot(\boldsymbol{r}-\boldsymbol{R})}(i\nabla_{\boldsymbol{k}}|u_{n,\boldsymbol{k}}\rangle),
\end{aligned}
\tag{1.41}
$$

where we have used an integration by parts for the last equality. Multiplying another Wannier function from left, we obtain

$$
\begin{aligned}
\langle w_{n,0}|(\boldsymbol{r} - \boldsymbol{R})|w_{n,\boldsymbol{R}}\rangle &= \langle w_{n,0}|\boldsymbol{r}|w_{n,\boldsymbol{R}}\rangle \\
&= \frac{V_{\text{cell}}}{(2\pi)^3}\int_{\text{BZ}} dk^3\,e^{-i\boldsymbol{k}\cdot\boldsymbol{R}}\langle u_{n,\boldsymbol{k}}|i\nabla_{\boldsymbol{k}}|u_{n,\boldsymbol{k}}\rangle \\
&= \frac{V_{\text{cell}}}{(2\pi)^3}\int_{\text{BZ}} dk^3\,e^{-i\boldsymbol{k}\cdot\boldsymbol{R}}\mathcal{A}^n(\boldsymbol{k}).
\end{aligned}
\tag{1.42}
$$

The first equality follows from the orthogonality relation $\boldsymbol{R}\langle w_{n,0}|w_{n,\boldsymbol{R}}\rangle = \boldsymbol{R}\delta_{0,\boldsymbol{R}}$. Thus, the expectation value of position operator for n-th band is given by the Fourier transform of its Berry connection. In particular, the diagonal matrix element of position operator is called the Wannier center and given by

$$
\boldsymbol{r}_n = \langle w_{n,0}|\boldsymbol{r}|w_{n,0}\rangle = \frac{V_{\text{cell}}}{(2\pi)^3}\int_{\text{BZ}} dk^3\,\mathcal{A}^n(\boldsymbol{k}).
\tag{1.43}
$$

The above expression is valid if the corresponding energy band is isolated from other bands for the entire Brillouin zone. By generalizing the Berry connection to a multiband structure, the expectation value of position operator for a group of occupied bands is obtained in Eq. (D.37):

$$
\tilde{\boldsymbol{r}} = \frac{V_{\text{cell}}}{(2\pi)^3}\int_{\text{BZ}} dk^3\,\text{tr}[\mathcal{A}(\boldsymbol{k})],
\tag{1.44}
$$

where $\mathcal{A}^{mn}(\boldsymbol{k}) = i\langle u_{n,\boldsymbol{k}}|\nabla_{\boldsymbol{k}}|u_{m,\boldsymbol{k}}\rangle$ with m, n labeling occupied states. Here, we should note that Eq. (1.44) holds even if there are degeneracies of the occupied states at some points in the Brillouin zone.

Noting that the electric polarization is given by the integration of Berry connection in the modern theory of polarization in Eq. (D.5), the electric polarization of periodic systems is simply given frp, Eq. (1.44) as

$$
P_i = -\tilde{r}_i \bmod 1
\tag{1.45}
$$

where we take the lattice constant $a = 1$ and $e = 1$ for simplicity. Here, we explicitly indicate that the electric polarization is only defined up to modulo integers by the gauge transformation.

Higher multipole moments can be defined in an analogous manner using the Wannier representation. In a two-dimensional system, a bulk quadrupole moment can be partitioned into two opposite dipole moments in each half of the unit cell split orthogonal to the dipole moments (see Fig. 1.1(b)). Now, we denote the Wannier centers along the y axis for the right/left half of unit cell as $\tilde{y}_x^{+/-}$. Similarly, the Wannier centers along the x axis for the top/bottom half of unit cell is $\tilde{x}_y^{+/-}$. Then, the bulk quadrupole moment is written as [80]

$$q_{xy} = (\tilde{y}_x^+ \tilde{x}_y^+ + \tilde{y}_x^- \tilde{x}_y^-) \text{ mod } 1. \tag{1.46}$$

This expression provides the topological invariant for reflection symmetric higher-order topological phases with quantized $\tilde{y}_x^{+/-}$ and $\tilde{x}_y^{+/-}$.

1.2.3   Symmetry constraints on bulk quadrupole moment

In the presence of crystalline symmetries, bulk multipole moments become quantized. Without formal arguments (see Ref. [80] for details), we consider the symmetry operation to quadrupole moments derived in Eq. (1.46). In a two-dimensional system with square geometry, the symmetry operation is described by combinations of $\{M_x, M_y, C_4\}$. Since quadrupole moments are only invariant under the tetrahedral subgroup $T(2) = \{1, C_4 M_x, C_4 M_y, C_4^2\}$ [80], they change the sign by $\{M_x, M_y, C_4\}$. The reflection symmetry acts on the Wannier centers for each sector as follows.

$$\tilde{y}_x^{+/-} \overset{M_x}{=} \tilde{y}_x^{+/-},$$
$$\tilde{y}_x^{+/-} \overset{M_y}{=} -\tilde{y}_x^{+/-} \quad \rightarrow \quad \tilde{y}_x^{+/-} = 0, \frac{1}{2} \text{ mod } 1. \tag{1.47}$$

Assuming the lattice constant to be unity, the symmetry constraint implies that the Wannier centers are quantized to be $\tilde{y}_x^{+/-} = 0, \frac{1}{2}$ mod 1. Similarly, we have

$$\tilde{x}_y^{+/-} \overset{M_x}{=} -\tilde{x}_y^{+/-} \quad \rightarrow \quad \tilde{x}_y^{+/-} = 0, \frac{1}{2} \text{ mod } 1,$$
$$\tilde{x}_y^{+/-} \overset{M_y}{=} \tilde{x}_y^{+/-}. \tag{1.48}$$

From Eq. (1.46), quadrupole moments are also quantized in the presence of both M_x and M_y.

$$q_{xy} = \begin{cases} 0, \text{ trivial} \\ \frac{1}{2}, \text{ nontrivial.} \end{cases} \tag{1.49}$$

Crucially, the nontrivial quadrupole moment results in a fractional corner charge Q_c as expected from Eq. (1.36).

In contrast, the C_4 rotational symmetry does not quantize the Wannier centers $\tilde{y}_x^{+/-}$ and $\tilde{x}_y^{+/-}$ but only quantize the bulk quadrupole moment. In this case, the bulk quadrupole
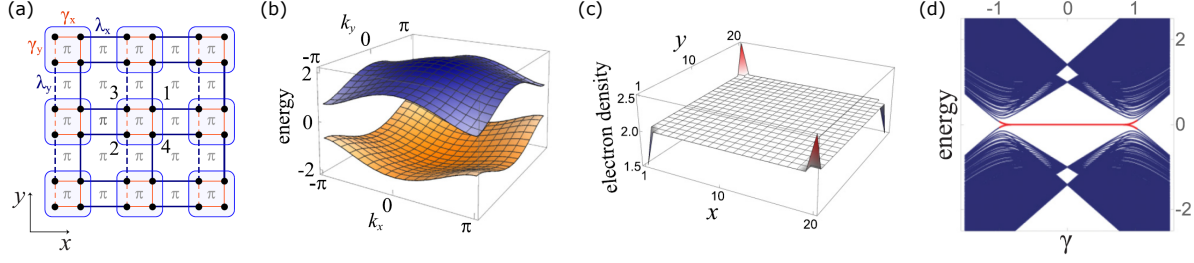
Figure 1.3: **Schematic representation of the minimal model with quadrupole moment and realization of fractional corner charge and corner states.** (a) Tight-binding model with four orbitals in a unit cell indicated by blue squares. Dashed lines imply a negative sign due to the π flux through each plaquette. (b) Band structure at $\gamma/\lambda = 0.5$. (c) Charge density at $T = 0\,\mathrm{K}$ for $\lambda = 1$, $\gamma = 10^{-3}$, and $\delta = 10^{-3}$. (d) Energy spectrum under open boundary conditions as a function of γ at $\lambda = 1$ and $\delta = 0$. Red flat bands represent four degenerate, exponentially localized corner states. They are obtained for $|\gamma/\lambda| < 1$. In (c) and (d), the half-filling condition is assumed. Adapted from [80].

moment is protected by the topology of bulk bands with its index determined by the C_4 eigenvalues [80]. Recently, it was shown that higher-order topological phases protected by rotational symmetries C_n are generally characterized by the Z_n Berry phase, which is computed along a C_n symmetric path in the momentum space [88–90].

1.2.4 Minimal model for quadrupole topological insulator

In Section 1.2.1, we have shown that the quadrupole moment in a bulk of sample induces the corner charge and edge dipole moment in classical theory of electromagnetism, which describes the central idea of higher-order topological phases. In this section, we briefly introduce a simple model that realize a quadrupole topological insulator proposed in Ref. [79, 80]. Our purpose is to illustrate the parallel between classical electromagnetism and higher-order topological phases with bulk quadrupole moments.

The minimal model Hamiltonian is defined in a two-dimensional square lattice. In each unit cell, it contains four spinless orbitals with the following Bloch Hamiltonian matrix

$$h(\boldsymbol{k}) = \begin{pmatrix} 0 & 0 & \gamma + \lambda e^{ik_x} & \gamma + \lambda e^{ik_y} \\ 0 & 0 & -\gamma - \lambda e^{-ik_y} & \gamma + \lambda e^{-ik_x} \\ \gamma + \lambda e^{-ik_x} & -\gamma - \lambda e^{-ik_y} & 0 & 0 \\ \gamma + \lambda e^{ik_x} & \gamma + \lambda e^{ik_y} & 0 & 0 \end{pmatrix}, \qquad (1.50)$$

where γ is the hopping amplitudes inside a unit cell and λ is the hopping amplitudes between nearest neighbors. The negative sign of hopping amplitudes along only one direction is realized by inserting a π flux inside unit cells and spacings between each unit
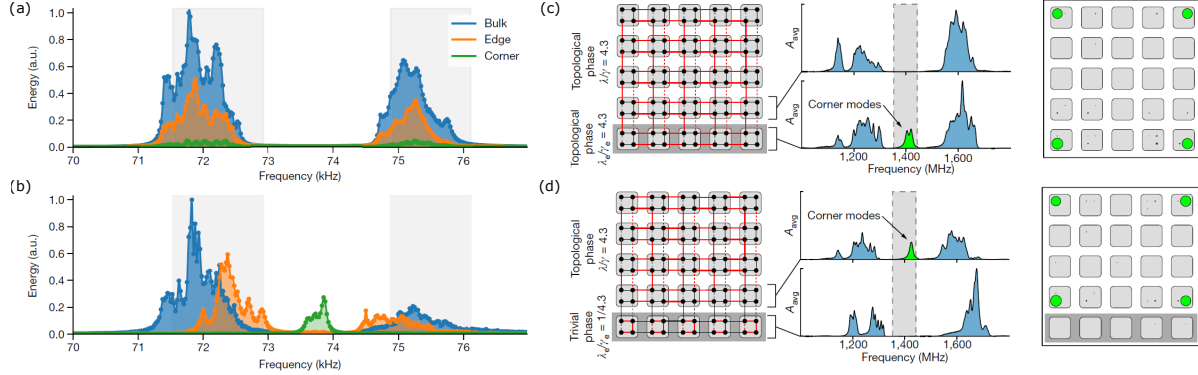
Figure 1.4: **Experimental detection of corner states in quadrupole topological insulators.** (a), (b) Spectrum of phononic crystals made from a mechanical metamaterial for (a) trivial and (b) non-trivial phases. While the trivial phase supports only bulk (blue) and edge (orange) states, corner states (green) are observed inside the band gap in the topologically nontrivial phase. (c), (d) Unit cells in the bottom row undergoes the topological phase transition from (c) nontrivial to (d) trivial phase, resulting in the translation of corner states in the microwave circuit. Left: schematic lattice model with dashed lines indicating the negative hopping. Middle: normalized absorption spectrum showing bulk (blue) and in-gap corner modes (green) for corresponding rows of the array. Right: measured spatial distribution of modes inside the band gap, indicated by shaded region. (a) are (b) are adapted from [91], while (c) and (d) are adapted from [92].

cell as shown schematically in Fig. 1.3(a). The eigenvalue is obtained as

$$\mathcal{E}(\boldsymbol{k}) = \pm\sqrt{\epsilon_x^2(k_x) + \epsilon_y^2(k_y)}, \tag{1.51}$$

where $\epsilon_i(k_i) = \sqrt{\gamma^2 + 2\gamma\lambda\cos(k_i) + \lambda^2}$ for $i = x, y$. The band gap closes at $|\gamma/\lambda| = 1$. Figure 1.3(b) shows the gapped band structure at $\gamma/\lambda = 0.5$.

This model has reflection symmetries, which are respectively defined as

$$\hat{M}_x = i\sigma_1 \otimes \sigma_3,$$
$$\hat{M}_y = i\sigma_1 \otimes \sigma_1, \tag{1.52}$$

where σ_i is the Pauli matrices. The symmetry transformation of Hamiltonian satisfies the following identities.

$$\hat{M}_x h(k_x, k_y)\hat{M}_x^{-1} = h(-k_x, k_y),$$
$$\hat{M}_y h(k_x, k_y)\hat{M}_y^{-1} = h(k_x, -k_y). \tag{1.53}$$

Therefore, it has a quantized quadrupole moment (see Section 1.2.3). Also, it has time-reversal, chiral, and charge-conjugation symmetries although they are not required for protecting quadrupole moments.

The bulk quadrupole moment takes the nontrivial value $q_{xy} = \frac{1}{2}$ for $|\gamma/\lambda| < 1$, while the topological phase transition occurs at the band gap closing point $|\gamma/\lambda| = 1$ [80]. The prominent signature of quadrupole topological insulator is the bulk-boundary correspondence:

$$q_{xy} = p_{x,y}^{\text{edge}} = Q_c = \frac{1}{2} \text{ mod } 1, \tag{1.54}$$

with the electric charge $e = 1$ and the lattice constant $a = 1$. Figure 1.3(c) and (d) demonstrates the emergence of corner charge and topologically protected corner states as a manifestation of bulk-boundary correspondence, obtained under the open boundary conditions.

For experimental realization, a difficulty arises from engineering systems with a negative hopping amplitude. Although it is difficult to introduce the π flux in electronic systems, they have successfully realized the quadrupole topological insulators in other systems, where it is relatively easy to control hopping amplitudes and phase factors [91–93]. Figure 1.4 shows the measurement of corner states in microwave circuits and phononic crystals [91, 92]. We should note that the topological band theory equally applies to classical systems and bosonic excitations even though they do not carry electric charge. Hence, corner states observed in these systems are indeed resulted from the bulk quadrupole moment.

1.3 Magnetic skyrmions

In Section 1.3, we review the theoretical and experimental background of magnetic skyrmions [94–99]. Starting from the brief history, we introduce the topological property of skyrmions, which results in their enhanced stability. The topological spin structure also results in the emergent gauge field that plays an important role in the transport phenomena. We also discuss the mechanism to realize skyrmions in magnetic systems. While there are several stabilization mechanisms, we focus on magnetic skyrmions stabilized by the competition between the Heisenberg exchange interaction and Dzyaloshinskii-Moriya interaction, paying a special attention to chiral magnets. Furthermore, the Dzyaloshinskii-Moriya interaction results in a unique boundary condition, known as edge twists [100–103]. The twisted edge magnetization in a confined system enhances the stability of magnetic skyrmions and leads to a critical behavior of the spin textures along edges [104, 105]. We end this section by reviewing the magnetic excitation of skyrmions and topologically nontrivial magnon band structure in skyrmion crystals, including our recent publication on bilayer skyrmions [106].

1.3.1 Brief history

Skyrmion was first derived as a topological soliton solution in a three-dimensional non-linear sigma model by T. H. R. Skyrme [107, 108]. Since skyrmions are characterized by an integer topological charge that cannot be changed continuously, he originally proposed them as a model for baryons to account for their stability. Later, skyrmion was

(a)   (b)   (c)

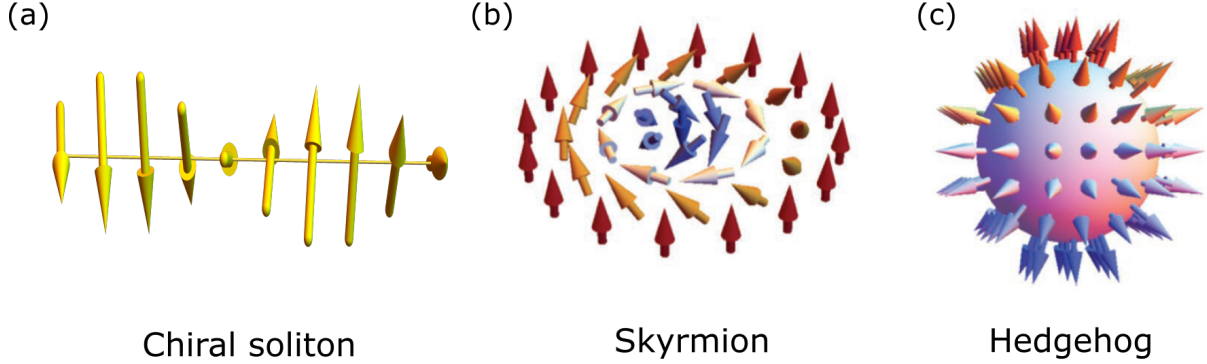Chiral soliton   Skyrmion   Hedgehog

Figure 1.5: **Schematic representation of topological solitons.** (a)-(c) Soliton solutions in (a) one-dimensional, (b) two-dimensional, and (c) three-dimensional systems. (a) Chiral soliton is formed by rotation of vector fields perpendicular to a single $\mathbf{q}$ vector. (b) Skyrmion is constructed from superposition of three helices, satisfying $\sum_i \mathbf{q}_i = 0$. The in-plane components are determined by the type of chiral interactions. Here, we show a Bloch type skyrmion in (b). (c) Hedgehog configuration consists of three helices with $\mathbf{q}$ vectors orthogonal to each other. (b) and (c) are adapted from Ref. [97].

rediscovered as a low energy effective model of quantum chromodynamics in the classical limit [109, 110], which describe strong interactions between quarks and gluons.

Depending on spatial dimensions, topological soliton solutions are now known as chiral solitons (1D) [111], skyrmions (2D) and hedgehogs (3D) as shown in Fig. 1.5. Those topological defects were also realized in a variety of condensed matter systems, including superliquid helium-3 [112–114], quantum Hall ferromagnets [115–119], liquid crystals [120–123], and Bose-Einstein condensates [124–128]. In particular, topological spin structures in magnetic systems have become important in the field of spintronics for fundamental research and device applications.

The first step towards magnetic skyrmions was made by Bogdanov and his collaborators, showing that chiral interactions stabilize skyrmions in magnetic systems [129–131]. Importantly, magnetic systems without inversion symmetry generally support chiral interactions called the Dzyaloshinskii-Moriya interaction $H_{DM} = \sum_{i<j} D\hat{n} \cdot \boldsymbol{S}_i \times \boldsymbol{S}_j$, which arises from the spin-orbit coupling (see Appendix A.3 for details). The unit vector $\hat{n}$ is determined by crystalline symmetries with the sign of D indicating the chirality [36, 132, 133]. Nowadays, skyrmions were reported in various magnetic systems such as chiral magnets [134–141], multiferroic insulators [142, 143], polar magnetic semiconductors [144], magnetic multilayer systems [145–150], ultrathin ferromagnetic layers [151, 152], and acentric tetragonal Heusler compounds [153].

There are other mechanisms that stabilizes magnetic skyrmions. In a centrosymmetric magetic systems without the Dzyaloshinskii-Moriya interaction, magnetic skyrmions are realized in a thin film sample by the dipole-dipole interaction and easy-axis anisotropy [154–158]. In addition, geometrically frustrated spin systems can support topological spin structures [159–162]. The typical size of magnetic skyrmions depends on the stabiliza-
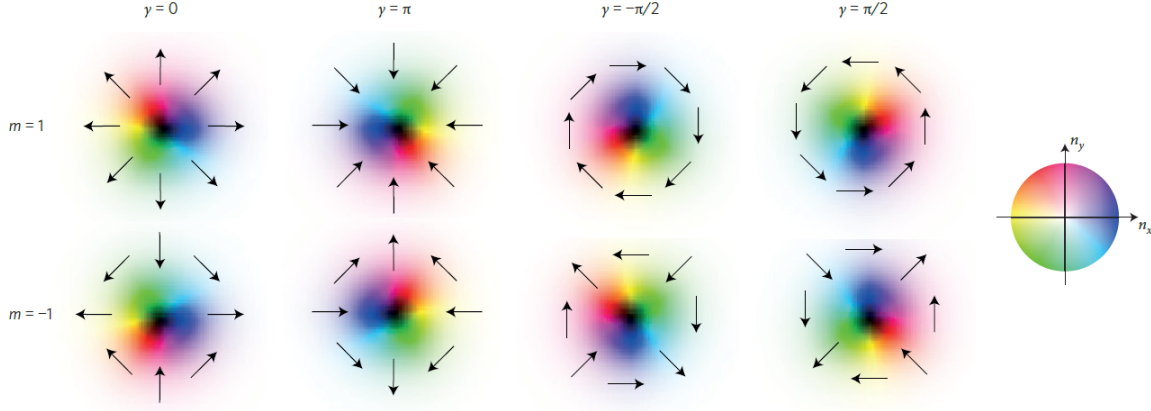
Figure 1.6: **Spin structures of magnetic skyrmions.** Magnetic textures of skyrmions characterized by vorticity m and helicity γ. The black arrow and color indicates the in-plane components of magnetization, while the brightness represents the out-of-plane components with denoting spin-down states in black and spin-up states in white. Adapted from [94].

tion mechanism: $10 \sim 100$ nm in non-centrosymmetric magnets; 100 nm to 1 μm in centrosymmetric magnets; ~ 1 nm in frustrated magnetic systems [94].

1.3.2 Topological charge

The noncollinear spin structure of magnetic skyrmions is characterized by the topological charge. It is defined as how many times a normalized vector field $\boldsymbol{n}(\boldsymbol{r})$ covers a unit sphere [94]

$$Q = \frac{1}{4\pi} \int d\boldsymbol{r} \, \boldsymbol{n}(\boldsymbol{r}) \cdot \left[\frac{\partial \boldsymbol{n}(\boldsymbol{r})}{\partial x} \times \frac{\partial \boldsymbol{n}(\boldsymbol{r})}{\partial y} \right]. \tag{1.55}$$

Imposing the periodic boundary conditions, this is a topological index for mapping from a torus to a unit sphere. This is characterized by the homotopy group $\pi_2(S^2) \cong \mathbb{Z}$ [9]. Hence, the topological charge Q is guaranteed to be integers.

Let us consider a topological charge of an isolated skyrmion in the ferromagnetic background. Using the rotational symmetry of skyrmions, a normalized spin vector is written as

$$\boldsymbol{n}(\boldsymbol{r}) = \{\cos\phi(\psi)\sin\theta(r), \sin\phi(\psi)\sin\theta(r), \cos\theta(r)\}, \tag{1.56}$$

where $\boldsymbol{r} = \{r\cos\psi, r\sin\psi\}$ is defined in the polar coordinates. From the chain rule, the derivative of $f(r, \psi)$ with respect to Cartesian coordinates is given by

$$\frac{\partial f}{\partial r} = \frac{\partial x}{\partial r}\frac{\partial f}{\partial x} + \frac{\partial y}{\partial r}\frac{\partial f}{\partial y},$$
$$\frac{\partial f}{\partial \psi} = \frac{\partial x}{\partial \psi}\frac{\partial f}{\partial x} + \frac{\partial y}{\partial \psi}\frac{\partial f}{\partial y}.$$
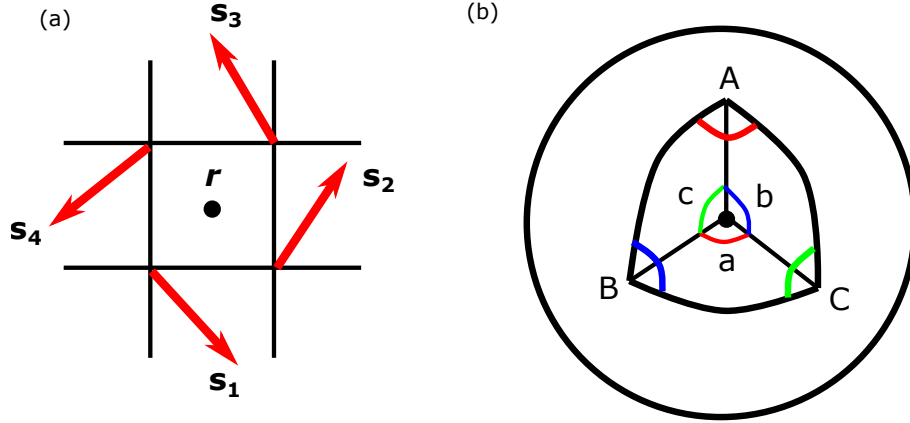
Figure 1.7: **Schematic representations of topological charge density and spherical triangle in a square lattice.** (a) The topological charge density is determined by spin vectors of four surrounding lattice points. (b) Spherical triangle on a unit sphere is constructed from three spin vectors. The surface area is given by Eq. (1.59) from angles A, B and C of triangle on the surface of sphere.

Then, we have

$$\frac{\partial \boldsymbol{n}}{\partial x} = \cos\psi \frac{\partial \boldsymbol{n}}{\partial r} - \frac{\sin\psi}{r} \frac{\partial \boldsymbol{n}}{\partial \psi},$$
$$\frac{\partial \boldsymbol{n}}{\partial y} = \sin\psi \frac{\partial \boldsymbol{n}}{\partial r} + \frac{\cos\psi}{r} \frac{\partial \boldsymbol{n}}{\partial \psi}.$$

Substituting them, the integration is evaluated as

$$Q = \frac{1}{4\pi} \int_0^\infty dr \int_0^{2\pi} d\psi \, \frac{\partial \phi}{\partial \psi} \frac{\partial \theta}{\partial r} \sin\theta(r)$$
$$= \frac{1}{4\pi} [-\cos\theta(r)]_{r=0}^{r=\infty} [\phi]_{\psi=0}^{\psi=2\pi}. \tag{1.57}$$

Assuming that an external field is applied along the z axis, a spin is pointing downwards at the skyrmion center and upwards at infinity. Hence, we obtain $Q = -m$ with $m = [\phi]_{\psi=0}^{\psi=2\pi}/2\pi$ denoting the vorticity. With the helicity γ defined as a phase ϕ at $\psi = 0$, magnetic skyrmions are classified as Fig. 1.6. Skyrmions with $m = -1$ are known as *antiskyrmions* due to their opposite topological charge to conventional skyrmions. In addition, skyrmions with $\gamma = 0, \pi$ are called Néel type skyrmions/antiskyrmions, while skyrmions with $\gamma = \pm\pi/2$ are called Bloch type skyrmions/antiskyrmions.

In a discrete lattice system, the topological charge can be defined as a summation of topological charge density at the center of each lattice point. It is given as [163]

$$Q = \sum_{\boldsymbol{r}} \rho(\boldsymbol{r}), \quad \rho(\boldsymbol{r}) = \frac{\sigma S(\mathbf{s}_1, \mathbf{s}_2, \mathbf{s}_3) + \sigma S(\mathbf{s}_1, \mathbf{s}_3, \mathbf{s}_4)}{4\pi}, \tag{1.58}$$
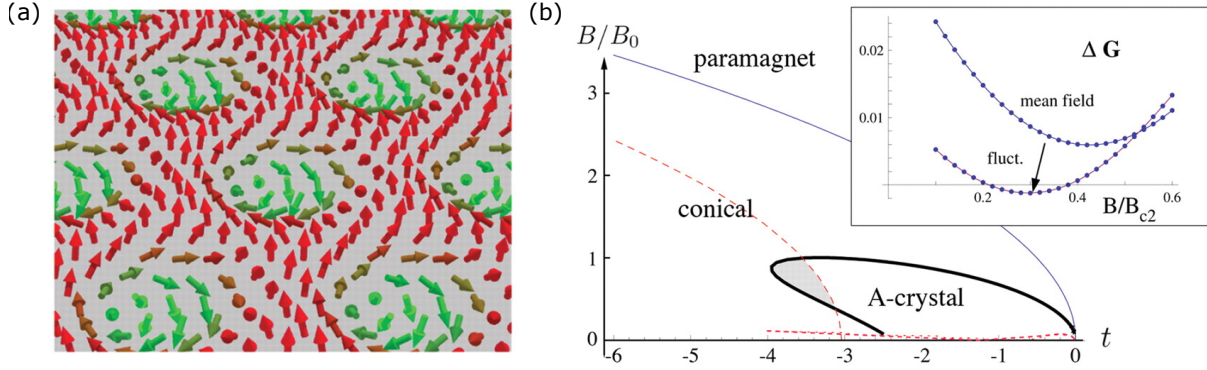
Figure 1.8: **Magnetic skyrmion crystals are stabilized by thermal fluctuations in a bulk sample.** (a) Magnetic textures of skyrmion crystals forming a triangular lattice. Along z axis, it is translationally invariant. (b) Magnetic phase diagram obtained by the Ginzburg-Landau theory near the critical temperatures T_c, where the horizontal axis represents temperature with $t \propto T - T_c$. The gray region corresponds to the well-defined skyrmion crystal phase (denoted as A-crystal) with modest thermal fluctuations, while those above and to the right of the red dashed line do not support a stable phase due to uncontrolled large fluctuations. The inset shows the energy difference between skyrmion crystal phase and conical phase in the mean-field approximation with and without corrections from thermal fluctuations. Skyrmion crystal is stable at intermediate fields for $\Delta G < 0$. Adapted from [134]. Reprinted with permission from AAAS.

where $\mathbf{s}_i$ is normalized spin vectors in a square lattice as depicted in Fig. 1.7(a) and $\sigma S(\mathbf{s}_1, \mathbf{s}_2, \mathbf{s}_3)$ is the signed area of the spherical triangle consisting of three spin vectors. The surface area of the spherical triangle in Fig. 1.7(b) is given by

$$S = A + B + C - \pi, \tag{1.59}$$

where $A, B,$ and C are angles of the spherical triangle, which are determined from angles $a, b,$ and c between three spin vectors. The sign σ for $\sigma S(\mathbf{s}_1, \mathbf{s}_2, \mathbf{s}_3)$ is defined by

$$\sigma = \text{sign}[\mathbf{s}_1 \cdot (\mathbf{s}_2 \times \mathbf{s}_3)]. \tag{1.60}$$

Crucially, this definition guarantees the topological charge to be integer in the periodic boundary condition. However, the integer quantization is violated in a finite sample with open boundaries. Nevertheless, we can estimate the topological charge of skyrmions in confined systems by summing over the topological charge density. In Section 5.3.2, we use the topological charge density to characterize fractional topological charge of edge localized skyrmions.

1.3.3 Mechanism to stabilize skyrmions in chiral magnets

In the work by Bogdanov and Hubert [130], the stability of vortex lattice phase under applied magnetic fields along z-axis was studied in chiral magnets with T symmetry and
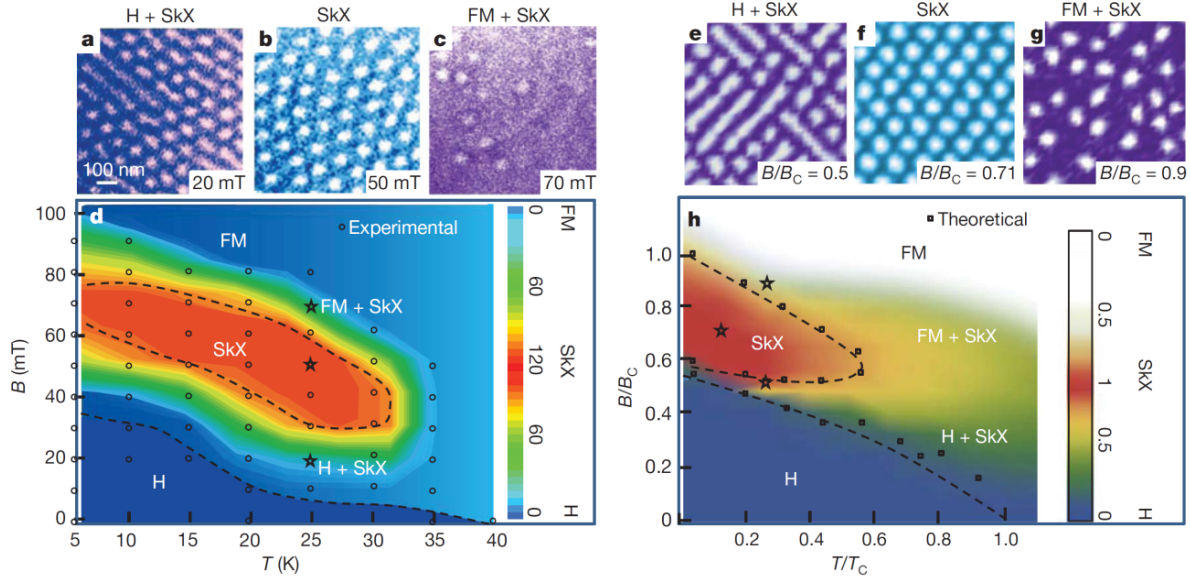
Figure 1.9: **Magnetic phase diagram obtained experimentally for a thin film sample of $Fe_{0.5}Co_{0.5}Si$ and theoretically for a two-dimensional model.** Spin textures (a)-(c) observed by Lorentz transmission electron microscopy and (e)-(g) obtained by Monte Carlo simulation. (d) and (h) respectively show the magnetic phase digram in the B-T plane obtained experimentally and theoretically. A magnetic phase labeled by H, SkX, and FM stands for helical phase, skyrmion crystal phase, and ferromagnetic phase, respectively. For the theoretical result in (h), both magnetic fields and temperatures are scaled by some constants T_c and B_c. Adapted from [136].

polar magnets with C_{nv} symmetry (see Section 2.1 for symmetry argument). Here, the vortex lattice phase corresponds to a triangular lattice of skyrmion crystals, whose magnetic textures is shown in Fig. 1.8(a). They showed that conical phase is always more stable than skyrmion crystal phase in chiral magnets, which is a magnetic helix characterized by a single $\mathbf{q}$ vector parallel to applied magnetic fields $\mathbf{B} \parallel \hat{z}$ (see Appendix A.4 for the mean-field solution). In contrast, skyrmion crystal phase was shown to be thermodynamically stable in polar magnets, whose symmetry does not allow the formation of conical phase along the z-axis. Intriguingly, magnetic skyrmions were first discovered in chiral magnets [134–137], although they were predicted to be only metastable. There are two reasons for the stability of skyrmion crystals in chiral magnets.

Firstly, it was shown that thermal fluctuations stabilize the skyrmion crystal phase near the phase boundary between the paramagnet and conical phase in three-dimensional systems [134, 164]. Using the Ginzburg-Landau theory, the mean-field solutions of conical phase and skrymion crystal phase were derived in Ref. [134], which is explained in Appendix A.4. An inset in Fig. 1.8(b) shows the energy difference between skyrmion crystals and conical phase as a function of magnetic fields in the mean-field approximation, showing that the energy of skyrmion crystals is always larger than conical phase as

predicted by Bogdanov [130]. In order to stabilize skyrmion crystals, we need to go beyond the mean-field approximation. For this purpose, the Gaussian thermal fluctuations were considered in Ref. [134]. The minimal free energy with thermal fluctuations is given by

$$G \approx \mathcal{F}[\boldsymbol{M}_{\mathrm{mf}}] + \frac{1}{2} \log \det\Big(\frac{\delta^2 \mathcal{F}}{\delta \boldsymbol{M} \delta \boldsymbol{M}} \Big)\Big|_{\boldsymbol{M}_{\mathrm{mf}}}, \qquad (1.61)$$

where $\mathcal{F}$ is the free energy functional and $\boldsymbol{M}_{\mathrm{mf}}$ is the mean-field solution for each phase. Remarkably, the correction from thermal fluctuations results in a narrow region where the skyrmion crystal has lower energy than conical phase. This is indicated by the gray shaded region in Fig 1.8(b), explaining the experimental observation of skyrmion crystals in bulk chiral magnets such as MnSi and $Fe_{0.5}Co_{0.5}Si$ [134, 135, 137].

Secondly, conical phase is suppressed in two-dimensional systems, leading to the enhanced stability of skyrmion crystals in thin film samples [136, 164, 165]. Using Monte Carlo simulated annealing [166], the magnetic phase diagram of chiral magnet was studied for two-dimensional systems [165]. The obtained magnetic phase diagram for small anisotropies consists of helical phase, triangular skyrmion crystal phase, and ferromagnetic phase at $T = 0$ and under various magnetic fields. Here, we should note that the helical phase is characterized by a single wave vector $\mathbf{q} \perp \hat{z}$, so it is different from the conical phase solution with $\mathbf{q} \parallel \hat{z}$. The prediction of the enhanced stability of skyrmion crystals in a two-dimensional system was confirmed by studying a thin film sample of $Fe_{0.5}Co_{0.5}Si$ [136]. In this work, magnetic configurations of skyrmion crystals were directly observed in the real space for the first time using high resolution Lorentz transmission electron microscopy, as shown in Fig. 1.9(a)-(c). In Fig. 1.9(b), a triangular lattice of skyrmion crystal was clearly observed. A crucial observation is that the skyrmion crystal phase was stable down to low temperatures, implying that they are thermodynamically stable in a thin film sample without thermal fluctuations. The theoretically obtained magnetic phase diagram for finite temperatures is in good agreement with the experimental result as shown in Fig. 1.9(d) and (h) .

1.3.4 Edge twist and edge instability

In this section, we comment on the stability of skyrmion crystals in thin film samples. While the skyrmion crystal phase is thermodynamically stable in a two-dimensional system, it is metastable and only stabilized by thermal fluctuations in a three-dimensional system. Then a natural question arises to fill in the gap between two limiting cases: *How does the stability of skyrmion crystals depends on the thickness of a sample?* This is related to the unique boundary condition imposed by the Dzyaloshinskii-Moriya interaction, resulting in the twisted magnetization along edges [100–103]. The derivation of edge twist is presented in Appendix A.7.1. The effect of twisted spin textures on surfaces and edges of a thin film sample is discussed below.

Firstly, we consider twisted spin textures on surfaces to films. The surface twist is localized to boundaries with its penetration length scaled by the zero-field helical wavelength $L_D = 4\pi A/D$ with the exchange stiffness A and the Dzyaloshinskii-Moriya
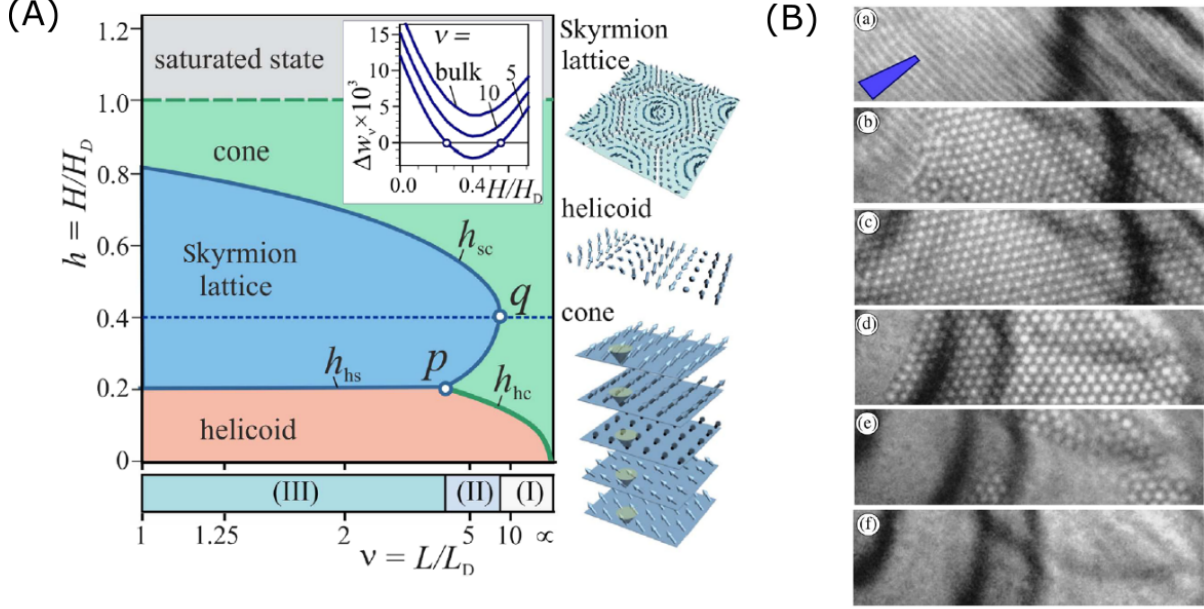
Figure 1.10: **Enhanced stability of skyrmion crystals in thin film samples due to the chiral surface twist.** (A) The magnetic phase diagram of chiral magnets in a thin film sample at $T = 0$. The dimensionless variables for the film thickness and applied fields are denoted as $\nu = L/L_D$ and $h = H/H_D$ (defined in Appendix A.7.1). Each phase is separated by the first order transitions (solid lines). The inset shows the energy density difference between the skyrmion crystal and conical phases along a dotted line at $H = 0.4H_D$ for various film thickness. (B) Lorentz transmission electron microscopy images of an FeGe wedge at $T = 250$ K with increasing the magnetic field: (a) 0.013 T, (b) 0.0873 T, (c) 0.1073 T, (d) 0.2215 T, (e) 0.2355 T, (f) 0.3728 T. The thickness changes from 120 nm (left) to 60 nm (right) in the direction parallel to a blue tetragon. The helical and skyrmion crystal phases coexist in (c), while the first order phase transition between the skyrmion crystal and conical phase is observed in (d) and (e). Adapted from [167].

interaction D [102]. If a film sample has a thickness much greater than L_D, the surface twist does not affect the bulk spin textures. In this case, the conical phase ($\mathbf{q} \parallel \hat{z}$) is stable, while the skyrmion crystal phase is metastable [134, 164]. In contrast, the surface twist induces chiral modulations of helicoids ($\mathbf{q} \perp \hat{z}$) and skyrmion crystals along z axis if a thickness of sample is comparable to L_D [169]. As a result, the energy of skyrmion crystals and helicoids are drastically modified, making them thermodynamically stable over a broad range of applied magnetic fields [167]. Figure 1.10(A) shows the magnetic phase diagram of chiral magnets in a thin film sample at $T = 0$, illustrating the enhanced stability of the helical and skyrmion crystal phases when a thickness of sample becomes comparable to L_D [167]. Furthermore, they experimentally confirmed the thickness dependence by studying a wedge sample of FeGe. As shown in Fig 1.10(B), the transition from a skyrmion lattice to a conical phase occurs at lower magnetic fields
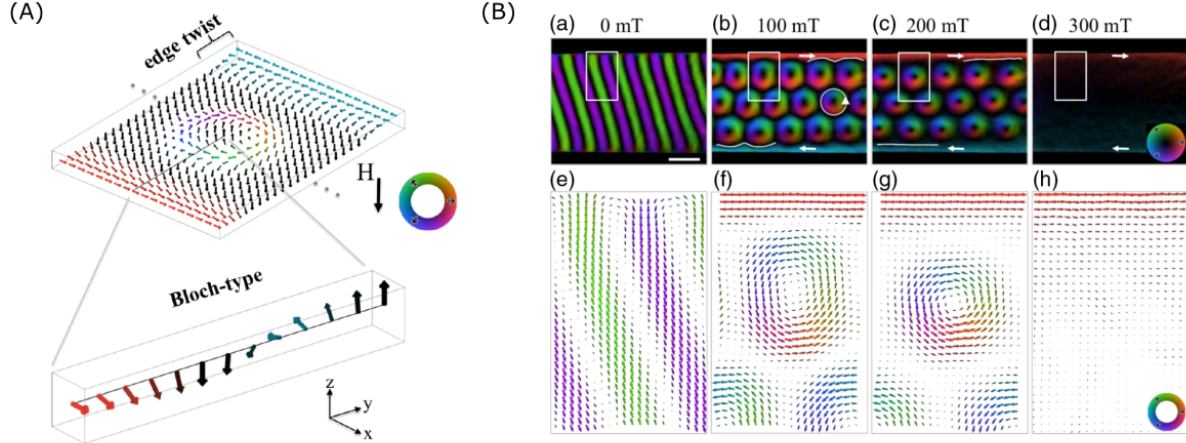
Figure 1.11: **Experimental observation of chiral edge twists at different magnetic fields.** (A) Schematic representation of magnetic structure in a nanostripe of chiral magnets. The edge twist is perpendicular to the radial vector pointing outwards from the center of a skyrmion. (B) Magnetic field dependence of edge spin textures in an FeGe nanostripe at 240 K. (a)-(d) In-plane magnetization M_{xy} obtained by off-axis electron holography. The applied magnetic field for each panel is (a) 0 mT, (b) 100 mT, (c) 200 mT, (d) 300 mT, respectively. (e)-(h) Enlarged spin textures near edges marked by a white rectangular in (a)-(d). Adapted from [168].

in a thicker region of the wedge (left-hand side of the wedge).

The twisting also occurs along edges of two-dimensional systems. Figure 1.11(A) shows the schematic representation of edge twists in a confined system. It should be noted that the twisted angle is inverted at opposite edges. The chiral orientation of edge twists results in the repulsive interaction with skyrmions near edges, which creates a topological barrier to confine isolated skyrmions inside nanodots [101]. Furthermore, it also prevents skyrmions from being pushed out of a nanostripe during the current driven motion [170, 171]. Therefore, the edge twist also contributes to the stability of skyrmions. Although the direct imaging of edge twists is challenging due to a necessary spatial resolution, it was observed using high-resolution Lorentz transmission electron microscopy and off-axis electron holography [104, 168]. Figure 1.11(B) shows the magnetic field dependence of edge twists observed in an FeGe nanostripe [168]. They showed that the penetration length of edge twists decreases with magnetic fields but twisted spin textures persist even in the ferromagnetic phase at 300 mT, which is consistent with the theory [100–103].

In addition, the chiral edge twist also acts as a source of topological charges of skyrmions. Since the quantization of topological charge is guaranteed by mapping from a torus to a unit sphere (see Section 1.3.2), the topological charge is no longer quantized in confinement. Consequently, it becomes possible to continuously deform twisted magnetizations along edges to create skyrmions. This is known as the edge instability, where the
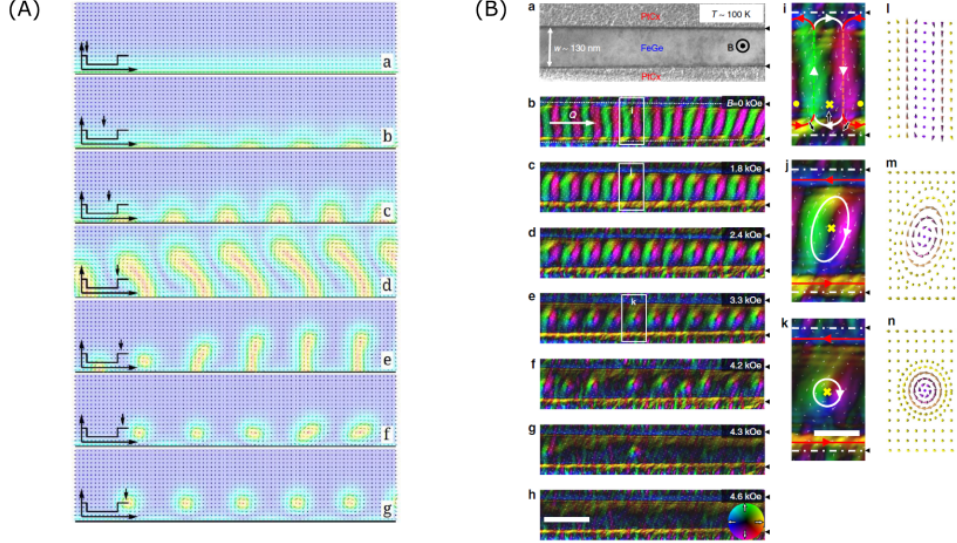
Figure 1.12: **Creation of edge-localized skyrmion chains due to the edge instability in the numerical simulation and experiment.** (A) Snapshots of spin configurations near the edge at various times, obtained by the classical spin dynamics simulations at $\kappa = 0$ and $\alpha = 0.4$. As shown in the inset, the magnetic field protocol is to start at $h = 1.0$ in (a), decrease it to $h = 0.39 < h_c = 0.4067$ in (b) and (c), and increase it back to $h = 1.0$ in (d)-(g). (B) The magnetic field dependence of spin textures near the edge, observed in a 130 nm FeGe nanostripe at $T = 100$ K with high-resolution Lorentz transmission electron microscopy (TEM). (a) TEM image of the FeGe nanostripe. (b)-(h) In-plane components of magnetizations with increasing magnetic fields. The wave vector $\vec{Q}$ for the helical phase is indicated. The white dot lines in (b) and small black triangles in (b)-(h) stand for the FeGe/PtCx interfaces. (i)-(k) Enlarged images of the white squared region in (b), (c), and (e). $\bullet/\times$ represents the upward/downward magnetization, respectively. (l-n) The schematic representation of spin textures in (i)-(k). (A) is adapted from [105], and (B) is adapted from [104].

bound states of magnons along twisted edges cause a local instability below the critical magnetic field [105]. For interested readers, a review of edge instability is provided in Appendix A.7.2.

One important consequence of the edge instability is nucleation of skyrmion chains along the edge. This is demonstrated by the micromagnetic simulation in Fig. 1.12(A). Starting from the ferromagnetic phase at large magnetic fields, the magnetic field is lowered below the critical value h_c for the edge stability in Fig. 1.12(A)(b) and (c), where edge magnetizations become unstable to nucleate helical domains. The observed edge localized half-moon skyrmions are characterized by a fractional topological charge. Since they are energetically more favorable than the ferromagnetic phase, they penetrate into the ferromagnetic background as time evolves. Finally, they turn into a chain of skyrmions by increasing the magnetic field above the critical value again (Fig. 1.12(A)(d)-(g)). We

should note that helical domains may be pushed out of edges or converted into skyrmions, depending on their sizes.

The formation of edge-mediated skyrmion chains was experimentally observed in an FeGe nanostripe as shown in Fig. 1.12(B) [104]. They showed that helical stripes directly turn into skyrmion chains along the edge without intermediate nucleation of half-moon skyrmions as the magnetic field is increased. Although it is consistent with the theoretical prediction of edge instability, there is no experimental observation of skyrmions with a fractional topological charge until now.

1.3.5 Emergent electromagnetism of skyrmions

In ferromagnetic metals, the coupling between noncoplanar spin structures and conduction electrons induces effective electromagnetic fields [172–174]. Assuming a long periodicity of magnetic order, the emergent magnetic field B_z^s and electric field E_i^s are given by [94, 173, 175] (see Appendix A.8 for derivation)

$$
\begin{aligned}
B_z^s &= \frac{\hbar c}{2e}\, \boldsymbol{m} \cdot (\partial_x \boldsymbol{m} \times \partial_y \boldsymbol{m}), \\
E_i^s &= \frac{\hbar}{2e}\, \boldsymbol{m} \cdot (\partial_i \boldsymbol{m} \times \partial_t \boldsymbol{m}),
\end{aligned}
\tag{1.62}
$$

where $\boldsymbol{m}$ is a unit vector parallel to the magnetization, c is the velocity of light, and $e > 0$ is the elementary charge. Since the emergent magnetic field is proportional to the topological charge density $\boldsymbol{m} \cdot (\partial_x \boldsymbol{m} \times \partial_y \boldsymbol{m})$, the total magnetic flux of skyrmions is quantized to be $-2\pi m \hbar c/e$ with vorticity m [94]. As a result, conduction electrons experience the Lorenz force in the presence of magnetic skyrmions, leading to the topological Hall effect [135, 176–183]. The topological Hall effect was experimentally measured in MnSi as an additional contribution in the Hall resistivity in the presence of skyrmion crystals [135, 183, 184]. Conversely, magnetic skyrmions can be driven by electric currents through the spin-transfer torque with some Hall angle, known as the skyrmion Hall effect [145, 175, 185–187]. A review of topological Hall effect and skyrmion Hall effect is provided in Appendix A.9.

1.3.6 Local magnetic excitation of skyrmions

Classical spin systems support collective excitations known as spin waves, which correspond to the precession of magnetizations at some resonance frequency ω and crystal momentum $\boldsymbol{k}$. Spin waves are the classical limit of magnons, and they can be numerically simulated in the classical spin dynamics described by the Landau-Lifshitz-Gilbert (LLG) equation (see Appendix A.6). In this section, we review spin wave modes of magnetic skyrmions arising from its particle nature and quantized topological charge [188, 191]. In particular, we discuss local spin wave excitations bounded to magnetic skyrmions at $\boldsymbol{k} = 0$. In Section 1.3.8, the full band spectrum of magnons for $\boldsymbol{k} \neq 0$ in the skyrmion crystal phase is discussed.
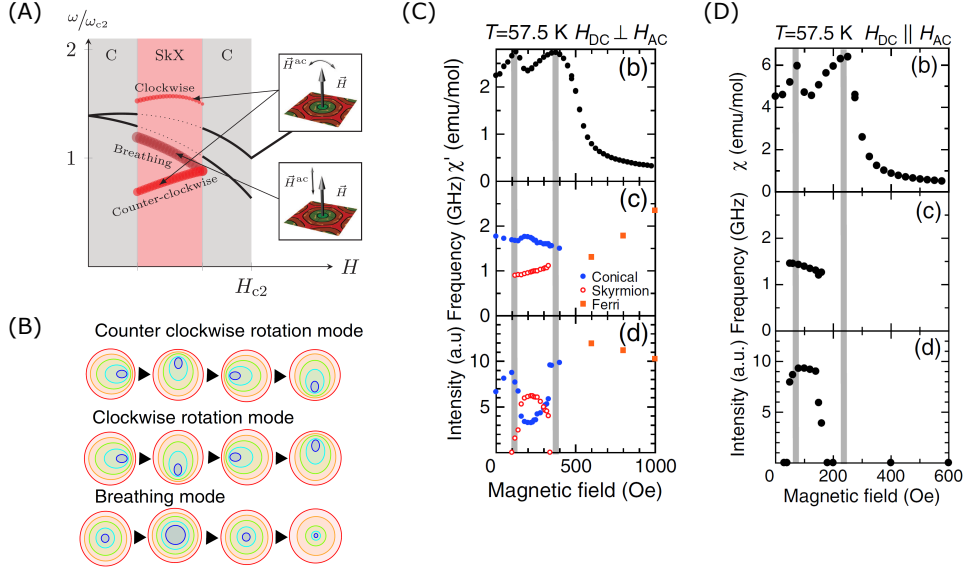
Figure 1.13: **Experimental observation of CCW and breathing modes of skyrmions in Cu_2OSeO_3.** (A) Theoretically obtained resonance frequencies of CCW, CW, and breathing modes plotted against magnetic fields, where SkX denotes the skyrmion crystal phase. (B) Schematic representation of elementary excitations of skyrmions. (C) Magnetic field dependence of (b) magnetic susceptibility, (c) peak frequency of microwave absorption, and (d) intensity of each mode in (c), obtained at 57.5 K under ac magnetic magnetic field along the in-plane direction. The skyrmion crystal phase was obtained between thick gray bars. (D) is the same as (C) but obtained under ac magnetic magnetic field along the out-of-plane direction. (A) is adapted from [188], and (B)-(D) are adapted from [189].

The low energy excitation of skyrmions has a gapless Goldstone mode, since the translational invariance is broken by magnetic skyrmions. As discussed in Section 1.3.5, topological spin structures of skyrmions induce an emergent magnetic field, which acts as a gauge field for spin waves [29, 34]. It was pointed out that the emergent gauge field results in the quadratic dispersion of Goldstone modes ($\omega \sim k^2$) as well as a gapped cyclotron mode of skyrmions [175, 192]. Soon after, three important low energy excitations of magnetic skyrmions were theoretically predicted in the GHz frequencies by M. Mochizuki [193], which were characterized by the following selection rules. With an ac magnetic field applied along in-plane directions ($\mathbf{H}_{AC} \perp \mathbf{H}_{DC}$), two rotational modes with opposite directions were excited using the numerical simulations of LLG equation, termed as counterclockwise (CCW) mode and clockwise (CW) mode. The resonance frequency of CCW mode was always found lower than CW mode in chiral magnets as shown in Fig. 1.13(A). The third mode was excited under an ac magnetic field applied along out-of-plane directions ($\mathbf{H}_{AC} \parallel \mathbf{H}_{DC}$) at resonance frequency between CCW and CW modes. This mode is associated with deformation of skyrmions in the radial direction, hence called breathing mode. Figure 1.13(B) shows schematic representations of
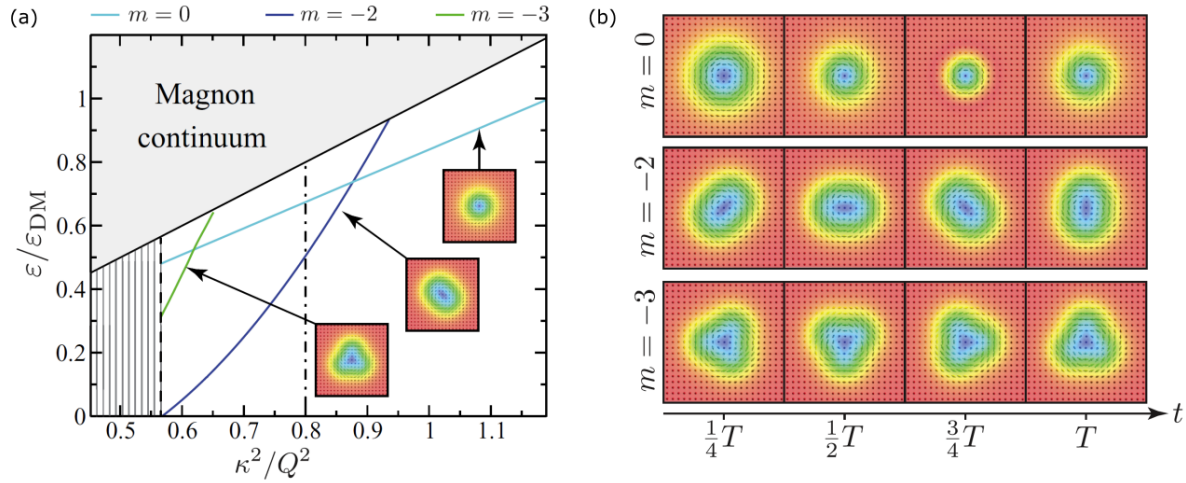
Figure 1.14: **Magnetic field dependence and temporal profile of magnon modes bounded to a single skyrmion.** (a) Magnetic field dependence of magnon spectrum in the presence of a single skyrmion, where κ^2/Q^2 represents the dimensionless magnetic field strength. Light blue, blue, and green line respectively corresponds to breathing mode ($m = 0$), elliptical mode ($m = -2$), and triangular mode ($m = -3$). (b) Snapshots of skyrmion textures for each magnon mode plotted as a function of time with T denoting the period of oscillation. Adapted from [190].

these spin wave modes.

Importantly, all of CCW, CW, and breathing modes are magnetically active, implying that they can be excited by spatially uniform ac magnetic fields. The experimental study of spin wave modes of skyrmions was first reported for a bulk sample of Cu_2OSeO_3 in Ref. [189], as shown in Fig.1.13(C) and (D). From microwave absorption spectra for GHz frequencies, resonance frequencies at various magnetic field were studied under in-plane and out-of-plane ac magnetic fields. They found a unique resonance mode in the skyrmion crystal phase for both in-plane and out-of-plane ac magnetic fields, identified as CCW mode at 1 GHz (red circles in Fig.1.13(C)(c)) and breathing mode at 1.5 GHz (black circles in Fig.1.13(D)(c)) [189]. In this experiment, it was not possible to resolve CW mode from a reminiscent of magnetic excitations of the conical phase (blue circles in Fig.1.13(C)(c)). Similar measurement was performed in other chiral magnets such as MnSi (metal) and $Fe_{0.8}Co_{0.2}Si$ (semiconductor), confirming the universal nature of these spin wave modes in skyrmion-hosting materials [194]. In addition, Cu_2OSeO_3 is a multiferroic insulator with strongly coupled electric and magnetic dipole moments [142, 143] (see Section 2.2.2 for details). Hence, spin waves can be excited by an oscillating electric field, known as electromagnons [195]. As an experimental signature of electromagnons, the nonreciprocal directional dichroism was predicted and experimentally observed in Cu_2OSeO_3, which is caused by the interference between oscillating magnetic and electric dipole moments [191, 196–199].

So far, we have discussed magnetic excitations of skyrmion crystals. The magnetic

excitation of isolated skyrmions has been also studied in the ferromagnetic background. In the presence of skyrmions, the propagation of spin waves was shown to be deflected due to the emergent magnetic field, giving rise to a topological magnon Hall effect [190, 200]. Skyrmions also act as a confining potential of spin waves, thus hosting several internal excitation modes below the bulk continuum [106, 190, 201]. In addition to CCW and breathing modes, the internal modes include deformations to m-th order polygons [201]. Figure 1.14(a) shows the magnon spectrum of single skyrmion at $\boldsymbol{k} = 0$ as a function of magnetic field, showing breathing mode ($m = 0$), elliptical ($m = -2$), and triangular ($m = -3$) deformations [190]. Deformations of skyrmions associated with each magnon mode is illustrated in Fig. 1.14(b). Although it is not shown in Fig. 1.14(a), CCW mode lies just below the bulk continuum [106]. Figure 1.14(a) indicates that the energy of elliptical mode becomes negative below the critical magnetic field, which leads to a local instability of skyrmions against elliptical deformations known as bimerons [202].

1.3.7   Spin wave radiation from a topological charge dipole

In this section, we briefly discuss our recent work on magnetic excitations of a skyrmion-antiskyrmion bilayer system. The main finding is that the interlayer interaction between a skyrmion and an antiskyrmion results in a rotational mode characterized by a topological charge dipole. The emitted spin wave also shows a dipole radiation pattern as shown in Fig. 1.15. The content of this section was published in Ref. [106].

The important technological goal of magnon spintronics is to achieve a controlled spin wave emission with nanoscale wavelength for device applications [25]. For example, an array of spin torque nano-oscillators, which convert electric currents into spin waves in a ferromagnetic layer, has been proposed as a directional spin wave emitter [203, 204]. More recently, a radial pattern of spin waves was observed in a stack of magnetic vortices characterized by an integer winding number of in-plane magnetization [205–207]. In Ref. [206], the radial spin wave pattern was resulted from gyrotropic motions of antiferromagnetically coupled vortices.

Analogously to magentic vortices, a rotational spin wave mode of single magnetic skyrmions could be used for a spin wave emitter. To achieve a better control, we consider a bilayer system, where each layer hosts a skyrmion or an antiskyrmion with a different topological charge and helicity (see Section 1.3.2 for definition). Each layer is described by

$$H_i \;\;=\;\; \tfrac{1}{2}\sum_{\langle \boldsymbol{r},\boldsymbol{r}'\rangle} (-J\boldsymbol{S}_{\boldsymbol{r}}^i \cdot \boldsymbol{S}_{\boldsymbol{r}'}^i + D\hat{n}_{\boldsymbol{r},\boldsymbol{r}'} \cdot \boldsymbol{S}_{\boldsymbol{r}}^i \times \boldsymbol{S}_{\boldsymbol{r}'}^i) - g\mu_B B_z \sum_{\boldsymbol{r}} \boldsymbol{S}_{\boldsymbol{r}}^i \cdot \hat{\boldsymbol{z}} \,, \qquad (1.63)$$

where $\boldsymbol{S}_{\boldsymbol{r}}^i$ represents a spin at $\boldsymbol{r}$ with $\boldsymbol{r}$ labeling a site defined on a two-dimensional square lattice in i-th layer for $i = 1, 2$. The subscript $\langle \boldsymbol{r}, \boldsymbol{r}' \rangle$ denotes summation over the nearest neighbors with lattice constant a. It contains the ferromagnetic exchange interaction $J > 0$, Dzyaloshinskii-Moriya interaction with a unit vector $\hat{n}_{\boldsymbol{r},\boldsymbol{r}'}$, and Zeeman term for coupling with external fields with g and μ_B denoting the g-factor and Bohr magneton, respectively. By choosing a Dzyaloshinskii-Moriya vector $\hat{n}_{\boldsymbol{r},\boldsymbol{r}'}$ for different
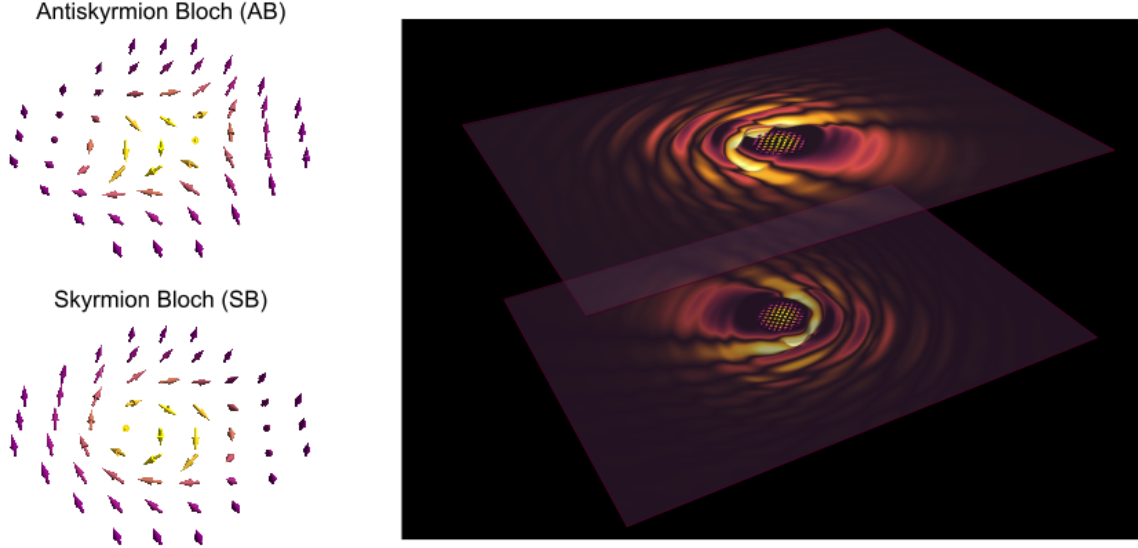
Figure 1.15: **Spin wave radiation from a skyrmion-antiskyrmion bilayer.** Left: spin textures for Bloch skyrmion and antiskyrmion characterized by opposite topological charges. Right: spin wave patterns emitted by a Bloch skyrmion-antiskyrmion bilayer under an in-plane ac magnetic field, showing a dipole radiation pattern. Adapted from [106].

crystalline symmetries in each layer (see Section 2.1 for expressions), we can prepare a bilayer system consisting of either a skyrmion-antiskyrmion, skyrmion-skyrmion, or antiskyrmion-antiskyrmion pair placed on top of each other. The full Hamiltonian is given by [106]

$$H = H_1 + H_2 + H_{\text{int}} + H_{\text{osc}}, \tag{1.64}$$

with

$$H_{\text{int}} = -J_{\text{int}} \sum_{\boldsymbol{r}} \boldsymbol{S}_{\boldsymbol{r}}^1 \cdot \boldsymbol{S}_{\boldsymbol{r}}^2, \tag{1.65}$$

$$H_{\text{osc}} = -\sum_{\boldsymbol{r}} g\mu_B B_0 \cos(\omega t)(S_{\boldsymbol{r},x}^1 + S_{\boldsymbol{r},x}^2). \tag{1.66}$$

The first term is the ferromagnetic interlayer coupling with $0 < J_{\text{int}} < J$. The second term denotes an applied in-plane ac magnetic field with frequency tuned at the resonance frequency of the lower energy rotational mode, which corresponds to counterclockwise (CCW) mode for skyrmions (see Section 1.3.6). For antiskyrmions, the magnon spectrum is the same as skyrmions, except that the direction of rotational mode is inverted, implying that clockwise (CW) mode has lower energy than CCW mode [106]. The resonance frequency of CCW (CW) mode for (anti)skyrmions was found as $\omega = g\mu_B B_z/\hbar$ [106].

Now, we discuss our main result. We consider a bilayer system consisting of Bloch skyrmion-antiskyrmion (type I) and Bloch skyrmion-Bloch skyrmion (type II). For the
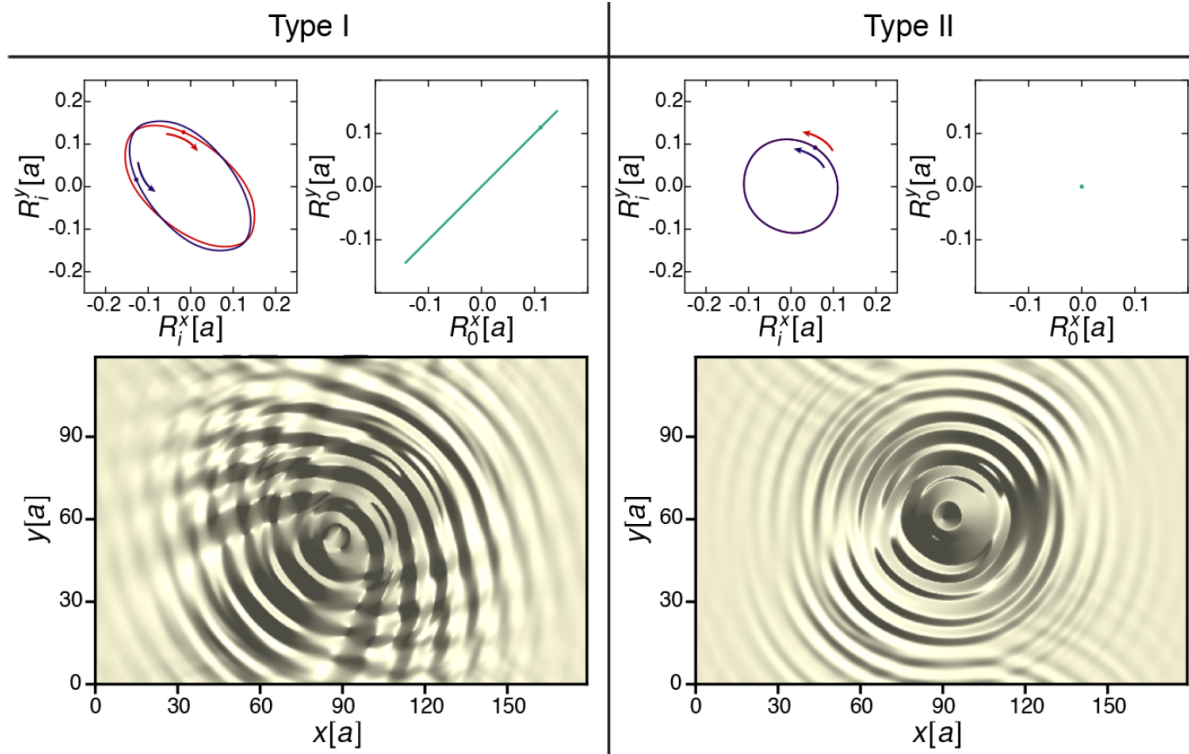
Figure 1.16: **Relationship between spin wave patterns and trajectory of skyrmion/antiskyrmion.** Top : the dynamics of the collective coordinates $\boldsymbol{R}_i(t)$ defined in Eq. (1.68) for each layer and the relative displacement defined as $\boldsymbol{R}_0 = \boldsymbol{R}_1 - \boldsymbol{R}_2$ in units of lattice constant a. Blue lines denote the trajectory of $\boldsymbol{R}_1(t)$ for layer 1, while red lines denote the trajectory of $\boldsymbol{R}_2(t)$ for layer 2. Bottom: snapshot of spin wave pattern $\delta m^1_{\boldsymbol{r},z}(t)$ for layer 1. Type I and type II corresponds to a bilayer consisting of Bloch skyrmion-antiskyrmion and Bloch skyrmion-Bloch skyrmion, respectively. The parameter is taken at $D/J = 1.0$, $g\mu_B B_z/JS = \hbar\omega/JS = 0.6$, $J_{\text{int}}/J = 0.3$, and $g\mu_B B_0/JS = 0.1$. The Gilbert damping constant is fixed at $\alpha = 0.08$. Adapted from [106].

results of all the possible combinations of skyrmions and antiskyrmions, we refer to Ref. [106]. The spin wave emission from the bilayer systems was studied by numerical simulations of the Landau-Lifshitz-Gilbert (LLG) equation (Appendix A.6). Under the in-plane ac magnetic fields, the skyrmion and antiskyrmion respectively undergoes the CCW and CW mode. As a result, deviations from the ferromagnetic state propagate outwards from the center of (anti)skyrmion. The emitted spin wave is characterized by

$$\delta m^i_{\boldsymbol{r},z}(t) = m^i_{\boldsymbol{r},z}(t) - m^i_{\text{FM},z}(t), \tag{1.67}$$

where $i = 1, 2$ is the layer index, $\boldsymbol{m}^i_{\boldsymbol{r}}(t)$ is a unit vector parallel to the magnetization, and $\boldsymbol{m}^i_{\text{FM}}(t)$ is a spatially uniform magnetization obtained far away from (anti)skyrmions where the spin wave contribution is negligible. Bottom panels of Fig. 1.16 show the snapshots of $\delta m^1_{\boldsymbol{r},z}(t)$ for both types in layer 1, obtained at $J_{\text{int}}/J = 0.3$ and $D/J = 1.0$.
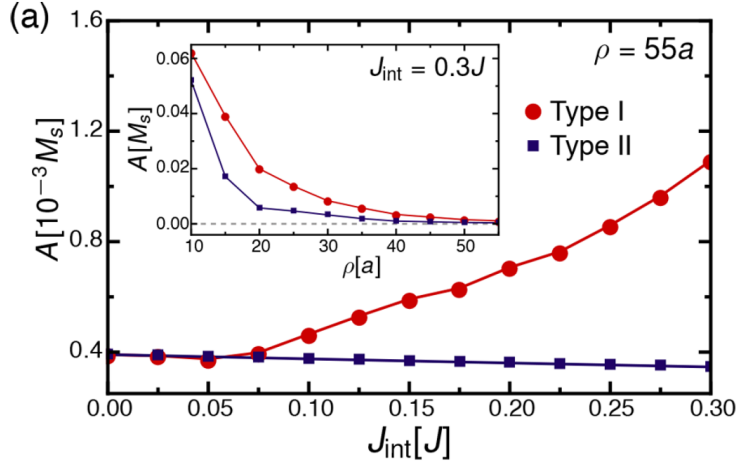
Figure 1.17: **Interlayer coupling dependence of far-field spin wave amplitude.**
Far-field amplitude A as a function of interlayer coupling J_{int} for $\rho = 55a$, obtained for
type I and II. The inset shows that A decays exponentially with ρ, expected for a non-
zero Gilbert damping constant. The parameter is the same as Fig. 1.16 except for J_{int}.
Adapted from [106].

Importantly, the spin wave pattern for type I is not radial but instead directed towards
a diagonal axis. In contrast, the result for type II shows a radial pattern similar to the
spin wave emission of single skyrmions. It should be noted that spin wave pattern in
layer 2 is almost identical with layer 1, given by $\delta m^2_{\boldsymbol{r},z}(t) \approx \delta m^1_{-\boldsymbol{r},z}(t)$ for type I and
$\delta m^2_{\boldsymbol{r},z}(t) \approx \delta m^1_{\boldsymbol{r},z}(t)$ for type II.

To analyze the skyrmion dynamics in each layer, we introduce a center of mass of
skyrmions in terms of topological charge density (see Section 1.3.2):

$$\boldsymbol{R}_i(t) = \frac{1}{Q_i} \int d^2r\, \boldsymbol{r} \left[\boldsymbol{m}^i_{\boldsymbol{r}}(t) \cdot \{ \partial_x \boldsymbol{m}^i_{\boldsymbol{r}}(t) \times \partial_y \boldsymbol{m}^i_{\boldsymbol{r}}(t) \} \right], \tag{1.68}$$

where Q_i is the total topological charge and $i = 1, 2$ is the layer index. Top panels of
Fig 1.16 show the trajectory of the collective coordinate $\boldsymbol{R}_i(t)$ over a single oscillation pe-
riod, which forms a closed path as the system is in a time-periodic steady state. From the
result for type I, we notice that the trajectories of skyrmions and antiskyrmions are an-
tisymmetric with opposite rotational directions. Furthermore, the relative displacement
between skyrmions and antiskyrmions oscillates along a straight diagonal line, which can
be interpreted as a dipole oscillation of topological charge. Therefore, the spin wave
pattern for type I is originated from the dipole radiation of topological charge. In con-
trast, the trajectory of type II is identical for both layers with no relative displacement,
implying the synchronized CCW mode of Bloch skyrmion in each layer.

We have also studied the parameter dependence of the far-field spin wave amplitude,

defined as the [106]

$$A = \frac{M_s}{N_{\mathcal{J}}} \sum_{\boldsymbol{r} \in \mathcal{J}} \frac{1}{2} (\max[\delta m^1_{\boldsymbol{r},z}(t)]_{t \in [0,T]} - \min[\delta m^1_{\boldsymbol{r},z}(t)]_{t \in [0,T]}), \qquad (1.69)$$

with $M_s = |\boldsymbol{S_r}|$ and $T = 2\pi/\omega$ being the period of oscillation of the applied ac magnetic field. Here, the angular dependence of spin waves is averaged out by taking summation over the area $\mathcal{J}$ of an annulus centered around the skyrmion core, with inner (outer) radius ρ ($P = \rho + 5a$), containing $N_{\mathcal{J}}$ sites. Figure 1.17 shows the interlayer coupling dependence of the far-field spin wave amplitude A for type I and II at $\rho = 55a$. For type I, it is linearly proportional to J_{int}, hence we can control the spin wave amplitude by tuning J_{int}. In contrast, the spin wave amplitude is unaffected by the interlayer coupling for type II. The difference arises from the formation of topological charge dipole in type I, which is enhanced by large J_{int}.

So far, we have discussed the result for $D/J = 1.0$. In Ref. [106], we also discuss the result for smaller D/J ratios and obtain the equivalent result. It should be noted that D/J sets the length scale in spin lattice model. This is because the Dzyaloshinskii-Moriya interaction is given as a first order spatial derivative in contrast to the exchange interaction proportional to a second order spatial derivative in the continuum limit (see Appendix A.5). Hence, we need to take into account a change in the length scale when evaluating the far-field spin wave amplitude A at various D/J ratios.

As a concluding remark, we have shown that the skyrmion-antiskyrmion bilayer system exhibits a strongly coupled rotational mode under in-plane ac magnetic fields, forming a topological charge dipole. The radiated spin wave pattern is directed parallel to the topological charge dipole, with its amplitude proportional to the ferromagnetic interlayer couping. Therefore, we suggest a skyrmion-antiskyrmion bilayer system as an efficient spin wave emitter. Bilayer skyrmion systems can be experimentally realized in a stack of nanodiscs separated by a spacer [149], allowing skyrmions and antiskyrmions placed on top of each other.

1.3.8   Topological magnon band structure in skyrmion crystals

In this section, we discuss the magnon band structure of skyrmion crystals for all $\boldsymbol{k}$ points in the first Brillouin zone. Using the general form of spin wave Hamiltonian derived in Section 1.1.3, the magnon spectrum for skyrmion crystals can be computed from a numerically obtained magnetic unit cell. Once the magnon spectrum is obtained, we could compute the Berry phase and Chern number for each magnon band to characterize its topological property (see Section 1.1.4).

The magnon band structure of skyrmion crystals for the entire Brillouin zone was first obtained by Roldán-Molina and his collaborators [208]. Using the above mentioned approach, it was shown that the low energy magnon bands consist of nearly flat bands, pointing out the presence of localized magnon modes. Later, they have shown that the nontrivial topological band structures are realized in the skrymion crystals [209], as

(a)

(b)
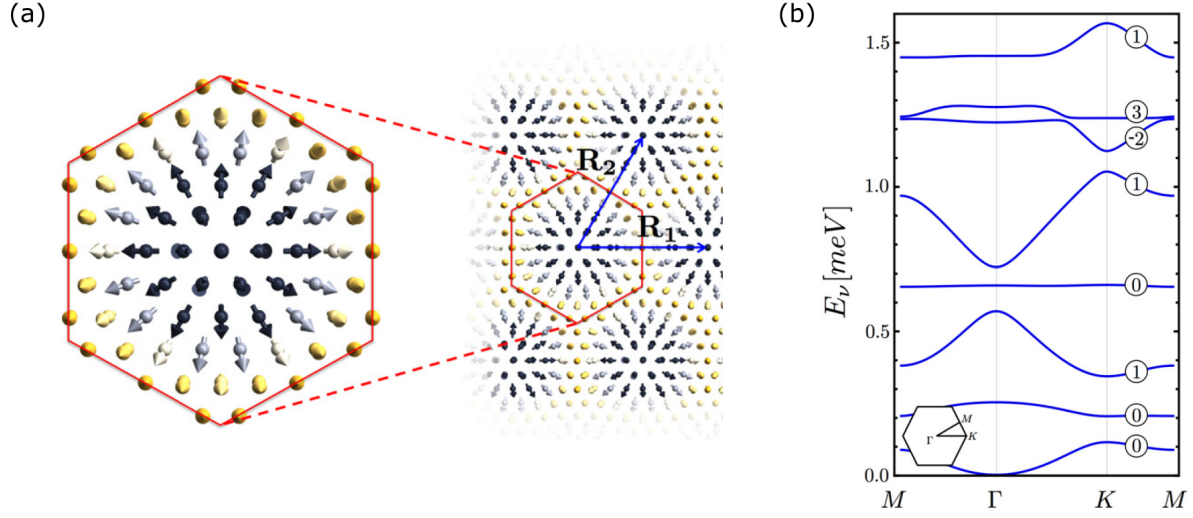
Figure 1.18: **Magnetic unit cell and magnon band structure of the skyrmion crystal.** (a) A hexagonal magnetic unit cell defined in a triangular lattice of skyrmion crystals. The Dzyaloshinskii-Moriya interaction stabilizes Néel type skyrmions. (b) Magnon band spectrum of the skyrmion crystal, computed from a hexagonal magnetic unit cell. The inset shows the first Brillouin zone. The Chern number for each band is indicated by an encircled number. Adapted from [209].

discussed below. The equivalent result was also obtained in the continuum limit using the nonlinear sigma model [188, 210].

In the following, we review Ref. [209] to introduce the magnon band structure and its topological property in the skyrmion crystals. In Ref. [209], a two-dimensional spin lattice model was considered on triangular lattice with the Hamiltonian similar to Eq. (1.3), where the Dzyaloshinskii-Moriya interaction was given as Eq. (2.5). In addition, they have considered the easy-axis anisotropy that does not affect the magnon band topology. In this model, Néel type skyrmions are stabilized by the competition between the exchange interaction and Dzyaloshinskii-Moriya interaction. Under a finite out-of-plane magnetic field, the classical gound-state spin texture forms triangular skyrmion crystals as shown in Fig. 1.18(a). For the calculation of magnon band structure, the hexagonal magnetic unit cell was used.

Figure 1.18(b) shows the magnon band spectrum of the skyrmion crystal along a path connecting the high symmetry momenta within the first Brillouin zone. Above the second bulk bands, topologically nontrivial band structures are obtained, indicated by an encircled number on each band that denotes the Chern number. The origin of the topological magnon band structure was explained by the emergent gauge field arising from both the topological spin structure and Dzyaloshinskii-Moriya interaction [29, 30].

Since the sum of Chern numbers below the third band is +1, we expect a chiral magnonic edge state connecting the third and fourth band from the bulk-edge correspondence of Eq. (1.22). In order to compute the edge spectrum, the ground-state spin
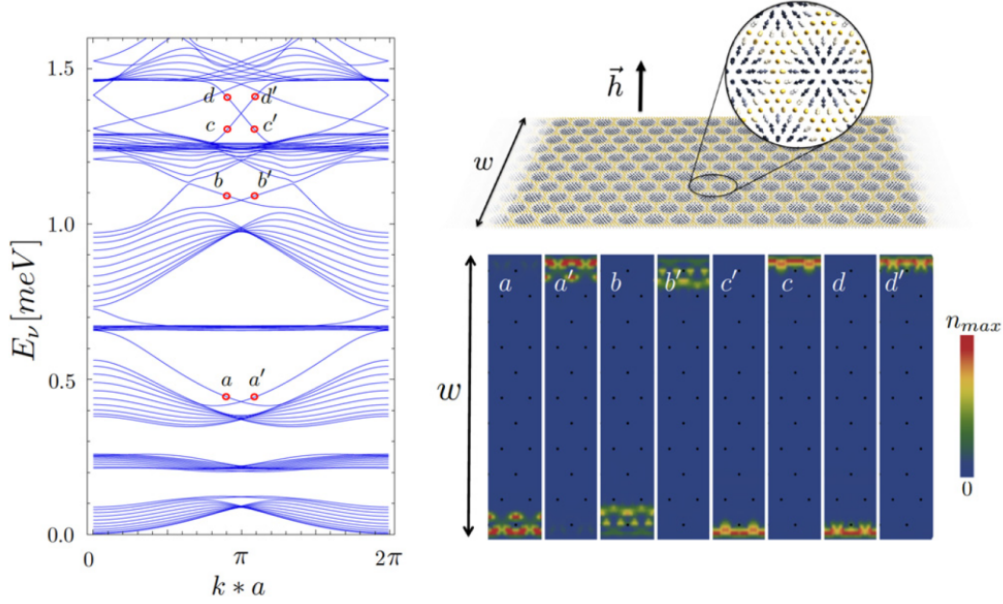
Figure 1.19: **Topologically protected chiral magnonic edge states in the skyrmion crystals.** Left: magnon band spectrum for a one-dimensional strip geometry. Top right: classical ground-state spin texture in a strip geometry with a finite width w, containing 11 skyrmions. Bottom right: probability density of chiral magnonic edge states. Adapted from [209].

texture for a one-dimensional strip geometry was numerically obtained as shown in the top right panel of Fig 1.19. While the spin structure near the sample edge is modified due to the edge twist (see Section 1.3.4), a periodic structure of skyrmions was realized inside the bulk of sample. The magnon spectrum for the one-dimensional system is shown in the left panel of Fig 1.19. The bulk subbands corresponding to the lowest two bulk bands are separated by global band gaps. In contrast, bulk subbands at higher energies are connected by in-gap states arising from the bulk-edge correspondence. For example, there is a single left- and right-moving state between the third and fourth bulk band gap, localized at opposite edges as shown in the bottom right panel of Fig 1.19.

1.4   Outline of this thesis

In Chapter 1, we have covered a wide range of topics. The main ideas are summarized as follows:

- The topological band theory for magnonic systems has been successfully formulated analogously to electronic systems in the literature.

- Beyond topological phases characterized by Chern numbers, multipole moments provide new topological invariants for higher-order topological phases.

- Magnetic skyrmion crystal is an ideal platform for topological magnonics due to the enhanced stability with the integer topological charge and the emergent gauge field arising from noncoplanar spin structures and Dzyaloshinskii-Moriya interaction.

So far, there has been no study on the magnetic field dependence of topological properties of magnon bands in skyrmion crystals. Since the external control over topologically protected boundary-localized states is crucial for applications, we have a following important problem: *Is it possible to drive a topological phase transition in skyrmion crystals by external fields?* Motivated by this question, we discuss the following three research projects in this thesis:

1. Magnetic-field driven topological phase transition for controlling chiral edge states.

2. Laser-driven topological phase transition with induced skyrmion motions.

3. Magnonic corner states arising from the magnonic quadrupole moment.

It should be noted that we focus on magnetic skyrmions stabilized by the competition between the exchange interaction and Dzyaloshinskii-Moriya interaction in this thesis.

For the first project, we investigate the magnetic field dependence of magnon band topology by tracking the change in Chern numbers with increasing magnetic fields. The low energy magnon spectrum is characterized by counterclockwise (CCW) rotational mode and breathing mode of skyrmions as well as flat bands arising from other magnon bound states (see Section 1.3.6). The important finding is that the topological phase transition can be driven by external magnetic fields, associated with the band inversion between the CCW mode and breathing mode. Since these spin wave modes have been experimentally measured, it could be used as a first experimental observation of topological phase transition in magnonic systems.

The second project stems from the result of the first project. Using the Floquet theory for spin systems under terahertz lasers, we propose an ultrafast topological phase transition under circularly polarized laser. Inspired by the skyrmion-hosting multiferroic material, Cu_2OSeO_3 (see Section 2.2.2), the classical spin dynamics of skyrmions carrying electric polarizations is investigated in the presence of time-dependent electromagnetic fields from laser. The main results are the laser-controlled skyrmion motion due to the magnetoelectric coupling and the laser-driven topological phase transition in Floquet magnon bands.

The third project is related with the instability of twisted edge magnetization that occurs below the critical magnetic field (see Section 1.3.4). Previously, the edge instability was proposed to explain the experimental observation of skyrmion chains along the sample edge [104, 105]. In these work, a change in the classical ground-state spin textures due to the edge instability was not considered. As will be shown later, it leads to the formation of fractional (anti)skyrmions localized to edges of a sample below the critical magnetic field. Furthermore, magnonic corner states emerge together with fractional (anti)skyrmions. By extending the multipole moment to magnonic systems, we

discover that the magnonic corner states corresponds to topologically protected states of quadrupole topological insulators.

The structure of this thesis is as follows. In Chapter 2, we review the crystalline structure and magnetic properties of skyrmion-hosting materials. We also derive the form of Dzyaloshinskii-Moriya interactions allowed for each crystalline symmetry. In Chapter 3, we discuss the magnetic-field driven topological phase transition in skyrmion crystals, employing the formulation of Section 1.1. The content of Chapter 3 is published in Ref. [76]. In Chapter 4, we discuss the laser-driven skyrmion motion and magnonic topological phase transition, employing the Floquet theory for classical spin systems formulated by S. Higashikawa and his collaborators in Ref. [211]. The content of Chapter 4 is in preparation for the submission to academic journals (List of Publication 4). In Chapter 5, we discuss the magnonic quadrupole topological insulator realized in antiskyrmion crystals, employing the Wilson loop formalism adapted to magnonic systems (see Appendix E for details). The content of Chapter 5 was published in Ref. [212].

Chapter 2

Materials hosting magnetic skyrmions

In Chapter 2, we introduce various non-centrosymmetric magnetic systems, where the competition between the ferromagnetic exchange interaction and Dzyaloshinskii-Moriya interaction stabilizes magnetic skyrmions and antiskyrmions. We classify skyrmion-hosting materials by thier crystalline symmetries: T symmetry for chiral cubic crystals; C_{3v} for rhombohedral crystals; D_{2d} symmetry for tetragonal crystals. For each crystalline symmetry, the Dzyaloshinskii-Moriya interaction is derived using the symmetry argument. Subsequently, we review the crystalline structure and magnetic properties of several materials for each crystalline symmetry.

2.1 Point group symmetries relevant for skyrmions

Since the alignment of magnetic ions in a unit cell is often complicated, it is challenging to construct an atomistic spin model taking account of all magnetic interactions. Instead, we often employ the symmetry argument to derive the free energy functional in the continuum limit as in Eq. (A.18), which could be used to construct a spin lattice model by discretization. The symmetry argument is based on the point group symmetry of materials, whose operations do not affect atoms inside the unit cell [213]. The symmetry operation of point group includes rotations about an axis, reflections with respect to a plane, inversion operation, and their combinations. It should be noted that the translation operator is not included in the point group symmetry.

The Dzyaloshinskii-Moriya interactions is written as Lifshitz invariants in the continuum limit (see Appendix A.5):

$$\mathcal{L}_{ij}^{k} = m_i \partial_k m_j - m_j \partial_k m_i, \tag{2.1}$$

where $\boldsymbol{m}$ is a normalized magnetization vector. Keeping only the Lifshitz invariants that respect the symmetry operation of the point group, we can obtain the Dzyaloshinskii-Moriya interaction vector for different materials. In Ref. [129], all the crystalline symme-
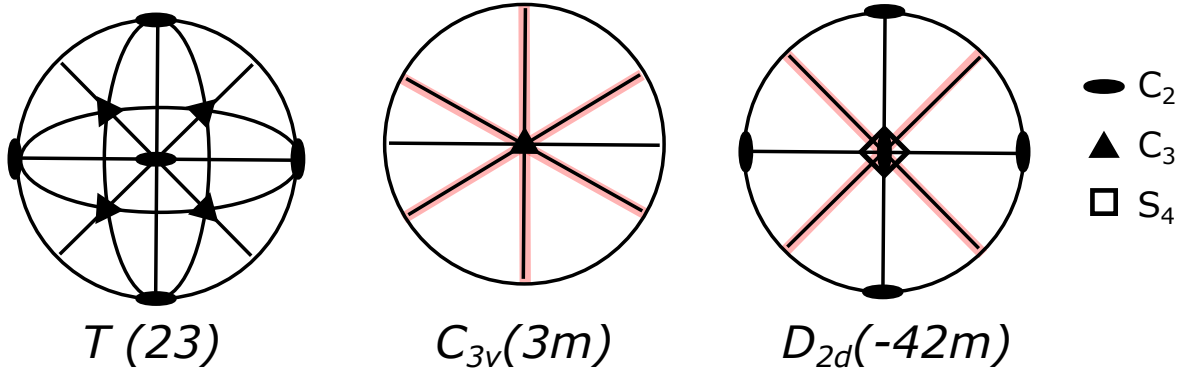
Figure 2.1: **Stereographic projection of point group symmetries that support magnetic skyrmions.** The symmetry operations are depicted schematically for T, C_{3v}, and D_{2d} symmetries, projected to the xy-plane. Ellipses and triangles filled by black respectively represent $C_{2\hat{z}}$ and $C_{3\hat{z}}$ rotations, while reflection planes are highlighted by red shaded lines. Empty squares indicate an improper rotation $S_{4\hat{z}}$ that is equivalent to a $C_{4\hat{z}}$ rotation followed by a reflection in the xy-plane.

tries that could host magnetic skyrmions are summarized with corresponding Dzyaloshinskii-Moriya interaction vectors. Furthermore, Ref. [214] contains a complete table of Lifshitz invariants for all 32 point groups. Among those listed in these references, we discuss the point group symmetries of skyrmion-hosting materials, including chiral cubic crystals with T symmetry, polar rhombohedral crystals with C_{3v} symmetry, and acentric tetragonal crystals with D_{2d} symmetry. The stereographic representation of these point group symmetries is shown in Fig. 2.1. In addition, we find that Ref. [215] is helpful for visualizing symmetry operations.

Firstly, we consider T symmetry for a cubic lattice, which is invariant by symmetry operations of $\{C_{2\hat{x}}, C_{2\hat{y}}, C_{2\hat{z}}, C_{3,[111]}\}$. Here, $C_{n\hat{m}}$ depicts the n-fold rotational symmetry about the axis parallel to a unit vector $\hat{m}$, where the cubic crystalline axes are taken parallel to the x, y, z-axes. From C_2 rotations, the Lifshitz invariant $\mathcal{L}_{ij}^k$ should be odd for each axis, implying $i \neq j \neq k$. Taking into account of $C_{3,[111]}$ that permutes $\{x, y, z\}$ cyclically, the Lifshitz invariant allowed by T-symmetry is

$$
\begin{aligned}
L_{yz}^x + L_{zx}^y + L_{xy}^z &= (m_y \partial_x m_z - m_z \partial_x m_y) + (m_z \partial_y m_x - m_x \partial_y m_z) + (m_x \partial_z m_y - m_y \partial_z m_x) \\
&= -\boldsymbol{m} \cdot (\nabla \times \boldsymbol{m}). \quad (2.2)
\end{aligned}
$$

By discretization, the Dzyaloshinskii-Moriya interaction is written in a cubic lattice as

$$
H_{\mathrm{DM}} = \sum_{\boldsymbol{r},\boldsymbol{r}'} \frac{D(\boldsymbol{r} - \boldsymbol{r}')}{|\boldsymbol{r} - \boldsymbol{r}'|} \cdot \boldsymbol{m_r} \times \boldsymbol{m_{r'}}, \quad (2.3)
$$

where $\boldsymbol{r} = (x, y, z)$ represents the position vector for a lattice point in cubic systems, and the sign of D is determined by the chirality of crystals (see Section 2.2.1). The bulk Dzyaloshinskii-Moriya interaction is supported in chiral magnets that typically belong to

space group $P2_1 3$, and it stabilizes Bloch skyrmions (Fig. 1.6 with $m = 1$ and $\gamma = \pm\pi/2$). Skyrmion-hosting materials of this type are B20 alloys such as MnSi [134, 135, 216–219], Fe$_{1-x}$Co$_x$Si [136–139], and FeGe [140, 167, 220, 221], as well as multiferroic insulator Cu$_2$OSeO$_3$ carrying the electric polarization induced by the magnetization [142, 143, 222, 223].

Secondly, we consider C_{3v} symmetry for trigonal lattice systems. As shown in Fig. 2.1, it is characterized by three reflection planes perpendicular to the xy-plane and $C_{3\hat{z}}$ rotation. Hence, the symmetry operation does not affect the z-component of magnetization. The reflection operation perpendicular to the xy-plane maps from (x, y, z) to $(x \cos 2\theta + y \sin 2\theta, x \sin 2\theta - y \cos 2\theta, z)$, where θ is an angle from the x-axis. It is then straightforward to show that $m_z \partial_x m_x + m_z \partial_y m_y$ and $m_x \partial_x m_z + m_y \partial_y m_z$ are invariant with the reflection symmetry as well as $C_{3\hat{z}}$ symmetry. The Lifshitz invariant is then given as

$$
\begin{aligned}
L_{zx}^x - L_{yz}^y &= (m_z \partial_x m_x - m_x \partial_x m_z) - (m_y \partial_y m_z - m_z \partial_y m_y) \\
&= (\hat{z} \cdot \boldsymbol{m})(\nabla \cdot \boldsymbol{m}) - (\boldsymbol{m} \cdot \nabla)(\boldsymbol{m} \cdot \hat{z}).
\end{aligned} \tag{2.4}
$$

By discretization, the Dzyaloshinskii-Moriya interaction is written as

$$
H_{\mathrm{DM}} = \sum_{\boldsymbol{r}, \boldsymbol{r}'} \frac{D\hat{z} \times (\boldsymbol{r} - \boldsymbol{r}')}{|\boldsymbol{r} - \boldsymbol{r}'|} \cdot \boldsymbol{m_r} \times \boldsymbol{m_{r'}}. \tag{2.5}
$$

In this case, Néel skyrmions are stabilized (Fig. 1.6 with $m = 1$ and $\gamma = 0, \pi$). So far, the polar semiconductor GaV$_4$S$_8$ is only the example for bulk C_{3v} crystalline symmetric systems, which is another example of multiferroic materials hosting skyrmions [144, 224]. Importantly, the Dzyaloshinskii-Moriya interaction perpendicular to $(\boldsymbol{r} - \boldsymbol{r}')$ is also obtained at the surface/interface where the inversion symmetry is broken [145–152, 225].

The symmetry operations for D_{2d} symmetry defined in tetragonal lattice systems are $\{S_{4\hat{x}}, C_{2\hat{x}}, C_{2\hat{y}}, C_{2\hat{z}}, M_{[110]}, M_{[-110]}\}$, where $M_{\hat{m}}$ is the reflection about a plane perpendicular to unit vector $\hat{m}$ and $S_{4\hat{z}}$ is a combined operation of $C_{4\hat{z}}$ and $M_{\hat{z}}$ (see Fig. 2.1). Similarly to the chiral cubic case with T symmetry, the C_2 rotations allow the Lifshitz invariant $\mathcal{L}_{ij}^k$ with $i \neq j \neq k$. Furthermore, $S_{4\hat{z}}$ maps $\{x, y, z\}$ to $\{-y, x, -z\}$. Hence, the Lifshitz invariant takes an anisotropic form with inverted chirality in the orthogonal directions:

$$
L_{yz}^x - L_{zx}^y = (m_y \partial_x m_z - m_z \partial_x m_y) - (m_z \partial_y m_x - m_x \partial_y m_z). \tag{2.6}
$$

In a square lattice, the Dzyaloshinskii-Moriya interaction is written as

$$
H_{\mathrm{DM}} = \sum_{\boldsymbol{r}, \boldsymbol{r}'} D(\mp\hat{\boldsymbol{x}}\delta_{\boldsymbol{r}-\boldsymbol{r}', \pm a\hat{\boldsymbol{x}}} \pm \hat{\boldsymbol{y}}\delta_{\boldsymbol{r}-\boldsymbol{r}', \pm a\hat{\boldsymbol{y}}}) \cdot \boldsymbol{m_r} \times \boldsymbol{m_{r'}}. \tag{2.7}
$$

This term stabilizes antiskyrmions with $m = -1$ and $\gamma = \pm\pi/2$ in Fig. 1.6, which was realized in a tetragonal Heusler material Mn$_{1.4}$Pt$_{0.4}$Pd$_{0.1}$Sn [153]. The spin texture of antiskyrmions can be interpreted as combinations of Néel skyrmions in $[110]/[0\bar{1}0]$ directions and Bloch skyrmions in $[100]/[010]$ directions, resulted from the anisotropic Dzyaloshinskii-Moriya interaction.
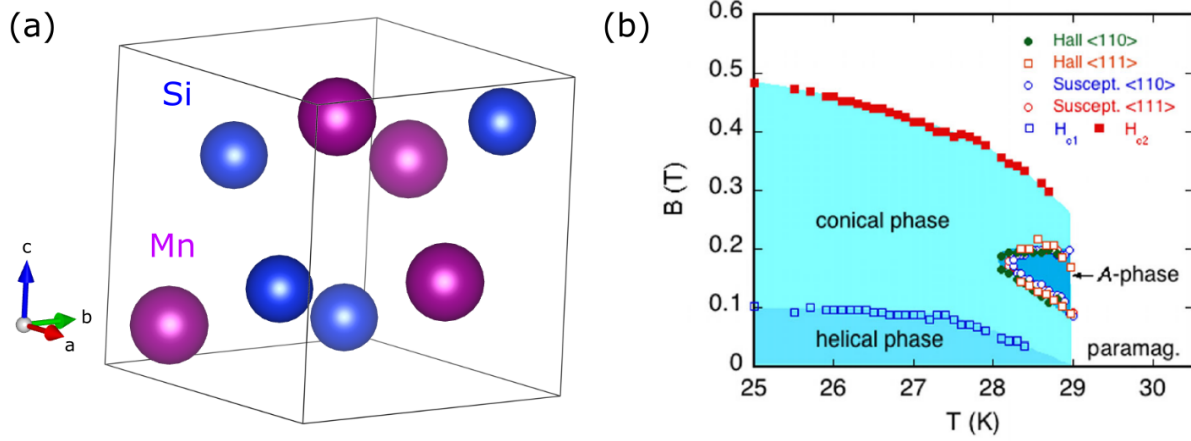
Figure 2.2: **Crystal structure and magnetic phase diagram of MnSi.** (a) The crystal structure of MnSi that belongs to the space group $P2_13$. (b) Magnetic phase diagram of MnSi, obtained from the topological Hall effect and the ac susceptibility measurement in Ref. [226–228]. (b) is adapted from [135].

Material	Lattice constant (nm)	Wavelength (nm)	D/J ratio
MnSi	0.45	18	0.16
$Fe_{1-x}Co_xSi$	0.45	37	0.076
FeGe	0.47	70	0.042
Cu_2OSeO_3	0.89	60	0.093
$Co_8Zn_8Mn_4$	0.63	125	0.032

Table 2.1: **Wavelength of the helical phase and the estimated relative strength of the Dzyaloshinskii-Moriya interaction in chiral magnets.** The lattice constant for each material is extracted from Ref. [95, 137, 229, 230], while the wavelength of the helical phase in a bulk sample is taken from Ref. [98].

2.2 Materials hosting Bloch skyrmions

2.2.1 B20 materials

B20 alloys refer to metals and semiconductors with the chiral cubic crystal structure shown in Fig. 2.2(a) (space group $P2_13$), including MnSi, $Fe_{1-x}Co_xSi$, and FeGe. For bulk crystals, the magnetic phase diagram consists of the helical phase, conical phase, and the ferromagnetic phase at zero temperature. In addition to these single $\mathbf{q}$ states, the skyrmion crystal phase characterized by the triple $\mathbf{q}$ vectors is stabilized by thermal fluctuations. The experimentally obtained magnetic phase diagram for MnSi is shown in Fig. 2.2(b), where the A-phase corresponds to the skyrmion crystal phase. The existence of the A phase in MnSi was first reported in 1984 by neutron small angle scattering [231], and remained elusive for more than 20 years.

Similar magnetic phase diagram was obtained for $Fe_{1-x}Co_xSi$ [137]. While MnSi and
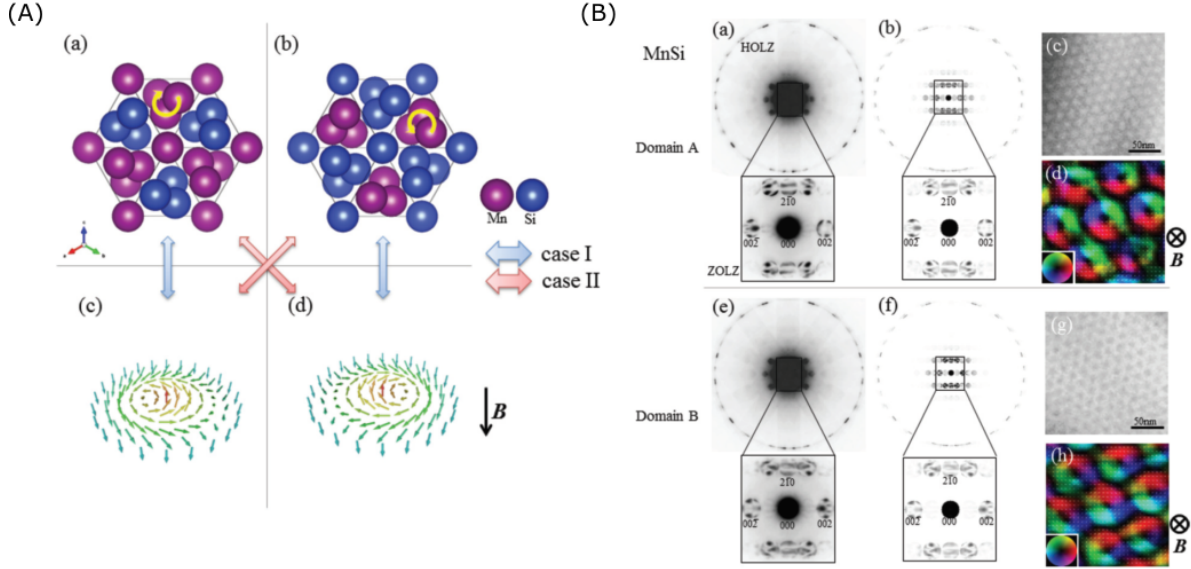
Figure 2.3: **Correlation between the chirality of crystals and magnetic skyrmions in MnSi.** (A) Crystal structure of (a) left-handed crystal and (b) right-handed crystal of MnSi, projected from [111] direction. Magnetic textures of skyrmions with opposite helicities characterized by (c) counterclockwise (CCW) and (d) clockwise (CW) rotation of the in-plane magnetizations. The magnetic field is applied along the negative z-axis. (B) Transmission electron microscopy images for two domains of MnSi with opposite chirality, where domain A is left-handed chiral and domain B is right-handed chiral. (a),(e) Convergent-beam electron diffraction pattern (CBED). (b),(f) simulated CBED pattern for left-handed/right-handed crystals. (c),(g) Observed skyrmion crystals in each domain, where the central contrast implies the helicity of skyrmions as (c) CCW and (g) CW. (d),(h) In-plane magnetization of skyrmion crystals. Adapted from [138].

$Fe_{1-x}Co_xSi$ become paramagnetic above 30 K, the skyrmion crystal phase was obtained near room temperature in FeGe [140]. Furthermore, skyrmions were observed in a thin film sample of FeGe over a wide range of temperatures from 50 K to 300 K, which is advantageous for device applications.

As discussed in Section 1.3.3 and Appendix A.4, the mean-field solution of the Ginzburg-Landau free energy is the conical phase under applied magnetic field with its wavelength $L_D = 2a\pi J/|D|$, where a is the lattice constant, J and D denotes the exchange coupling and Dzyaloshinskii-Moriya interaction, respectively. Hence, the D/J ratio can be estimated from the period of helical modulation in each material. For example, the wavelength of helicoids in MnSi is roughly 18 nm. From the lattice constant $a = 0.45$ nm in MnSi, we obtain $D/J = 0.16$. Using the extensive list of experimental results in Ref. [98], we estimate the D/J ratio for B20 alloys, Cu_2OSeO_3 and $Co_8Zn_8Mn_4$ as shown in Table 2.1. We should note that Co-Zn-Mn alloys belong to the space group $P4_132/P4_332$ with slightly higher symmetry than B20 alloys but still characterized by the same chiral

cubic point group symmetry [97, 232].

The chirality of helical modulation is determined by the sign of the Dzyaloshinskii-Moriya interaction. Importantly, this is fixed by the chirality of underlying crystalline structures. Figure 2.3 shows the experimental study of the correlation between the chirality of crystal structure and skyrmions in MnSi [138]. While the chirality of crystals are defined by positions of Mn atoms in a projected view from [111] directions, the helicity of skyrmions is defined by the rotation of in-plane magnetization as shown in Fig 2.3(A). The relationship between the chirality of crystal structure and helicity of skyrmions depends on materials, as indicated by case I and case II. Combining convergent-beam electron diffraction and Lorentz transmission electron microscopy, the crystal structure and in-plane magnetizations skyrmion crystals were compared in two different domains of MnSi. This is illustrated in Fig. 2.3(B), showing that MnSi corresponds to case I. Furthermore, the correlation between crystal structure and chiral spin textures showed the reversal from case I to case II as the composition of $Mn_{1-x}Fe_xGe$ was varied from $x = 0.3$ to $x = 1.0$ [233].

2.2.2   Multiferroic insulator Cu_2OSeO_3

In this section, we first introduce multiferroics in magnetic systems, followed by a detailed account of skyrmion-hosting multiferroic insulator Cu_2OSeO_3 [142]. Multiferroic materials were originially proposed by Schmid as materials with two or all three properties of ferroelectricity, ferromagnetism, and ferroelasticity [234]. For the coexistence of electric and magnetic dipole moments, the inversion symmetry and time-reversal symmetry must be simultaneously broken. In such systems, the electric polarization could be induced by applying magnetic fields, known as the magnetoelectric effect [235, 236]. Following the theoretical prediction by Dzyaloshinskii [237], the linear magnetoelectric effect was first observed in Cr_2O_3 [238, 239]. However, the linear magnetoelectric effect was too small for applications. The breakthrough was made by the discovery of $TbMnO_3$, where electric polarization was induced with the magnetic order below the critical temperature at 27 K [240]. The fundamental difference is the spin-driven ferroelectricity in contrast with the two independent order parameter for ferroelectricity and ferromagnetism in previously found multiferroic materials.

The key insight for the spin-driven electric polarization was provided from the microscopic point of view by H. Katsura and his collaborators [37]. As illustrated in Fig. 2.4(A), they have shown that the electric polarization is induced by interactions between two magnetic ions mediated by a ligand ion. The electric polarization was derived as

$$\mathbf{P} \propto (\boldsymbol{r} - \boldsymbol{r}') \times (\boldsymbol{S_r} \times \boldsymbol{S_{r'}}), \tag{2.8}$$

where $\boldsymbol{S_r}$ and $\boldsymbol{S_{r'}}$ are localized spins of magnetic ions at $\boldsymbol{r}$ and $\boldsymbol{r}'$. Eq. (2.8) implies that rotations of spins parallel to the bond axis results in the electric polarization perpendicular to the spin rotation axis and bond axis. We should note that this type of helical order is called cycloids and realized by the Dzyaloshinskii-Moriya interaction of Eq. (2.5). Conversely, the applied electric field induces the Dzyaloshinskii-Moriya interaction through
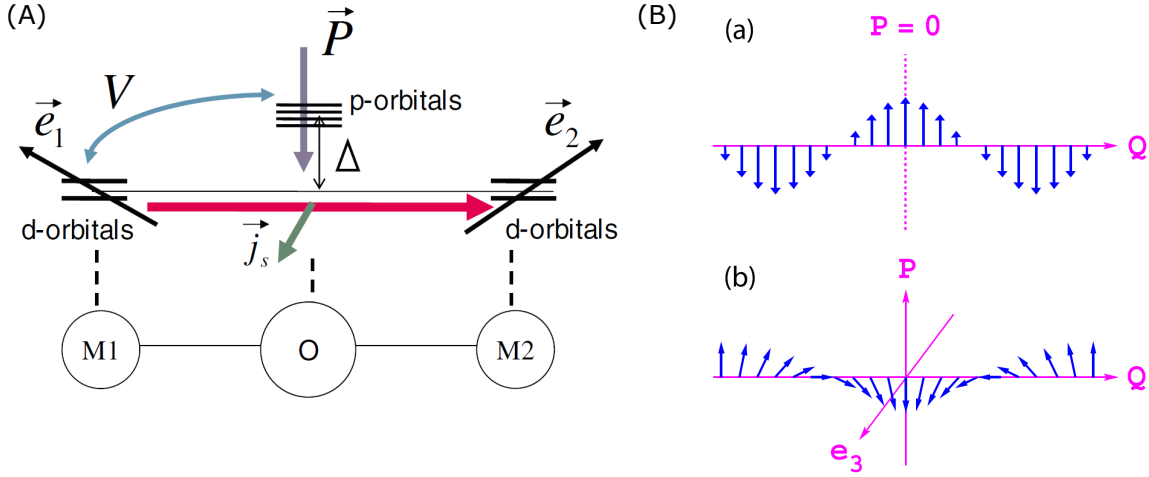
Figure 2.4: **Electric polarization induced by the noncollinear spin structure.** (A) Schematic representation of the induced electric polarization from interactions between two transition metal ions M1 and M2 with the oxygen atom O between them. Localized spins of transition metal ions are represented by $\vec{e}_1$ and $\vec{e}_2$, which leads to the spin current $\vec{j}_s \propto \vec{e}_1 \times \vec{e}_2$. The electric polarization is induced in the transverse direction, described by $\mathbf{P} \propto \vec{e}_{12} \times \vec{j}_s$ with $\vec{e}_{12}$ denoting the unit vector connecting M1 and M2. (B)(a) The total electric polarization $\mathbf{P}$ vanishes for a sinusoidal spin structure. (b) The macroscopic electric polarization is induced by the cycloidal modulation with wave vector $\mathbf{Q}$. Here, $\mathbf{P} \propto \hat{e}_3 \times \mathbf{Q}$, with $\hat{e}_3$ representing a unit vector along the spin rotation axis. (A) is adapted from [37] and (B) is adapted from [243].

the magnetoelectric coupling of Eq. (2.8), given as $\mathbf{D} \propto \mathbf{E} \times (\mathbf{r} - \mathbf{r}')$ [37]. From the spin current $\hat{j}_s \propto \mathbf{S}_\mathbf{r} \times \mathbf{S}_{\mathbf{r}'}$, this is called the spin current mechanism, or equivalently the inverse Dzyaloshinskii-Moriya mechanism [241]. Soon after, the magnetic phase of $TbMnO_3$ below 27 K, where it becomes ferroelectric, was indeed shown to be an incommensurate cycloid as a result of frustrated exchange interactions [242]. The equivalent result was obtained using the symmetry argument [243]. This is illustrated in Fig. 2.4(B). We can see that the cycloidal order breaks inversion symmetry, resulting in the macroscopic electric polarization. In contrast, the sinusoidal modulation conserves inversion symmetry with its axis indicated by a dotted line.

The above arguments do not take into account of displacement of constituent ions. Considering ionic displacements, the exchange striction could also induce the electric polarization [236, 244, 245]:

$$H_{\text{ex}} = J(\mathbf{r}, \mathbf{r}')\mathbf{S}_\mathbf{r} \cdot \mathbf{S}_{\mathbf{r}'}, \tag{2.9}$$

where the coefficient of superexchange coupling $J(\mathbf{r}, \mathbf{r}')$ depends on the bond length $|\mathbf{r} - \mathbf{r}'|$ and the bond angle θ between magnetic ions and an anion. Usually, we assume that the bond length and bond angle is fixed as the energy scale for lattice deformation is much larger. However, we could interpret this term with the fixed scalar product $\mathbf{S}_\mathbf{r} \cdot \mathbf{S}_{\mathbf{r}'}$ modifying the bond length and angle. Consequently, the electric polarization
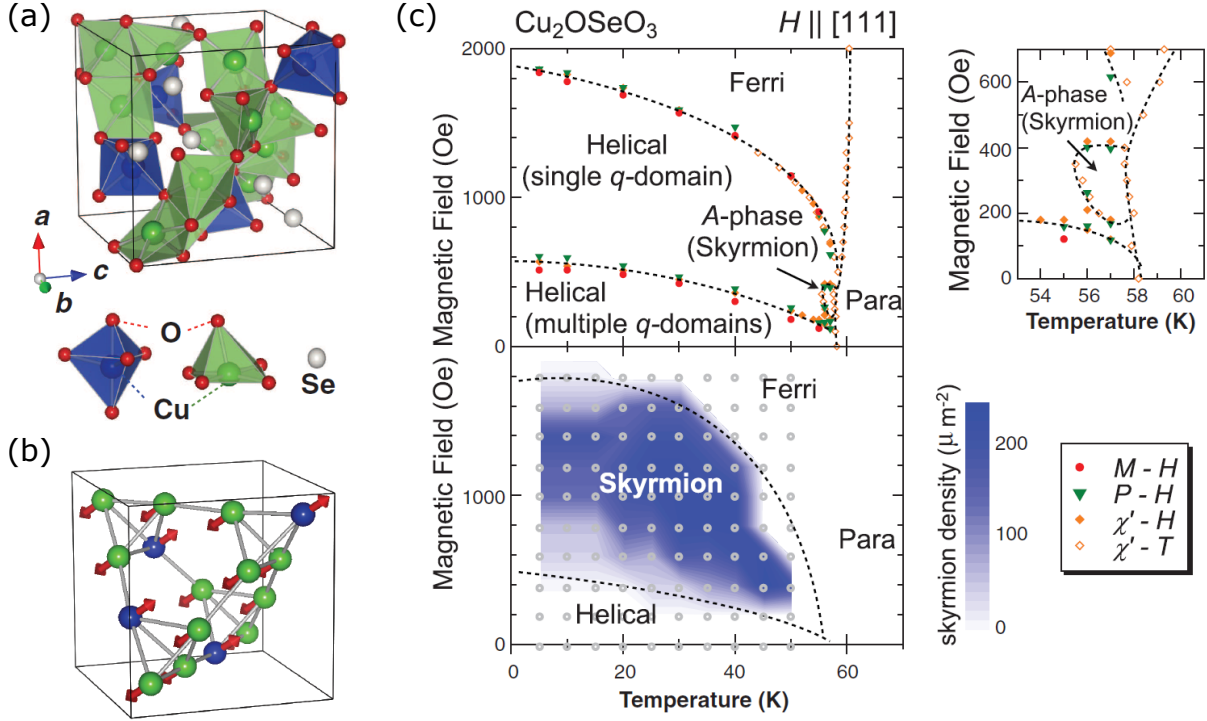
Figure 2.5: **Crystal structure and magnetic phase diagram of Cu_2OSeO_3.** (a) Crystal structure of Cu_2OSeO_3, showing two inequivalent Cu^{2+} sites surrounded by oxygen atoms. (b) Ferrimagnetic spin arrangement with (anti)ferromagnetic interactions between (in)equivalent Cu^{2+} ions. Each Cu^{2+} ion has a $S = \frac{1}{2}$ spin. (c) Magnetic phase diagram for bulk and thin film samples of Cu_2OSeO_3, respectively shown in the top and bottom panel. Right panel shows the enlarged view of phase diagram near the skyrmion crystal phase of the bulk sample. Adapted from [142]. Reprinted with permission from AAAS.

could be induced. Depending on the bond angle θ, the exchange striction mechanism could become more significant than the spin current mechanism in the cycloid phase as found in $RMnO_3$ [246].

So far, we have discussed the electric polarization arising from interactions between adjacent magnetic ions. Another mechanism is based on the modulation of d-p hybridization between magnetic ions and ligand anions, caused by the parallel alignment of magnetic moment with respect to the bond axis through the spin-orbit coupling [247–249]. This is called the d-p hybridization mechanism, where the induced local electric polarization is written as [236, 249]

$$\mathbf{p}_{ij} \propto (\hat{e}_{ij} \cdot \boldsymbol{m}_i)^2 \hat{e}_{ij}, \tag{2.10}$$

where $\hat{e}_{ij}$ is a unit vector pointing from a magnetic ion to an anion and $\boldsymbol{m}_i$ is the magnetic moment carried by the magnetic ion. If magnetic ions and anions are alternatively aligned in a straight line, the macroscopic electric polarization is canceled out. We should note
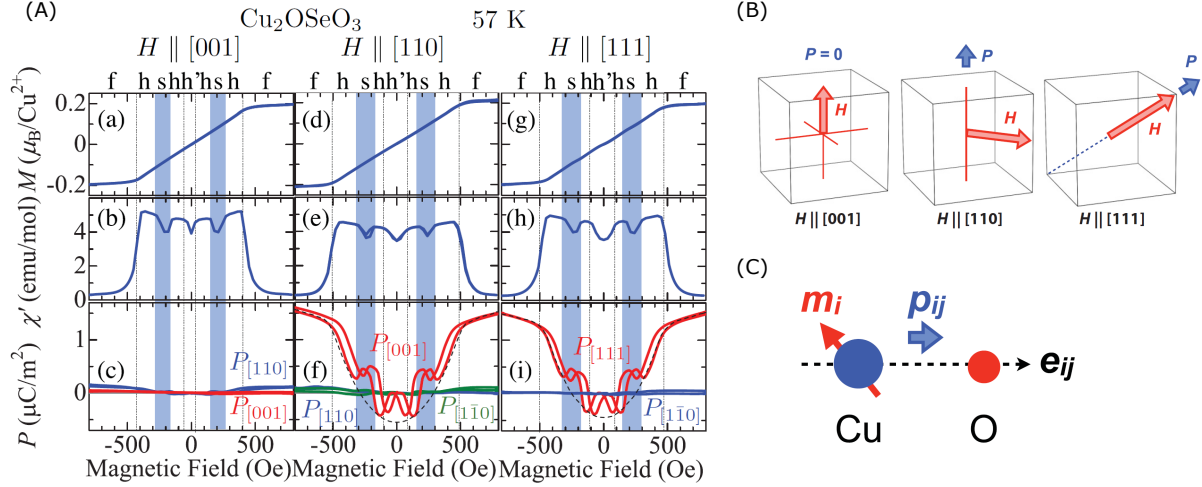
Figure 2.6: **Electric polarization induced in Cu_2OSeO_3.** (A) Magnetic field dependence of (a)/(d)/(g) magnetization, (b)/(e)/(h) ac magnetic susceptibility, and (c)/(f)/(i) electric polarization under magnetic fields along [001]/ [110]/ [111] direction. Each magnetic phase is denoted as f (ferromagnetic), h (helical with single q domain), h' (helical with multiple q domains), and s (skyrmion crystal), with the skyrmion crystal phase highlighted by blue. Dashed lines are the theoretical prediction from Eq. (2.11) for the single-domain helical (conical) phase. (B) Directions of the induced electric polarization in Cu_2OSeO_3 under various magnetic fields. (C) Schematic representation of d-p hybridization mechanism, inducing a local polarization $\mathbf{p}_{ij}$ longitudinal to the bond axis between Cu and O ions. $\boldsymbol{m}_i$ and $\hat{e}_{ij}$ represent the magnetic moment at Cu site and the unit vector from Cu site to O site, respectively. Adapted from [143].

that this contribution is important in Cu_2OSeO_3 (see Fig. 2.6(C)), which is the first example of multiferroic insulator hosting skyrmions [95, 142, 143, 191, 222, 223].

Figure 2.5(a) shows the crystal structure of Cu_2OSeO_3. Compared to B20 alloys, it is more complicated as a unit cell contains 16 Cu^{2+} ions ($S = \frac{1}{2}$) with two inequivalent positions characterized by different coordination of oxygen bonds. Still, the crystal structure of Cu_2OSeO_3 also belongs to the same space group $P2_13$ as B20 alloys. Only keeping Cu^{2+} ions in the unit cell, it forms a ferrimagnetic order as shown in Fig. 2.5(b). Taking the average magnetic moment of each tetrahedron consisting of four Cu^{2+} ions, we see that the same cubic chiral structure appears as in the crystal structure of MnSi shown in Fig. 2.2(a). Hence, the magnetic phase diagram of Cu_2OSeO_3 is similar to B20 alloys. Figure 2.2(c) shows that the skyrmion crystal phase is stable near the paramagnetic transition temperature for bulk samples, while its stability is strongly enhanced for a thin film sample.

Since Cu_2OSeO_3 is insulating material, it is suitable for studying the dielectric properties in the presence of magnetic skyrmions [142, 222, 223]. In Ref. [143], the magnetoelectric nature of Cu_2OSeO_3 was investigated in details. Figure 2.6(A) shows the magnetic field dependence of electric polarization at 57 K under magnetic fields applied along
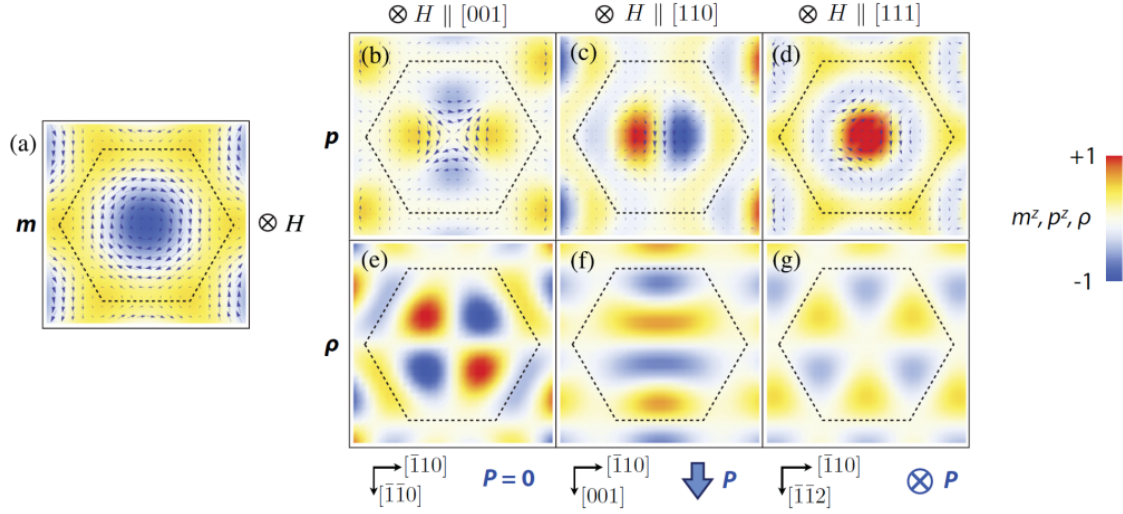
Figure 2.7: **Electric polarization in skyrmion crystal phase.** Spatial distribution of (a) magnetization, (b)-(d) local electric polarization vector $\mathbf{p}$, and (e)-(g) local electric charge ρ in skyrmion crystals under various magnetic fields. The out-of-plane direction is taken parallel to magnetic fields with the horizontal axis fixed in $[\bar{1}10]$ direction. Adapted from [143].

[001], [110], and [111] axes. As indicated by no directional dependence of magnetization and ac magnetic susceptibility, the magnetic phase diagram is the same for all magnetic fields due to the cubic crystalline structure. In contrast, the electric polarization shows a strong directional dependence, induced by magnetic fields parallel to [110] and [111] but not along [001] direction. This is illustrated in Fig. 2.6(B). Furthermore, the anomalous magnetic field dependence is observed in the electric polarization with a sudden increase in the skyrmion crystal phase under $H \parallel [110], [111]$. Therefore, the electric polarization arises from the spin arrangement in this material.

The experimentally obtained electric polarization under various magnetic fields was explained by the d-p hybridization mechanism [143, 247–249]. As illustrated in Fig. 2.6(C), it induces a longitudinal electric polarization for each Cu-O bond. Assuming the ferri-magnetic spin arrangement, the total electric polarization for each tetrahedron made of four Cu^{+2} ions was computed by summing over all Cu-O bonds. Denoting the average magnetization of a tetrahedron at $\mathbf{r}$ as $\mathbf{m}_{\mathbf{r},abc} = (m_{\mathbf{r},a}, m_{\mathbf{r},b}, m_{\mathbf{r},c})$, its polarization is given as [143, 197]

$$\mathbf{P}_{\mathbf{r},abc}(\mathbf{m}_{\mathbf{r},abc}) = (p_{\mathbf{r},a}, p_{\mathbf{r},b}, p_{\mathbf{r},c}) = \lambda(m_{\mathbf{r},b}m_{\mathbf{r},c}, m_{\mathbf{r},c}m_{\mathbf{r},a}, m_{\mathbf{r},a}m_{\mathbf{r},b}), \qquad (2.11)$$

with the subscript a, b, c implying that it is defined in the orthogonal basis of cubic crystalline axis. The coupling strength λ is extracted from the experimental result as $\lambda = 5.64 \times 10^{-27} \ \mu$Cm [143]. The total electric polarization is defined as $\mathbf{P} = (1/NV) \sum_{\mathbf{r}} \mathbf{P}_{\mathbf{r}}$, where N is the number of tetrahedra, $V = 1.76 \times 10^{-28} \ \text{m}^3$ is the volume of each tetrahedron, and the summation is taken over all tetrahedra.

In order to study the directional dependence of electric polarization, we define another orthogonal basis labeled by xyz-coordinates with z-axis parallel to applied magnetic fields. In this basis, the magnetization profile of skyrmion crystal is obtained identically regardless of the direction of magnetic fields as shown in Fig 2.7(a). Here, it is convenient to take $[\bar{1}10]$ direction as x-axis for all cases of $z \parallel [001]$, $z \parallel [110]$, and $z \parallel [111]$. Now, we define the rotation matrix $\hat{R}_{abc,xyz}$ for mapping from xyz-coordinates to abc-coordinates:

$$\boldsymbol{m}_{\boldsymbol{r},abc} = \hat{R}_{abc,xyz}\boldsymbol{m}_{\boldsymbol{r},xyz}, \tag{2.12}$$

where $\boldsymbol{m}_{\boldsymbol{r},abc}$ and $\boldsymbol{m}_{\boldsymbol{r},xyz}$ is the average magnetization of a tetrahedron formed by Cu^{2+} ions defined in abc-coordinates and xyz-coordinates, respectively. The electric polarization in xyz-coordinates is written as

$$\mathbf{P}_{\boldsymbol{r},xyz}(\boldsymbol{m}_{\boldsymbol{r},xyz}) = \hat{R}_{abc,xyz}^{-1}\mathbf{P}_{\boldsymbol{r},abc}(\hat{R}_{abc,xyz}\boldsymbol{m}_{\boldsymbol{r},xyz}). \tag{2.13}$$

Using Eq. (2.13), the local electric polarization under $z \parallel [001]$, $z \parallel [110]$, and $z \parallel [111]$ are obtained as

$$\mathbf{P}_{\boldsymbol{r},xyz} = \lambda\Big(-m_{\boldsymbol{r},z}m_{\boldsymbol{r},x}, m_{\boldsymbol{r},y}m_{\boldsymbol{r},z}, \frac{-m_{\boldsymbol{r},x}^2 + m_{\boldsymbol{r},y}^2}{2}\Big) \quad \text{for } z \parallel [001], \tag{2.14}$$

$$\mathbf{P}_{\boldsymbol{r},xyz} = \lambda\Big(-m_{\boldsymbol{r},x}m_{\boldsymbol{r},y}, \frac{-m_{\boldsymbol{r},x}^2 + m_{\boldsymbol{r},z}^2}{2}, m_{\boldsymbol{r},y}m_{\boldsymbol{r},z}\Big) \quad \text{for } z \parallel [110],$$

$$\mathbf{P}_{\boldsymbol{r},xyz} = \lambda\Big(-\frac{m_{r,x}(\sqrt{2}m_{r,y} + m_{r,z})}{\sqrt{3}}, \frac{-m_{r,x}^2 + m_{r,y}(m_{r,y} - \sqrt{2}m_{r,z})}{\sqrt{6}}, -\frac{m_{r,x}^2 + m_{r,y}^2 - 2m_{r,z}^2}{2\sqrt{3}}\Big)$$
$$\text{for } z \parallel [111].$$

Assuming $\boldsymbol{m}_{\boldsymbol{r}} = (0,0,1)$ for the ferromagnetic phase, we immediately find $\mathbf{P}_{\boldsymbol{r},xyz} = 0$ for $z \parallel [001]$, $\mathbf{P}_{\boldsymbol{r},xyz} = \frac{\lambda}{2}\hat{y}$ for $z \parallel [110]$ ($\hat{y} \parallel [001]$), and $\mathbf{P}_{\boldsymbol{r},xyz} = \frac{\lambda}{\sqrt{3}}\hat{z}$ for $z \parallel [111]$, with $\hat{i}$ representing a unit vector along xyz-axes. Hence, it successfully reproduces the experimental result (see Fig. 2.6(B)).

Figure 2.7 shows the local electric polarization and local electric charge of skyrmion crystals [143]. Here, the local electric charge is computed by $\rho = \nabla \cdot \mathbf{P}_{\boldsymbol{r},xyz}$. While the direction of macroscopic polarizations is the same as the ferromagnetic phase, the internal spatial profile also depends on the direction of applied magnetic fields, characterized by quadrupole moment for $H \parallel [001]$, in-plane electric dipole moment for $H \parallel [110]$, and out-of-plane electric dipole moment for $H \parallel [111]$, respectively.

Since magnetic skyrmions can carry electric dipole moments in Cu_2OSeO_3, it provides a route for energy efficient manipulation of skyrmions without electric currents. For this purpose, the electrical control of skyrmion dynamics and nonreciprocal directional dichroism were studied extensively [191, 196–199, 223, 250, 251]. In Chapter 4, we discuss the laser-controlled skyrmion dynamics in Cu_2OSeO_3 using its magnetoelectric nature.
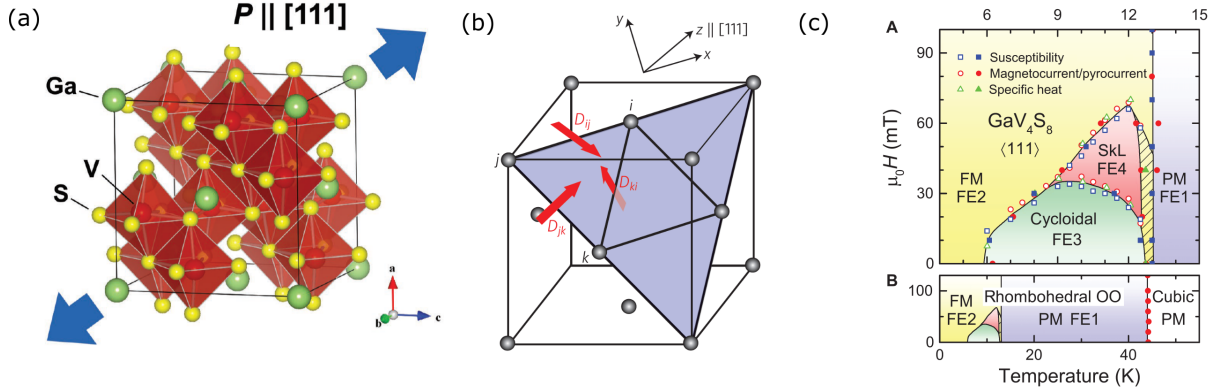
Figure 2.8: **Crystal structure and magnetic phase diagram of GaV$_4$S$_8$.** (a) Crystal structure of GaV$_4$S$_8$ that belongs to the space group $F\bar{4}3m$ ($R3m$) above (below) the structural transition temperature $T_s \sim 44$ K. The cubic crystal is elongated along [111] direction to become rhombohedral below T_s. (b) Face centered cubic lattice of V_4 clusters carrying $S = \frac{1}{2}$. The red vectors indicate the Dzyaloshinskii-Moriya vectors on the triangular lattice within the (111) plane. (c) Magnetic phase diagram of bulk GaV$_4$S$_8$ under magnetic fields along [111] axis. PM, SkL, and FM respectively denotes paramagnetic phase, skyrmion lattice phase, and ferromagnetic phase. (a) is adapted from [97] and (b) is adapted from [144]. (c) is reprinted from Science Advances [224]. © The Authors, some rights reserved; exclusive licensee AAAS. Distributed under a CC BY-NC 4.0 license http://creativecommons.org/licenses/by-nc/4.0/.

2.3   Materials hosting Néel skyrmions

As discussed in Section 2.1, Néel skyrmions are realized in rhombohedral crystals with C_{3v} symmetry. So far, GaV$_4$S$_8$ is the only example for this case [97, 144]. Figure 2.8(a) illustrates the crystal structure of GaV$_4$S$_8$ consisting of $(V_4S_4)^{5+}$ cubane-type cluster ions and $(GaS_4)^{5-}$ tetrahedra cluster ions arranged in NaCl manner [253]. It undergoes the structural transition from cubic to rhombohedral crystal at $T_s \sim 44$ K, resulting in the electric polarization along [111] axis. The ferromagnetic order appears at even lower temperature with $T_c \sim 13$ K. The magnetism is originated from V$_4$ clusters with $S = \frac{1}{2}$, forming a triangular lattice within the (111) plane as shown in Fig. 2.8(b). Similarly to chiral magnets, the magnetic phase diagram consists of cycloidal phase, skyrmion crystal phase, and ferromagnetic phase. Figure 2.8(c) shows the magnetic phase diagram of a bulk sample of GaV$_4$S$_8$ [224], where the skyrmion crystal phase exist over a wide range of temperatures and magnetic fields. This is in contrast to bulk chiral magnets stabilizing skyrmions within a narrow region near the Curie temperature. The enhanced stability of skyrmions in C_{3v} symmetric systems is due to the absence of conical phase [130]. In addition to the electric polarization induced by the structural transition, the spin-driven ferroelectricity was reported in this material arising from the exchange striction mechanism [224].
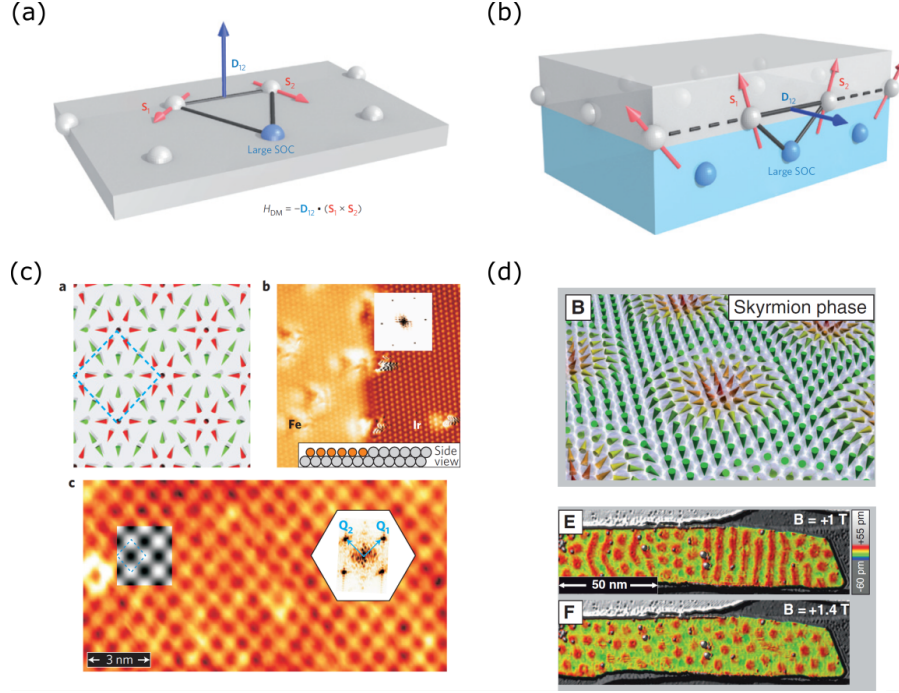
Figure 2.9: **Néel skyrmions stabilized on single and bilayer ferromagnetic films.** (a) Dzyaloshinskii-Moriya interaction between S_1 and S_2 generated by RKKY interaction with an atom having a large spin-orbit coupling. (b) Interfacial Dzyaloshinskii-Moriya interaction between a ferromagnetic metal (gray) and a heavy metal with a large spin-orbit coupling (blue). (c) Nanoskyrmion lattice in an Fe monolayer on Ir(111). a, Schematic picture of spin configurations. b, Scanning tunneling microscopy (STM) image. c, Spin-polarized STM image at $T \sim 11$ K and $B = 2$ T applied normal to the surface. (d) Skyrmion crystal phase on a PdFe bilayer, observed by spin-polarized STM at 8 K. (a),(b) are adapted from [145], (c) is adapted from [152], and (d) is adapted from [252]. (d) is reprinted with permission from AAAS.

The interfacial Dzyaloshinskii-Moriya interaction could also stabilize Néel skyrmions in ferromagnetic ultrathin films [151, 152] and multilayer systems [145–150]. The underlying mechanism is the Ruderman-Kittel-Kasuya-Yosida (RKKY) interaction in the presence of the Rashba spin-orbit coupling on the interface/surface [225, 254], which describes an indirect exchange interaction between two localized spins mediated by conduction electrons [255–257]. This is illustrated in Fig. 2.9(a) and (b), showing the Dzyaloshinskii-Moriya vector perpendicular to a triangle formed by two magnetic ions and a heavy metal atom with a large spin-orbit coupling.

Figure 2.9(c) shows a square lattice of nanoscale skyrmion crystals on an Fe monolayer prepared on the hexagonal Ir(111) surface [152]. The real space magnetic texture was studied by spin-polarized scanning tunning microscopy (STM), showing the magnetization parallel/antiparallel to a magnetic tip as bright/dark spots (Fig. 2.9(c)c). Compared to skyrmion crystals found in chiral magnets, the size of magnetic unit cell is much smaller
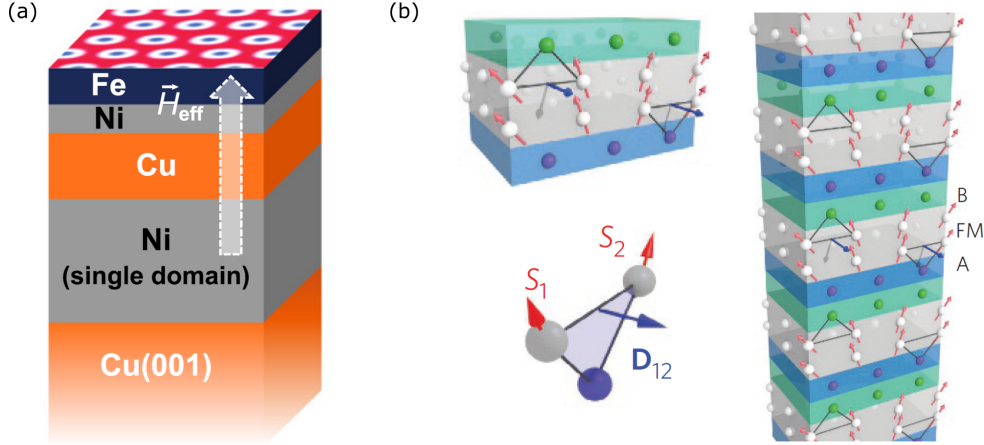
Figure 2.10: **Engineering of magnetic skyrmions at room temperatures and zero external magnetic field.** (a) Schematic representation of an Fe/Ni/Cu/Ni/Cu(001) multilayer, where the perpendicularly magnetized Ni layer in the middle introduces an effective magnetic field on a Fe/Ni bilayer. (b) Left: trilayer system composed by a ferromagnetic layer (gray) inserted between different heavy metals A (blue) and B (green), which induce the interfacial Dzyaloshinskii-Moriya vector in the same direction. Right: asymmetric multilayer system consisting of a stack of the A/FM/B trilayers. (a) is adapted from [146] and (b) is adapted from [149].

in this system (~ 1 nm$\times$ 1 nm). Using a two-dimensional spin lattice model guided by the first-principles calculations, it was shown that the four-spin interaction is crucial to realize a square lattice of topological spin structures as a magnetic ground state without external magnetic fields. We note that the four-spin interaction is resulted from electron hopping between four adjacent sites [258]. In addition, the Dzyaloshinskii-Moriya interaction is generated by the spin-orbit coupling of Ir atoms on the interface with Fe atoms, which favors skyrmions over antiskyrmions.

In a PdFe bilayer system on the Ir(111) surface, more conventional Néel skyrmions were reported as shown in Fig. 2.9(d) [252]. As the magnetic field was increased, the helical phase, skyrmion crystal phase, and ferromagnetic phase were stabilized in turn at 8K, implying that it is dominated by the competition between the exchange interaction and interfacial Dzyaloshinskii-Moriya interaction. Furthermore, it was demonstrated that single skyrmions can be reversibly created and annihilated on the ferromagnetic phase using the STM tip at 4.2 K. The mechanism for switching process was not due to the local heating of a sample. Instead, the energy of injected electrons from the STM tip was shown to determine the switching rate, which helped overcome the energy barrier for nucleation of metastable skyrmions.

A great advantage of multilayer magnetic systems is that the interlayer interaction could be engineered to enhance the stability of magnetic skyrmions at room temperature and zero external magnetic field [99]. A zero-field magnetic skyrmion at room temperature
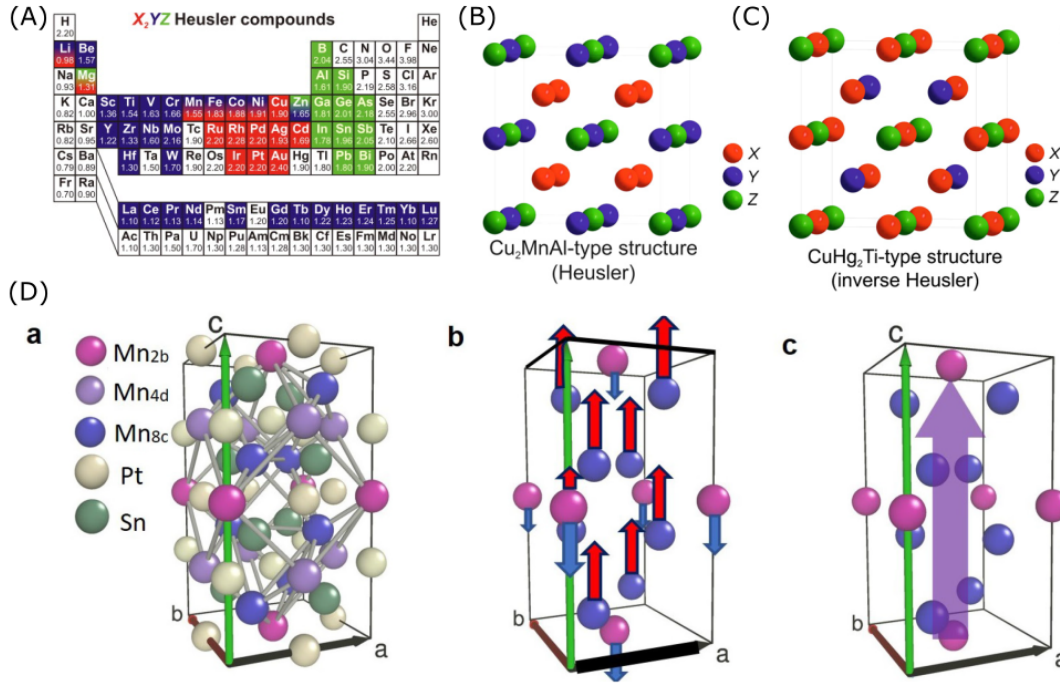
Figure 2.11: **Brief introduction of Heusler compounds (top), crystal and magnetic structure of $Mn_{1.4}Pt_{0.4}Pd_{0.1}Sn$ (bottom).** (A) Periodic table of composite elements for Heusler compounds (X_2YZ), highlighted by red for X atom, blue for Y atom, and green for Z atom. (B),(C) Crystal structures of (B) Heusler compounds and (C) inverse Heusler compounds. (D)a, crystal structure of $Mn_{1.4}Pt_{0.4}Pd_{0.1}Sn$. b, ferrimagnetic order at two inequivalent Mn sites. c, total ferromagnetic moment in the unit cell. (A)-(C) are adapted from [262] and (D) is adapted from [153].

was first demonstrated in an FeNi bilayer at the top of Fe/Ni/Cu/Ni/Cu(001) [146]. The key idea is to insert a perpendicularly magnetized Ni underneath the FeNi bilayer system, which introduces a virtual magnetic field as illustrated in Fig 2.10(a). Another idea is to prepare a trilayer system made of a ferromagnetic layer sandwiched between different heavy metal atoms as shown in Fig. 2.10(b). Since the sign of the interfacial Dzyaloshinskii-Moriya interaction depends on heavy metal elements [259], it is possible to realize additive Dzyaloshinskii-Moriya interactions from the bottom and top interfaces as demonstrated in an Ir/Co/Pt trilayer [149]. Furthermore, stacking of trilayers improve the thermal stability of skyrmions due to the increased magnetic volume. Up to now, a zero-field magnetic skyrmion has been realized in various magnetic multilayer systems [98, 147, 150]. Furthermore, it was shown that the velocity of skyrmion motion in Pt/CoFeB/MgO multilayer stacks can exceed $100\ ms^{-1}$ by current densities of a few $10^{11}\ A/m^2$ [148], which is important for applications in racetrack memory [260, 261].
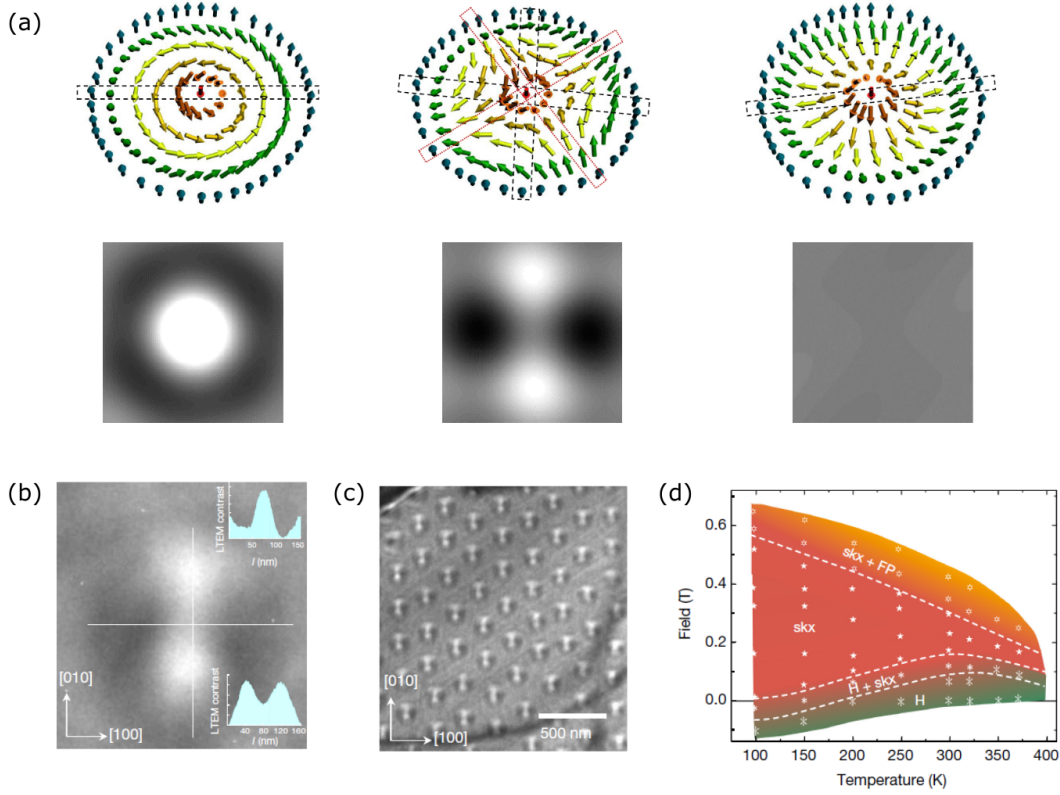
Figure 2.12: **Real space observation of antiskyrmions in $Mn_{1.4}Pt_{0.4}Pd_{0.1}Sn$.** (a) Spin textures for skyrmions and antiskyrmions with the simulated LTEM images, showing Bloch skyrmions, antiskyrmions, and Néel skrymions from left. (b),(c) Under-focused LTEM images of (b) a single antiskyrmion and (c) antiskyrmion lattices, both obtained at 300 K and 0.29 T applied along [001] direction. (d) Magnetic phase diagram derived from LTEM measurements. Each phase is represented as "H" for a helical phase, "skx" for antiskymions, and "FP" for a field-polarized state. Adapted from [153].

2.4   Materials hosting antiskyrmions

Antiskyrmions are stabilized by the Dzyaloshinskii-Moriya interaction allowed by D_{2d} crystalline symmetry. The first experimental observation was reported in the Mn-Pt-Sn inverse Heusler compound [153]. Heusler compounds refer to a large class of materials with the composition of X_2YZ, where X and Y are transition metals and Z is a main group element as shown in Fig. 2.11(A) [262]. They show a remarkably wide range of functionalities such as thermoelectricity, half metallic ferromagnetism, topological insulators, superconductivity, and multiferroics [263]. The crystal structure of Heusler compounds is shown in Fig 2.11(B). Another configuration, called the inverse Heusler compounds, is realized by exchanging the positions of X and Y atoms, as shown in Fig 2.11(C). In addition to cubic Heusler compounds, the tetragonal distortion can occur due to the Jahn-Teller distortion [263].

Manganese-rich Heusler compounds attract much attention as a rare earth free magnet. They are often crystallized in the inverse Heusler structure with ferrimagnetic order, where magnetic moments at two inequivalent Mn sites are antiferromagnetically coupled [263]. The tetragonal Heusler compound $Mn_{1.4}Pt_{0.4}Pd_{0.1}Sn$ belongs to this class of materials, whose crystalline structure is shown in Fig 2.11(D)a. The space group of this material is $I\bar{4}2m$ with D_{2d} point group symmetry. The ferrimagnetic order of Mn site results in a net out-of-plane magnetization as shown in Fig. 2.11(D)b,c. By taking the average magnetization for each unit cell, we can treat it as a ferromagnetic system defined in a square lattice. Furthermore, the Dzyaloshinskii-Moriya interaction arises from the large spin orbit coupling of Pt atom, stabilizing antiskyrmions in this material.

In Ref. [153], Lorentz transmission electron microscopy (LTEM) was used for the real space observation of antiskyrmions in $Mn_{1.4}Pt_{0.4}Pd_{0.1}Sn$. The main advantage of LTEM is that the in-plane magnetization of skyrmions and antiskyrmions can be distinguished due to the additional phase acquired by electrons interacting with local magnetizations. This is illustrated in Fig. 2.12(a) using micromagnetic simulations. While the LTEM image of Bloch skyrmions appears to have a ring structure, the LTEM image of antiskyrmions is characterized by a quadrupole-like feature with two bright spots and two dark spots. In the case of Néel skyrmions, no feature is expected in the LTEM measurement. Figure 2.12(b) shows the LTEM image of a single object, observed in $Mn_{1.4}Pt_{0.4}Pd_{0.1}Sn$ at 300 K and under applied fields of 0.29 T in [001] axis. Remarkably, the LTEM image exhibits a quadrupole-like feature in agreement with the simulation, confirming the presence of antiskyrmions. In addition, a triagular lattice structure of antiskyrmions was observed under the same condition as shown in Fig. 2.12(c). Here, we should note that there exist two half-moon shaped objects along the sample edge, shown at the top left corner of Fig. 2.12(c). Although it is not possible to identify the topological properties of these objects in this experiment, we will discuss the stability of such edge-localized objects with fractional topological charges in Chapter 5.3.2. They play an important role to realize magnonic corner states in antiskyrmion crystals.

Similarly to C_{3v} symmetric systems stabilizing Néel skyrmions, the conical phase is not stable in systems with D_{2d} symmetry. Hence, the stability of antiskyrmions is expected to be enhanced in comparison to bulk samples of chiral magnets. Figure 2.12(d) supports this prediction, as the magnetic phase diagram of $Mn_{1.4}Pt_{0.4}Pd_{0.1}Sn$ shows a wide range of temperatures and magnetic fields where antiskyrmions were observed. It should be noted that the transition to a state with larger magnetization was reported at low temperatures around 125 K, which could be resulted from a reorientation of the magnetic moments at the Mn sublattices [153]. Below this transition temperature, it was found difficult to nucleate antiskyrmions. The result shown in Fig. 2.12(d) at 100 K was thus obtained by cooling antiskyrmion lattices formed at room temperatures.

Chapter 3

Field-driven topological phase transition

As introduced in Section 1.3.8, ferromagnetic skyrmion crystals support topologically nontrivial magnon bands [209]. It makes skyrmion crystals a promising platform for magnon spintronics, where topologically protected magnonic chiral edge states can be used for dissipationless spin transports [25, 188]. For device applications, it is highly desirable to achieve an external control of these edge states by magnetic fields. Since magnons depend on the classical ground-state spin textures, it is a nontrivial question whether or not a magnetic field can drive a topological phase transition without destroying the underling spin texture.

In Chapter 3, we show that the magnetic-field driven topological phase transition is indeed possible in a thin film sample of skyrmion-hosting materials. Remarkably, the topological phase transition of magnon bands in skyrmion crystals is associated with the band inversion between the breathing and counterclockwise modes of skyrmions [193]. These low energy spin wave modes have been experimentally measured at various magnetic fields [30, 194, 198] (see Section 1.3.6). Hence, our prediction could be tested experimentally. Our finding suggests that an external magnetic field could be used as a knob to switch on and off magnonic chiral edge states. The content of this chapter was published in Ref. [76].

3.1 Model

We consider a simple two-dimensional spin lattice model for Néel skyrmion crystals with the following Hamiltonian:

$$
H = \tfrac{1}{2} \sum_{\langle \boldsymbol{r}, \boldsymbol{r}' \rangle} (-J_{\boldsymbol{r}, \boldsymbol{r}'} \boldsymbol{S}_{\boldsymbol{r}} \cdot \boldsymbol{S}_{\boldsymbol{r}'} + \boldsymbol{D}_{\boldsymbol{r}, \boldsymbol{r}'} \cdot \boldsymbol{S}_{\boldsymbol{r}} \times \boldsymbol{S}_{\boldsymbol{r}'}) - g\mu_B B_z \sum_{\boldsymbol{r}} \boldsymbol{S}_{\boldsymbol{r}} \cdot \hat{\boldsymbol{z}}, \qquad (3.1)
$$

where $\boldsymbol{S}_{\boldsymbol{r}}$ is a spin operator at site $\boldsymbol{r}$ on a triangular lattice with lattice constant a. The nearest-neighbor coupling includes ferromagnetic exchange $J_{\boldsymbol{r}, \boldsymbol{r}'} = J > 0$, and interfacial
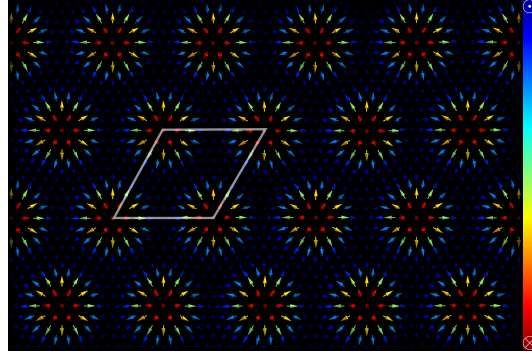
Figure 3.1: **Classical ground-state spin configurations of Néel skyrmion crystals.** The crystal structure with hexagonal symmetry is obtained at $D/J = 1.0$ and $b = \frac{g\mu_B B_z}{JS} = 0.8$. The color of arrows indicates the out-of-plane component. A white parallelogram is added to indicate a magnetic unit cell containing 9×9 spins. Adapted from [76].

Dzyaloshinskii-Moriya interaction $\boldsymbol{D}_{\boldsymbol{r},\boldsymbol{r}'} = D\hat{z} \times (\boldsymbol{r}-\boldsymbol{r}')/|\boldsymbol{r}-\boldsymbol{r}'|$. The last term represents the coupling to the external magnetic field, $B_z\hat{\boldsymbol{z}}$, where g and μ_B denote the g-factor and Bohr magneton, respectively.

The classical-ground state spin textures are obtained by Monte Carlo simulated annealing [166]. The energy is further minimized by solving the Landau-Lifshitz-Gilbert equation at zero temperature. Since the wavelength of magnetic helices and the radius of skyrmions is proportional to the D/J ratio (see Appendix A.4), it is computationally demanding to use experimental parameters of $D/J \sim 0.1$. To obtain skyrmion crystals in a modest system size, we take $D/J = 1.0$ in the following calculations. In Section 3.4, we discuss that our result can be rescaled for smaller values of D/J ratio. Figure 3.1 shows the obtained classical ground-state spin configurations of Néel skyrmion crystals, indicating the magnetic unit cell with hexagonal rotational symmetry by a white parallelogram.

The spin-wave Hamiltonian for Eq. (3.1) was obtained in Section 1.1.3. Here, a local orthonormal basis is denoted as $(\boldsymbol{e}_{\boldsymbol{r}}^1, \boldsymbol{e}_{\boldsymbol{r}}^2, \boldsymbol{m}_{\boldsymbol{r}})$, where $\boldsymbol{m}_{\boldsymbol{r}}$ is a unit vector parallel to the ground-state spin texture and $\boldsymbol{e}_{\boldsymbol{r}}^1 \times \boldsymbol{e}_{\boldsymbol{r}}^2 = \boldsymbol{m}_{\boldsymbol{r}}$. From Eq. (1.10), the Fourier transform of the spin-wave Hamiltonian is given as

$$H_{\text{SW}} = \frac{S}{2} \sum_{\boldsymbol{k}} (a_{\boldsymbol{k}i}^\dagger, a_{-\boldsymbol{k}i}) \begin{pmatrix} \Omega_{ij}(\boldsymbol{k}) & \Delta_{ij}(\boldsymbol{k}) \\ \Delta_{ij}^*(-\boldsymbol{k}) & \Omega_{ij}^*(-\boldsymbol{k}) \end{pmatrix} (a_{\boldsymbol{k}i}, a_{-\boldsymbol{k}i}^\dagger)^T + \mathcal{E}_0 \,, \tag{3.2}$$

where $a_{\boldsymbol{k}i}/a_{\boldsymbol{k}i}^\dagger$ denote the annihilation/creation operators for magnons with $i = 1, \ldots, N$ for the magnetic unit cell containing N spins. The first term is the free magnon Hamiltonian with $\Omega_{ij}(\boldsymbol{k}) = \delta_{ij}\Lambda_i + \frac{1}{2}[-J_{ij}(\boldsymbol{k})\boldsymbol{e}_i^+\cdot\boldsymbol{e}_j^- + \boldsymbol{D}_{ij}(\boldsymbol{k})\cdot\boldsymbol{e}_i^+\times\boldsymbol{e}_j^-]$, $\Delta_{ij}(\boldsymbol{k}) = \frac{1}{2}[-J_{ij}(\boldsymbol{k})\boldsymbol{e}_i^+\cdot\boldsymbol{e}_j^+ + \boldsymbol{D}_{ij}(\boldsymbol{k})\cdot\boldsymbol{e}_i^+\times\boldsymbol{e}_j^+]$, and $\Lambda_i = \sum_j[J_{ij}(\boldsymbol{k}=0)\boldsymbol{m}_i\cdot\boldsymbol{m}_j - \boldsymbol{D}_{ij}(\boldsymbol{k}=0)\cdot\boldsymbol{m}_i\times\boldsymbol{m}_j] + b J\hat{\boldsymbol{z}}\cdot\boldsymbol{m}_i$, where $J_{ij}(\boldsymbol{k}) = \sum_{\boldsymbol{R}} J_{\boldsymbol{R}+r_i,r_j} e^{-i\boldsymbol{k}\cdot(\boldsymbol{R}+r_i-r_j)}$, $\boldsymbol{D}_{ij}(\boldsymbol{k}) = \sum_{\boldsymbol{R}} \boldsymbol{D}_{\boldsymbol{R}+r_i,r_j} e^{-i\boldsymbol{k}\cdot(\boldsymbol{R}+r_i-r_j)}$, $b = g\mu_B B_z/JS$, and $\boldsymbol{e}_{\boldsymbol{r}}^\pm = \boldsymbol{e}_{\boldsymbol{r}}^1 \pm i\boldsymbol{e}_{\boldsymbol{r}}^2$. The second term corresponds to the total classical energy $\mathcal{E}_0 =$
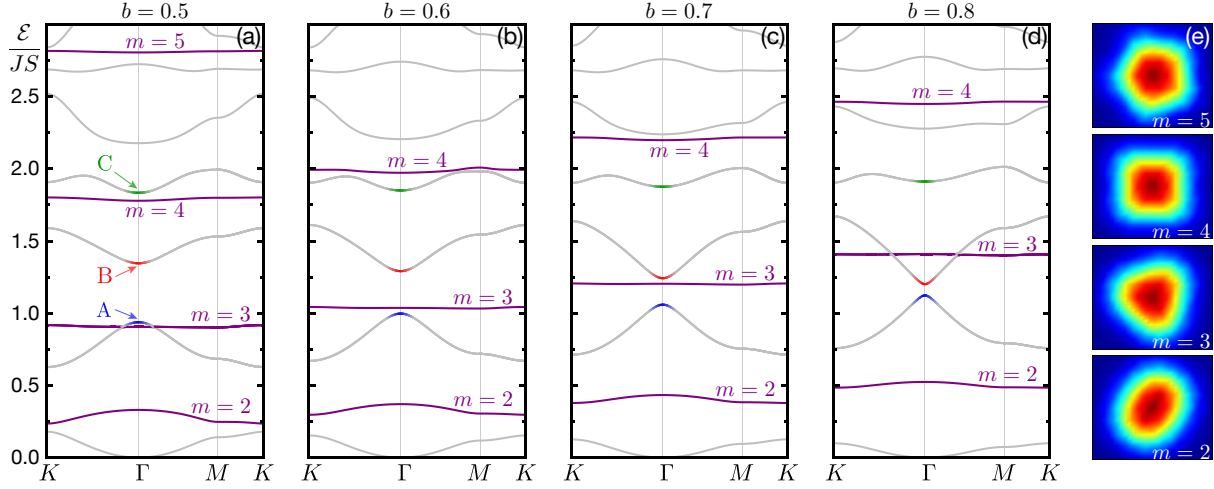
Figure 3.2: **Magnon band structures at different magnetic fields.** (a)-(d) Bulk spectrum of the ferromagnetic skyrmion crystals with increasing magnetic field $b = \frac{g\mu_B B_z}{JS}$. Nearly flat and dispersive bands are depicted in purple and grey, respectively. The counterclockwise (A), breathing (B), and clockwise (C) modes are highlighted by blue, red and green. (e) Distortions of skyrmions to m-th order polygons corresponding to nearly flat bands from (a)-(d). Adapted from [76].

$-\frac{1}{2}S^2 \sum_i \Lambda_i$. The magnon band structure is obtained numerically by the paraunitary diagonalization [77].

3.2 Low energy magnon band structures

Now, we discuss the magnon band structures of ferromagnetic skyrmion crystals. In Fig. 3.2(a), the low energy magnon spectrum at $b = 0.5$ is presented, which consists of nearly flat bands (purple) and dispersive bands with characteristic local excitations at Γ point (gray). Nearly flat bands in skyrmion crystals are originated from bound states of isolated skyrmions, corresponding to distortions to m-th order polygons [190, 201] (see Section 1.3.6). Almost completely flat bands indicate that magnons are strongly localized near skyrmions. This is illustrated in Figure 3.2(e), showing distortions in the skyrmion spin textures caused by the four lowest energy eigenmodes of flat bands. They are labeled by the azimuthal number following Ref. [201], with $m = 2$ for elliptical deformations, $m = 3$ for triangular deformations, and so on. As time evolves, deformed skyrmions rotate in a clockwise manner with a phase difference $\theta_{\mathbf{k}}$ from their neighbors.

For dispersive bands (gray bands in Fig. 3.2(a)), the lowest energy band is the Goldstone mode with a quadratic dispersion [175, 192]. It is resulted from breaking the translational symmetry in the presence of skyrmion crystals. Above the Goldstone mode, there are three dispersive bands respectively hosting local magnetic excitations of skyrmions at Γ point, labeled as (A) for counterclockwise mode, (B) for breathing mode, and (C) for clockwise mode. These low energy spin wave modes are particularly important for
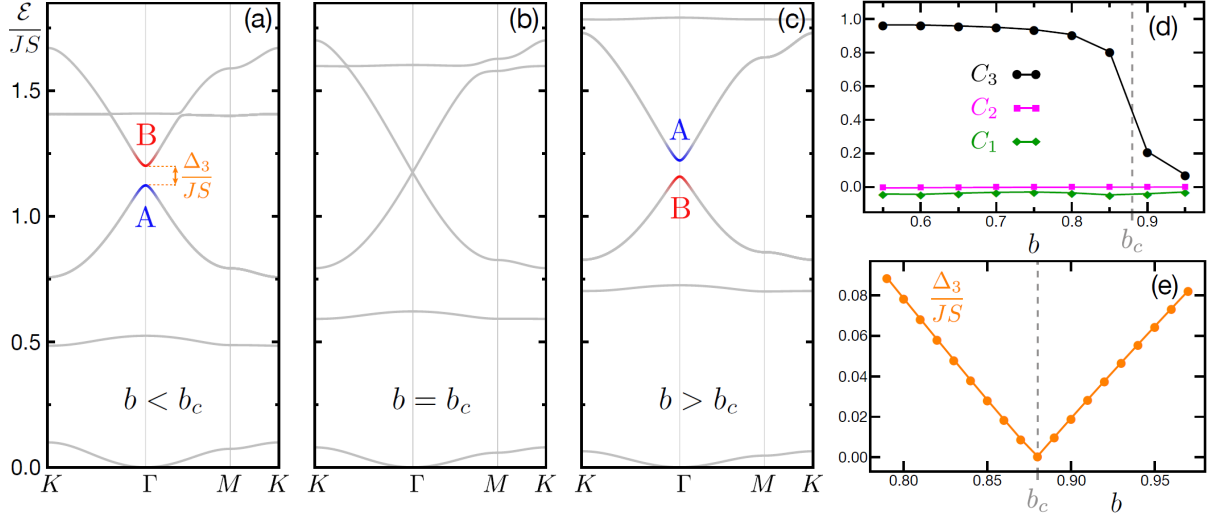
Figure 3.3: **Topological phase transition driven by external magnetic fields.** (a)-(c) Bulk spectrum of the ferromagnetic skyrmion crystals near the topological phase transition obtained at (a) $b = 0.8$, (b) $b = b_c = 0.88$, and (c) $b = 0.95$. The band inversion occurs between the counterclockwise (A) and breathing modes (B), which is respectively shown in blue and red. (d) Chern numbers of the lowest three bands, denoted as $\{C_1, C_2, C_3\}$, are computed with increasing magnetic fields. A sharp drop in C_3 from $+1$ to 0 at $b = b_c$ shows the topological phase transition in the third band. (e) Size of the third band gap as a function of magnetic fields. It is linearly dependent on magnetic fields and vanishes at $b = b_c$. Adapted from [76].

experimental observations, since they are magnetically active and get excited by spatially uniform AC magnetic fields as shown in Ref. [193].

3.3 Main result

3.3.1 Magnetic-field driven topological phase transition

In this section, we discuss our main finding of the magnonic topological phase transition at the critical magnetic field. Figure 3.2(b)-(d) shows the magetic field dependence of magnon bands. We find a strong magnetic field dependence in nearly flat bands, while dispersive bands are less affected by magnetic fields. At $b = 0.6$, the nearly flat band for $m = 3$ passes through the second dispersive band that host the counterclockwise mode. During this process, there is a little overlapping between their eigenstates, resulting in no signature of avoided band crossings at degenerate points between the flat and dispersive bands. Furthermore, the Chern number of each band does not change after the flat band pass through the dispersive band. In fact, the Chern numbers of flat bands are always zero regardless of magnetic fields. They are topologically decoupled from other bulk bands. We also notice that the band gap between (A) counterclockwise mode and (B)
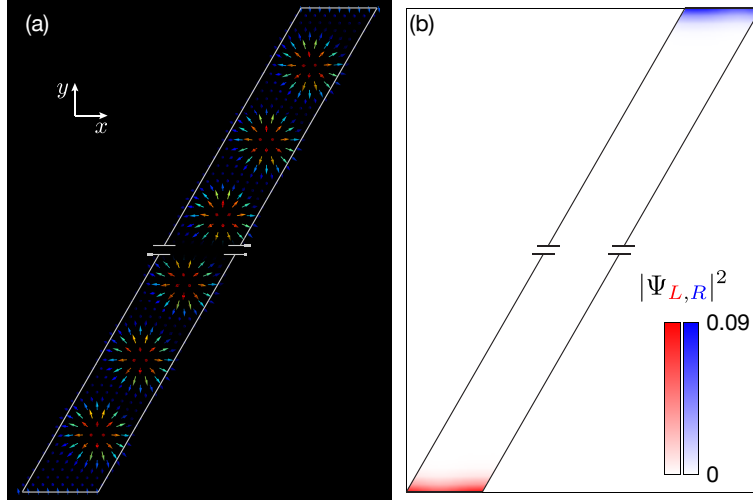
Figure 3.4: **Probability distribution of chiral magnonic edge states.** (a) One-dimensional magnetic unit cell of the ferromagnetic skyrmion crystal in the strip geometry at $b = 0.8$. Only the magnetic textures near the top and bottom edges are presented. (b) Probability density of magnon wave functions for the left-moving (red) and right-moving (blue) edge states. They are degenerate states with $k_x = \mp 0.45 G_s$ with G_s denoting the size of the one-dimensional Brillouin zone. Adapted from [76].

breathing mode becomes smaller at higher magnetic fields, which is consistent with the experimental results [189, 194, 198] (see Fig. 1.13). As discussed below, these two modes undergo the band inversion at the critical magnetic field b_c, resulting in the topological phase transition.

Figure 3.3(a)-(c) show the magnon spectrum near the band inversion between (A) the counterclockwise mode and (B) breathing mode. The band gap between third and fourth bands at Γ point is closed at the critical field $b_c = 0.88$ and reopened for higher magnetic fields as shown in Figure 3.3(e). The fundamental difference from the band touching with flat bands is the strong hybridization between eigenstates. This is clear from the interchanged spin wave excitations at Γ point. While the third (fourth) band hosts the counterclockwise (breathing) mode before the band inversion, the inverted order is found after the band gap closing as indicated by Fig. 3.3(c). To confirm the topological phase transition, the change in the Chern number is calculated as a function of magnetic fields near b_c. Figure 3.3(d) shows the Chern number of the lowest three bands at various magnetic fields. Crucially, the Chern number of the third band changes from $C_3 = +1$ below b_c to $C_3 = 0$ above b_c. We also confirm that the change in the Chern number of the fourth band from $C_4 = +1$ to $C_4 = +2$. Hence, a transfer of the Chern number occurs during the band touching at b_c, which makes the third band topologically trivial. We should also note that the lowest two bands are found to be always topologically trivial in agreement with the literatures [188, 209].
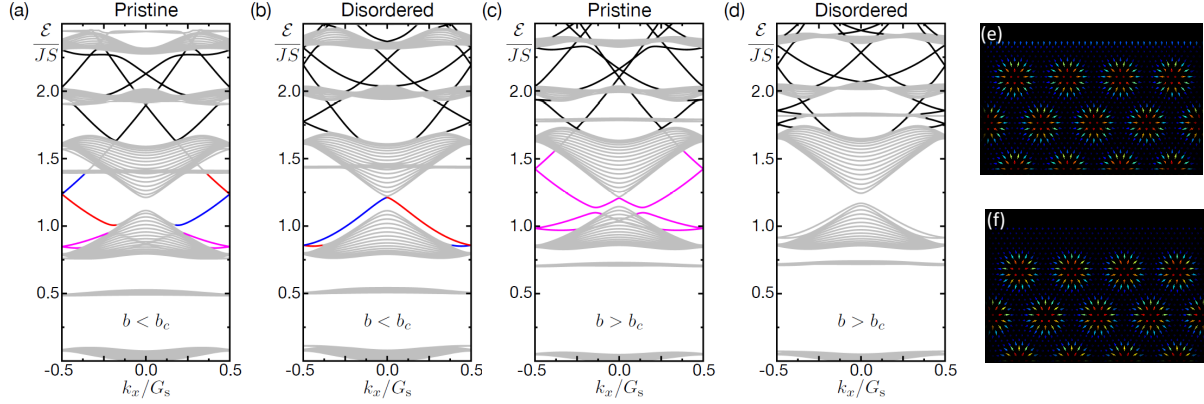
Figure 3.5: **Robust chiral magnonic edge states in a strip geometry.** (a)-(d) Magnon edge spectra in a one-dimensional periodic system along the x axis with (a) pristine system at $b = 0.8$, (b) disordered system at $b = 0.8$, (c) pristine system at $b = 0.95$, and (d) disordered system at $b = 0.95$. Bulk subbands are shown in gray and G_s is the size of Brillouin zone. In (a) and (b), topologically protected edge states within the third band gap are highlighted by blue (red) for right (left) movers. In addition, there exists topologically trivial edge states (purple) that vanish in disordered systems. Edge states within higher energy gaps are shown in black. (e)-(f) Magnetic texture near the sample edges for (e) a pristine system under a uniform magnetic field at $b = 0.8$ and (f) disordered system under a magnetic field at $b = 0.8$ except for five rows of spins near the edges where $b = 3.0$. Adapted from [76].

3.3.2 Switching of chiral magnonic edge states

From the bulk-edge correspondence of Eq. (1.22), the number of chiral magnonic edge states inside a band gap is determined by the sum of Chern numbers below the band gap. Since $\sum_{n=1}^{3} C_n = 1$ below the critical magnetic field b_c, there should be a single chiral magnonic edge state inside the third band gap. Above b_c, it should vanish as a consequence of the topological phase transition. However, there is a subtle issue with the bulk-boundary correspondence because we cannot always prepare an integer number of magnetic unit cells within finite sized samples. In particular, the Dzyaloshinskii-Moriya interaction imposes a twisted boundary condition, known as the edge twist [100–103] (see Section 1.3.4). As a result, the magnetic unit cell of skyrmion crystals is distorted near edges.

To account for modifications in spin textures near edges, Monte Carlo simulated annealing is carried out for a strip geometry. Here, the system size should be sufficiently large compared to the size of magnetic unit cell of skyrmion crystals. On this new geometry, the skyrmion crystal is reconstructed well inside the sample but repelled from edges as shown in Fig. 3.4(a). Using the obtained spin textures, one-dimensional magnon bands are computed. Figure 3.5(a) shows the edge spectrum before the topological phase transition ($b < b_c$). As expected from the bulk-edge correspondence, we find edge localized modes connecting the third and forth bulk subbands (gray). These edge states propagate

in a chiral manner, supporting left movers on one edge (red) and right movers (blue) on the other edge as shown in Fig 3.4(b). For further confirmation, Figure 3.5(c) shows that these chiral magnonic edge states vanish above the critical magnetic field. We also find topologically trivial edge states inside the third band gap (purple). Since they are not resulted from the bulk topology, they are present in both below and above b_c. They are expected to be magnon bound states confined within the twisted edge magnetization (see Appendix A.7.2).

The important property of topologically protected edge states is the robustness against disorder. In order to demonstrate it, we introduce a special type of disorder by applying a larger magnetic field near edges. This results in fully polarized spins near edges indicated by Fig. 3.5(f), while some tilting along the edge is observed in a pristine sample (Fig. 3.5(e)). The magnon spectrum for a disordered system is shown in Fig. 3.5(b) and (d). Since the applied magnetic field is unchanged in the bulk, bulk subbands are not affected by disorder. However, it strongly modifies the dispersion of edge localized modes, removing topologically trivial edge states. In contrast, the topologically protected edge states persist to stay inside the third band gap for $b < b_c$, hence clearly distinguishing themselves from trivial edge states.

3.4 Discussion and Conclusion

So far, we have not considered the effect of long-range dipolar interactions. They are particularly important for magnonic crystals consisting of ferromagnetic domains, which can be designed to realize topological magnon insulators [2]. For a thin sample considered in this chapter, the dipolar interaction results in the demagnetization field and it could enhance the stability of magnetic skyrmions [136]. Also, the dipolar interaction can be approximated as an effective easy-plane anisotropy as discussed in Appendix A.3.3 [101, 130, 166]. In this approximation, the numerical simulation suggests that skyrmion crystals persist up to higher magnetic fields due to the easy-plane anisotropy [264]. Hence, the dipolar interaction could play an important role to stabilize magnetic skyrmions up to the critical magnetic field predicted in the previous section. In addition, it was shown that the magnon spectrum obtained by neglecting dipolar interactions is qualitatively in agreement with experiments [194].

The ratio between the exchange coupling and Dzyaloshinskii-Moriya interaction is fixed to be $D/J = 1.0$, although it is much smaller than unity in real materials. However, our result can be rescaled to experimental parameters without any fundamental difference, since the free energy functional in the continuum limit can be expressed independently of the D/J ratio (see Appendix A.7.2). In the continuum limit, the physical length and magnetic field is scaled proportional to D/J and $(D/J)^2$. Assuming a more realistic parameter of $J = 1$ meV, $S = 1$, $D/J = 0.05$, and $a = 0.5$ nm, the skyrmion size and critical magnetic field is respectively estimated as $8a(J/D) = 80$ nm and $B'_c = (b_c JS/g\mu_B)(D/J)^2 \approx 20$ mT.

In several skyrmion-hosting materials, the resonance frequencies of the counterclock-

wise, breathing, and clockwise modes have been measured [189, 194, 198]. In agreement with our work, the band gap between counterclockwise mode and breathing mode was found to decrease with magnetic fields. Both theoretically and experimentally, the ferromagnetic skyrmion crystal phase was shown to be stable for broader parameters in a thin film sample [136, 167]. Hence, we expect that the development in crystal growth techniques could stabilize the skyrmion crystal phase at sufficiently high magnetic fields, allowing observation of the magnonic topological phase transition. Indeed, the band inversion predicted in this chapter has been experimentally observed in the metastable skyrmion lattice of Cu_2OSeO_3 [265].

In addition to the the microwave absorption for magnetically active modes [189, 193], the state-of-art ferromagnetic resonance techniques could be used to excite the bulk or edge magnon modes [266, 267]. Within the energy window of the third bulk band gap, we could selectively excite magnonic edge states. Their spatial profile and localization to the edges could be probed by Brillouin light scattering spectroscopy [268].

As a concluding remark, we have predicted the band inversion between two magnetically active modes in ferromagnetic skyrmion crystals, namely the counterclockwise and breathing modes at higher magnetic fields. It results in the topological phase transition between the third and fourth magnon bands, leading to the vanishing of chiral magnonic edge states within the third band gap. Our results suggest a simple way to control the robust magnonic spin currents along edges by external magnetic fields.

Chapter 4

Laser-driven skyrmions

As discussed in Chapter 3, the magnonic topological phase transition is predicted in skyrmion crystals at the critical magnetic field [76]. In Chapter 4, we discuss a possible route towards ultrafast control of magnon band topology in skyrmion crystals, focusing on the multiferroic insulator Cu_2OSeO_3. We first introduce the Floquet theory and its extension to classical spin systems based on Ref. [211]. Combining the numerical simulation of Landau-Lifshitz-Gilbert equation and the Floquet theory, we study the classical spin dynamics of skyrmion crystals under circularly polarized laser. Remarkably, we discover that the magnetoelectric nature of Cu_2OSeO_3 results in a novel mechanism for the laser-driven motion of skyrmions. Furthermore, we demonstrate the band inversion between counterclockwise and breathing modes of skyrmions under circularly polarized laser, which is associated with the magnonic topological phase transition (see Section 3.3.1). The content of this chapter is in preparation for the submission to academic journals (List of Publication 4).

4.1 Introduction

4.1.1 Ultrafast control of spins and Floquet magnons

In this section, we introduce important topics of this chapter, namely ultrafast control of spins and Floquet magnons [269, 270]. Historically, ultrafast demagnetization was first reported in a Ni film using a 60 femtosecond (fs $=10^{-15}$ s) optical laser pulse [271]. This experiment corresponds to the thermal process [269], where photons are absorbed by electrons, resulting in elevated temperatures of electrons in a subpicosecond (ps $= 10^{-12}$ s) time scale. In a next few picoseconds, the relaxation through electron-phonon and electron-spin interactions increase the temperature of the lattice and spins, leading to ultrafast demagnetization. The problem of thermal process is that the speed of control is limited by internal interactions between electrons and spins. In contrast, the nonthermal process does not involve the absorption of photons as the light is directly coupled with spin degrees of freedom [269]. For example, ultrafast magnetization was demonstrated by circularly polarized laser due to the inverse Faraday effect, showing the opposite sign

65

of induced magnetizations for left- and right-handed circularly polarized lasers [272]. Furthermore, the direct coupling between magnetic component of terahertz (THz $=10^{12}$ Hz) laser and spins was observed in antiferromagnetic NiO [273].

Recently, a novel method for nonthermal ultrafast magnetization was proposed based on the Floquet theory [274, 275]. Using the Floquet theory, quantum spin systems under time-periodic electromagnetic fields from lasers can be described by the effective time-independent Hamiltonians (see Appendix B.1). In Ref. [274, 275], it was shown that circularly-polarized lasers induces an effective magnetic field, which was predicted to be sufficiently strong to control magnetization without static magnetic fields (see Eq. (4.7)). Importantly, this is a general mechanism that is independent of magnetic systems as long as the frequency of laser is much larger than the energy scale of internal interactions between spins, based on the approximation called the *high frequency expansion* (see Appendix B.1.2). Applying the same approach to multiferroic systems, the ultrafast control of Dzyaloshinskii-Moriya interaction was also proposed to induce a vector spin chirality between two spins $\mathcal{V}_{12} = \boldsymbol{S}_1 \times \boldsymbol{S}_2$ in one-dimensional spin chains [276]. While the Floquet theory was initially developed for quantum spin systems, it was extended to classical spin systems in Ref. [211].

The application of Floquet theory is not limited to ultrafast control of spins, but it covers a wide range of topics as it provides a tool to engineer the effective Hamiltonians under time-periodic drives [277]. One prominent example is the topological phase transition of graphene irradiated by circularly polarized laser [278]. In this seminal work, the band structure obtained from the effective Floquet Hamiltonian, termed as Floquet bands, were characterized by a nontrivial Chern number under the laser. Remarkably, the anomalous Hall effect arising from the nontrivial Floquet bands in graphene was experimentally observed [279]. The study of laser-irradiated graphene in Ref. [278] has opened up a new research field of Floquet topological insulators [280].

The magnonic analogue of Floquet topological insulators has been also discussed [270, 281–284]. The standard recipe to construct Floquet magnons is to apply the Floquet theory on magnon Hamiltonians, which are obtained as magnetic excitations of classical ground-state spin textures in static spin Hamiltonians (see Section 1.1.3). A problem of this approach is that the classical spin dynamics is neglected for the construction of magnon Hamiltonians. In fact, we could think of two possible formulations of Floquet magnons if the classical spin dynamics is taken into account: magnetic excitations of time-averaged magnetic unit cells; magnetic excitations of time-periodic magnetic unit cells. To establish a correct formulation, we need to understand the classical limit of Floquet magnons.

Motivated by this problem, we investigate the Floquet magnon excitations from classical spin dynamics in this chapter. For this purpose, we employ the Floquet theory for classical spin systems [211], which is introduced in Section 4.1.2.

4.1.2 Floquet theory in classical spin systems

In this section, we briefly introduce the Floquet theory in classical spin systems, following Ref. [211]. Our purpose is to provide necessary theoretical tools for later sections of this chapter, where we discuss magnetic skyrmions under applications of circularly polarized lasers. We should note that Appendix B provides a review of the Floquet theory and its extension to classical systems [211, 285].

The main advantage of the Floquet theory for classical spin systems is that it includes the effect of phenomenological Gilbert damping [286]. In the presence of damping, the Floquet magnon is naturally defined as magnetic excitations from a non-equilibrium steady state of classical spins, thus providing a physically intuitive definition, as discussed in Section 4.3.2. In contrast, the previous study of Floquet magnons is based on Floquet theory for quantum spin systems [270], which does not take into account of classical spin dynamics. Consequently, the correspondence between Floquet magnons and classical spin dynamics has not been clarified.

Another point is the coupling between magnons and electric fields. Many literatures on Floquet magnons have discussed the coupling between electric fields and magnons arising from the Aharonov-Casher effect [270, 281–284], which gives rise to a geometric phase $\phi_{\text{A-C}} \propto E_0$ with E_0 denoting the applied electric fields analogously to the Aharonov-Bohm effect for electrons [66, 287]. Although the topological phase transition can be induced by the geometric phase $\phi_{\text{A-C}}$, it requires a very large amplitude of electric field E_0 to obtain a nontrivial effect in the order of 10^{12} V/m [68, 283]. To overcome this problem, we consider multiferroic insulators characterized by a strong coupling between ferromagnetism and ferroelectricity [236]. Since the electric polarization is induced by magnetic dipole moments in multiferroic insulators, the coupling with electric fields can be studied with classical spin Hamiltonians.

Under the application of laser fields, the time-dependent spin Hamiltonian of a multiferroic insulator is generally written as

$$H(t) = H_0 - g\mu_B \sum_{\boldsymbol{r}} \mathbf{B}(t) \cdot \boldsymbol{S_r} - \mathbf{E}(t) \cdot \mathbf{P_r}, \tag{4.1}$$

where $\boldsymbol{S_r}$ is the classical spin vector at site $\boldsymbol{r}$, $\mathbf{P_r}$ is the electric dipole moment induced by the magnetic order, g and μ_B respectively denotes the g-factor and Bohr magneton, and H_0 is the static part of the spin Hamiltonian. The externally applied electromagnetic field introduces the periodicity in time as $\mathbf{E}(T + t) = \mathbf{E}(t)$ and $\mathbf{B}(T + t) = \mathbf{B}(t)$.

The time-evolution of classical spin systems in Eq. (4.1) is described by the Landau-Lifshitz-Gilbert (LLG) equation (see Appendix A.6). In addition to the numerical simulation of the LLG equation, the Floquet theory provides a valuable insight on the behavior of non-equilibrium steady states, employing the high frequency expansion introduced in Appendix B.1. Here, we should note that a system under a time-periodic drive reaches a non-equilibrium steady state in the presence of a sufficiently large Gilbert damping coefficient. In such case, precessions of magnetizations around the classical ground-state spin textures are expected to occur at the frequency of applied field $\omega = 2\pi/T$. However,

a system becomes unstable when the amplitude of driving fields is too large, resulting in random magnetic configurations (thermal states). The Floquet theory is reliable only for the former case where a system is in the steady state.

Using the Floquet theory, the time-evolution of classical spin systems is described by Eq. (B.39) as

$$U(t_2, t_1) = e^{g_F(t_2)} e^{(t_2 - t_1)\mathcal{L}_F} e^{-g_F(t_1)}, \tag{4.2}$$

where $\mathcal{L}_F$ and $ig_F(t)$ are respectively called the effective Fokker-Plank operator and kick operator, defined in Eq. (B.40). While $e^{(t_2-t_1)\mathcal{L}_F}$ describes the long-time dynamics of spin configurations, $e^{-g_F(t_1)}$ and $e^{g_F(t_2)}$ describe precessions around the time-averaged spin configurations. Crucially, for a driving frequency larger than the energy scale of Hamiltonian $\hbar\omega \gg H_0$, we can derive simple expressions of the LLG equations corresponding to each unitary operator, as shown below (see Appendix B.1).

To discuss the slow dynamics of time-averaged spin configurations, it is sufficient to solve the following effective LLG equation [211] (see Appendix B.3):

$$\frac{d\boldsymbol{m_r}}{dt} = -\frac{\gamma \boldsymbol{m_r}}{1 + \alpha^2} \times [\boldsymbol{H}_{F,\boldsymbol{r}} + \alpha \boldsymbol{m_r} \times \boldsymbol{H}_{F,\boldsymbol{r}}], \tag{4.3}$$

where $\boldsymbol{m_r}$ is a unit vector parallel to the magnetization at site $\boldsymbol{r}$, $\gamma = g\mu_B/\hbar$ is the gyromagnetic ratio, and α is the Gilbert damping constant. The static solution of Eq. (4.3) corresponds to the time-averaged spin configuration of non-equilibrium steady state. The effective microscopic field $\boldsymbol{H}_{F,\boldsymbol{r}}$ up to the first order in $1/\omega$ is given as

$$\boldsymbol{H}_F = \boldsymbol{H}_F^{(0)} + \boldsymbol{H}_F^{(1)} = \boldsymbol{H}_{\boldsymbol{r},0}^{\text{eff}} + \sum_{m \neq 0} \frac{i\gamma [\boldsymbol{H}_{\boldsymbol{r},-m}^{\text{eff}}, \boldsymbol{H}_{\boldsymbol{r},m}^{\text{eff}}]_{\text{mag}}}{2m\omega(1 + \alpha^2)}, \tag{4.4}$$

with the microscopic field $\boldsymbol{H}_{\boldsymbol{r}}^{\text{eff}}(t) = -[1/(\hbar\gamma S)]\partial H(t)/\partial \boldsymbol{m_r}$, and its Fourier transform given as $\boldsymbol{H}_{\boldsymbol{r},m}^{\text{eff}} = \frac{1}{T}\int_0^T dt\, \boldsymbol{H}_{\boldsymbol{r}}^{\text{eff}}(t)e^{im\omega t}$, and the commutation relation $[\,,\,]_{\text{mag}}$ defined in Eq. (B.74). For example, the magnetic field from lasers is written as

$$\mathbf{B}(t) = B_d(\cos(\omega t), -\sin(\omega t + \delta), 0), \tag{4.5}$$

where B_d is the amplitude of magnetic fields and $\delta = 0, \pi/2, \pi$ corresponds to the right-circularly, linearly, and left-circularly polarized light, respectively. The Fourier component of microscopic field is obtained as

$$\boldsymbol{H}_{\boldsymbol{r},\pm 1}^{\text{eff}} = \mathbf{B}_{\pm 1} = \frac{B_d}{2}(1, \mp i\cos\delta - \sin\delta, 0). \tag{4.6}$$

Substituting $\boldsymbol{H}_{\boldsymbol{r},\pm 1}^{\text{eff}}$, the effective magnetic field $\boldsymbol{H}_F^{(1)}$ in Eq. (4.4) is derived as [211]

$$\boldsymbol{H}_F^{(1)} = \mathbf{B}_F \hat{z} = \frac{\gamma B_d^2 \cos\delta}{2(1 + \alpha^2)\omega}\hat{z}. \tag{4.7}$$

Hence, the effective magnetic field is induced by circularly polarized lasers, with its direction determined by the chirality of light. We should note that the equivalent results

are obtained in quantum spin systems, although corrections from damping are missing in the denominator [274–276].

For the short-time dynamics represented by $e^{g_F(t)}$, we need to solve the following LLG equation from $\tau = 0$ to $1/\omega$ [211] (see Eqs.(B.56) and (B.58)):

$$\frac{d\boldsymbol{m_r}}{d\tau} = -\frac{\gamma \boldsymbol{m_r}}{1+\alpha^2} \times \left[\boldsymbol{H}^{(1)}_{\mathrm{mic},\boldsymbol{r}}(t) + \alpha \boldsymbol{m_r} \times \boldsymbol{H}^{(1)}_{\mathrm{mic},\boldsymbol{r}}(t) \right], \qquad (4.8)$$

with

$$\boldsymbol{H}^{(1)}_{\mathrm{mic},\boldsymbol{r}}(t) = -i \sum_{m \neq 0} \frac{\boldsymbol{H}^{\mathrm{eff}}_{\boldsymbol{r},-m} e^{im\omega t}}{m}. \qquad (4.9)$$

In the Euler method for $\omega \gg 1$, the approximate solution is given as

$$\boldsymbol{m}_{\mathrm{mic},\boldsymbol{r}}(t) = \boldsymbol{m_r}(t) - \frac{\gamma \boldsymbol{m_r}}{\omega(1+\alpha^2)} \times \left[\boldsymbol{H}^{(1)}_{\mathrm{mic},\boldsymbol{r}}(t) + \alpha \boldsymbol{m_r} \times \boldsymbol{H}^{(1)}_{\mathrm{mic},\boldsymbol{r}}(t) \right]. \qquad (4.10)$$

As shown in Appendix C.2, the short-time dynamics of Eq. (4.8) describes the spin precession mode under laser fields for non-equilibrium steady states.

As a summary, the full-time evolution of classical spin systems is obtained by evaluating $U(t_2, t_1)$ in turn. Given the initial configuration of spin textures $\boldsymbol{m_r}(t_1)$, $\boldsymbol{m_r}(t_2)$ is obtained by the following three steps. Firstly, we evaluate Eq. (4.8) from $\tau = 0$ to $\tau = 1/\omega$ with substituting $-\boldsymbol{H}^{(1)}_{\mathrm{mic},\boldsymbol{r}}(t_1)$ on the right-hand side. Secondly, we evaluate Eq. (4.3) from $t = t_1$ to $t = t_2$. As a final step, we evaluate Eq. (4.8) from $\tau = 0$ to $\tau = 1/\omega$ with substituting $\boldsymbol{H}^{(1)}_{\mathrm{mic},\boldsymbol{r}}(t_2)$ on the right-hand side.

4.2 Model

We consider a thin film sample of the multiferroic insulator Cu_2OSeO_3 that has a chiral cubic crystal structure with space group $P2_13$ [143]. The spin lattice Hamiltonian defined on a square lattice is given as

$$H_0 = \frac{1}{2} \sum_{\langle \boldsymbol{r},\boldsymbol{r}' \rangle} (-J_{\boldsymbol{r},\boldsymbol{r}'} \boldsymbol{S_r} \cdot \boldsymbol{S_{r'}} + \boldsymbol{D}_{\boldsymbol{r},\boldsymbol{r}'} \cdot \boldsymbol{S_r} \times \boldsymbol{S_{r'}}) - g\mu_B B_z \sum_{\boldsymbol{r}} \boldsymbol{S_r} \cdot \hat{\boldsymbol{z}}, \qquad (4.11)$$

where $\boldsymbol{S_r} = S\boldsymbol{m_r}$ is the total magnetization at site $\boldsymbol{r}$ with $S = 1$ [196, 197]. The nearest-neighbour interactions are the ferromagnetic exchange coupling $J_{\boldsymbol{r},\boldsymbol{r}'} > 0$ and the DM interaction $\boldsymbol{D}_{\boldsymbol{r},\boldsymbol{r}'} = D(\boldsymbol{r} - \boldsymbol{r}')/|\boldsymbol{r} - \boldsymbol{r}'|$ from the point group symmetry of $P2_13$ (see Section 2.1). It also contains the Zeeman term with g and μ_B denoting the g-factor and Bohr magneton, respectively.

As discussed in Section 2.2.2, noncollinear spin textures of Cu_2OSeO_3 induce local electric polarizations due to the d-p hybridization mechanism [143, 196, 197, 236, 249]:

$$\mathbf{P}_{\boldsymbol{r},abc} = \lambda(m_{\boldsymbol{r},b}m_{\boldsymbol{r},c}, m_{\boldsymbol{r},c}m_{\boldsymbol{r},a}, m_{\boldsymbol{r},a}m_{\boldsymbol{r},b}), \qquad (4.12)$$
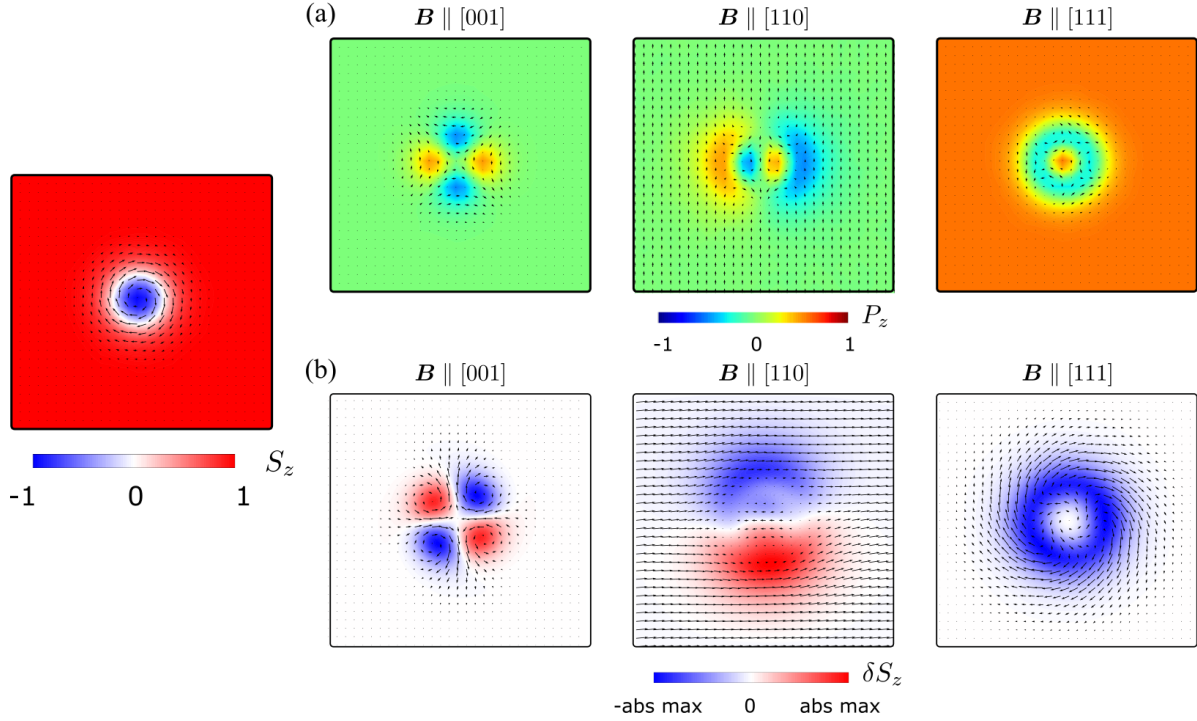
Figure 4.1: **Electric polarization and induced distortions in skyrmion spin textures under laser.** Left: spin textures of magnetic metastable skyrmions in the ferromagnetic background, obtained at $D/J = 0.09$ and $g\mu_{\rm B}B_z J/D^2 = 0.9$. (a) Spatial distribution of electric polarization $\mathbf{P_r}$, computed from Eq. (2.14). (b) Induced distortion of skyrmions under LCP ($\delta = \pi$) by the magnetoelectric coupling $\delta \mathbf{S_r} = \mathbf{m_r}(\mathcal{E}_d = 0.1) - \mathbf{m_r}(\mathcal{E}_d = 0)$, obtained by the effective LLG equation derived in Appendix C.1. The other parameters are fixed as $g\mu_B B_d/D = 2.0$, $\hbar\omega_0/J = 10$, and $\alpha = 0.04$. In (a) and (b), the results for $\mathbf{B}_0 \parallel [001]$, $\mathbf{B}_0 \parallel [110]$, and $\mathbf{B}_0 \parallel [111]$ are shown from left. The black arrows represent the in-plane components, while the out-of-plane componets are represented by color.

where the coupling strength $\lambda = 5.64 \times 10^{-27}$ μCm extracted from the experiment [143]. The subscript abc indicates that the coordinates are defined with respect to the crystallographic axes. The macroscopic electric polarization is generated when the out-of-plane vector of the skyrmion lattice is not parallel to [001] direction. Here, we mainly consider the skyrmion crystal phase under the magnetic field $\mathbf{B}_0 \parallel [110]$. Taking the z-axis along [110] and x-axis along $[\bar{1}10]$, the electric polarization is given from Eq. (2.14) as

$$\mathbf{P_r} = \lambda(-m_{\mathbf{r},x}m_{\mathbf{r},y}, \frac{-m_{\mathbf{r},x}^2 + m_{\mathbf{r},z}^2}{2}, m_{\mathbf{r},y}m_{\mathbf{r},z}). \tag{4.13}$$

In this rotated basis, the electric polarization is induced along the y-axis, while the total electric vanishes for $\mathbf{B}_0 \parallel [001]$ and the out-of-plane electric polarization is induced for $\mathbf{B}_0 \parallel [111]$ (see Section 2.2.2). The distribution of electric polarization in skyrmions for

each case is shown in Fig. 4.1(a), characterized by the dipole moment for $\mathbf{B}_0 \parallel [110]$ and quadrupole moment for $\mathbf{B}_0 \parallel [001]$. For $\mathbf{B}_0 \parallel [110]$ and $\mathbf{B}_0 \parallel [111]$, the in-plane electric polarization is canceled out.

The time-dependent electric and magnetic fields under laser is introduced as [276]

$$\mathbf{E}(t) = E_d(\sin(\omega_0 t + \delta), \cos(\omega_0 t), 0), \tag{4.14}$$

$$\mathbf{B}(t) = B_d(\cos(\omega_0 t), -\sin(\omega_0 t + \delta), 0), \tag{4.15}$$

with $B_d = E_d/c$ and c is the speed of light. The polarization of light is determined by δ, where $\delta = 0, \pi/2, \pi$ corresponds to the right-circularly polarized (RCP), linearly polarized (LP), and left-circularly polarized (LCP) light, respectively. The ratio between the coupling with the electric and magnetic fields is given by

$$\frac{\lambda E_d}{g\mu_B B_d} = \frac{c\lambda}{g\mu_B} = 0.092. \tag{4.16}$$

However, the coupling strength λ in the THz regime might be different from the reference value obtained from the magnetoelectric effect at low frequencies [143]. Hence, we introduce a dimensionless parameter defined as

$$\mathcal{E}_d = \frac{\lambda E_d}{g\mu_B B_d}. \tag{4.17}$$

The parameter $\mathcal{E}_d$ represents the strength of magnetoelectric coupling in the THz regime, which is varied from $\mathcal{E}_d = 0.1$ to $\mathcal{E}_d = 0.3$ in this chapter.

From the time-periodic Hamiltonian of Eq. (4.1) with substituting Eqs. (4.11) and (4.13) for H_0 and $\mathbf{P_r}$, respectively, the effective Floquet Hamiltonian is obtained from Eq. (C.13) as

$$H_F = H_0 + \sum_{\mathbf{r}} g\mu_B B_F\left[- \{1 + \mathcal{E}_d^2(-2m_{\mathbf{r},x}^2 + m_{\mathbf{r},y}^2)\}(\hat{z} \cdot \mathbf{m_r}) + \mathcal{E}_d m_{\mathbf{r},z} m_{\mathbf{r},x}\right], \tag{4.18}$$

with the effective magnetic field B_F given in Eq. (4.7). Here, we ignore small contributions proportional to the Gilbert damping constant. From Eq. (4.18), we notice that the first order term proportional to ω^{-1} vanishes for the linearly polarized laser ($\delta = \pi/2$). The microscopic field for the kicked operator $\mathbf{H}_{\mathrm{mic},\mathbf{r}}^{(1)}(t)$ is given in Eq. (C.14). The Floquet Hamiltonian and kicked operators for $\mathbf{B}_0 \parallel [001], [111]$ are also derived in Appendix C.1.

Additional terms in the effective Hamiltonian of Eq. (4.18), denoted as $H_F^{(1)} = H_F - H_0$, imply a modification in the spin textures of skyrmions under laser. To understand its effect, a metastable skyrmion with the ferromagnetic background is prepared for 150×150 spin systems at $D/J = 0.09$ using Monte Carlo simulated annealing under the static external magnetic field of $g\mu_B B_z J/D^2 = 0.9$ and the periodic boundary condition [166] (Left panel of Fig. 4.1). We should note that the magnetic phase diagram of Eq. (4.11) was obtained in the literatures [193, 288], where the skyrmion crystal phase was found stable for $0.23 < g\mu_B B_z J/D^2 < 0.78$. The obtained configuration is then relaxed by

	Dimensionless	Physical Unit
Time	$\bar{t} = \hbar t / J$	≈ 0.66 ps
Distance	$\bar{x} = x/a$	0.5 nm
Velocity	$\bar{v} = \bar{x}/\bar{t}$	$\approx 7.6 \times 10^2$ m/s
Magnetic field (static)	$\bar{B}_z = g\mu_{\mathrm{B}} B_z J/D^2$	≈ 0.07 T
Magnetic field (laser)	$\bar{B}_d = g\mu_{\mathrm{B}} B_d/D$	≈ 0.78 T
Frequency of spin waves	$\bar{\omega} = \hbar\omega J/D^2$	≈ 2.0 GHz
Frequency of laser	$\bar{\omega}_0 = \hbar\omega_0/J$	≈ 250 GHz

Table 4.1: Unit conversion table for $S = 1$, $J = 1$ meV, $D/J = 0.09$ and $a = 0.5$ nm.

the corresponding effective LLG equation to investigate changes in spin textures. The parameters are taken at $g\mu_B B_d/D = 2.0$, $\hbar\omega_0/J = 10$, $\delta = \pi$ (LCP), and $\alpha = 0.04$, giving the effective magnetic field $g\mu_B B_F J/D^2 \approx -0.4$.

Since the magnetic component of circularly polarized laser only gives the effective out-of-plane magnetic field, nontrivial effects should arise from electric components, in particular from the cross term that is proportional to $\mathcal{E}_d$. To see the effect of cross term, we define the induced distortions in skyrmion spin textures $\delta \boldsymbol{S_r}$:

$$\delta \boldsymbol{S_r} = \boldsymbol{m_r}(\mathcal{E}_d = 0.1) - \boldsymbol{m_r}(\mathcal{E}_d = 0), \tag{4.19}$$

where $\boldsymbol{m_r}(\mathcal{E}_d)$ depicts the magnetic configuration obtained by the effective LLG equation with the coupling strength $\mathcal{E}_d$.

The middle panel of Fig. 4.1(b) shows the spatial profile of $\delta \boldsymbol{S_r}$ for $\mathbf{B}_0 \parallel [110]$. Crucially, the dipole-like distortion is observed in $\delta \boldsymbol{S_r}$, exhibiting a similar feature to the electric polarization. This is explained by the contribution of the cross term given as $\mathcal{E}_d m_{\boldsymbol{r},z} m_{\boldsymbol{r},x}$. Since the x component of magnetization changes the sign across the center of skyrmions, the cross term induces a dipole-like distortion. Equivalent results are obtained for $\mathbf{B}_0 \parallel [001], [111]$ in Fig. 4.1(b), showing a quadrupole feature and a ring pattern centered at skyrmions, respectively. Therefore, the magnetoelectric coupling results in the imprinting of electric multipole moments on the time-averaged spin textures of skyrmions under LCP. For the RCP, the induced distortion pattern is flipped with a change in the sign of B_F.

4.3   Main result

4.3.1   Laser-driven skyrmion motion

In this section, we discuss the non-equilibrium steady state of skyrmions under circularly polarized laser. As shown in Section 4.2, the time-averaged spin textures of skyrmions under circularly polarized laser are distorted due to the magnetoelectric coupling, resulting in the broken rotational symmetry of skyrmions. An important consequence is the laser-driven skyrmion motion, as shown below.
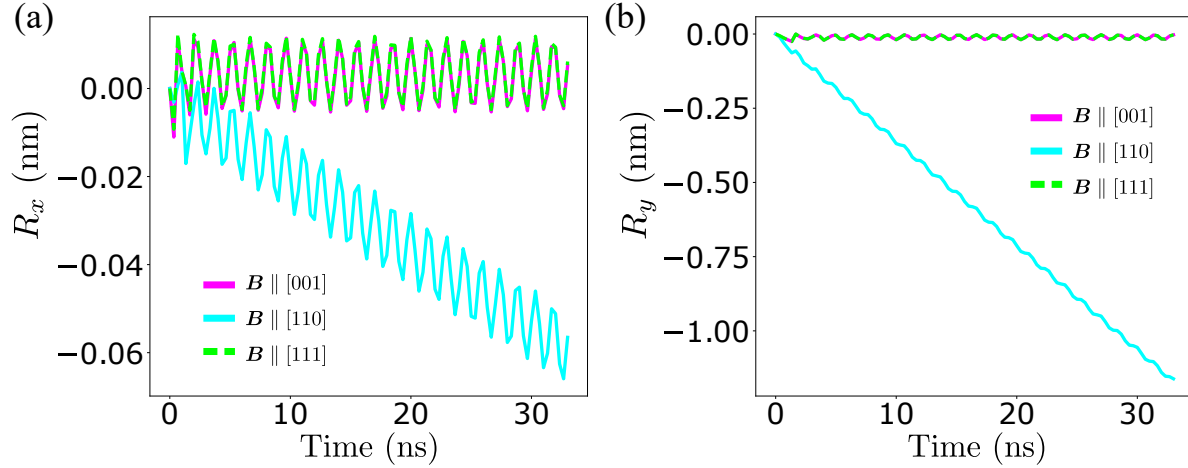
Figure 4.2: **Laser-driven skyrmion motion under the left-circularly polarized laser.** (a)-(b) Displacement of the center of skyrmions (a) R_x and (b) R_y under LCP as a function of time, defined in the text. The result for $\mathbf{B}_0 \parallel [001]$, $\mathbf{B}_0 \parallel [110]$, and $\mathbf{B}_0 \parallel [111]$ is respectively depicted in magenta (solid), cyan (solid), and lime (dashed). The parameters are taken as $D/J = 0.09$, $\overline{B}_z = g\mu_{\mathrm{B}}B_z J/D^2 = 0.9$, $\overline{B}_d = g\mu_B B_d/DS = 2.0$, $\mathcal{E}_d = 0.1$, $\delta = \pi$, $\alpha = 0.04$, and $\overline{\omega}_0 = \hbar\omega_0/J = 10$.

Using the single skyrmion configuration of Fig. 4.1 with the periodic boundary condition, the time-dependent LLG equation corresponding to Eq. (4.1) is numerically solved to compute the time-evolution for 50000 steps under LCP. The model parameters are defined as $J = 1$ meV, $D/J = 0.09$, and the lattice constant $a = 0.5$ nm [191, 196, 197] (see Table 2.1). In addition, the parameters for the LLG equation are fixed as $\overline{B} = g\mu_{\mathrm{B}}B_z J/D^2 = 0.9$, $\overline{B}_d = g\mu_B B_d/D = 2.0$, $\mathcal{E}_d = 0.1$, $\delta = \pi$, $\alpha = 0.04$, and $\overline{\omega}_0 = \hbar\omega_0/J = 10$. In Table 4.1, we summarize the conversion between dimensionless parameters and physical units. The skyrmion motion under LCP is tracked by computing the collective coordinate of skyrmions, which is defined as $R_i = \int d\mathbf{r}^2 \rho(\mathbf{r}) r_i/Q$ for $i = x, y$ with $\rho(\mathbf{r})$ and $Q = \int d\mathbf{r}^2 \rho(\mathbf{r})$ denoting the topological charge density and total topological charge, respectively (see Section 1.3.2).

Figure 4.2 shows the change in R_x and R_y as a function of time after irradiation of LCP. The result for $\mathbf{B}_0 \parallel [001]$, $\mathbf{B}_0 \parallel [110]$, and $\mathbf{B}_0 \parallel [111]$ is depicted in magenta, cyan, and lime, respectively. The crucial observation is that the skyrmion under $\mathbf{B}_0 \parallel [110]$ exhibits a translational motion along the negative y-axis as well as a small drift velocity along the negative x-axis. As shown in Fig. 4.1, the electric polarization is along the positive y-axis for $\mathbf{B}_0 \parallel [110]$, so the driven motion is mostly directed antiparallel to the net electric polarization. In contrast, the result for $\mathbf{B}_0 \parallel [001], [111]$ show no net displacement with almost the identical trajectories. This is consistent with the symmetry of time-averaged skyrmion textures, where a directional distortion $\delta \mathbf{S_r}$ is induced only for $\mathbf{B}_0 \parallel [110]$ as shown in Fig. 4.1(b).

To explain the numerical result of Fig. 4.2, we employ Thiele's approach [289]. Our

formulation follows Ref. [290], where the skyrmion motion under microwave fields was discussed in the presence of in-plane static magnetic fields (see Section 4.4 for difference from our work). The main idea is to separate the time-dependent magnetization $\boldsymbol{m_r}(t)$ into a slow part $\boldsymbol{m_{r,s}}(t)$ and a fast part $\boldsymbol{n_r}(t)$:

$$\boldsymbol{m_r}(t) = \boldsymbol{m_{r,s}}(t) + \boldsymbol{n_r}(t), \tag{4.20}$$

where spin precession is represented by $\boldsymbol{n_r}(t+T) = \boldsymbol{n_r}(t)$ with $T = 2\pi/\omega_0$ denoting the period of driving field. The velocity of skyrmion $\boldsymbol{v}$, which is assumed to be much slower compared to ω, gives rise to the time-dependence of slow part as $\boldsymbol{m_{r,s}}(t) = \boldsymbol{m_s}(\boldsymbol{r} - \boldsymbol{v}t)$. As derived in Appendix A.10, the drift velocity $\boldsymbol{v}$ is given in terms of the net force exerted on skyrmions for each period of oscillations as

$$v_x = \frac{4\pi Q \mathrm{F}_y + \alpha\eta \mathrm{F}_x}{(4\pi Q)^2 + \alpha^2\eta^2},$$
$$v_y = \frac{-4\pi Q \mathrm{F}_x + \alpha\eta \mathrm{F}_y}{(4\pi Q)^2 + \alpha^2\eta^2}, \tag{4.21}$$

where $\eta \approx 4\pi$ depends on the spatial profile of skyrmions defined in Eq. (A.86), and Q is the total topological charge. The net force $\mathbf{F}$ is given from Eq. (A.88) as

$$\mathrm{F}_i = -\gamma \int \tilde{\boldsymbol{m}}_{\boldsymbol{r},s} \cdot \left[\partial_i \tilde{\boldsymbol{m}}_{\boldsymbol{r},s} \times \langle \boldsymbol{m_r} \times \mathbf{H}_{\boldsymbol{r}}^{\mathrm{eff}} \rangle_T \right] dx dy, \tag{4.22}$$

with $i = x, y$, the microscopic field $\boldsymbol{H}_{\boldsymbol{r}}^{\mathrm{eff}}(t) = -[1/(\hbar\gamma S)]\partial H(t)/\partial \boldsymbol{m_r}$, and $\tilde{\boldsymbol{m}}_{\boldsymbol{r},s} = \langle \boldsymbol{m_{r,s}} \rangle_T$, where the time-averaged quantity is denoted as $\langle f \rangle_T = \frac{1}{T}\int_0^T dt f(t)$.

To obtain the net force $\mathbf{F}$, the analytical expressions for $\boldsymbol{m_{r,s}}(t)$ and $\boldsymbol{n_r}(t)$ are needed. Remarkably, the Floquet theory provides a simple analytical expression for $\boldsymbol{n_r}(t)$, provided that a system is in a non-equilibrium steady state. In Appendix C.2, the expression for $\boldsymbol{n_r}(t)$ are obtained as

$$\boldsymbol{n_r}(t) \approx \frac{\boldsymbol{f}_{\mathrm{mic}}^{(1)}(t)}{\omega_0} = -\frac{\gamma \tilde{\boldsymbol{m}}_{\boldsymbol{r},s}}{\omega_0(1+\alpha^2)} \times \left[\boldsymbol{H}_{\mathrm{mic},\boldsymbol{r}}^{(1)}(t) + \alpha \tilde{\boldsymbol{m}}_{\boldsymbol{r},s} \times \boldsymbol{H}_{\mathrm{mic},\boldsymbol{r}}^{(1)}(t) \right], \tag{4.23}$$

where $\boldsymbol{H}_{\mathrm{mic},\boldsymbol{r}}^{(1)}(t)$ is given in Appendix C.1. In the above expression, we only keep the leading order term proportional to ω^{-1}. Ignoring the drift velocity of skyrmions, the time-dependent magnetization is written as

$$\boldsymbol{m_r}(t) = \tilde{\boldsymbol{m}}_{\boldsymbol{r},s} + \boldsymbol{n_r}(t). \tag{4.24}$$

In this approximation, the non-equilibrium steady state solution is described by the spin precession $\boldsymbol{n_r}(t)$ around the time-averaged spin configuration $\tilde{\boldsymbol{m}}_{\boldsymbol{r},s}$ with $\boldsymbol{n_r}(t) \perp \tilde{\boldsymbol{m}}_{\boldsymbol{r},s}$.

For the calculation of $\mathbf{F}$, it is convenient to take the continuum limit. As the lowest order approximation, we assume a rotationally symmetric configuration of skyrmions for $\tilde{\boldsymbol{m}}_{\boldsymbol{r},s}$, given as

$$\boldsymbol{m}(\boldsymbol{r}) = \{\cos\phi(\psi)\sin\theta(r), \sin\phi(\psi)\sin\theta(r), \cos\theta(r)\}, \tag{4.25}$$

where $\boldsymbol{m}(\boldsymbol{r})$ is a continuous magnetization vector defined in the polar coordinates $\boldsymbol{r} = \{r\cos\psi, r\sin\psi\}$. This approximation does not account for distortions in the time-averaged spin textures (see Section 4.2), which gives higher order contributions as discussed below. Taking the continuum limit of Eq. (4.1) (see Appendix A.5), the free energy functional is written as

$$\mathcal{F} = \int dr^2 \left[\frac{J}{2}(\nabla \boldsymbol{m})^2 - \frac{D}{a}\boldsymbol{m}\cdot(\nabla\times\boldsymbol{m}) - \frac{g\mu_B}{a^2}(\mathbf{B}_0 + \mathbf{B}(t))\cdot\boldsymbol{m} - \frac{\mathbf{E}(t)\cdot\mathbf{P}}{a^2} \right],\ (4.26)$$

where a denotes the lattice constant. The microscopic field $\boldsymbol{H}^{\mathrm{eff}}(t)$ is derived as

$$\boldsymbol{H}^{\mathrm{eff}}(t) = -\frac{\delta\mathcal{F}}{\hbar\gamma\delta\boldsymbol{m}}$$
$$= \frac{a^2 J}{2\hbar\gamma}\nabla^2\boldsymbol{m} - \frac{aD}{\hbar\gamma}\nabla\times\boldsymbol{m} - \mathbf{B}_0 - \mathbf{B}(t) - \boldsymbol{H}_{\mathrm{ME}}(t),\ (4.27)$$

where $\boldsymbol{H}_{\mathrm{ME}}(t)$ is the contribution from magnetoelectric coupling, which is given in Eq. (C.10). Substituting $\boldsymbol{m}(\boldsymbol{r},t) = \boldsymbol{m}(\boldsymbol{r}) + \boldsymbol{n}(\boldsymbol{r},t)$ and $\boldsymbol{H}_{\mathrm{ME}}(t)$ into Eq. (4.22), the net driving force acting on skyrmions for $\mathbf{B}_0 \parallel [110]$ is obtained as

$$\begin{aligned}
\mathrm{F}_x &= -\gamma \int_0^\infty rdr \int_0^{2\pi} d\psi\, \boldsymbol{m}\cdot[\partial_x\boldsymbol{m}\times\langle\boldsymbol{m}(t)\times\boldsymbol{H}^{\mathrm{eff}}(t)\rangle_T] \\
&= -\frac{\pi\gamma B_F \mathcal{E}_d a\alpha}{16}\int_0^\infty d\bar{r}\left[\bar{r}\frac{d\theta}{d\bar{r}}(25\cos\theta + 7\cos 3\theta) + 17\sin\theta + 5\sin 3\theta\right], \\
\mathrm{F}_y &= -\gamma \int_0^\infty rdr \int_0^{2\pi} d\psi\, \boldsymbol{m}\cdot[\partial_y\boldsymbol{m}\times\langle\boldsymbol{m}(t)\times\boldsymbol{H}^{\mathrm{eff}}(t)\rangle_T] \\
&= \frac{\pi\gamma B_F \mathcal{E}_d a}{2}\int_0^\infty d\bar{r}\left[2\bar{r}\frac{d\theta}{d\bar{r}}\cos 2\theta + \sin 2\theta\right] = 0,\ (4.28)
\end{aligned}$$

where $\bar{r} = r/a$ is the dimensionless variable (see Table 4.1). For angular integrals over ψ, we have used $\phi = \psi - \pi/2$ for Bloch skyrmions. The y-component of $\mathbf{F}$ vanishes from the integration by parts. Therefore, the velocity of skyrmions for $\mathbf{B}_0 \parallel [110]$ is derived from Eq. (4.21) as

$$\begin{aligned}
v_x &= \frac{\alpha\eta\mathrm{F}_x}{(4\pi Q)^2 + \alpha^2\eta^2} \approx \frac{\alpha\eta\mathrm{F}_x}{(4\pi Q)^2} = -\frac{\alpha\eta}{4\pi Q}v_0\overline{B}_F\mathcal{E}_d\alpha C, \\
v_y &= \frac{-4\pi Q\mathrm{F}_x}{(4\pi Q)^2 + \alpha^2\eta^2} \approx -\frac{F_x}{4\pi Q} = v_0\overline{B}_F\mathcal{E}_d\alpha C,\ (4.29)
\end{aligned}$$

with the characteristic velocity $v_0 = a\gamma D^2/g\mu_B J \approx 6.16$ m/s, the dimensionless effective magnetic field $\overline{B}_F = g\mu_B B_F J/D^2$ (see Table 4.1 and Eq. (4.7)), and the constant C is defined as

$$C = \frac{1}{64Q}\int_0^\infty d\bar{r}\left[\bar{r}\frac{d\theta}{d\bar{r}}(25\cos\theta + 7\cos 3\theta) + 17\sin\theta + 5\sin 3\theta\right].\ (4.30)$$
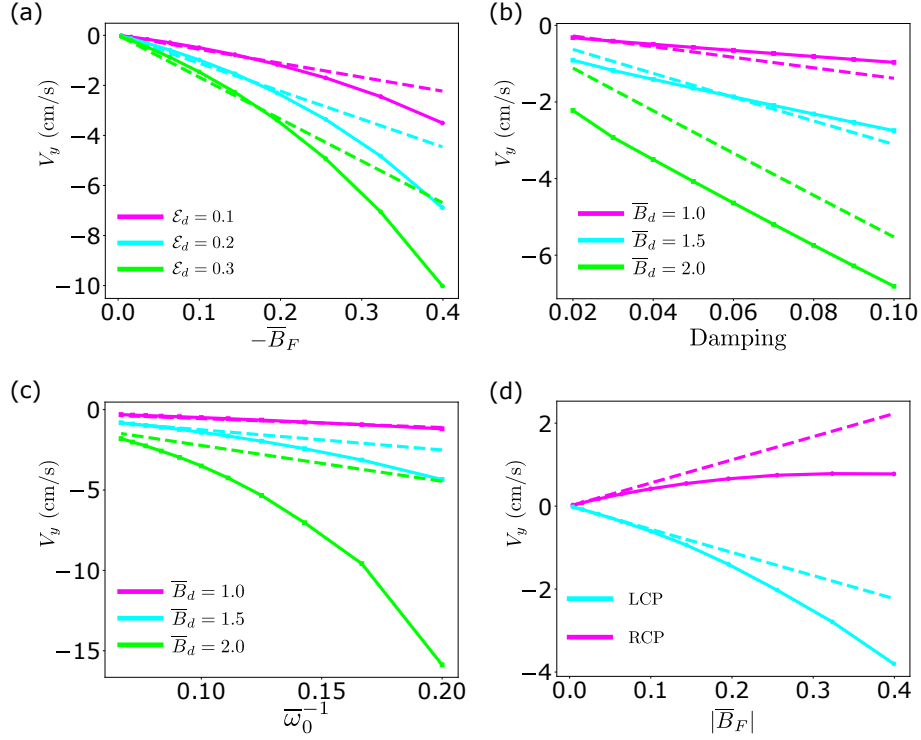
Figure 4.3: **Parameter dependence of laser-driven skyrmion velocity.** (a)-(c) Skyrmion velocity as a function of (a) effective magnetic fields $\overline{B}_F = g\mu_B B_F J/D^2$ at various magnetoelectric couplings $\mathcal{E}_d$, (b) phenomenological damping constants α, (c) frequencies of applied laser fields $\overline{\omega}_0$. The initial configuration is the same as Fig. 4.2. The static magnetic field is fixed at $\overline{B}_z = 0.9$ and other parameters are found in the text. (d) Velocity of skyrmion crystals under RCP and LCP. The spin configuration of skyrmion crystals is prepared at $\overline{B}_z = 0.4$. The parameters for LLG simulation is the same as (a) with $\mathcal{E}_d = 0.1$. In all panels, solid and dashed lines indicate the result of LLG simulation and the analytical result of Eq. (4.29).

Extracting $\theta(\overline{r})$ from the numerically obtained skyrmion configuration in Fig. 4.1, we estimate $C \approx -2.25/Q$.

Now, we compare the numerical result in Fig 4.2 and the expression of $\boldsymbol{v}$ in Eq. (4.29). From Fig. 4.2, the velocity for $\mathbf{B}_0 \parallel [110]$ is estimated as $v_x = -0.17$ cm/s and $v_y = -3.52$ cm/s. In comparison, we obtain $v_x = -0.088$ cm/s and $v_y = -2.22$ cm/s by substituting $Q = -1$, $\eta = 4\pi$, $\overline{B}_F = -0.4$, $\alpha = 0.04$, and $\mathcal{E}_d = 0.1$. Hence, our analytical expression is in good agreement with the numerical LLG simulation. Furthermore, the equivalent calculation of $\boldsymbol{v}$ for $\mathbf{B}_0 \parallel [001], [111]$ yields $\boldsymbol{v} = 0$ for the leading order term proportional to ω_0^{-1}. Therefore, Eq. (4.29) quantitatively explains the numerical result of Fig 4.2.

Furthermore, we investigate the parameter dependence of v_y for $\mathbf{B}_0 \parallel [110]$, as illustrated in Fig. 4.3(a)-(c). Using the same initial magnetic configuration as in Fig. 4.2, the average velocity is estimated for 30000 steps under the left-circularly polarized laser. Before calculations of the velocity, we wait for 20000 steps to make sure that the system

reaches a steady state. We fix parameters as $\alpha = 0.04$ for (a) and (c), $\overline{\omega}_0 = 10$ for (a) and (b), and $\mathcal{E}_d = 0.1$ for (b) and (c), while other parameters are depicted in the inset of each panel.

Each panel of Fig. 4.3 shows the dependence on (a) the effective magnetic field $\overline{B}_F$ by changing the amplitude of driving field $\overline{B}_d$ at various $\mathcal{E}_d$, (b) the damping constant α, and (c) the inverse of driving frequency $\overline{\omega}_0^{-1}$. Solid and dashed lines represent the time-dependent LLG simulation and the analytical expression of $\boldsymbol{v}$ in Eq. (4.29). In Fig. 4.3(a), the agreement with numerical simulation is remarkable for small $|\overline{B}_F|$ for all $\mathcal{E}_d$. As we increase the effective field $|\overline{B}_F|$, we find deviations from Eq. (4.29) arising from quadratic contributions in $\overline{B}_F$. We also find that v_y is proportional to the magnetoelectric coupling strength $\mathcal{E}_d$, predicted by Eq. (4.29). Similarly, we find the linear dependence in α and $\overline{\omega}_0^{-1}$ in Fig. 4.3(b) and (c), although higher order contributions results in discrepancies for a larger values of $\overline{B}_d$. In our simulation, the maximum velocity was obtained as $v_y = -15.9$ cm/s at $\overline{\omega}_0 = 5$ and $\overline{B}_d = 2.0$, but an even larger velocity is possible by tuning $\overline{\omega}_0$, $\overline{B}_d$, and α.

Lastly, we also demonstrate the laser-driven motion under RCP. Since the effective magnetic field $\overline{B}_F$ of RCP is positive, the total effective magnetic field becomes too large for skyrmions to be metastable. Hence, we prepare another configuration at lower static magnetic field of $\overline{B}_z = 0.4$, where the skyrmion crystal is stable. Using the same method as above, we compute the velocity of skyrmion crystals under RCP and LCP. The parameters for the LLG simulations are $\mathcal{E}_d = 0.1$, $\alpha = 0.04$, and $\overline{\omega}_0 = 10$ with various $\overline{B}_d$. Figure 4.3(d) shows that the sign of v_y of skyrmion crystals is inverted between RCP and LCP, as the sign of $\overline{B}_F$ changes with RCP and LCP. Although Eq. (4.29) is derived for a single skyrmion, it shows an excellent agreement with the numerical results for skyrmion crystals for small $|\overline{B}_F|$. Interestingly, quadratic contributions in $\overline{B}_F$ have the same contribution in RCP and LCP, resulting in a suppression of v_y for RCP and an enhancement for LCP. We expect that they arise from the distortions in the time-averaged spin configurations discussed in Section 4.2.

4.3.2 Laser-induced topological phase transition

In this section, we discuss the Floquet magnon band structure of skyrmion crystals under laser. Our purpose is to establish the connection between classical spin dynamics and Floquet magnons. For this purpose, we study the low energy spin wave modes under circularly polarized laser, following Ref. [193]. We discover that the resonance frequencies of low energy spin wave modes are modulated under the circularly polarized laser, which is consistent with the Floquet formalism applied to magnons, as discussed below. Throughout this section, we assume $\mathbf{B}_0 \parallel [110]$ that supports a net in-plane electric polarization. However, the effect of magnetoelectric coupling on Floquet magnon band structures turns out to be not significant. Hence, we expect that our result also applies to $\mathbf{B}_0 \parallel [001], [111]$.

For the calculation of Floquet magnon band structures, we choose $D/J = 1.0$ to reduce the computational time (see Section 3.1). Using the same argument as in Sec-
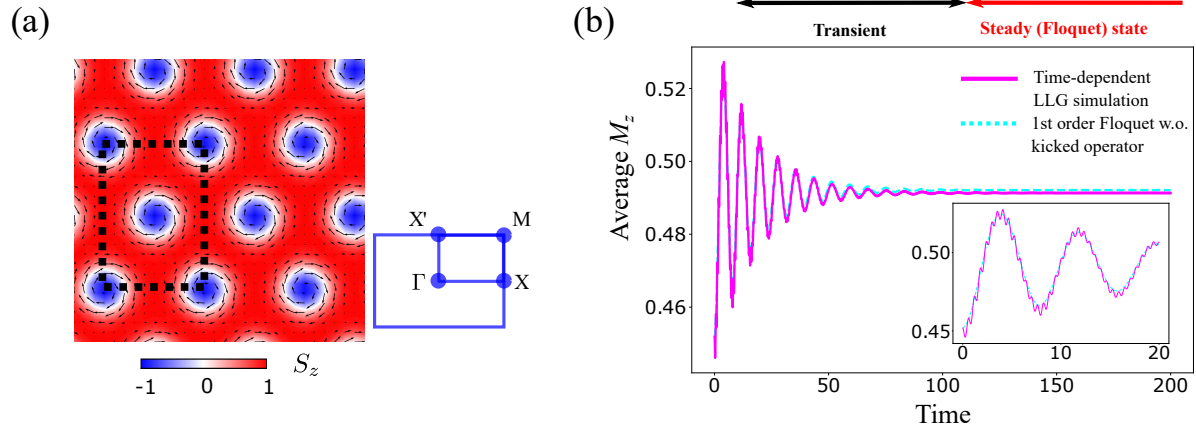
Figure 4.4: **Comparison between LLG and Floquet theory.** (a) Classical ground-state spin textures of skyrmion crystals at $D/J = 1.0$ and $\overline{B}_z = 0.4$. The magnetic unit cell is indicated by black dashed lines with the corresponding first Brillouin zone in a blue square. (b) The average magnetization is plotted against time for the time-dependent LLG equation of Eq. (4.1) (magenta solid) and the effective LLG equation of Eq. (4.3) (cyan dashed), obtained at $D/J = 1.0$, $\overline{B}_z = 0.4$, $\overline{B}_d = 1.0$, $\mathcal{E}_d = 0.1$, $\overline{\omega}_0 = 10.0$, $\delta = 0$ (RCP), and $\alpha = 0.04$ for 30×30 spins ($\mathbf{B}_0 \parallel [110]$). The inset shows the result for a shorter time scale.

tion 3.4, our result can be rescaled for experimental parameters of $D/J = 0.09$. Table 4.1 provides the ratio for conversion between dimensionless quantities used in this section and experimental values with physical units. Taking $D/J = 1.0$, the classical ground-state spin textures of skyrmion crystals are obtained by Monte Carlo simulated annealing at $\overline{B}_z = 0.4$ for 30×30 spin systems under the periodic boundary condition, which is shown in Fig. 4.4(a).

The obtained spin texture is used for the initial configuration of the time-dependent LLG simulation of Eq. (4.1) under RCP for 10000 steps. Figure 4.4(b) shows the time-dependence of average magnetization under RCP with $\overline{B}_d = 1.0$, $\mathcal{E}_d = 0.1$, $\overline{\omega}_0 = 10.0$, and $\alpha = 0.04$, which is depicted in the magenta solid line. Initially, we find a large oscillation in the average magnetization, which corresponds to a transient regime. We should note that the frequency of oscillation in this regime is much slower than the applied field, as indicated by the inset of Fig. 4.4(b). Thus, the driving frequency is decoupled from resonance frequencies of the system. After about 100 LLG steps, the system reaches a non-equilibrium steady state, whose time-averaged spin texture corresponds to the classical ground-state spin textures of the effective Floquet Hamiltonian defined in Eq. (4.18). This is confirmed by solving the effective LLG equation of Eq. (4.3) with the same parameters, depicted in cyan dashed line of Fig. 4.4(b). The result for the effective LLG equation shows an excellent agreement with the time-dependent LLG equation. Only the difference is that the time-dependent LLG equation contains the precession mode around the time-averaged magnetization, which could be reproduced in the Floquet theory by evaluating
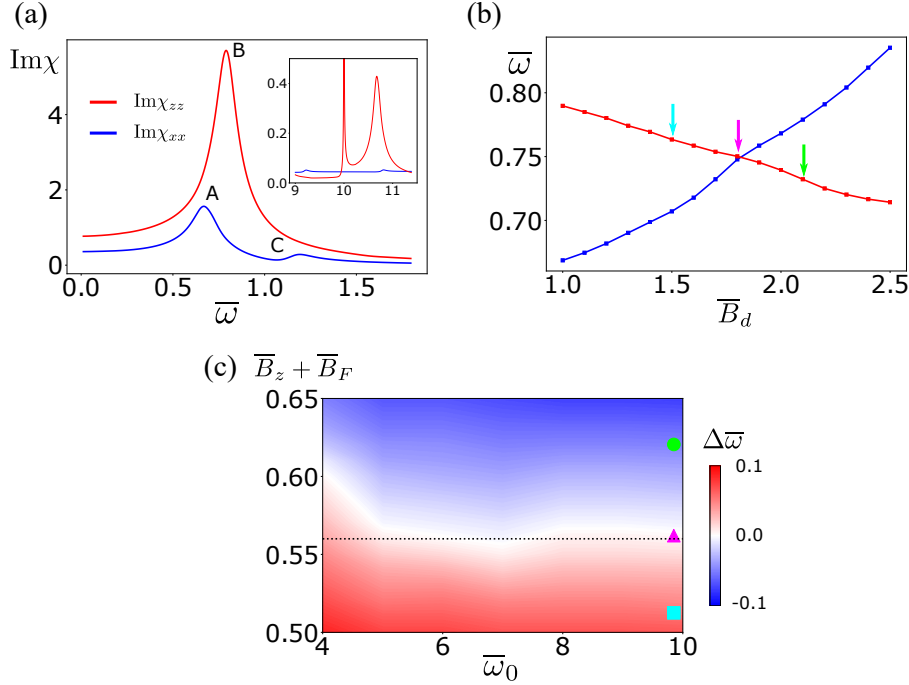
Figure 4.5: **Laser-driven magnonic topological phase transition under RCP.**
(a) Imaginary parts of dynamical susceptibilities depicted in blue for $\mathrm{Im}\chi_{xx}$ and red for
$\mathrm{Im}\chi_{zz}$, respectively. The parameters for the time-dependent LLG equation are the same
as in Fig 4.4(b). The resonance peaks for (A) the counterclockwise, (B) breathing, and
(C) clockwise modes are indicated. The inset shows the result near the driving frequency
$\overline{\omega}_0 = 10$. (b) Resonance frequencies of the counterclockwise (blue) and breathing (red)
modes as a function of amplitudes of applied fields $\overline{B}_d$ at $\overline{\omega}_0 = 10$. (c) Band gap between
the counterclockwise and breathing modes $\Delta\overline{\omega}$ as a function of frequencies of applied
fields $\overline{\omega}_0$ and total effective magnetic fields $\overline{B}_F + \overline{B}_z$. A dashed line indicates the critical
magnetic field $\overline{B}'_c = 0.56$ for $\overline{\omega}_0 = 10$. Arrows in (b) correspond to the parameters
indicated by polygons with the same color in (c).

the kicked operator of Eq. (4.8).

Following Ref. [193], we introduce a pulse field $\overline{\mathbf{B}}_{\mathrm{pulse}} = 3\overline{B}_d(\hat{x} + \hat{z})\delta(\overline{t} - \overline{t}_0)$ with $\hat{x}$
and $\hat{z}$ respectively denoting the unit vector along x- and z-axis, and $\overline{t}_0 = 3000$. Here,
the relaxation time $\overline{t}_0$ is taken sufficiently long to ensure that the system reaches a
steady state. By applying the pulse field along both in-plane and out-of-plane directions,
we can excite the low energy local excitations of skyrmions, known as counterclockwise
(CCW), clockwise (CW), and breathing modes [193] (see Section 1.3.6). Since the driving
frequency of laser ω_0 is much higher than resonance frequencies of these low energy
excitations, they can be detected analogously to static systems. Therefore, the Γ point
excitation of Floquet magnon bands in skyrmion crystals can be directly investigated in
the time-dependent LLG simulation.

To investigate resonance frequencies of CCW, CW, and breathing modes, the imagi-
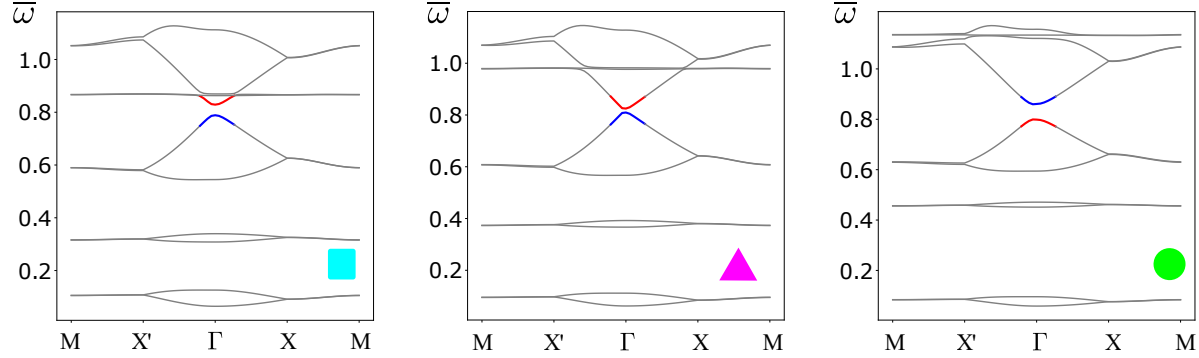
Figure 4.6: **Topological phase transition in Floquet magnon bands.** Floquet magnon band spectra near the critical magnetic field $\overline{B}'_c$ at $\overline{\omega}_0 = 10$. From left, the amplitude of applied fields is taken as $\overline{B}_d = 1.5$, $\overline{B}_d = 1.8$, and $\overline{B}_d = 2.1$, corresponding to the parameters indicated by arrows and polygons in Fig. 4.5(b) and (c). The CCW and breathing modes at Γ points are highlighted by blue and red, respectively.

nary part of susceptibility is defined as [193, 197]

$$\mathrm{Im}\chi_{ij}(\overline{\omega}) = \frac{M_{\overline{\omega},i}}{\overline{B}_{\overline{\omega},j}}, \tag{4.31}$$

with $M_{\overline{\omega},i}$ and $\overline{B}_{\overline{\omega},j}$ denoting the Fourier transformation of the average magnetization $\boldsymbol{M}(\overline{t})$ and $\overline{\mathbf{B}}(\overline{t}) = \overline{\mathbf{B}}_{\mathrm{pulse}} + \overline{\mathbf{B}}_{\mathrm{laser}}$ for $i, j = x, y, z$.

Figure 4.5(a) shows the $\mathrm{Im}\chi_{xx}$ (blue) and $\mathrm{Im}\chi_{zz}$ (red) with the same parameters as Fig. 4.4. At low frequencies $\omega \ll \omega_0$, we find the three resonance peaks for CCW, breathing, and CW modes, which are labeled as A, B, and C in Fig. 4.5(a), respectively. As pointed out in Ref. [193], the CCW and CW modes are excited in the in-plane direction, while the breathing mode is obtained in the out-of-plane direction. Hence, the low energy excitations of Floquet magnons are successfully obtained by the time-dependent LLG equation. In addition, an important property of Floquet states is that their eigenvalues, termed as quasienergy, is well-defined only modulo $\hbar\omega$, related by $\epsilon_{nm} = \epsilon_n + m\hbar\omega$ for integer m (See Appendix B.1.1). Consistent with the Floquet theory, the periodic structure of quasienergy of Floquet magnon excitations is indeed found near $\overline{\omega}_0 = 10$ in $\mathrm{Im}\chi_{zz}$ at $\overline{\omega} = \overline{\omega}_0 + \overline{\omega}_{\mathrm{br}}$, where $\overline{\omega}_{\mathrm{br}} \approx 0.8$ denotes the resonance frequency of breathing mode. This is illustrated in the inset of Fig. 4.5(a). We should note that a large peak at $\overline{\omega}_0 = 10$ for $\mathrm{Im}\chi_{zz}$ corresponds to the laser fields. However, the signal from $\mathrm{Im}\chi_{xx}$ is too weak to observe clear resonance peaks, although there exists a very small peak below and above $\overline{\omega}_0 = 10$.

Next, we investigate the dependence of resonance frequencies $\overline{\omega}$ on the driving amplitude $\overline{B}_d$. As given in Eq. (4.7), the circularly polarized laser generates the effective magnetic field, which is positive for RCP. Thus, the topological phase transition can be induced by increasing $\overline{B}_d$, analogously to the magnetic-field driven magnonic topological phase transition discussed in Chapter 3 [76]. This is illustrated in Fig. 4.5(b), where

the resonance frequencies of CCW (blue) and breathing (red) modes are plotted against $\overline{B}_d$. We clearly see that the resonance frequency of each mode depends linearly on $\overline{B}_d$ with opposite signs, and it eventually results in the band inversion between CCW and breathing mode. The critical value of the effective magnetic field at the band inversion point is given as

$$\overline{B}'_c = \overline{B}_F + \overline{B}_z \approx 0.56. \tag{4.32}$$

Remarkably, it is found to be almost equal to the critical magnetic field $\overline{B}_c = 0.58$ for skyrmion crystals under static external magnetic fields [76], which is related to the critical magnetic field derived in Chapter 3 by a factor of $3/2$ (see Appendix A.5.2).

We also study the dependence on driving frequency $\overline{\omega}_0$. Since the contributions proportional to ω^{-2} or even higher order terms become larger as $\overline{\omega}_0 \to 1$, the critical magnetic field $\overline{B}'_c$ should deviate from $\overline{B}_c$ with decreasing $\overline{\omega}_0$. Figure 4.5(c) shows the band gap between CCW and breathing mode denoted as $\Delta\overline{\omega}$ at various $\overline{\omega}_0$ and $\overline{B}_F + \overline{B}_z$. Intriguingly, the value of $\overline{B}'_c$ is roughly constant up to $\overline{\omega}_0 = 5$, while it shows an increase at $\overline{\omega}_0 = 4$. For $\overline{\omega}_0 \leq 3$, we find that the system becomes unstable without reaching steady states, thus the Floquet theory is no longer valid.

Finally, we comment on the calculation of the Floquet magnon band spectrum. As implied from Fig. 4.5, the effective Floquet Hamiltonian given in Eq. (4.18) correctly describes the classical limit of spin wave modes under circularly polarized laser for $\overline{\omega}_0 \geq 5$. Hence, the spin wave Hamiltonian for Floquet magnon bands can be constructed from Eq. (4.18) using the standard method for static systems (see Section 1.1.3). In this formulation, the Floquet magnon is defined as excitations from the time-averaged configuration. In Appendix C.3, we derive additional terms in the spin wave Hamiltonian for $\mathbf{B}_0 \parallel [110]$ as well as for $\mathbf{B}_0 \parallel [001], [111]$ arising from magnetoelectric couplings. However, their contributions do not change the Floquet magnon band structures significantly. In comparison, the effective magnetic field B_F defined in Eq. (4.7) has a dominant contribution. Figure 4.6 shows the full band structures of Floquet magnon bands, corresponding to the parameters indicated by arrows and polygons in Fig. 4.5(b) and (c). The obtained Floquet magnon band structures are consistent with the result of LLG simulation in Fig. (4.5), showing the band inversion near $\overline{B}'_c \approx 0.56$.

4.4 Discussion and Conclusion

Firstly, we discuss the experimental parameters for this work. Our estimates for model parameters are $J = 1$ meV, $D/J = 0.09$ and $a = 0.5$ nm based on the experimental result of Cu_2OSeO_3 [95, 142, 196, 197] (see Table 2.1). While the D/J ratio is extracted from the periodicity of helical phases, the estimate for exchange coupling J provides a reasonable estimate for resonance frequencies for the CCW, CW and breathing modes around 1 GHz that is consistent with the experiment [189]. Using this model parameter, Table 4.1 provides estimates for the required frequency for laser to be greater than 1.25 THz for $\overline{\omega}_0 \geq 5$ with the maximum amplitude of 1.6 T for $\overline{B}_d \sim 2.0$. Hence, the current THz laser technology provides a readily available equipment [291].
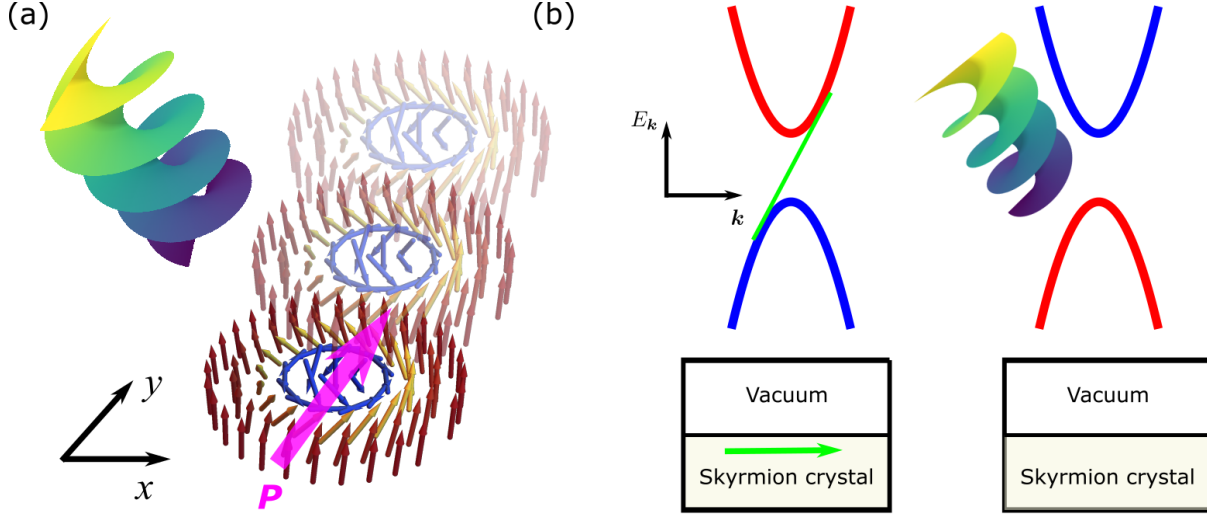
Figure 4.7:   **Topological spin structure of skyrmions and their magnon band topology are controlled by applying circularly polarized lasers.** (a) Skyrmions carrying the in-plane electric polarization undergoes the translational motion under the circularly polarized laser. (b) The topological phase transition occurs in the Floquet magnon bands of skyrmion crystals due to the effective magnetic field induced by the circularly polarized laser.

Another issue for the experimental realization of Floquet states is heating. We note that the direct absorption of photons is not possible for THz lasers as the energy of photons for THz regime is much smaller than the bulk band gap of Cu_2OSeO_3, $\Delta_g \approx 2$ eV [292]. Thus, the spontaneous heating of electrons should not occur. Nevertheless, we cannot completely suppress the heating effect that could eventually lead to breaking the long-range magnetic order, although our calculation predicts a stable non-equilibrium steady state in the presence of phenomenological Gilbert damping. To avoid potential heating effects, we suggest repeated applications of subpicosecond pulses of circularly polarized laser, which was used for the experimental observation of anomalous Hall effect of Floquet states in graphene [279].

In Section 4.3.1, we have demonstrated the laser-driven motion due to the in-plane electric polarization carried by skyrmions in Cu_2OSeO_3. Here, we comment the difference between our work and the previous works on skyrmions driven by microwave fields in GHz frequencies [290, 293, 294]. In Ref. [290], the microwave-driven skyrmion motion was first proposed by applying the in-plane magnetic fields, which breaks the rotational symmetries of skyrmions. As a result of the broken rotational symmetry, it was shown that skyrmions experience a net driving force defined in Eq. (4.22) when the low energy spin wave modes such as CCW and breathing modes were excited by microwaves. Thus, the velocity of skyrmions depends on the amplitude of in-plane magnetic field but not on the amplitudes of microwaves. Also, it has a strong dependence on frequencies as the translational motion is only induced at resonance frequencies of CCW, CW, and

breathing modes. The maximum velocity obtained in Ref. [290] was 2.8 cm/s that is comparable or slightly smaller than our result. In comparison, we have proposed a laser-driven motion using THz lasers based on the Floquet theory. The velocity of skyrmions can be easily controlled by frequnecies and amplitudes of applied laser fields, providing a greater control of skyrmion motions.

As a concluding remark, we have predicted the laser-driven skyrmion motion in multiferroic insulator Cu_2OSeO_3 with its velocity described by a simple analytical expression (Fig 4.7(a)). We found that the magnetoelectric coupling plays a fundamental role for this phenomenon. Furthermore, we have established the connection between the classical spin dynamics and Floquet magnon modes, demonstrating the topological phase transition of Floquet magnon bands in skyrmion crystals under circularly polarized laser. From the bulk-boundary correspondence discussed in Section 3.3.2, it allows the ultrafast switching of magnonic chiral edge states (Fig. 4.7(b)). Our study suggests a novel approach for ultrafast control of the real and reciprocal space topology in skyrmion-hosting materials.

Chapter 5

Magnonic quadrupole topological insulator

As introduced in Section 1.2, higher-order topological phases, which support corner states in a two-dimensional system, are characterized by bulk multipole moments. Although they were originally proposed in electronic systems, they have been experimentally realized in bosonic systems such as phonons [91, 295–297] and photons [93, 298–300]. In contrast, the magnonic analogue of higher-order topological insulators has not been understood well, with only a few theoretical predictions for their existence [301]. To establish the higher topological phases of magnons, we need to define the bulk multipole moments of magnonic wave functions.

In Chapter 5, we discuss the magnonic quadrupole topological insulators realized in ferromagnetic skyrmion crystals. We first introduce the extention of multipole moments to magnonic systems, where a subtle yet critical modification must be implemented to account for the bosonic nature. Employing the Wilson loop formalism adapted for magnonic systems, we demonstrate the quantized magnonic quadrupole moment with its fractional boundary signatures of edge polarizations and corner charges. The content of this chapter was published in Ref. [212].

5.1 Multipole moments in magnonic systems

5.1.1 Difference from electronic systems

According to the modern theory of polarization [82–86], the electric polarization is given by $\mathbf{p} = -\tilde{\boldsymbol{r}}$ up to modulo integers from Eq. (1.45), where $\tilde{\boldsymbol{r}}$ is the expectation value of position operator for occupied states and we take $a = e = 1$ for the elementary charge e and the lattice constant a. The key idea is that the expectation value of position operator can be only defined up to modulo integers for periodic systems.

The magnonic polarization can be defined analogously, although we need to make several modifications as follows. Firstly, magnons do not carry electric charge, so we cannot define the electric polarization induced by magnons. Instead, we focus on the expectation

value of position operator for magnons. Then, we define the magnonic polarization as

$$\mathbf{p} = \tilde{\boldsymbol{r}} \text{ mod } 1, \tag{5.1}$$

with the lattice constant $a = 1$. We note that Eq. (5.1) does not mean a physical dipole moment but the displacement of magnonic wave functions from the center of unit cell in the Wannier representation. In Section 1.2, we have discussed the analogy between higher-order topological phases and classical electromagnetism that provides a physically intuitive picture. Nevertheless, the higher-order topological phase is not originated from the electric charge, but from the quadrupole moment arising from topologically nontrivial Wannier spectra [79, 80], which is extended to magnonic systems in Section 5.1.3. We also discuss the fractional boundary signatures in the presence of magnonic quadrupole moment in Section 5.4.2, where the fractional corner "charge" is introduced.

Secondly, the magnon Hamiltonian takes the form of the Bogoliubov-de Gennes Hamiltonian. As a result, the full magnon spectrum contains redundant information in "particle" and "hole" magnon bands as shown in Eq. (1.14) [2]. In practice, only the energy eigenstates corresponding to either "particle" or "hole" magnon bands are necessary to define magnonic multipole moments. Another point is that the occupied states of magnons are not well-defined as they are bosonic excitations from the classical spin ground state with a finite energy. Hence, we simply consider the bulk multipole moment carried by some of the lowest energy magnon bands separated by a band gap.

Thirdly, we need to account for the paraunitary nature of $T_{\boldsymbol{k}}$ that diagonalize the magnon Hamiltonian. In Section 1.1.4, we point out that the Berry connection for n-th magnon band can be expressed as $\mathcal{A}_\mu^n(\boldsymbol{k}) = i \langle t^n(\boldsymbol{k})|\partial_{k_\mu} t^n(\boldsymbol{k})\rangle$ with $|t^n(\boldsymbol{k})\rangle$ and $\langle t^n(\boldsymbol{k})|$ denoting n-th column of $T_{\boldsymbol{k}}$ and n-th row of $T_{\boldsymbol{k}}^{-1}$, respectively. Inspired by this observation, we construct an orthogonal basis for magnon bands as follows. We define a Bloch wave function of n-th magnon band as $|u_{\boldsymbol{k}}^n\rangle = T_{\boldsymbol{k}} v_n$, where v_n is a vector whose components are given by $v_n^j = \delta_{nj}$. Since $T_{\boldsymbol{k}}$ is a paraunitary matrix, the orthogonality relation of magnonic wave functions is obtained by introducing the following inner product

$$\langle u_{\boldsymbol{k}}^m | u_{\boldsymbol{k}}^n \rangle_{\text{para}} \equiv \xi v_m^T T_{\boldsymbol{k}}^\dagger \Sigma T_{\boldsymbol{k}} v_n = \delta_{mn} \,, \tag{5.2}$$

with $\xi = \pm 1$ for "particle"/"hole" bands and Σ is defined in Eq. (1.12). This is the natural basis for defining the topological invariants in magnonic systems. For example, the Berry connection of magnon bands is defined as

$$\mathcal{A}_x^{mn}(\boldsymbol{k}) = i \langle u_{\boldsymbol{k}}^m | \partial_{k_x} | u_{\boldsymbol{k}}^n \rangle_{\text{para}} = i\xi v_m^T T_{\boldsymbol{k}}^\dagger \Sigma \partial_{k_x} T_{\boldsymbol{k}} v_n \,, \tag{5.3}$$

which is a generalization of the Berry connection for a single band [2]. The expression for single band in Eq. (1.15) is derived as

$$\begin{aligned} \mathcal{A}_{n,x}(\boldsymbol{k}) &= i \langle u_{\boldsymbol{k}}^n | \partial_{k_i} | u_{\boldsymbol{k}}^n \rangle_{\text{para}} = i\xi v_n^T T_{\boldsymbol{k}}^\dagger \Sigma \partial_{k_i} T_{\boldsymbol{k}} v_n \\ &= \text{tr}[i\xi V_n T_{\boldsymbol{k}}^\dagger \Sigma \partial_{k_i} T_{\boldsymbol{k}}] = \text{tr}[i V_n \Sigma T_{\boldsymbol{k}}^\dagger \Sigma \partial_{k_i} T_{\boldsymbol{k}}], \end{aligned} \tag{5.4}$$

where V_n is a diagonal matrix with only the n-th element to be $+1$ and zero elsewhere.

5.1.2 Magnonic polarization

In this section, we introduce the magnonic polarization using the Wannier representation. For applications to skyrmion crystals in later sections of this chapter, we focus on a two-dimensional system and the lattice constant is taken to be unity. Similarly to electronic systems, a Wannier function for an isolated magnon band is defined as

$$
\begin{aligned}
|w_{n,\boldsymbol{R}}\rangle &= \frac{1}{(2\pi)^2} \int_{\text{BZ}} dk^2 \, e^{-i\boldsymbol{k}\cdot\boldsymbol{R}} \, |u_{n,\boldsymbol{k}}\rangle \,, & (5.5) \\
|u_{n,\boldsymbol{k}}\rangle &= \sum_{\boldsymbol{R}} e^{i\boldsymbol{k}\cdot\boldsymbol{R}} \, |w_{n,\boldsymbol{R}}\rangle \,, & (5.6)
\end{aligned}
$$

where $\boldsymbol{R}$ is the lattice vector and n is the index for magnon bands. Given that a n-th Bloch wave function $|u_{n,\boldsymbol{k}}\rangle$ is a smooth function with $\boldsymbol{k}$, the corresponding Wannier function $|w_{n,\boldsymbol{R}}\rangle$ is strongly localized inside a unit cell labeled by $\boldsymbol{R}$. The same argument as in Section 1.2.2 can be used to show that the Wannier function is an eigenvector of the position operator for magnonic systems. The Wannier center for magnons is given as

$$
\begin{aligned}
\nu_x^n &= \langle w_{n,0}|\hat{x}|w_{n,0}\rangle_{\text{para}} \,, & (5.7) \\
\nu_y^n &= \langle w_{n,0}|\hat{y}|w_{n,0}\rangle_{\text{para}} \,, & (5.8)
\end{aligned}
$$

where the subscript stands for the paraunitary inner product defined in Eq. (5.2). Assuming that the entire magnon band structure consists of isolated bands, the magnonic polarization for the lowest M bands is obtained as

$$
p_x = \sum_{n=1}^{M} \nu_x^n, \tag{5.9}
$$

$$
p_y = \sum_{n=1}^{M} \nu_y^n. \tag{5.10}
$$

When a magnon band has degeneracies with other bands, its wave function cannot be smoothly defined over the entire Brillouin zone. As a result, Wannier functions defined in the above equation are no longer localized in the real space (see Appendix D.2). In such cases, we need to use the Wilson loop formalism to calculate Wannier centers. As explained in Appendices D.3 and D.4 for electronic systems, a Wilson loop is a unitary matrix constructed by parallel transport of occupied states over a noncontractible loop across the Brillouin zone. Crucially, eigenvalues of a Wilson loop are equal to Wannier centers, which are eigenvalues of the position operator $P_{\text{occ}}\hat{x}P_{\text{occ}}$ with P_{occ} denoting the projection operator to occupied states.

Similarly, a Wilson loop in magnonic systems provides an efficient method to compute the Wannier centers of magnon bands. To construct a Wilson loop in magnonic systems, we simply need to replace the inner product between Bloch wave functions to the paraunitary inner product of Eq. (5.2). In Appendix E.1, we provide technical details on the

calculation of a Wilson loop in magnonic systems. Using Wannier centers obtained from the Wilson loop, the magnonic polarization for the lowest M magnon bands is given by

$$p_x = \frac{1}{2\pi} \int dk_y \sum_{j=1}^{M} \nu_x^j(k_y) \bmod 1, \qquad (5.11)$$

$$p_y = \frac{1}{2\pi} \int dk_x \sum_{j=1}^{M} \nu_y^j(k_x) \bmod 1. \qquad (5.12)$$

We should note that Wannier centers along x/y-axis are obtained as a function of k_y/k_x using a Wilson loop in a two-dimensional system.

In Section 1.2.3, we have introduced the symmetry constraints on electronic multipole moments. The magnonic polarization can be also quantized by symmetries of magnetic systems, which depend on crystal structures as well as spin textures of a magnetic unit cell. The difference from electronic systems is that the time-reversal symmetry is broken in magnetic systems. We consider the combination of spatial symmetries such as rotational symmetries with the time-reversal symmetry, including $C_{2x}\mathcal{T}$ for a twofold rotation about the x axis together with time reversal, $C_{2y}\mathcal{T}$ for a twofold rotation about the y axis together with time reversal, and C_{2z} for a twofold rotation about the z axis. We should note that these symmetries are relevant for antiskyrmions as shown in Section 5.3.1. In Appendix E.4, the constraints by these symmetries on Wannier centers are derived. From Eqs. (E.28) and (E.29), we have

$$p_x \overset{C_{2y}\mathcal{T}}{=} -p_x \bmod 1, \qquad (5.13)$$

$$p_y \overset{C_{2x}\mathcal{T}}{=} -p_y \bmod 1, \qquad (5.14)$$

which leads to the quantization of the magnonic polarization as $p_x = 0, 1/2$ and $p_y = 0, 1/2$.

Lastly, we comment on the topological phase characterized by a nontrivial magnonic polarization $p_i = 1/2$ for $i = x, y$. As discussed in Appendix D.4, the electric polarization is related to the Berry phase, or equivalently the Zak phase by $Z_i = 2\pi P_i$ [7]. When the Zak phase is nontrivial with $Z_i = \pi$ for periodic systems, it is known that a bound state is obtained under open boundary conditions along the edges orthogonal to i-axis. The prominent example is the Su-Schrieffer-Hegger (SSH) model, describing a one-dimensional chain with alternating hopping integrals [13, 14]. We could interpret this bulk-boundary correspondence as a bound charge of magnitude p induced by an electric polarization of magnitude p per unit length [80]. The same relationship between the polarization and the Zak phase holds in magnonic systems from Eq. (E.8). Hence, the nontrivial magnonic polarization also results in the bound state of magnons at the edges of a finite system, which can be interpreted as the bound "charge" of magnons. This is illustrated in Section 5.4.1 as the correspondence between the edge-localized magnonic polarization and the emergence of magnonic corner states.
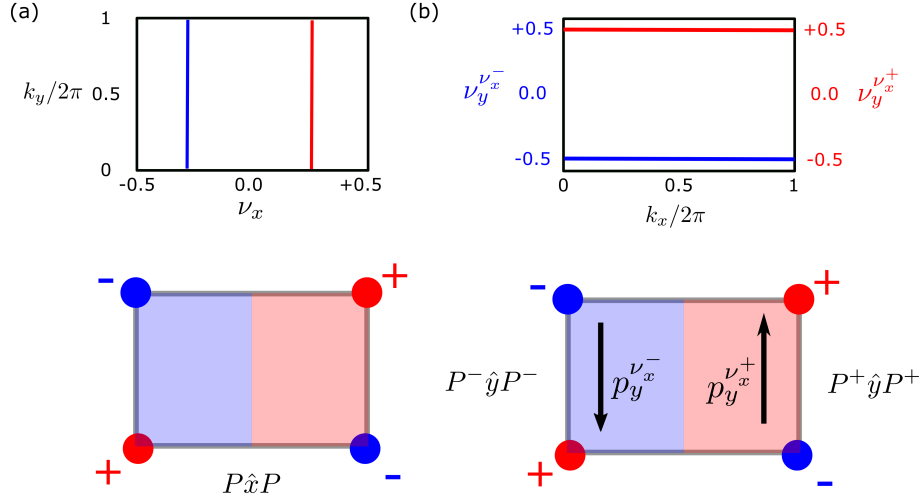
Figure 5.1: **Schematic representation of Wannier sector polarization.** (a) Top: Wannier spectrum ν_x plotted as a function of k_y. Bottom: real space image of Wannier functions inside unit cell, which are eigenstates of $P\hat{x}P$. (b) Top: Wannier spectrum $\nu_y^{\nu_x^{\pm}}$ of a nested Wilson loop plotted as a function of k_x. They are eigenvalues of $P^{\pm}\hat{y}P^{\pm}$, where $P^{\pm}$ are defined in the text. Bottom: real space image of Wannier sector polarizations with opposite signs in the right and left half of unit cell, denoted as $p_y^{\nu_x^{\pm}}$.

5.1.3 Magnonic quadrupole moment

Similarly to the magnonic polarization, the magnonic quadrupole moment does not mean a physical quadrupole moment, but only refers to the spatial arrangement of magnonic Wannier functions that exhibit a quadrupole feature. In a system with a vanishing magnonic polarization, a magnonic quadrupole moment can be defined as two opposite magnonic polarizations analogously to Eq. (1.46) for electronic systems, which are introduced as a Wannier sector polarization for magnonic systems in the following. The definition of magnonic quadrupole moment is given at the end of this section in terms of the Wannier sector polarization.

In Section 5.1.2, we argue that a quantized magnonic polarization characterizes a topological phase of a gapped magnon spectrum. Noting that Wannier centers $\nu_{x/y}$ are given as a function of k_y/k_x, it can be interpreted as a one-dimensional spectrum, termed as *Wannier spectra*. The Wannier sector polarization is a magnonic polarization defined for a gapped Wannier spectrum, characterizing its topological phase.

We briefly outline the calculation of the magnonic Wanner sector polarization along y-axis for a magnetic system with $C_{2x}\mathcal{T}$ and $C_{2y}\mathcal{T}$ symmetries. Due to the symmetry constraint of Eq. (E.28), the Wannier spectra along x-axis are given as $\nu_x = 0, 1/2$ or a pair of eigenvalues satisfying $\nu_x^1(k_y) = -\nu_x^2(-k_y)$. The top panel of Fig. 5.1(a) shows a schematic illustration of gapped magnonic Wannier spectra $\nu_x(k_y)$ consisting of two flat bands with opposite signs. From Eq. (5.11), the total magnonic polarization p_x vanishes for this case. Since Wannier centers are expectation values of position operator $P\hat{x}P$ with

P representing a projection operator to the magnon bands used in a Wilson loop, two clouds of magnon density are distributed to the right-hand side and left-hand side of a magnetic unit cell in the Wannier representation. This is shown in the bottom panel of Fig. 5.1(a).

Given a gapped Wannier spectra, we then define a projection operator for positive and negative Wannier sectors obtained above/below a gap at $\nu_x = 0$, denoted as $P^{\pm}$. In the real space picture, it implies partitioning a group of magnon bands into those localized within the right-hand side and left-hand side of the magnetic unit cell in the Wannier representation. For each Wannier sector, we compute a so-called nested Wilson loop along y-axis [79, 80], denoted as $\tilde{W}^{\nu_x^{\pm}}_{y,\boldsymbol{k}}$ with a superscript $\nu_x^{\pm}$ indicating the corresponding Wannier sector. The difference from a Wilson loop is that it is constructed from Wannier functions of each sector instead of Bloch wave functions. We refer to Appendix E.2 for technical details of the nested Wilson loop for magnonic systems. It should be noted that the eigenvalue of the nested Wilson loop, denoted as $\nu_y^{\nu_x^{\pm}}$, is obtained as a function of k_x as it corresponds Wannier centers along y-axis for each sector. The Wannier sector polarization along y-axis for each sector is given by

$$p_y^{\nu_x^{\pm}} = \frac{1}{2\pi} \int dk_x \sum_{p=1}^{M_w} \nu_y^{\nu_x^{\pm},p}(k_x) \bmod 1 \,, \tag{5.15}$$

where M_w is the number of Wannier bands that belong to a positive or negative sector of ν_x. Likewise, the Wannier sector polarization along x-axis is given by

$$p_x^{\nu_y^{\pm}} = \frac{1}{2\pi} \int dk_y \sum_{p=1}^{M_w} \nu_x^{\nu_y^{\pm},p}(k_y) \bmod 1 \,. \tag{5.16}$$

The symmetry constraint on the Wannier sector polarization is equivalent to the magnonic polarization. From Eqs. (E.30) and (E.31), we have

$$p_x^{\nu_y^{\pm}} \overset{C_{2y}\mathcal{T}}{=} -p_x^{\nu_y^{\pm}} \bmod 1, \tag{5.17}$$

$$p_y^{\nu_x^{\pm}} \overset{C_{2x}\mathcal{T}}{=} -p_y^{\nu_x^{\pm}} \bmod 1, \tag{5.18}$$

where $C_{2x/2y}$ represents a two-fold rotation about x/y-axis and $\mathcal{T}$ is the time-reversal symmetry. Hence, they are quantized to 0 or 1/2 in the presence of $C_{2y}\mathcal{T}/C_{2x}\mathcal{T}$ symmetry.

The top panel of Fig. 5.1(b) shows a schematic Wannier spectrum $\nu_y^{\nu_x^{\pm}}$ of a nested Wilson loop with quantized values under $C_{2x}\mathcal{T}$ symmetry, indicating the Wannier spectrum for a positive (negative) Wannier sector in red (blue). From Eq. (5.15), the Wannier sector polarization along y-axis are given as $p_y^{\nu_x^{\pm}} = \pm 1/2$. In the real space, it implies that two clouds of magnon density within the left-hand side and right-hand side of magnetic unit cell carries the opposite magnonic polarization, as illustrated in the bottom panel of Fig. 5.1(b). We should note that a nontrivial Wannier sector polarization in positive and negative Wannier sectors, which cancels out each other, is a signature of the magnonic quadrupole moment as discussed below.
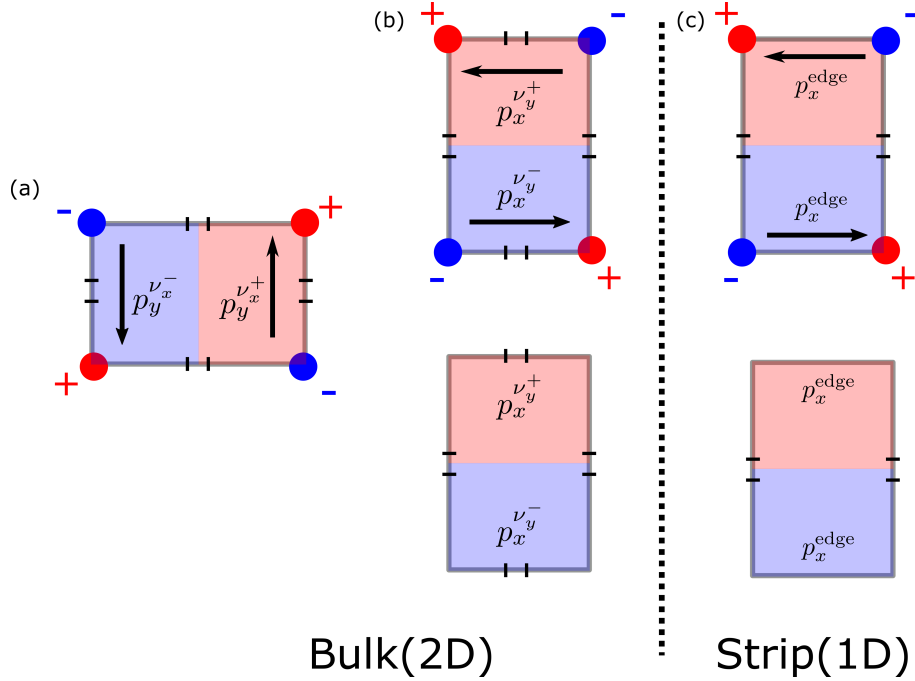
Figure 5.2: **Schematic illustration of relationship between Wannier sector polarization and edge polarizations.** (a) Wannier sector polarization $p_y^{\nu_x^\pm} = \pm 1/2$ for both top and bottom panels in (b) and (c). (b) Wannier sector polarization $p_x^{\nu_y^\pm} = \pm 1/2$ in the top panel and $p_x^{\nu_y^\pm} = 0$ in the bottom panel. (c) Edge polarization $p_x^{\text{edge}} = \pm 1/2$ in the top panel and $p_x^{\text{edge}} = 0$ in the bottom panel, obtained by opening the boundary parallel to x-axis in (b). In all panels, we add pairs of parallel lines to indicate periodic boundaries.

Analogously to magnonic polarizations, the magnonic Wannier sector polarization acts as a topological invariant for gapped Wannier spectra under protecting symmetries such as $C_{2x}\mathcal{T}$ and $C_{2y}\mathcal{T}$. To understand the consequence of bulk-boundary correspondence, we need to prepare a strip geometry. Treating it as a one-dimensional periodic system, we can compute the Wannier spectra as explained in Appendix E.3. While the study of Wannier spectra in strip geometry is shown in Section 5.4.1 for anitskyrmion crystals, we briefly summarize important points below. We should note that Ref. [80] contains a detailed account for electronic systems that is also relevant for magnonic systems.

When the magnonic Wannier sector polarization is quantized as $p_y^{\nu_x^\pm} = \pm 1/2$, the Wannier bands $\nu_x^\pm$ have nontrivial topology. In a strip geometry with boundaries periodic in x-axis and open in y-axis, the obtained Wannier spectrum ν_x contains bulk subbands as well as in-gap Wannier states with the quantized eigenvalues at $\nu_x = 0$ or $\nu_x = \pm 1/2$. Remarkably, these Wannier states are localized to edges of the strip, corresponding to Wannier edge states arising from the bulk-boundary correspondence. Furthermore, the eigenvalue of Wannier edge states ν_x is determined by $p_x^{\nu_y^\pm}$. With the nontrivial magnonic

Wannier sector polarization $p_x^{\nu_y^\pm} = \pm 1/2$, the eigenvalues of Wannier edge states are quantized as $\pm 1/2$. Consequently, it supports edge-localized magnonic polarizations with $p_x^{\mathrm{edge}} = \pm 1/2$, as defined in Eq. (E.22). This implies that edges of the strip is also topologically nontrivial. By introducing open boundaries along x-axis to make the strip into a fully finite system, the magnonic edge polarization induces a magnon bound state at each corner. This is the origin of magnonic corner states. In contrast, the magnonic Wannier sector polarization $p_x^{\nu_y^\pm} = 0$ leads to vanishing eigenvalues of Wannier edge states and $p_x^{\mathrm{edge}} = 0$. As a result, no magnonic corner state is obtained in the open boundary condition. This is illustrated schematically in Fig. 5.2.

In summary, the magnonic corner states are realized only when both $p_y^{\nu_x^\pm}$ and $p_x^{\nu_y^\pm}$ are quantized to be a nontrivial value. To diagnose this novel topological phase, we define a magnonic quadrupole moment analogously to the bulk quadrupole moment of electronic systems defined in Ref. [79, 80] as

$$q_{xy} = p_y^{\nu_x^+} p_x^{\nu_y^+} + p_y^{\nu_x^-} p_x^{\nu_y^-} . \tag{5.19}$$

From Eqs. (5.17) and (5.18), the magnonic quadrupole moment is quantized under $C_{2x}\mathcal{T}$ and $C_{2y}\mathcal{T}$ as

$$q_{xy} = \begin{cases} 0, & \text{if trivial} \\ \frac{1}{2}, & \text{if nontrivial.} \end{cases} \tag{5.20}$$

As demonstrated in Section 5.4 for antiskyrmion crystals, the bulk-boundary correspondence for magnonic quadrupole topological insulators is described as

$$|q_{xy}| = |p_x^{\mathrm{edge}}| = |p_y^{\mathrm{edge}}| = |Q_c| = \frac{1}{2} \bmod 1. \tag{5.21}$$

Although both p_x^{edge} and p_y^{edge} are nontrivial in magnonic quadrupole topological insulators, there exists only a single magnonic corner state at each corner. This is of fundamental importance originating from the higher order topology, which cannot be realized by a superposition of two magnonic analogue of SSH chains. In magnonic quadrupole topological insulators, magnonic corner states emerge as a simultaneous end state of two converging edges. This is analogous to the distinction between a corner charge induced by a pair of edge polarizations and a bulk quadrupole moment in classical electromagnetism (see Section 1.2.1).

Before ending this section, we note three necessary conditions for a well-defined magnonic quadrupole moment in the lowest M magnon bands, which are equivalent to electronic systems [80]. Firstly, we need more than one magnon band to construct a quadrupole moment ($M > 1$), implying that the possible lowest energy of magnonic corner states lies within the second bulk band gap. Secondly, the sum of Chern numbers below the M-th band gap must be zero. This is because a non-zero Chern number results in gapless Wannier spectra due to the Thouless charge pumping [302]. From Eq. (1.17), we obtain

$$C = \sum_{i=1}^{M} C_i = \frac{1}{2\pi} \int_{\mathrm{BZ}} \mathrm{tr}[\partial_{k_x} A_y(\boldsymbol{k})] = \int_0^{2\pi} dk_x \sum_{i=1}^{M} \partial_{k_x} \nu_y^i(k_x), \tag{5.22}$$
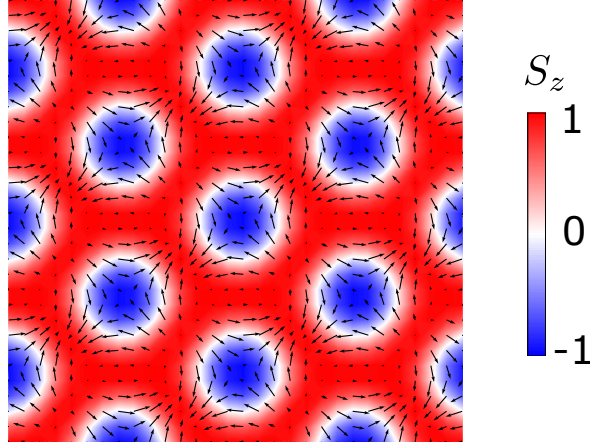
Figure 5.3: **Classical ground state spin textures of antiskyrmion crystals.** Magnetic textures obtained at $D/J = 1.0$, $h = g\mu_B B_z/(JS) = 0.3$, and $T = 0$ under the periodic boundary conditions. The system size is 30×30. The color code represents the out-of-plane spin component, while the in-plane magnetization is represented by black arrows.

where we take the gauge such that $\partial_{k_y} A_x(\boldsymbol{k}) = 0$ and C_i depicts the Chern number of i-th band. Thirdly, the magnonic polarization for the lowest M magnon bands must vanish.

5.2 Model

In this chapter, we consider a following two-dimensional spin lattice Hamiltonian as a minimal model for tetragonal Heusler compounds hosting antiskyrmions (see Section 2.4) [153]:

$$H \;=\; \tfrac{1}{2} \sum_{\langle \boldsymbol{r}, \boldsymbol{r}' \rangle} (-J_{\boldsymbol{r},\boldsymbol{r}'} \boldsymbol{S}_{\boldsymbol{r}} \cdot \boldsymbol{S}_{\boldsymbol{r}'} + \boldsymbol{D}_{\boldsymbol{r},\boldsymbol{r}'} \cdot \boldsymbol{S}_{\boldsymbol{r}} \times \boldsymbol{S}_{\boldsymbol{r}'}) - g\mu_B B_z \sum_{\boldsymbol{r}} \boldsymbol{S}_{\boldsymbol{r}} \cdot \hat{\boldsymbol{z}}\,, \qquad (5.23)$$

where $\boldsymbol{S}_{\boldsymbol{r}}$ is a spin operator at site $\boldsymbol{r}$ on a square lattice with lattice constant a. The nearest-neighbor coupling includes ferromagnetic exchange $J_{\boldsymbol{r},\boldsymbol{r}'} = J(\delta_{\boldsymbol{r}-\boldsymbol{r}',\pm a\hat{\boldsymbol{x}}} + \delta_{\boldsymbol{r}-\boldsymbol{r}',\pm a\hat{\boldsymbol{y}}})$ with $J > 0$, and Dzyaloshinskii-Moriya interaction $\boldsymbol{D}_{\boldsymbol{r},\boldsymbol{r}'} = D(\mp\hat{\boldsymbol{x}}\delta_{\boldsymbol{r}-\boldsymbol{r}',\pm a\hat{\boldsymbol{x}}} \pm \hat{\boldsymbol{y}}\delta_{\boldsymbol{r}-\boldsymbol{r}',\pm a\hat{\boldsymbol{y}}})$ consistent with D_{2d} crystal symmetry as shown in Section 2.1. Throughout this chapter, we take $D/J = 1.0$ unless stated otherwise. Our result can be rescaled for smaller D/J ratios as discussed in Section 3.4. Compared to the cubic chiral magnets such as B20 alloys, the Dzyaloshinskii-Moriya interaction is anisotropic with opposite signs along x and y axes. The last term represents the coupling to the external magnetic field, $B_z\hat{\boldsymbol{z}}$, where g and μ_B denote the g-factor and Bohr magneton, respectively.

Depending on the external magnetic field, this model hosts three distinct magnetic phases: helical phase; antiskyrmion crystal phase; ferromagnetic phase. Using the Monte

Carlo simulated annealing [166] and minimizing the energy further by solving the Landau-Lifshitz-Gilbert equations, a triangular crystal of antiskyrmions is obtained for $0.27 \leq g\mu_B B_z/(JS) \leq 0.7$ at $D/J = 1.0$. The magnetic configuration of antiskyrmion crystals is shown in Fig. 5.3. The in-plane magnetization rotates in a counterclockwise manner during a rotation around the core of antiskyrmions in a clockwise manner, implying the opposite topological charge of antiskrymions compared to skyrmions.

Here, we comment a difference from Chapter 3 where the underlying spin lattice is chosen to be a triangular lattice. In the continuum limit, it is obvious that the free energy functional for triangular and square lattices become the same. Only the difference is that the magnetic field is scaled by a factor of 2/3 in the square lattice compared to the triangular lattice, because the number of the nearest neighbors is different (see Appendix A.5). Similarly, Chern numbers of magnon bands are identical in both lattice systems. However, the choice of lattice system becomes relevant for higher-order topological phases as they are protected by crystalline symmetries such as rotations and reflections combined with time-reversal symmetry. From the crystal structure of tetragonal Heusler compounds, we choose a square spin lattice in this chapter.

5.3   Main result

5.3.1   Magnonic quadrupole moment in antiskyrmion crystals

In this section, we discuss the magnon band structure of antiskyrmion crystals and show that they support a nontrivial magnonic quadrupole moment for the lowest four magnon bands. The magnetic unit cell of antiskyrmion crystals that is commensurate with the square lattice is shown in Fig. 5.4(a), which contains two antiskyrmions. There are three important symmetries in this magnetic unit cell: C_{2z}, twofold rotation about the z-axis; $C_{2x}\mathcal{T}$, twofold rotation about the x-axis together with time reversal; $C_{2y}\mathcal{T}$, twofold rotation about the y-axis together with time reversal. Each symmetry operation is defined by the Cartesian axes with the origin taken at the center of the magnetic unit cell as depicted in Fig. 5.4(a).

The spin wave Hamiltonian for Eq. (5.23) is obtained in Section 1.1.3 by substituting the expression for the Dzyaloshinskii-Moriya interaction allowed by D_{2d} symmetry. The bottom panel of Fig. 5.4(a) shows the magnon spectrum at $g\mu_B B_z/(JS) = 0.35$. Since we have chosen the enlarged magnetic unit cell with two antiskyrmions inside, the number of bands is doubled compared to the triangular lattice discussed in Section 3.2. In addition, there is a double degeneracy along boundaries of the first Brillouin zone, XM and MX'. The double degeneracy is in fact protected by $C_{2x/2y}\mathcal{T}$ symmetries, which respectively transforms the spin wave Hamiltonian $H_{\boldsymbol{k}}$ as

$$\hat{C}_{2x} K H_{(k_x,k_y)} K \hat{C}_{2x}^{\dagger} = H_{(-k_x,k_y)} \,,$$
$$\hat{C}_{2y} K H_{(k_x,k_y)} K \hat{C}_{2y}^{\dagger} = H_{(k_x,-k_y)} \,, \tag{5.24}$$
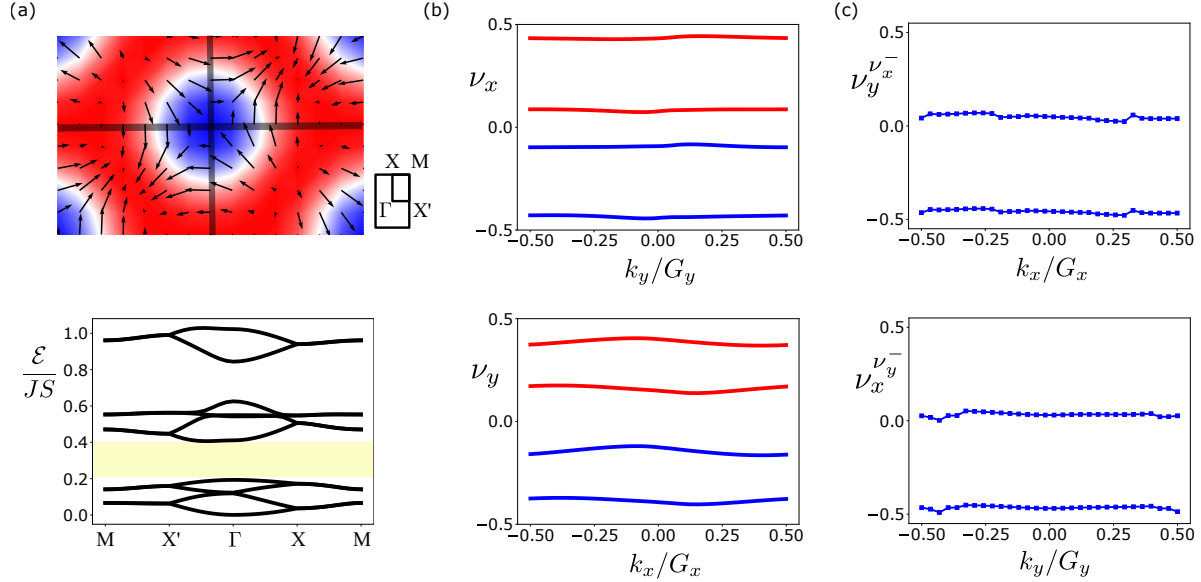
Figure 5.4: **Symmetries of the magnetic unit cell and Wannier spectra of anti-skyrmion crystals.** (a) Top: magnetic unit cell of the antiskyrmion crystals together with the first Brillouin zone. The symmetry axes are defined from the center of magnetic unit cell, showing symmetry lines for C_{2x} and C_{2y} by black lines. Bottom: bulk magnon band structures for the lowest ten bands. The fourth bulk band gap is indicated by a yellow shaded region. (b) Wannier spectrum of the four lowest energy magnon bands along x (top panel) and y (bottom panel) axis, respectively. Positive Wannier sectors $\nu_{x/y}^+$ is shown in red, while negative Wannier sectors $\nu_{x/y}^-$ are shown in blue. (c) Wannier centers of the negative Wannier sectors $\nu_{x/y}^-$ along y/x axes. All panels are obtained at $h = g\mu_B B_z/(JS) = 0.35$. The reciprocal lattice vector is represented by $G_{x/y} = 2\pi/(L_{x/y}a)$ with $L_{x/y}$ denoting the size of magnetic unit cell along the x/y axis. Adapted from [212].

where K is the complex conjugation operator and $\hat{C}_{2x/2y}$ is the unitary operator for $C_{2x/2y}$ symmetry.

Now, we consider the magnonic quadrupole moment in antiskyrmion crystals. As discussed in Section 5.1.3, the quadrupole moment is quantized by the combined action of $C_{2x}\mathcal{T}$ and $C_{2y}\mathcal{T}$ symmetries. Employing the nested Wilson loop calculation (see Appendix E.2), we show that the lowest four bulk magnon bands below the highlighted band gap in Fig 5.4(a) carries the nontrivial magnonic quadrupole moment in the following.

In order for magnonic quadrupole moments to be well-defined, there are three important requirements to be fulfilled (see Section 5.1.3): (1) the number of magnon bands below the band gap is greater than one; (2) the total Chern number below the band gap is zero so that it is insulating in both bulk and edge; (3) the magnonic polarization vanishes. The first condition is satisfied for the four lowest magnon bands. Also, the Chern number of the four lowest magnon bands is always zero in the ferromagnetic

skyrmion/antiskyrmion crystals as shown in Fig. 3.3(d). From Eqs. (5.11) and (5.12), the magnonic polarization is given as

$$p_x = \frac{1}{2\pi} \int dk_y \sum_{j=1}^{M} \nu_x^j(k_y) \bmod 1 \,, \tag{5.25}$$

$$p_y = \frac{1}{2\pi} \int dk_x \sum_{j=1}^{M} \nu_y^j(k_x) \bmod 1 \,, \tag{5.26}$$

where $M = 4$ is the number of bulk bands below the gap and $\nu_{x/y}$ is the Wannier centers along x/y axis. Furthermore, $C_{2x/2y}\mathcal{T}$ symmetries give a constraint to the Wannier spectra as (see Appendix E.4)

$$\nu_x^j(k_y) \stackrel{C_{2y}\mathcal{T}}{=\!=} -\nu_x^j(-k_y) \bmod 1 \,, \tag{5.27}$$

$$\nu_y^j(k_x) \stackrel{C_{2x}\mathcal{T}}{=\!=} -\nu_y^j(-k_x) \bmod 1 \,, \tag{5.28}$$

allowing either a flat band at $\nu_x(k_y) = 0, \frac{1}{2}$ or a pair of eigenvalues $\nu_x^1(k_y) = -\nu_x^2(-k_y)$. Similar values are allowed for $\nu_y(k_x)$. Figure 5.4(b) shows the Wannier spectra of the lowest four magnon bands, consisting of pairs of eigenvalues with opposite signs. Therefore, the magnonic polarization is canceled out, i.e., $(p_x, p_y) = (0, 0)$.

With the three conditions satisfied, we compute the magnonic quadrupole moment carried by the lowest four magnon bands. From the gapped Wannier spectra in Figure 5.4(b), we define two Wannier sectors below and above a gap at $\nu_{x/y} = 0$. In the real space, it corresponds to projection to the subspace of occupied states localized to the positive (red) and negative (blue) directions in x/y axes from the center of magnetic unit cell, which is denoted as $\nu_{x/y}^+$ and $\nu_{x/y}^-$, respectively. The nested Wilson loop is constructed within these subspace to calculate polarization in the orthogonal directions for each Wannier sector as explained in Appendix E.2. Figure 5.4(c) shows the Wannier centers of Wannier sectors ν_x^- and ν_y^-. Similarly to Wannier centers of occupied states, Wannier centers of a Wannier sector are also constrained by $C_{2x}\mathcal{T}$ and $C_{2y}\mathcal{T}$ as shown in Eqs. (E.30) and (E.31). Within numerical errors, we obtain two flat bands quantized at 0 and $-\frac{1}{2}$ for both $\nu_y^{\nu_x^-}(k_x)$ and $\nu_x^{\nu_y^-}(k_y)$. Since the C_{2z} symmetry relates Wannier centers of different Wannier sectors from Eqs. (E.32) and (E.33), the magnonic quadrupole moment is obtained as

$$q_{xy} = p_y^{\nu_x^-} p_x^{\nu_y^-} = \frac{1}{2} \,. \tag{5.29}$$

with the Wannier sector polarization given as

$$p_y^{\nu_x^\pm} = \frac{1}{2\pi} \int dk_x \sum_{p=1}^{2} \nu_y^{\nu_x^\pm, p}(k_x) \bmod 1 = \frac{1}{2} \,, \tag{5.30}$$

$$p_x^{\nu_y^\pm} = \frac{1}{2\pi} \int dk_y \sum_{p=1}^{2} \nu_x^{\nu_y^\pm, p}(k_y) \bmod 1 = \frac{1}{2} \,. \tag{5.31}$$

Importantly, the magnonic quadrupole moment is always nontrivial for the lowest four bulk bands in the range of magnetic fields where the antiskyrmion crystal is stable. Furthermore, the nontrivial magnonic quadrupole moment remains intact for $D/J <$ 1.0, because the equivalent band structure is obtained with energy scaled by $(D/J)^2$ as expected from the continuum model (see Section 3.4). In the following sections, we investigate the bulk-boundary correspondence in the magnonic quadrupole topological insulators supported by antiskyrmion crystals.

5.3.2 Fractional antiskyrmions and Magnonic corner states

In this section, we study the classical ground-state spin textures in a finite system and their magnon spectrum for the search of magnonic corner states arising from the nontrivial magnonic quadrupole moment. In Section 1.3.4, we have introduced the local instability of ferromagnetic phase against creation of helical domains, which was predicted to occur at edges of thin film samples in chiral magnets due to the Dzyaloshinskii-Moriya interaction [105]. A similar critical behavior occurs in D_{2d} symmetric systems, as shown below. Since antiskyrmion crystals are thermodynamically stable at the critical magnetic field of the edge instability, the formation of helical domains leads to repulsive interactions between them. As a result, they are confined to edges with a fractional topological charge, termed as *fractional antiskyrmions*. We show that the formation of fractional antiskyrmions is essential to realize magnonic corner states in the following.

Before discussing the ground state magnetic textures in confined systems, we evaluate the critical magnetic fields for the edge instability in the spin lattice model of Eq. (5.23), in order to compare with $h_c = g\mu_B B_z J/(D^2 S) = 0.4067$ obtained in the continuum limit [105] (see Appendix A.7.2). Solving the Landau-Lifshitz-Gilbert (LLG) equation (see Appendix A.6), we compute the time evolution of 50×50 spins in a strip geometry periodic along x-axis and open along y-axis. The initial state is a field-polarized phase prepared by Monte Carlo simulated annealing at $h = 1.0$. The critical magnetic field is then estimated by lowering the magnetic field until we find a growth of helical domains from small seeds of negative polarized spins near the edge. In Table 5.1, the numerical results are summarized for different D/J ratios. Consistent with Ref. [105], the critical value is found to be $h \approx 0.41$ regardless of the strength of Dzyaloshinskii-Moriya interaction. Hence, we fix the ratio $D/J = 1.0$ without loss of generality in the following sections.

D/J	1.0	0.9	0.7	0.5	0.3
h_c	0.403	0.405	0.413	0.417	0.409

Table 5.1: **The estimated values of the critical magnetic field for the edge instability at various D/J ratios.** This is estimated by the LLG simulation of one-dimensional systems consisting of 50×50 spins with the periodic boundary condition along x axis. Below the critical magnetic fields, a small seed of negatively polarized spins along edges grows into helical domains. Adapted from [212].
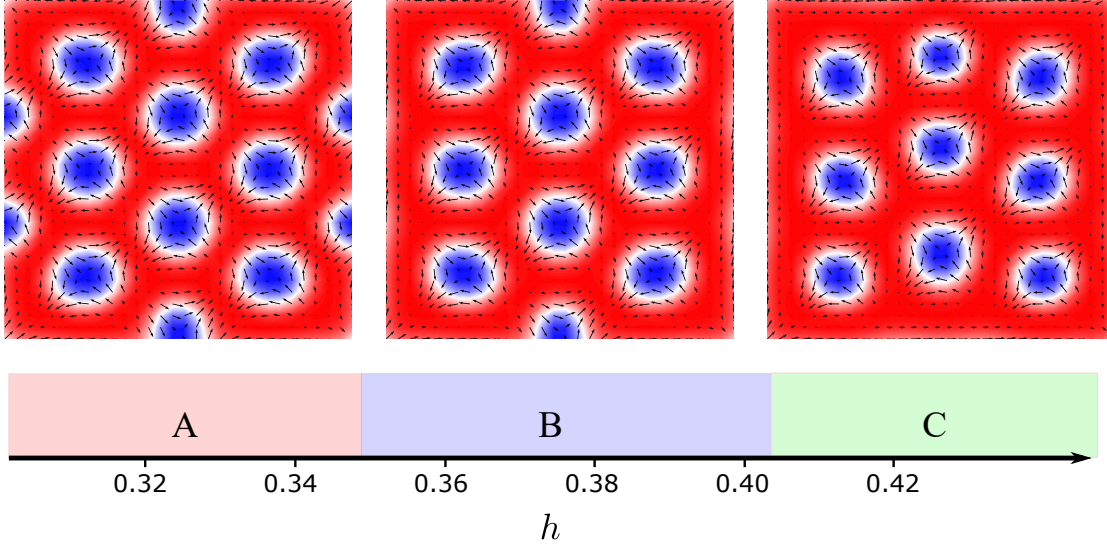
Figure 5.5: **Fractional antiskyrmions stabilized below the critical magnetic fields in a finite system.** Three magnetic configurations are stabilized as a function of magnetic fields $h = g\mu_B B_z/(JS)$ at $D/J = 1.0$. The boundaries between them are determined by comparing the total energy of each configuration.

After confirming the edge instability for antiskyrmion systems, we proceed to investigate the classical ground state spin textures of finite-sized samples. A finite system of 30×30 spins is relaxed to the classical ground state at $T = 0$ by Monte Carlo simulated annealing and solving the Landau-Lifshitz-Gilbert equation. Near the critical magnetic field for the edge instability h_c, we have identified three different configurations as shown in Fig. 5.5. Above h_c, twisted magnetizations along edges are observed in configuration C. As magnetic field is lowered below the critical value, fractional antiskyrmions are progressively stabilized along edges of a sample. Below $h \approx 0.35$, fractional antiskyrmions are obtained on all edges in configuration A. We should note that the total topological charge of a finite sample is not quantized to be integers, and the topological charge of fractional antiskyrmions is not necessarily equal to $\frac{1}{2}$ like merons. Using Eq. (1.58), we estimate the fractional topological charge of objects localized on the vertical edges as $Q \sim 0.44$ and on the horizontal edges as $Q \sim 0.47$ in configuration A.

The magnon spectrum of finite samples is computed analogously to periodic systems. Given a finite system with N total spins, a new local orthogonal basis is introduced as (e_r^1, e_r^2, m_r), where m_r is parallel to the ground-state spin texture and $e_r^1 \times e_r^2 = m_r$. Employing the Holstein-Primakoff transformation [72], the spin operators with respect to the new basis is given by $\mathsf{S}_r^+ = (2S - a_r^\dagger a_r)^{\frac{1}{2}} a_r$, $\mathsf{S}_r^- = a_r^\dagger (2S - a_r^\dagger a_r)^{\frac{1}{2}}$, and $\mathsf{S}_r^3 = S - a_r^\dagger a_r$, where $\mathsf{S}_r^\pm = \mathsf{S}_r^1 \pm i\mathsf{S}_r^2$, and a_r, $a_r^\dagger$ are the bosonic operators. The quadratic magnon
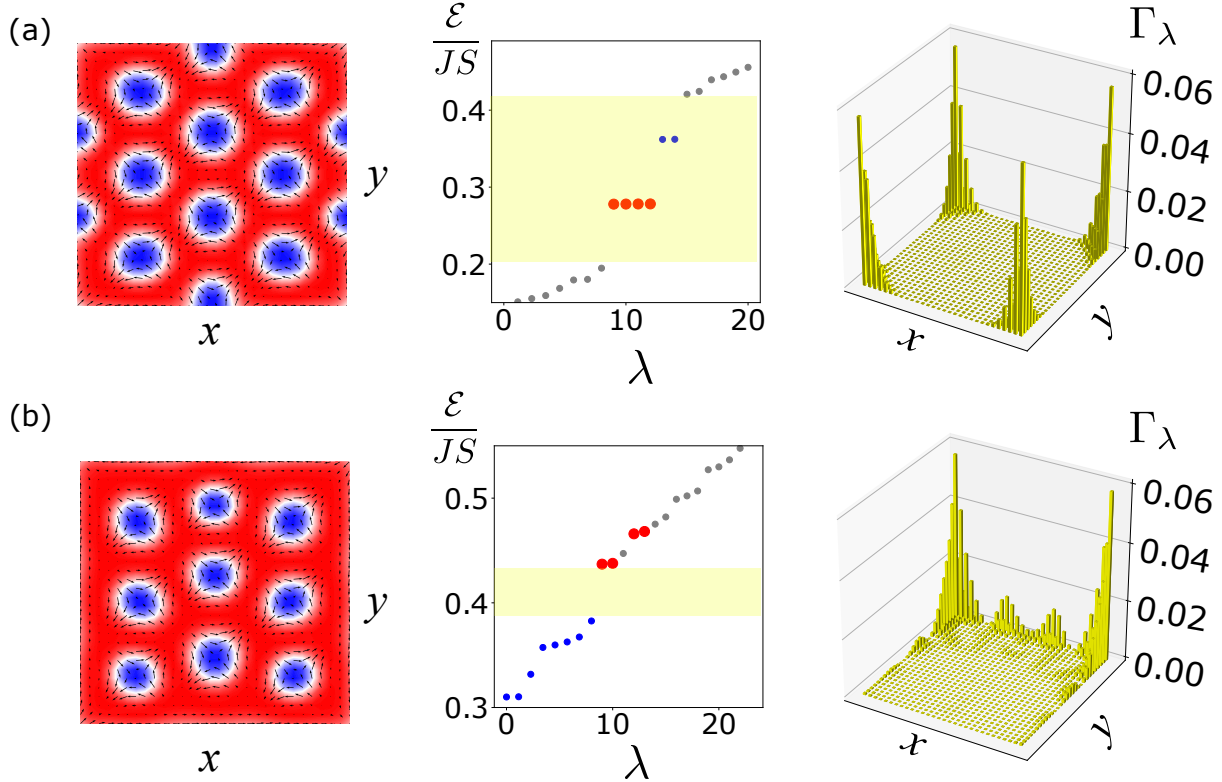
Figure 5.6: **Magnonic corner states in confined antiskyrmion crystals.** (a)-(b) Magnon excitations in (a) configuration A at $h = 0.3$ and (b) configuration C at $h = 0.42$, respectively. Left: magnetic textures of the classical ground state. Middle: magnon spectrum near the fourth bulk band gap (yellow squares). Right: probability density of corner states, Γ_λ defined in Eq. (5.36). Bulk modes are represented by gray, while corner states and trivial edge localized modes are highlighted by red and blue, respectively. Adapted from [212].

Hamiltonian is then derived as

$$H_{\text{sw}} = \frac{S}{2} \sum_{\boldsymbol{r}, \boldsymbol{r}'} \psi_{\boldsymbol{r}}^\dagger H_{\boldsymbol{r}, \boldsymbol{r}'} \psi_{\boldsymbol{r}'} + \mathcal{E}_0 \,, \tag{5.32}$$

where $\psi_{\boldsymbol{r}} = (a_{\boldsymbol{r}}, a_{\boldsymbol{r}}^\dagger)^T$, $\mathcal{E}_0 = -\frac{1}{2} S^2 \sum_{\boldsymbol{r}} \Lambda_{\boldsymbol{r}}$ and

$$H_{\boldsymbol{r}, \boldsymbol{r}'} = \begin{pmatrix} \Omega_{\boldsymbol{r}, \boldsymbol{r}'} & \Delta_{\boldsymbol{r}, \boldsymbol{r}'} \\ \Delta_{\boldsymbol{r}, \boldsymbol{r}'}^* & \Omega_{\boldsymbol{r}, \boldsymbol{r}'}^* \end{pmatrix} \,. \tag{5.33}$$

Each expression is a $N \times N$ matrix, and given by $\Omega_{\boldsymbol{r}, \boldsymbol{r}'} = \delta_{\boldsymbol{r}, \boldsymbol{r}'} \Lambda_{\boldsymbol{r}} + \frac{1}{2}[-J_{\boldsymbol{r}, \boldsymbol{r}'} \boldsymbol{e}_{\boldsymbol{r}}^+ \cdot \boldsymbol{e}_{\boldsymbol{r}'}^- + \boldsymbol{D}_{\boldsymbol{r}, \boldsymbol{r}'} \cdot \boldsymbol{e}_{\boldsymbol{r}}^+ \times \boldsymbol{e}_{\boldsymbol{r}'}^-]$, $\Delta_{\boldsymbol{r}, \boldsymbol{r}'} = \frac{1}{2}[-J_{\boldsymbol{r}, \boldsymbol{r}'} \boldsymbol{e}_{\boldsymbol{r}}^+ \cdot \boldsymbol{e}_{\boldsymbol{r}'}^+ + \boldsymbol{D}_{\boldsymbol{r}, \boldsymbol{r}'} \cdot \boldsymbol{e}_{\boldsymbol{r}}^+ \times \boldsymbol{e}_{\boldsymbol{r}'}^+]$, and $\Lambda_{\boldsymbol{r}} = \sum_{\boldsymbol{r}'}[J_{\boldsymbol{r}, \boldsymbol{r}'} \boldsymbol{m}_{\boldsymbol{r}} \cdot \boldsymbol{m}_{\boldsymbol{r}'} - \boldsymbol{D}_{\boldsymbol{r}, \boldsymbol{r}'} \cdot \boldsymbol{m}_{\boldsymbol{r}} \times \boldsymbol{m}_{\boldsymbol{r}'}] + \frac{g \mu_B B_z}{S} \hat{\boldsymbol{z}} \cdot \boldsymbol{m}_{\boldsymbol{r}}$, with $\boldsymbol{e}_{\boldsymbol{r}}^\pm = \boldsymbol{e}_{\boldsymbol{r}}^1 \pm i \boldsymbol{e}_{\boldsymbol{r}}^2$.

Using a paraunitary matrix

$$T_{\boldsymbol{r}} = \begin{pmatrix} U_{\boldsymbol{r}} & V_{\boldsymbol{r}}^* \\ V_{\boldsymbol{r}} & U_{\boldsymbol{r}}^* \end{pmatrix} \,, \tag{5.34}$$
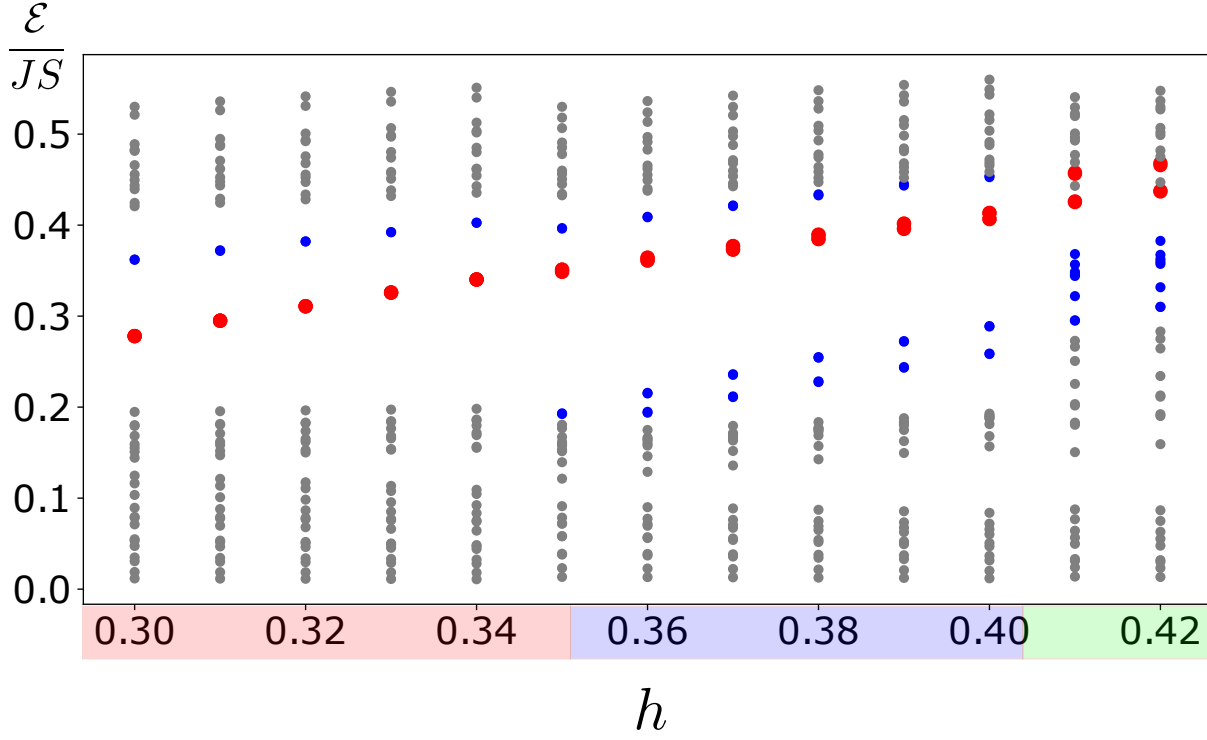
Figure 5.7: **Magnon spectrum as a function of applied magnetic fields.** Magnetic field dependence of magnon spectrum is plotted with the bottom colorbar indicating the corresponding spin configuration in Fig. 5.5. Bulk modes are represented by gray, while corner states and trivial edge localized modes are highlighted by red and blue, respectively. Adapted from [212].

the spin wave Hamiltonian is diagonalized as

$$H_{\mathrm{sw}} = S \sum_{\lambda} \mathcal{E}_{\lambda}\big(\alpha_{\lambda}^{\dagger}\alpha_{\lambda} + \tfrac{1}{2}\big) + \mathcal{E}_0 \,, \tag{5.35}$$

where λ is the index for each magnon mode, $\mathcal{E}_{\lambda}$ is the corresponding eigenvalue, and $(a_{\boldsymbol{r}}, a_{\boldsymbol{r}}^{\dagger})^T = T_{\boldsymbol{r}}(\alpha_{\lambda}, \alpha_{\lambda}^{\dagger})^T$. The spatial distribution of the λ-th magnon mode is characterized by

$$\Gamma_{\lambda}(\boldsymbol{r}) = |\langle GS| a_{\boldsymbol{r}} \alpha_{\lambda}^{\dagger} |GS\rangle|^2 = |U_{\boldsymbol{r}\lambda}|^2 \,, \tag{5.36}$$

where $|GS\rangle$ is the vacuum state of magnons, i.e., $\alpha_{\lambda} |GS\rangle = 0$.

Figure 5.6(a) shows the magnon spectrum of configuration A, where we find four degenerate states (red) inside the fourth bulk band gap. They correspond to corner states, one for each corner of the sample as indicated by the probability density Γ_{λ}, which originates from the nontrivial magnonic quadrupole moment of the lowest four bands. There also exists trivial bound states localized to fractional antiskyrmions on top and bottom edges (blue). On the other hand, for configuration C in Fig. 5.6(b), these four
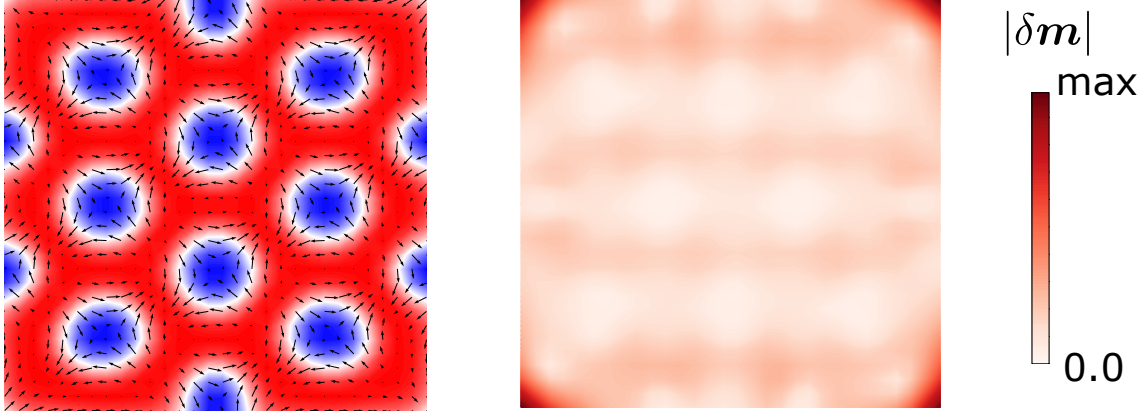
Figure 5.8: **Magnonic corner states excited by an in-plane AC magnetic field.** Left: configuration A at $h = 0.3$. Right: amplitude of oscillations of spins under an in-plane AC magnetic field at resonance with corner states, defined in Eq. (5.37). The phenomenological damping constant is fixed at $\alpha = 0.04$. Adapted from [212].

degenerate corner states are split into a pair of doubly degenerate states (red). They are buried among bulk modes with nonzero overlaps. As a result, their probability density is no longer exponentially localized to corners. Another point is that trivial edge modes localized to the edge magnetization (blue) are obtained, as predicted in Ref. [105] (see Appendix A.7.2).

In order to demonstrate the relationship between fractional antiskyrmions and magnonic corner states, we plot the magnon spectrum as a function of the applied magnetic field in Figure 5.7. When fractional antiskyrmions are stabilized below the critical magnetic field h_c, magnonic corner states emerge inside the fourth band gap. In this regime, the energy of corner states is linearly proportional to the magnetic field. On the other hand, the in-gap corner states are absorbed into bulk bands above h_c.

We should emphasize that the absence of corner states above h_c is not due to the topological phase transition of bulk bands. Even though the magnonic quadrupole moment remains nontrivial, the bulk-boundary correspondence for higher-order topological phases requires the protecting symmetries, namely $C_{2x}\mathcal{T}$ and $C_{2y}\mathcal{T}$, to be preserved in the presence of boundaries. Remarkably, the self-assembly of fractional antiskymions restore the symmetries of magnetic unit cells even in a confined system. This is clearly illustrated in configuration A of Fig. 5.5. In contrast, the arrangement of antiskyrmion lattices is distorted inside the bulk of sample in configuration C, because antiskyrmions are repelled from edges above the critical magnetic field. Therefore, magnonic corner states are realized only in configuration A and B that conserve symmetries protecting the magnonic quadrupole moment.

For experimental observations, the magnonic corner states can be excited by spatially

uniform AC magnetic fields. This is illustrated by the Landau-Lifshitz-Gilbert simulation (see Appendix A.6). To selectively excite a magnon mode, the frequency of the AC magnetic field should be at resonance with the energy of the corresponding state. From Fig. 5.7, the energies of the corner states are found to be approximately at $\mathcal{E}/(JS) \approx h$. Taking the initial states as configuration A at $h = 0.3$, the in-plane magnetic field $\boldsymbol{B}_\parallel(t) = B_0 \cos(\omega t)\hat{\boldsymbol{x}}$ is applied with frequency $\hbar\omega/(JS) = 0.3$ and amplitude $g\mu_B B_0/(JS) = 0.01$. Naively speaking, the amplitude of spin precession is proportional to the magnon number of corresponding eigenstates, which is defined as

$$|\delta\boldsymbol{m_r}| = \left[\sum_{i=1}^{3}(\max_t\{m_{\boldsymbol{r}}^i(t)\} - \min_t\{m_{\boldsymbol{r}}^i(t)\})^2\right]^{1/2}, \qquad (5.37)$$

with $\max_t$ and $\min_t$ evaluated in the interval $[t_0, t_0 + T]$, i.e., over one period T of the AC magnetic field after a long time $t_0 = 10^4$, to ensure that the system has reached a steady state. Figure 5.8 plots the amplitude of oscillations of spins $|\delta\boldsymbol{m_r}|$ at each site, clearly showing large oscillation amplitudes at the corners of the sample. We note that an out-of-plane AC magnetic field can also excite the magnonic corner states.

5.4   Bulk-boundary correspondence

The hallmark signatures of a nontrivial quadrupole moment are fractional edge dipole moments and fractional corner charges as shown for electronic systems in Section 1.2.4 [79, 80]. Analogously to classical electromagnetism, they are related by

$$|q_{xy}| = |p_x^{\text{edge}}| = |p_y^{\text{edge}}| = |Q_c| = \frac{1}{2} \text{ mod } 1. \qquad (5.38)$$

In this section, we illustrate that fractional boundary signatures are also realized in the magnonic quadrupole topological insulator.

5.4.1   Magnonic edge polarization

In this section, the magnonic edge polarization is calculated in a strip geometry with open boundaries along one direction and periodic boundaries in the other direction, as described in Appendix E.3. Similarly to the calculation of magnonic polarizations, we construct the Wilson loop out of the lowest four bulk subbands along the periodic direction. While the total magnonic polarization of the strip should be the same as the magnonic polarization of the bulk sample, it is possible to have polarizations localized to edges that cancel out each other.

Importantly, the magnonic edge polarization can be interpreted as a topological invariant for one-dimensional systems in a strip geometry, characterized by topologically protected Wannier edge states as discussed in Section 5.1.3. In higher-order topological phases, topologically protected boundary modes are often hindered by the broken symmetries near boundaries. Using the magnonic edge polarization, we compare the topological
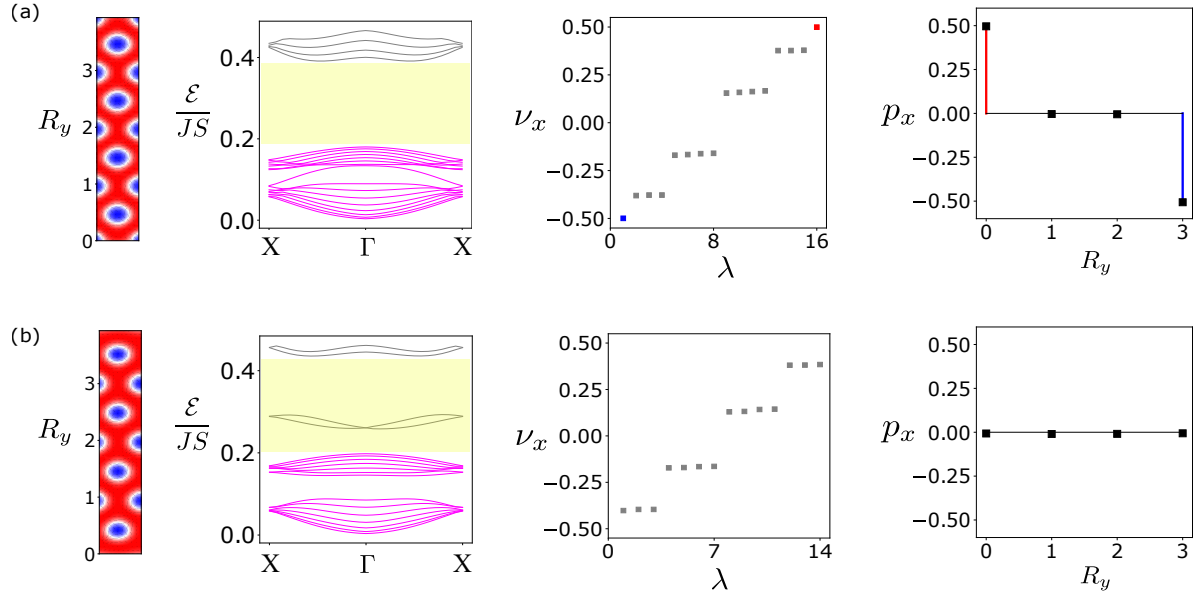
Figure 5.9: **Magnonic edge polarization in a strip geometry.** Wilson loop calculation of one-dimensional systems (a) below ($h = 0.3$) and (b) above ($h = 0.41$) the edge instability. Column 1: classical ground state spin textures with the periodic boundary condition along the x axis and the open boundary condition along the y axis (10×60 sites). It contains four magnetic unit cells in the confined direction with their positions depicted on the vertical axis. Column 2: edge magnon spectrum with bands below the fourth bulk band gap (yellow squares) indicated by magenta. Column 3: Wannier spectrum ν_x showing four bulk bands (gray) and edge localized Wannier states (red and blue), where λ is the band index. Column 4: polarization $p_x(R_y)$ with R_y labeling the position of unit cells as shown in (a). $p_x(R_y)$ is defined in Eq. (E.22). Adapted from [212].

properties of the strip sample above and below the critical magnetic field h_c, and show the topological phase transition caused by the edge instability. Our result is summarized in Figure 5.9.

For the computation of edge polarizations, we prepare antiskyrmion crystals in a strip geometry that is periodic only along the x axis. Choosing a system size to be compatible with the size of the magnetic unit cell in the bulk, we obtain the magnetic unit cell of the strip containing four of the bulk magnetic unit cells along the y axis. Only below the critical magnetic field h_c, fractional antiskyrmions are stabilized on the top and bottom edges as shown in the leftmost panels of Fig 5.9(a). We should note that those along vertical boundaries are connected across periodic boundaries, so they are not fractional antiskyrmions. The Wilson loop is constructed from the group of bands corresponding to the lowest four magnon bands (magenta) in the edge spectrum of Fig 5.9. Above h_c, additional in-gap states appear inside the fourth bulk band gap (yellow squares) that correspond to trivial edge states.

The obtained Wannier spectra for both cases show four bulk bands (gray) with oppo-
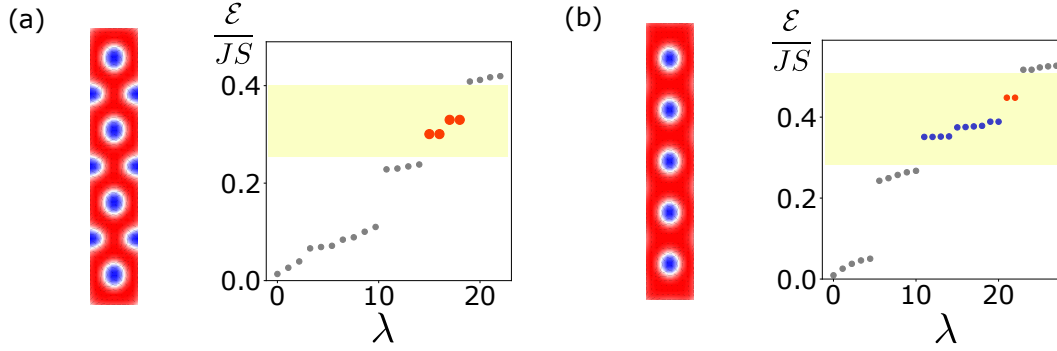
Figure 5.10: **Corner states induced by magnonic edge polarization.** (a)-(b) Magnon spectrum of the finite samples obtained from Fig. 5.9 with the same parameters but connecting boundaries along the y axis. Left: classical ground state spin textures. Right: magnon spectrum showing corner states (red) and edge states (blue). Adapted from [212].

site signs so that the bulk polarizations vanish. The important difference arises from the two additional modes with quantized Wannier centers $\nu_x = \pm\frac{1}{2}$ (red and blue), which is found only below h_c. Remarkably, the corresponding hybrid Wannier functions for these modes are localized at the core of fractional antiskyrmions along edges of the strip. Using Eq. (E.22), we obtain the edge polarization below h_c with opposite values at opposite edges: $-\frac{1}{2}/\frac{1}{2}$ at the top/bottom edge (red and blue). In contrast, the edge polarization vanishes above the edge instability as fractional antiskyrmions that support Wannier edge states are no longer stable. We also confirmed that $p_y(R_x)$ shows a similar behavior above and below the critical field.

In Figure 5.9, we have demonstrated that the topological phase transition in the strip geometry occurs as fractional antiskyrmions become unstable above h_c. For further confirmation, we show that a quantized magnonic edge polarization translates into magnonic corner states by turning the strip geometry unit cell into a fully finite system with open boundary conditions as depicted in Fig. 5.10(a). In contrast for $h > h_c$, Figure 5.10(b) shows trivial corner states that are twofold degenerate and merge with bulk bands at higher magnetic fields.

The magnonic edge polarization is originated from the Wannier edge states with quantized Wannier centers $\nu_x = \pm\frac{1}{2}$. Since Wannier centers are eigenvalues of the position operator (see Appendix D.3), they depend on the choice of the magnetic unit cell [303]. This is demonstrated in Fig. 5.11, showing the Wannier spectrum and polarization of a strip magnetic unit cell shifted by half the lattice vector with respect to the one shown in Fig. 5.10(a). In this new configuration, fractional antiskyrmions are located in the center of edges. Hence, the Wannier centers of edge states are shifted from $\frac{1}{2}$ to 0, resulting in vanishing edge polarizations. This implies that it would not host magnonic corner states if boundaries orthogonal to the x-axis were introduced in this configuration. However, this choice of magnetic unit cell is energetically less favorable, so the quantized edge polarization is expected in the thermodynamic limit, satisfying the bulk-boundary
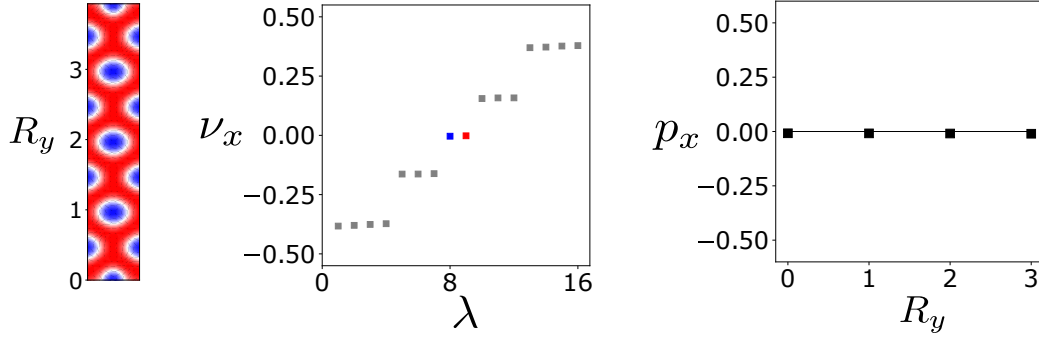
Figure 5.11: **Magnonic edge polarization defined in a different choice of magnetic unit cells.** Left: magnetic unit cell in Fig. 5.9(a) is shifted by the half lattice vector. Middle: Wannier spectrum ν_x showing four bulk bands (gray) and edge localized Wannier states (red and blue) with quantized Wannier centers at zero. Right: polarization $p_x(R_y)$ with R_y labeling the position of unit cells. Adapted from [212].

correspondence. We should note that a local configuration equivalent to Fig. 5.11 can be realized due to finite size effects as shown in Section 5.5.1.

5.4.2 Fractional corner "charge"

Unlike electrons, magnons carry no electric charge. Nevertheless, the magnonic quadrupole moment results in a fractional magnon density at corners of finite samples. Here, we introduce the magnon corner "charge" analogously to the boundary charge in one-dimensional electronic systems, which is defined as the difference between the charge near the boundary and the background charge from the bulk states [13, 14, 304–308].

Let us consider a finite system that contains $N_x \times N_y$ magnetic unit cells. The magnon density carried by the lowest M bulk magnon bands of the antiskyrmion crystal is given by

$$\rho(\boldsymbol{r}) = \sum_{n=1}^{N_x \times N_y \times M} \langle u_{\boldsymbol{r}}^n | u_{\boldsymbol{r}}^n \rangle_{\text{para}} , \qquad (5.39)$$

where $\langle u_{\boldsymbol{r}}^n | u_{\boldsymbol{r}}^n \rangle_{\text{para}}$ is the magnon density of the n-th magnonic wave function at site $\boldsymbol{r}$ on this finite system. The dot product is evaluated with a paraunitary matrix as defined in Eq. (5.2). The corresponding bulk-like magnon density is computed from an auxiliary periodic system obtained by connecting the edges orthogonal to one of the axes of the finite sample. It is defined as

$$\rho_i(\boldsymbol{r}) = \sum_{n=1}^{N_x \times N_y \times M} \langle u_{\boldsymbol{r},i}^n | u_{\boldsymbol{r},i}^n \rangle_{\text{para}} , \qquad (5.40)$$

where $|u_{\boldsymbol{r},i}^n\rangle$ is the n-th magnonic wave function of the auxiliary system, evaluated at the Γ point, with the periodic condition along x axis for $i = 1$ and y axis for $i = 2$.
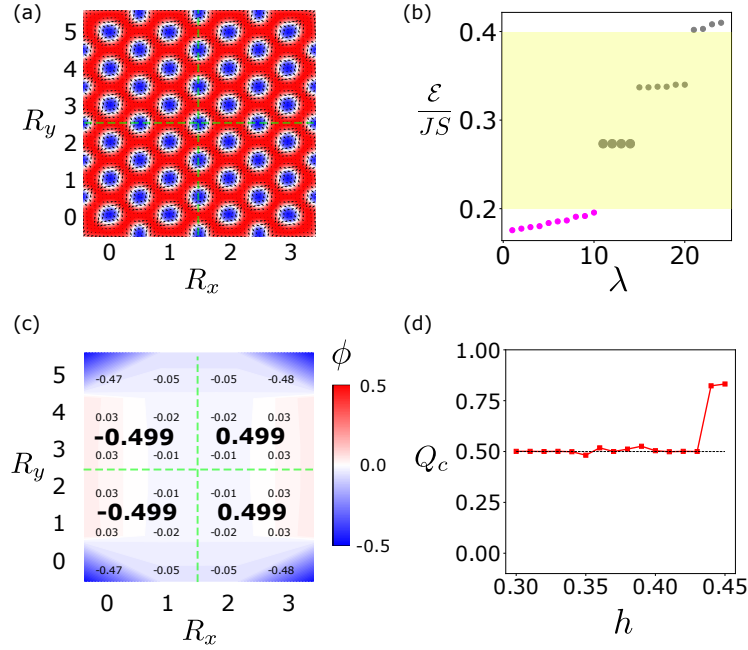
Figure 5.12: **Fractional corner charge induced by the bulk quadrupole moment.**
(a) Classical ground state magnetic texture of a 60×60 spin lattice at $h = 0.3$. As
indicated by vertical and horizontal axes, it contains $N_x \times N_y$ magnetic unit cells, with
$(N_x, N_y) = (4, 6)$. (b) Magnon spectrum near the fourth bulk band gap indicated by a
yellow square, showing eigenstates that belong to the lowest four bulk bands in magenta.
The corner states are depicted by larger gray circles. (c) The value of the magnon charge
density $\phi(\boldsymbol{r})$ is indicated for each magnetic unit cell. Green dashed lines divide the sample
into four symmetry sectors whose net magnon charge is denoted by large bold numbers.
(d) The magnetic field dependence of Q_c, obtained by relaxing the classical ground-state
configuration at $h = 0.3$ with increasing magnetic fields. Adapted from [212].

Based on the magnon density defined above, the fractional corner "charge" carried by
the lowest four bulk magnon bands of the antiskyrmion crystal in a finite system is given
by [309]

$$Q_c = \sum_{\boldsymbol{r} \in \text{one sector}} \phi(\boldsymbol{r}) \bmod 1 \,, \tag{5.41}$$

with $\phi(\boldsymbol{r}) = \rho(\boldsymbol{r}) - [\rho_1(\boldsymbol{r}) + \rho_2(\boldsymbol{r})]$. We should note that the corner "charge" includes
not only the magnon density of a unit cell at corners but also of all unit cells within a
symmetry sector related by $C_{2x}\mathcal{T}$ and $C_{2y}\mathcal{T}$, which is indicated by green dashed lines in
Fig. 5.12(a). From the symmetry, we expect that Q_c for each symmetry sector is equal to
each other. Hence, the fractional corner "charge" defined in Eq. (5.41) remains quantized
regardless of the correlation length of magnon wave functions as long as the symmetry is
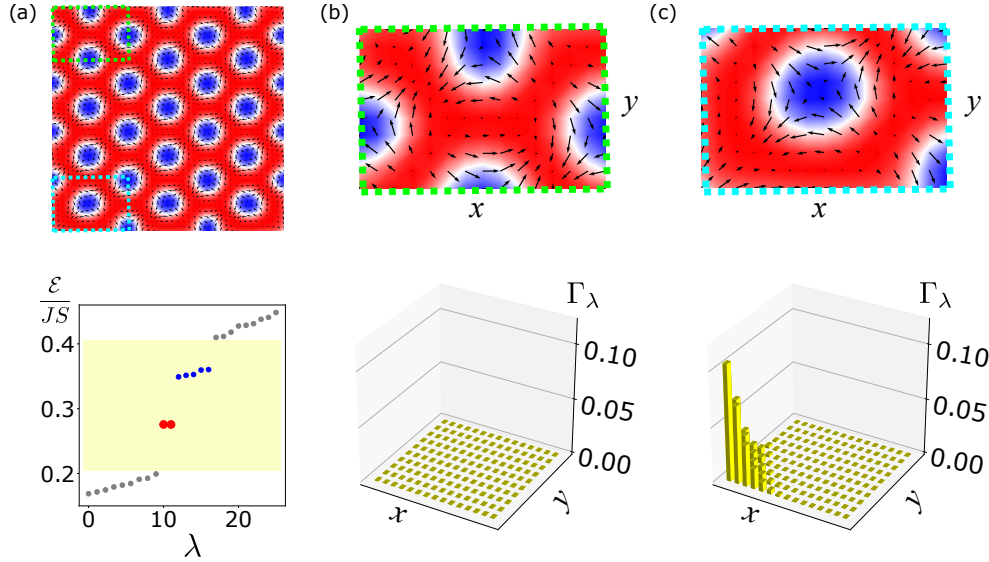conserved, as shown below.

Figure 5.13: **Magnonic corner states at select corners.**   (a) Top: classical ground state spin textures of 45×45 spins at $h = 0.3$. Bottom: magnon spectrum with only two corner states (red) and trivial edge modes (blue). (b) and (c) Top: enlarged spin textures of (b) the top left corner (green dashed lines) and (c) the bottom left corner (light blue dotted lines) shown in (a). Bottom: probability density distribution of the corner state at each corner. Adapted from [212].

Figure 5.12 illustrates the calculation of Q_c of a 60×60 spin lattice with open boundary conditions at $h = 0.3$, where $(N_x, N_y) = (4, 6)$, and $M = 4$ as shown in Fig. 5.12(a). The corresponding auxiliary, periodic system is prepared by the identification procedure described above and then letting the magnetic texture relax using the LLG equation for a long time $t_0 = 10^4$. The magnon density $\rho(\boldsymbol{r})$ for the finite system is calculated from the eigenstates within the lowest four bulk bands (magenta) as shown in Fig. 5.12(b). As shown in Figure 5.12(c), we find that the magnon charge density $\phi(\boldsymbol{r})$ is corner-localized and Q_c is quantized to $\frac{1}{2}$ at each symmetry sector. Furthermore, Figure 5.12(d) shows that Q_c remains quantized below and suddenly increases above the edge instability critical field, signaling a topological phase transition.

5.5 Discussion

5.5.1 Corner state engineering

In section 5.4.1, we have shown that two different choice of magnetic unit cells is possible, and the one that support magnonic corner states is the thermodynamically stable configuration. Hence, we always expect four degenerate corner states to be obtained for a sufficiently large system. Even if there is a mismatch between the magnetic unit cell and sample size, antiskyrmion crystals can deform slightly to form the thermodynamically
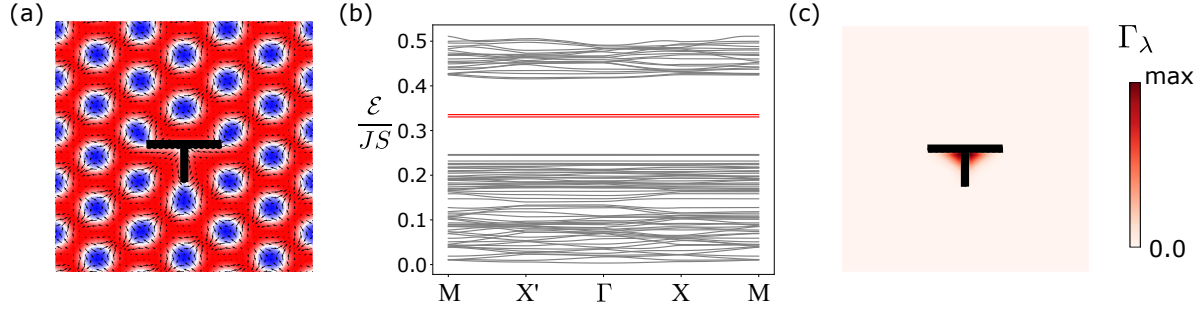
Figure 5.14: **Magnonic corner states induced by a T-shaped hole.**   (a) Classical ground state spin textures of a 45×45 periodic system at $h = 0.31$. A T-shaped hole is introduced at the center of a sample. (b) Magnon band structure of the first Brillouin zone, showing almost doubly degenerate flat bands in red and bulk states in gray. (c) Probability density distribution Γ_λ of the flat band at Γ point. (a) and (c) are adapted from [212].

stable configuration, and support a magnonic corner state at each corner. On the other hand, the finite size effect cannot be neglected for small samples. In such cases, there is an additional criterion for the formation of magnonic corner states as discussed below.

Figure 5.13(a) shows the classical ground-state texture of a 45×45 spin lattice system containing 4.5 magnetic unit cells along the vertical direction, and the spin configurations at the top and bottom corners are different. This is indicated by enlarged spin textures in Fig. 5.13(b) and (c). At the top corner in Fig. 5.13(b), fractional antiskyrmions are close to each other across the corner compared to the bottom corner configuration in Fig. 5.13(c). Although the configuration of Fig. 5.13(b) is energetically less favorable due to the repulsion between fractional antiskyrmions, it is enforced by the mismatch between the magnetic unit cell and system size. Furthermore, the configuration of Fig. 5.13(b) corresponds to the magnetic unit cell with zero edge polarization (see Figure 5.11). As a result, magnonic corner states are not supported by the top corners, resulting in only two corner states in this sample. Therefore, the location of magnonic corner states could be controlled by adjusting the size of the sample.

It is also possible to engineer the location of corner states by introducing artificial holes within the bulk of the sample. In Figure 5.14, we show the classical ground state spin textures in the presence of a T-shaped hole at $h = 0.31$ with the periodic boundary condition. Taking the whole sample as a magnetic unit cell, we obtain the magnon spectrum with two perfectly flat bands (red) inside the fourth bulk band gap as shown in Fig. 5.14(b). A non-dispersive band structure generally implies local excitations. Indeed, those two flat bands correspond to the magnonic corner states. Figure 5.14(c) shows the probability density of the flat band magnon mode at Γ point defined in Eq. (5.36), which is localized at the inner corners of the T-shaped hole. Therefore, topologically protected magnonic corner states can be engineered at desired locations as long as the symmetries are preserved in the presence of holes.
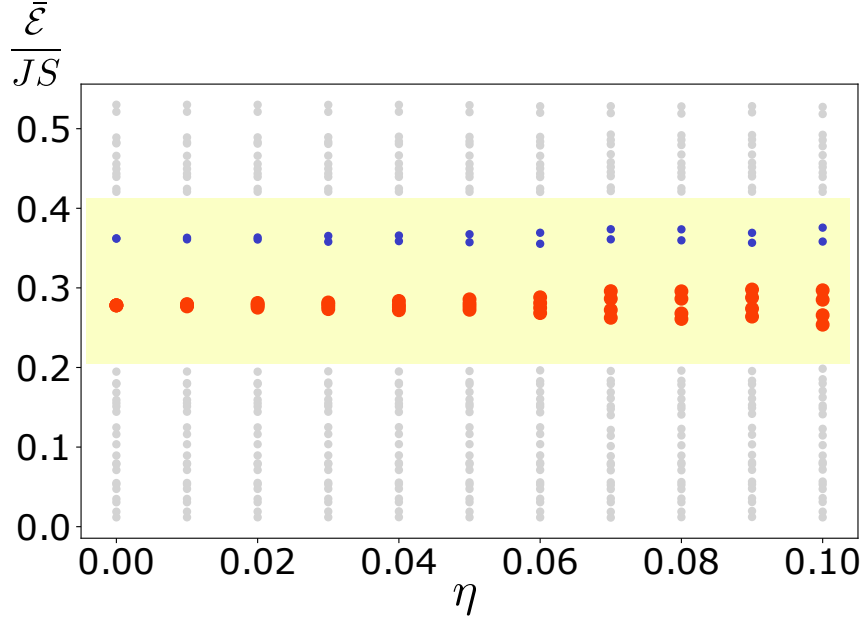
Figure 5.15: **Robust magnonic corner states in the presence of disorder.** Disorder-averaged magnon spectrum as a function of the disorder strength η at $h = 0.3$, showing the corner states in red and edge localized states in blue. Adapted from [212].

5.5.2 Robustness of corner states

In this section, we investigate the robustness of magnonic corner states against weak perturbations. In magnonic systems, adding a disorder in the spin wave Hamiltonian is not sufficient as it may also affect the underlying spin textures. In order to account for it, we compute the classical ground state spin textures for each disorder realization. The spin wave Hamiltonian is constructed from each configuration with the perturbation term, which is used to compute the magnon band structure. In this way, we evaluate the robustness of corner states against disorder.

We consider random fluctuations in the z component of the external magnetic field across the sample: $\delta B_z(\boldsymbol{r})$. Adding the random field $\delta B_z(\boldsymbol{r})$ on top of the uniform magnetic field at $h = 0.3$, the stable configuration is obtained for a 30×30 system by Monte Carlo simulated annealing. The disorder in magnetic fields adds a following term to the spin wave Hamiltonian:

$$H_{\mathrm{dis}} = \sum_{\boldsymbol{r}} g\mu_B \delta B_z(\boldsymbol{r}) \hat{\boldsymbol{z}} \cdot \boldsymbol{m_r} a_{\boldsymbol{r}}^\dagger a_{\boldsymbol{r}} \,. \tag{5.42}$$

The random fluctuations are modeled as $\delta B_z(\boldsymbol{r}) = B_z \chi_{\boldsymbol{r}} \eta$, where $\chi_{\boldsymbol{r}}$ is uniformly distributed in the interval $[-1, 1]$ and η is a parameter for the disorder strength. In Figure 5.15, we plot the disorder-averaged magnon spectrum $\bar{\mathcal{E}}$ at various disorder strength η. For each value of η, we take a statistical average over 20 disorder realizations. While
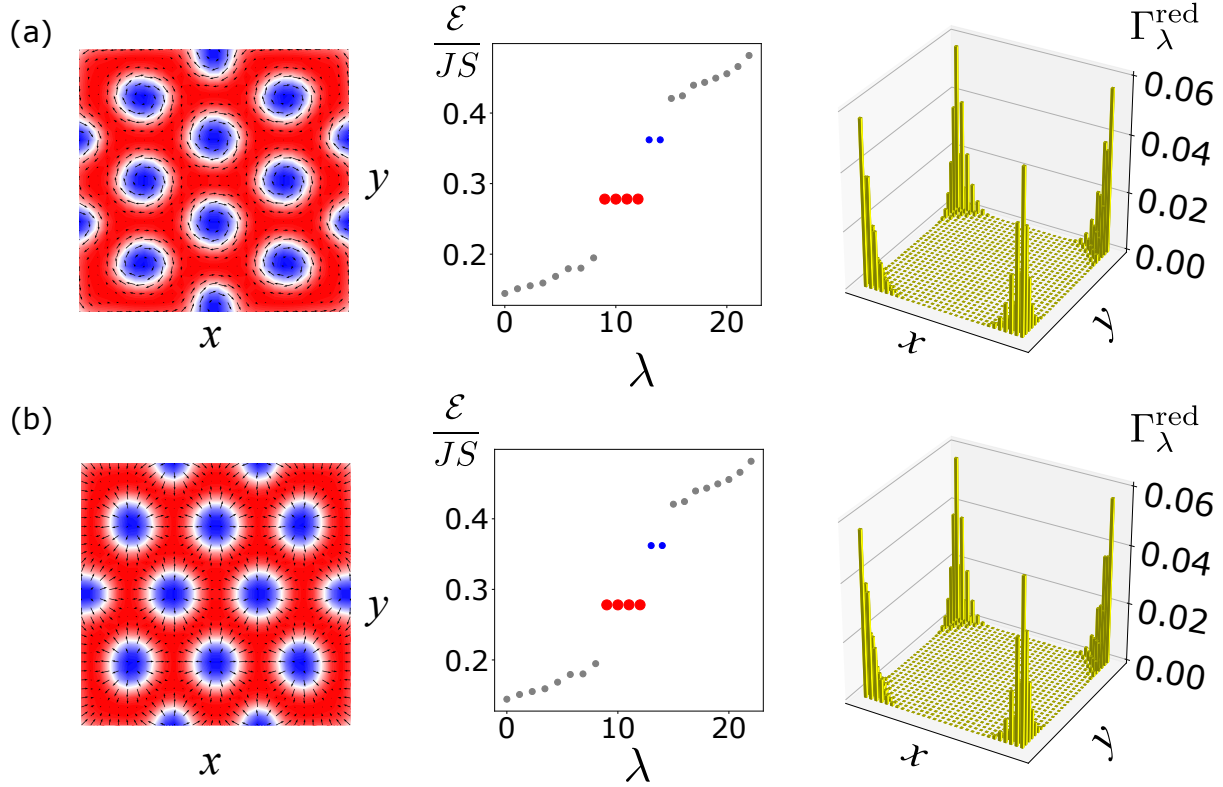
Figure 5.16: **Magnonic corner states realized in Bloch and Néel skyrmion crystals.**   Ferromagnetic (a) Bloch and (b) Néel skyrmions in a finite sample at $h = 0.3$. Left: classical ground state spin textures with fractional skyrmions along edges. Middle: magnon spectrum shwoing corner states (red) and trivial edge states (blue). Right: probability density $\Gamma_\lambda^{\mathrm{red}}$ of the corner states. Adapted from [212].

the fourfold degeneracy of corner states is broken by disorder, they remain inside the band gap, isolated from bulk bands. Therefore, we conclude that the magnonic corner states are robust against moderate disorder.

5.5.3   Bloch and Néel skyrmion crystals

So far, we have focused on the antiskyrmion crystals realized in tetragonal Heusler compounds with D_{2d} symmetry, where the magnonic bulk quadrupole moment is quantized by $C_{2x}\mathcal{T}$ and $C_{2y}\mathcal{T}$ symmetries. It is straightforward to generalize our theory to conventional skyrmions. For Bloch skyrmion crystals, the symmetries of magnetic unit cell is the same as antiskyrmion crystals. Hence, they also support magnonic corner states below the critical magnetic field of the edge instability, originating from the quantized bulk quadrupole moment. Similarly, the symmetries of Néel skyrmion crystals are given by $M_x\mathcal{T}$ and $M_y\mathcal{T}$, which leads to the identical constrains on Wannier centers and bulk multipole moments as $C_{2x}\mathcal{T}$ and $C_{2y}\mathcal{T}$ symmetries. Figure 5.16 illustrates that the magnonic

corner states are obtained in both Bloch and Néel ferromagnetic skyrmion crystals in the presence of fractional skyrmions.

5.5.4 Magnon-magnon interaction

Throughout this chapter, we have studied the quadratic spin wave Hamiltonian, neglecting magnon-magnon interactions arising from higher order contributions. Here, we discuss its effect on the magnonic higher-order topological phase realized in antiskyrmion crystals. Firstly, the magnonic corner states was observed using the Landau-Lifshitz-Gilbert equation in Fig. 5.8. This implies that it is robust against all the nonlinear contributions in the classical limit [41]. Furthermore, the perturbative expansion of magnon-magnon interaction in skyrmion crystals was recently performed up to the third order terms in magnon operators [310]. They have shown that the four lowest magnon bands do not undergo spontaneous quasiparticle decay into lower energy states, which guarantees the robustness of the magnonic quadrupole moment against magnon-magnon interactions. Therefore, the magnonic corner states protected by the quadrupole moment should persist even beyond the linear spin wave theory.

5.5.5 Dipolar interactions

Our model Hamiltonian consists of the short-range interactions between neighboring spins. In practice, the long-range interaction exists in ferromagnetic systems due to the dipolar fields (see Appendix A.3.3). In order to account for it, we consider a simplified expression obtained in the two-dimensional limit, given as an effective easy-plane anisotropy [101, 130, 188]. Adding the crystalline easy-axis anisotropy, it is written as

$$H_{\mathrm{dip+MC}} = -\sum_{\boldsymbol{r}} K S_{\boldsymbol{r},z}^2 \,, \tag{5.43}$$

with $K = K_{\mathrm{MC}} - \frac{1}{2}\mu_0 M_s^2$, where K_{MC} is the uniaxial crystalline anisotropy coefficient and the second term is the effective anisotropy from the dipole-dipole interaction with M_s and μ_0 denoting the saturation magnetization and the permeability of free space, respectively. Using this term to model the dipolar interactions, we discuss its effect on the magnonic corner states.

The effect of anisotropy on the stability of skyrmions has been discussed in the literatures [264, 311]. The easy-axis anisotropy ($K > 0$) favors the out-of-plane magnetizations, while the easy-plane anisotropy ($K < 0$) favors the in-plane magnetizations. As a result, the skyrmion crystal phase remains stable up to higher magnetic fields for the easy-plane anisotropy. Similarly, the critical magnetic field for the edge instability becomes higher for $K < 0$ as shown in Fig A.2 [105]. Therefore, negative anisotropy of a modest strength could support magnonic corner states at higher magnetic fields. However, we find that a strong negative anisotropy leads to the band inversion between the fourth and fifth bands at $K/J = -0.6$ and $h = 0.3$, resulting in the topological phase transition. Therefore, the magnonic corner states are expected to be robust against dipolar interaction although
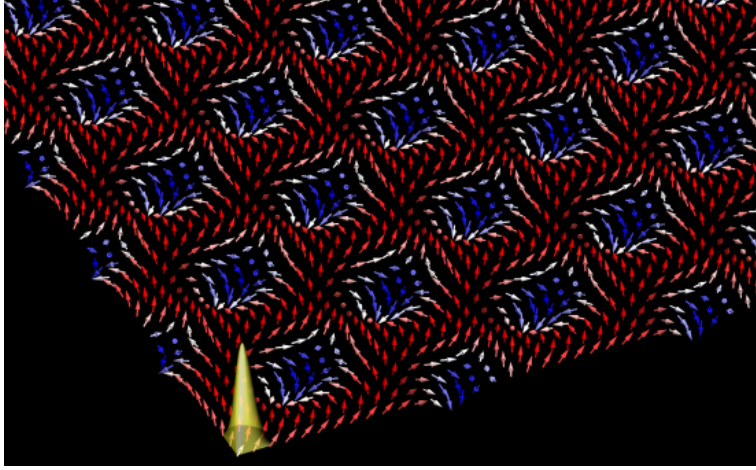
Figure 5.17: **Schematic representation of magnonic corner states in anti-skyrmion crystals.**   Adapted from [212].

there exists the critical values of the effective anisotropy for the topological phase transition for $K < 0$. We should note that the magnonic corner states may be found within the bulk states for $K < 0$. Even in this case, the topologically protected corner states are not overlapped with bulk states so that they can be brought into a bulk band gap by applying a local magnetic field at the corners of the sample [309].

5.6   Conclusion

We have uncovered that magnetic antiskyrmion crystals can realize a magnonic quadrupole topological insulator, whose hallmark signatures are robust magnonic corner states (Figure 5.17). The magnonic quadrupole moment is quantized by $C_{2x}\mathcal{T}$ and $C_{2y}\mathcal{T}$ symmetries of the magnetic unit cell, whose value remains nontrivial for a broad range of parameters. Tuning an applied magnetic field induces the self-assembly of fractional antiskyrmions along the sample edges, which, remarkably, restore the protecting symmetries that allow the formation of magnonic corner states. Acentric tetragonal Heusler compounds, where antiskyrmion crystals have already been observed, constitute a readily available experimental platform to test our predictions. We should note that our theory also applies to ferromagnetic Bloch and Néel skyrmion crystals, with equivalent symmetries that quantize the magnonic quadrupole moment.

For experimental observations, the magnonic corner states can be excited by spatially uniform AC magnetic fields. The main challenge is a high spatial resolution to resolve the corner localized modes. We suggest NV center magnetometry [312] or near-field Brillouin light scattering technique [268] for such measurements. Ferromagnetic resonance spectroscopy could be also used for measuring the energy of magnonic corner states. In addition, the quantized magnon corner "charge" Q_c can be used to characterize the magnonic quadrupole moment similarly to Ref. [309]. Q_c is defined in terms of magnon

densities as given Eq. (5.41), so it can be estimated from the amplitude of spin precession using the aforementioned techniques.

Another point is that the formation of fractional (anti)skyrmions is essential to obtain topologically protected magnonic corner states. So far, there is no clear evidence of their existence, although the edge twisting and edge-mediated skyrmion chains were observed in Bloch skyrmions [104, 168]. In constrast, fractions of topologically trivial magnetic bubbles have been observed along the sample edges in the acentric tetragonal Heusler compound $Mn_{1.4}Pt_{0.9}Pd_{0.1}Sn$ [153] (see Fig. 2.12). Our numerical simulations indicate that the presence of the (anti)skyrmion crystal is of paramount importance for the stabilization of fractional (anti)skyrmions along the edges of the sample, and the field-cooling protocol is necessary for that. We hope that fractional (anti)skyrmions will be experimentally observed in near future.

Finally, we comment on possible applications of magnonic corner states. Recently, a hybrid system between magnons and other bosonic excitation has been actively studied for quantum computing and quantum information applications [313–315]. Since magnonic corner states are exponentially localized at corners and isolated from bulk states in the spectrum, they can be used as as a magnon cavity with a high Q factor [299] to enhance magnon-photon interactions. Our study highlights a new form of topological excitation in magnetic systems and its potential use in the design of future magnonic devices.

Chapter 6

Summary and Outlook

In this thesis, we have studied the topological magnon excitations in magnetic skyrmion crystals, where the noncollinear spin structure provides an attractive platform for topological magnonics. We have shown that an increase in the magnetic field triggers the topological phase transition of magnon bands. Furthermore, it is caused by the band inversion between two magnetically active modes, namely the counterclockwise and breathing modes. This implies that the predicted band inversion can be experimentally measured by the microwave absorption, as demonstrated previously. Dictated by the bulk-boundary correspondence, the chiral magnonic edge state exists inside the band gap between these two modes below the critical magnetic field, but it vanishes above the critical field. Hence, the chiral magnonic edge state can be controlled by external fields in skyrmion crystals.

We have further extended the discussion to non-equilibrium systems driven by THz lasers, where Floquet magnons were defined as slow excitations from rapidly oscillating non-equilibrium steady states. Using the LLG simulations, we have shown that an effective magnetic field induced by the circularly polarized laser also leads to the band inversion analogously to static magnetic fields. Thus, it opens a possibility of ultrafast laser-driven topological phase transition.

We have also extended the magnon band topology to higher-order topological insulators characterized by the bulk multipole moments. Establishing the Wilson loop formalism adapted for magnons, we have shown that antiskyrmion crystals as well as conventional skyrmion crystals support the magnonic higher-order topological phase with a nontrivial quadrupole moment. The hallmark signature is the magnonic corner state, which requires the conservation of protecting symmetries in a finite sized sample. We have pointed out that this condition is satisfied in the presence of fractional antiskyrmions that are stabilized at low magnetic fields.

As a summary, we have shown that the various magnonic topological phases can be induced and controlled by externally applied magnetic fields in magnetic skyrmion crystals. Our study suggests the potential application of magnetic skyrmion crystals in spintronic devices, supporting both magnonic corner states and chiral edge states.

For the future work, we would like to comment on the recent progress of collaboration work with an experimental group in Germany. As predicted by our result, we have suc-

cessfully observed fractional antiskyrmions and skyrmions in the Heusler material [316]. Since their presence restores the symmetries of magnetic unit cell, it is an important step towards the realization of magnonic corner states. Intriguingly, this material is the only known example where antiskyrmions and Bloch skyrmions coexist, although the crystal symmetry favors the formation of antiskyrmions [153]. It was reported that antiskyrmions are stable at room temperatures, while Bloch skyrmions become more favorable at low temperatures [317]. They have even demonstrated a continuous transformation between Bloch skyrmions and antiskyrmions [318]. To understand this behavior, the importance of dipole-dipole interaction has been pointed out at low temperatures. Hence, our next goal is to fully incorporate the long-range dipolar interactions in antiskyrmion crystals. While we expect that our result holds at high temperatures where antiskyrmions were observed, it is an interesting question whether a strong dipole-dipole interaction at low temperatures leads to a novel magnonic topological phase.

Appendices

Appendix A

Theoretical and experimental background

A.1 Sum rule of Chern number

The sum of Chern number over whole "particle" bands is zero as shown below [2].

$$\sum_{n=1}^{N} C_n = 0. \tag{A.1}$$

The condition for this sum rule is that energy eigenvalues satisfy $\mathcal{E}_n(\boldsymbol{k}) > 0$ for $n = 1, \ldots, N$, implying that there is no gapless excitation such as Goldstone modes.

To prove Eq. (1.23), we interpolate from a $2N \times 2N$ unit matrix to a magnon BdG Hamiltonian $H(\boldsymbol{k})$ of Eq. (1.10) with a parameter λ ($0 \leq \lambda \leq 1$).

$$H(\boldsymbol{k}, \lambda) = (1 - \lambda)\mathbb{1}_{2\times 2} + \lambda H(\boldsymbol{k}). \tag{A.2}$$

From the assumption that all energy eigenvalues are positive, $H(\boldsymbol{k})$ is paraunitarily equivalent to a positive definite diagonal matrix:

$$T_{\boldsymbol{k}}^{\dagger} H(\boldsymbol{k}) T_{\boldsymbol{k}} = \begin{pmatrix} \mathcal{E}_\lambda(\boldsymbol{k}) & 0 \\ 0 & \mathcal{E}_\lambda(-\boldsymbol{k}) \end{pmatrix}. \tag{A.3}$$

Sylvester's law of inertia states that $H(\boldsymbol{k})$ can be transformed to a diagonal matrix with all positive elements by a unitary matrix.

$$U_{\boldsymbol{k}}^{\dagger} H(\boldsymbol{k}) U_{\boldsymbol{k}} = E_{\boldsymbol{k}} > 0. \tag{A.4}$$

It is straightforward to see that this holds true for $0 \leq \lambda \leq 1$ using the same unitary matrix.

$$U_{\boldsymbol{k}}^{\dagger} H(\boldsymbol{k}, \lambda) U_{\boldsymbol{k}} = (1 - \lambda)I_{2N\times 2N} + \lambda E_{\boldsymbol{k}} > 0. \tag{A.5}$$

This guarantees that the magnon spectrum of $H(\boldsymbol{k}, \lambda)$ is always positive definite. Thus, all "particle" bands have positive energies during the interpolation from $\lambda = 1$ to $\lambda = 0$,
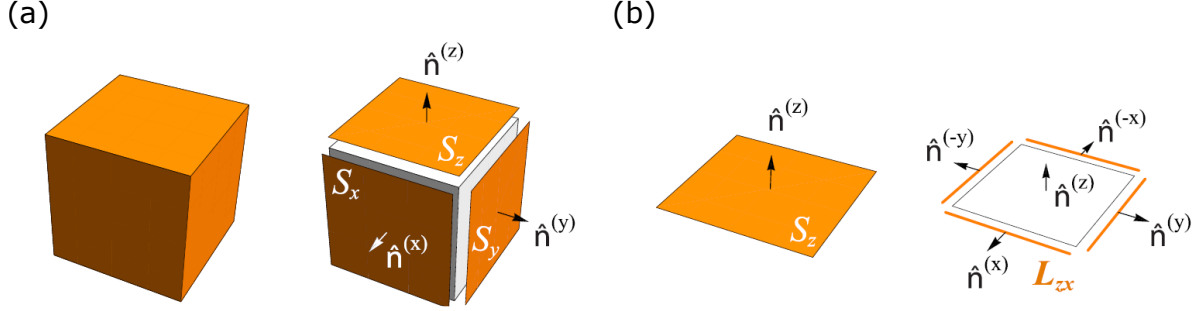
(a)

(b)

Figure A.1: **Schematic picture of boundary segmentation of a cubic system.** (a) Boundaries of a cuboid consists of two-dimensional squares S_a. The unit vector orthogonal to the surface is denoted as $n_i^{(a)} = \pm\delta_i^a$ with its sign determined by the orientation of surfaces. (b) Boundaries of a square consists of one-dimensional lines L_{ab}. Adapted from [80].

which excludes possibility of band crossings with "hole" bands. The sum of the Chern numbers over a group of bands does not change, unless some band in the group forms a band touching with bands outside the group. Therefore, the Chern number does not change during the interpolation, resulting in the sum rule of Eq. (1.23).

A.2   Multipole expansion in classical electromagnetism

Following Ref. [80], we decompose the electric potential due to the quadrupole moment $\phi^2(\boldsymbol{r})$ in Eq. (1.29) into boundary localized charges.

$$
\begin{aligned}
q_{ij}\frac{3d_id_j - |\mathbf{d}|^2\delta_{ij}}{2|\mathbf{d}|^5} &= \frac{1}{2}q_{ij}\partial_i\partial_j\frac{1}{|\mathbf{d}|} \\
&= \frac{1}{2}\partial_i\partial_j\big(q_{ij}\frac{1}{|\mathbf{d}|}\big) - \partial_i\Big[\big(\partial_jq_{ij}\big)\frac{1}{|\mathbf{d}|}\Big] + \frac{1}{2}(\partial_i\partial_jq_{ij})\frac{1}{|\mathbf{d}|}, \quad \text{(A.6)}
\end{aligned}
$$

where ∂_i is a derivative with respect to i-th component of $\boldsymbol{R}$. We have used $q_{ij} = q_{ji}$ for the last equality. By applying the divergence theorem, the integral in Eq. (1.29) is rewritten as

$$
\phi^2(\boldsymbol{r}) = \frac{1}{4\pi\epsilon}\int_{\partial V} dR^2\Big[\frac{1}{2}n_i\partial_j\big(q_{ij}\frac{1}{|\mathbf{d}|}\big) - n_i\big(\partial_jq_{ij}\big)\frac{1}{|\mathbf{d}|}\Big] + \frac{1}{4\pi\epsilon}\int_V dR^3\Big[\frac{1}{2}(\partial_i\partial_jq_{ij})\frac{1}{|\mathbf{d}|}\Big], \quad \text{(A.7)}
$$

where ∂V is the surface of system and $\hat{n}$ is a unit vector perpendicular to the surface. Assuming the cubic geometry, we can simplify the integral further. The first term in the above equation is simplified as

$$
\begin{aligned}
\frac{1}{4\pi\epsilon}\int_{\partial V} dR^2\Big[\frac{1}{2}n_i\partial_j\big(q_{ij}\frac{1}{|\mathbf{d}|}\big)\Big] &= \frac{1}{4\pi\epsilon}\sum_a\int_{S_a} dR^2\Big[\frac{1}{2}n_i^{(a)}\partial_j\big(q_{ij}\frac{1}{|\mathbf{d}|}\big)\Big] \\
&= \frac{1}{4\pi\epsilon}\sum_{a,b}\int_{L_{ab}} dR\Big(\frac{1}{2}n_i^{(a)}n_j^{(b)}q_{ij}\frac{1}{|\mathbf{d}|}\Big), \quad \text{(A.8)}
\end{aligned}
$$

where $\hat{n}^{(a)}$ is a unit vector normal to a surface S_a and L_{ab} is the edge shared by two surfaces S_a and S_b (see Fig. A.1(a) and (b)). The last equality is derived from the application of the divergence theorem on a two-dimensional surface. The final expression is derived as [80]

$$
\begin{aligned}
\phi^2(\boldsymbol{r}) \;=\;& \frac{1}{4\pi\epsilon}\sum_{a,b}\int_{L_{ab}} dR\Big(\frac{1}{2}n_i^{(a)}n_j^{(b)}q_{ij}\Big)\frac{1}{|\mathbf{d}|} - \frac{1}{4\pi\epsilon}\sum_a\int_{S_a} dR^2\Big(n_i^{(a)}\partial_j q_{ij}\Big)\frac{1}{|\mathbf{d}|} \\
+\;& \frac{1}{4\pi\epsilon}\int_V dR^3\Big(\frac{1}{2}\partial_i\partial_j q_{ij}\Big)\frac{1}{|\mathbf{d}|}.
\end{aligned}
\tag{A.9}
$$

A.3 Interactions between localized spins

Magnetism in materials is originated from magnetic dipole moments carried by localized electronic states. They can interact among themselves through the Coulomb interaction and a virtual hopping process. In the following, we review magnetic interactions as a basis for theoretical models of classical spin systems.

A.3.1 Heisenberg exchange coupling

Let us consider a tight-binding model constructed from strongly localized electronic wave functions, called Wannier functions. The tight-binding Hamiltonian is generally written as [319]

$$
H = \sum_{ii'}\sum_{\sigma} a_{i\sigma}^{\dagger} t_{ii'} a_{i'\sigma} + \sum_{ii'jj'}\sum_{\sigma\sigma'} U_{ii'jj'} a_{i\sigma}^{\dagger} a_{i'\sigma'}^{\dagger} a_{j'\sigma'} a_{j\sigma},
\tag{A.10}
$$

where $a_{i\sigma}/a_{i\sigma}^{\dagger}$ is the annihilation/creation operator of electrons at i-th site with spin σ, $t_{ii'}$ is the hopping matrix, and $U_{ii'jj'}$ is the matrix element for the Coulomb interaction. The matrix elements of $U_{ii'jj'}$ are given by

$$
U_{ii'jj'} = \frac{1}{2}\int d^d r \int d^d r'\, \psi_{\boldsymbol{R}_i}^*(\boldsymbol{r})\psi_{\boldsymbol{R}_j}(\boldsymbol{r})V(\boldsymbol{r}-\boldsymbol{r}')\psi_{\boldsymbol{R}_{i'}}^*(\boldsymbol{r}')\psi_{\boldsymbol{R}_{j'}}(\boldsymbol{r}'),
\tag{A.11}
$$

with $V(\boldsymbol{r})$ and $\psi_{\boldsymbol{R}_i}(\boldsymbol{r})$ denoting the Coulomb interaction and Wannier function localized in the atom labeled by $\boldsymbol{R}_i$, respectively.

The Coulomb interaction matrix $U_{ii'jj'}$ can be decomposed into two nearest neighbor interaction terms. The first term is the direct interaction between electron densities at different sites for $U_{ii'ii'} \equiv V_{ii'}$:

$$
\sum_{i\neq i'}\sum_{\sigma\sigma'} U_{ii'ii'} a_{i\sigma}^{\dagger} a_{i'\sigma'}^{\dagger} a_{i'\sigma'} a_{i\sigma} = \sum_{i\neq i'} V_{ii'}\hat{n}_i\hat{n}_{i'},
\tag{A.12}
$$

with $\hat{n}_i = \sum_{\sigma} a_{i\sigma}^{\dagger} a_{i\sigma}$ representing the electron density at i-th site. This term describes the electrostatic interaction between electrons, associated with global instabilities of charge

distribution known as the charge density wave. The second term is the exchange interaction of spins at different sites for $U_{ijji} \equiv J_{ij}$, which leads to the ferromagnetic interaction:

$$\sum_{i \neq j} \sum_{\sigma\sigma'} U_{ijji} a_{i\sigma}^\dagger a_{j\sigma'}^\dagger a_{j\sigma'} a_{i\sigma} = -2 \sum_{i \neq j} J_{ij} \left(\hat{\boldsymbol{S}}_i \cdot \hat{\boldsymbol{S}}_j + \frac{1}{4} \hat{n}_i \hat{n}_j \right), \tag{A.13}$$

where the spin operator is defined as $\hat{\boldsymbol{S}}_i = \frac{1}{2} a_{i\alpha}^\dagger \boldsymbol{\sigma}_{\alpha\beta} a_{i\beta}$ with Pauli matrices $\boldsymbol{\sigma}$. The equality was obtained using the identity $\boldsymbol{\sigma}_{\alpha\beta} \cdot \boldsymbol{\sigma}_{\gamma\delta} = 2\delta_{\alpha\delta}\delta_{\beta\gamma} - \delta_{\alpha\beta}\delta_{\gamma\delta}$.

The magnetic interaction in the form of $-J\boldsymbol{S}_i \cdot \boldsymbol{S}_j$ with $J > 0$ is called the Heisenberg exchange coupling in magnetic systems, which favors the ferromagnetic order. As derived above, it arises from the Coulomb interaction between electrons. The physically intuitive picture is provided by the Pauli exclusion principle that prohibits occupation of the same electronic state. This implies that a pair of electrons with a parallel spin are repelled from each other, lowering their Coulomb interaction energy in comparison to a pair of electrons with opposite spins.

A.3.2 Superexchange interaction

Magnetic ions hosting localized spins are often surrounded by non-magnetic ions, so the direct exchange coupling in the previous section is not sufficient to describe magnetic interactions. To account for this problem, P.W. Anderson considered virtual hopping processes between distant magnetic ions through non-magnetic ions, called the superexchange interaction [245, 320]. The key idea is to simplify the perturbation expansion by choosing molecular orbitals as a basis set, which are constructed from overlapping of d-orbital electrons in magnetic ions and p-orbitals in non-magnetic ions. His idea was further developed by T. Moriya to include the spin-orbit coupling [36].

Here, we briefly outline the perturbation theory to derive superexchange interactions based on Ref. [36]. Suppose that Wannier functions localized at magnetic ions are constructed from hybridized bonds with non-magnetic ions, denoted as $\Psi_{n\uparrow}(\boldsymbol{r} - \boldsymbol{R})$ and $\Psi_{n\downarrow}(\boldsymbol{r} - \boldsymbol{R})$ with $\boldsymbol{R}$ and n respectively labeling the magnetic ion and the molecular orbital. Since the spin-orbit coupling is included, $\uparrow$ and $\downarrow$ indicate almost spin up and spin down with some mixtures between them. Using this basis, a single particle Hamiltonian is evaluated:

$$H_1 = \sum_i \left[\frac{p_i^2}{2m} + V(\boldsymbol{r}_i) + \frac{\hbar}{2m^2c^2} \boldsymbol{S}_i \cdot (\nabla \cdot V(\boldsymbol{r}_i) \times \mathbf{p}_i) \right], \tag{A.14}$$

where the third term is the spin-orbit coupling. Taking $\Psi_{n\uparrow}(\boldsymbol{r} - \boldsymbol{R})$ and $\Psi_{n\downarrow}(\boldsymbol{r} - \boldsymbol{R})$ as unperturbed states, we can perform the perturbation expansion in this general setup. Up to the first order expansion, only a non-zero contribution comes from two-body Hamiltonian $H_{12} = \sum_{i<j} \frac{e^2}{r_{ij}}$. This contribution is the direct exchange interaction discussed previously, which vanishes for a pair of opposite spins. The second order perturbation corresponds to a virtual hopping from n orbital at $\boldsymbol{R}$ to n' orbital at $\boldsymbol{R}'$ with/without spin flipping, and returning to the original electronic state. This process induces magnetic interactions

between $\boldsymbol{S}(\boldsymbol{R})$ and $\boldsymbol{S}(\boldsymbol{R}')$. The general form was derived as [36]

$$E^{(2)}_{\boldsymbol{R},\boldsymbol{R}^2} = J_{\boldsymbol{R},\boldsymbol{R}'}\boldsymbol{S}(\boldsymbol{R}) \cdot \boldsymbol{S}(\boldsymbol{R}') + \mathbf{D} \cdot [\boldsymbol{S}(\boldsymbol{R}) \times \boldsymbol{S}(\boldsymbol{R}')] + S_i(\boldsymbol{R})\Gamma^{ij}_{\boldsymbol{R},\boldsymbol{R}'}S_j(\boldsymbol{R}'). \qquad (A.15)$$

The first term is the symmetric part of superexchange interaction. Unlike the direct exchange interaction, the sign of this term depends on the details of systems such as number of electrons in d-orbitals, which is known as the Goodenough-Kanamori rules [244, 321]. The second term is the antisymmetric part of superexchange interaction arising from the spin-orbit coupling, first discussed by Dzyaloshinskii using symmetry arguments [132, 133]. This is now called the Dzyaloshinskii-Moriya interaction from the two important contributers. The Dzyaloshinskii-Moriya interaction is crucial to realize noncollinear magnetic textures, since it favors canting of spins. As summarized in Ref. [36], it is only present in a system lacking the inversion symmetry with the Dzyaloshinskii-Moriya vector $\mathbf{D}$ determined by the crystalline symmetry. The third term is the anisotropic exchange interaction.

A.3.3 Other magnetic interactions

The magnetic ion itself may have single-ion anisotropy (also called magnetocrystalline anisotropy) [322]. The simplest example is the uniaxial anisotropy $-K(\boldsymbol{m} \cdot \hat{z})^2$, where the magnetization parallel/antiparallel to the z-axis is favored for easy-axis anisotropy ($K > 0$) and the in-plane magnetization is favored for easy-plane anisotropy ($K < 0$).

Another interaction is the dipole-dipole interaction from the classical electromagnetic theory of dipole moments [87, 166]. It is written as

$$H_{\mathrm{dip}} = \frac{\mu_0}{4\pi} \sum_{i<j} \left[\frac{\boldsymbol{S}_i \cdot \boldsymbol{S}_j}{r_{ij}^3} - 3\frac{(\boldsymbol{S}_i \cdot \boldsymbol{r}_{ij})(\boldsymbol{S}_j \cdot \boldsymbol{r}_{ij})}{r_{ij}^5} \right], \qquad (A.16)$$

where μ_0 is the vacuum permeability and $\boldsymbol{r}_{ij}$ is the vector pointing from site i to site j with $r_{ij} = |\boldsymbol{r}_{ij}|$. The microscopic magnetic fields felt by other magnetic dipole moments ($\mathbf{H}_{\mathrm{demag}} = -\partial H_{\mathrm{dip}}/\partial \boldsymbol{m}_i$) is referred to as the demagnetization field, because it tends to reduce the total magnetization of magnets. Although the long-range dipolar interaction takes a complex form, it can be simplified in a two-dimensional limit to an effective easy-plane anisotropy [101, 130, 166]:

$$K_{\mathrm{dip,2D}} = -\frac{1}{2}\mu_0 M_s^2, \qquad (A.17)$$

where M_s is the saturation magnetization. Together with the ferromagnetic exchange interaction, the in-plane vortex phase is stabilized by the effective easy-plane anisotropy. This is also consistent with the result of Monte Carlo simulation, where the long-range dipolar interaction was fully evaluated [323].

A.4 Ginzburg-Landau theory

The spin Hamiltonian for chiral magnets such as MnSi was proposed in the continuum limit as [324]

$$H = \int dr^3 \Big[\frac{J}{2}(\nabla \boldsymbol{M})^2 + D\boldsymbol{M}\cdot(\nabla\times\boldsymbol{M}) - \mathbf{B}\cdot\boldsymbol{M} + A_1\sum_i M_i^4 - \frac{A_2}{2}\sum_i(\nabla_i M_i)^2 \Big], \quad (A.18)$$

where $\boldsymbol{M}$ is the magnetization and the lattice constant is taken to be unity. The first two terms represent the exchange coupling J and the Dzyaloshinskii-Moriya interaction D, while the third term is the Zeeman coupling under an applied magnetic field $\mathbf{B}$. The last two terms are magnetic anisotropies allowed by a cubic crystal symmetry, which are not necessary to stabilize magnetic skyrmions. This model takes the most general form up to the fourth order of magnetizations, which respects the crystalline symmetry of MnSi (space group $P2_13$).

Employing this model, the Ginzburg-Landau free energy functional near the critical temperature was written as [134]

$$F = \int dr^3 \big[r_0 M^2 + J(\nabla \boldsymbol{M})^2 + 2D\boldsymbol{M}\cdot(\nabla\times\boldsymbol{M}) + UM^4 - \mathbf{B}\cdot\boldsymbol{M} \big], \quad (A.19)$$

where $U > 0$ and r_0 is a linear function of temperatures T. As discussed below, the free energy functional is minimized by a magnetic helix with a wave vector $|\mathbf{Q}| = |D|/J$. In the following, we fix the Dzyaloshinskii-Moriya interaction $D > 0$ to choose a left-handed chirality of helices. The functional can be simplified by rewriting it in terms of dimensionless units, with the length, magnetization, and magnetic field rescaled as $\tilde{\boldsymbol{r}} = Q\boldsymbol{r}$, $\tilde{\boldsymbol{M}} = \sqrt{U/JQ^2}\boldsymbol{M}$, and $\tilde{\mathbf{B}} = \sqrt{U/(JQ^2)^3}\mathbf{B}$, respectively. Finally, we obtain

$$F = \gamma\int d\tilde{r}^3 \Big[(1+t)\tilde{M}^2 + (\tilde{\nabla}\tilde{\boldsymbol{M}})^2 + 2\tilde{\boldsymbol{M}}\cdot(\tilde{\nabla}\times\tilde{\boldsymbol{M}}) + \tilde{M}^4 - \tilde{\mathbf{B}}\tilde{\boldsymbol{M}} \Big], \quad (A.20)$$

where $t = r_0/JQ^2 - 1 \propto T - T_c$ and $\gamma = J^2Q/U$. For notational simplicity, we drop the tildes from now on.

The mean-field ground state of Eq. (A.20) is known to be the conical phase, a magnetic spiral with out-of-plane components parallel to the applied magnetic field [325]. In order to prove it, we first rewrite the free energy functional as

$$\begin{aligned} F &= -\frac{\gamma V(t^2 + B^2)}{4} \\ &+ \gamma\int dr^3 \Big[\Big(M^2 + \frac{t}{2}\Big)^2 + \Big(\boldsymbol{M} - \frac{\mathbf{B}}{2}\Big)^2 + (\nabla\boldsymbol{M})^2 + 2\boldsymbol{M}\cdot(\nabla\times\boldsymbol{M}) \Big], \quad (A.21) \end{aligned}$$

where V is the total volume. Now, we introduce the order parameter for a spiral phase as $\boldsymbol{\Phi} = \boldsymbol{M} - \boldsymbol{M}_f$ with the ferromagnetic component $\boldsymbol{M}_f = \int dr^3 \boldsymbol{M}$. Replacing the

magnetization $\boldsymbol{M}$ and performing the Fourier transform by noting $\boldsymbol{\Phi} = \sum_{\mathbf{q} \neq 0} \boldsymbol{m_q} e^{-i\mathbf{q}\cdot\mathbf{r}}$, we have

$$
\begin{aligned}
F &= -\frac{\gamma V(t^2 + B^2)}{4} + \gamma \int dr^3 \left[\left(M^2 + \frac{t}{2} \right)^2 + \left(\boldsymbol{M}_f - \frac{\mathbf{B}}{2} \right)^2 \right] \\
&+ V \sum_{\mathbf{q} \neq 0} \left[(q^2 + 1) \boldsymbol{m_{-q}} \cdot \boldsymbol{m_q} + 2i\mathbf{q} \cdot (\boldsymbol{m_{-q}} \times \boldsymbol{m_q}) \right].
\end{aligned}
\tag{A.22}
$$

As shown below, all the terms in square brackets vanishes for the conical phase solution:

$$
\boldsymbol{M}(\boldsymbol{r}) = m\hat{z} + \frac{a}{\sqrt{2}}(\hat{e}_+ e^{-iqz} + \hat{e}_- e^{iqz}),
\tag{A.23}
$$

where $\hat{e}_\pm = (\hat{x} \pm i\hat{y})/\sqrt{2}$ with $\hat{x}/\hat{y}/\hat{z}$ denoting a unit vector along $x/y/z$-axis. After substitution, it is straightforward to derive

$$
m = \frac{B}{2}, \quad a = \frac{1}{2}\sqrt{-2t - B^2}, \quad q = 1.
\tag{A.24}
$$

The minimized free energy is then given as

$$
\min[F] = -\frac{\gamma V(t^2 + B^2)}{4}.
\tag{A.25}
$$

We should note that the conical phase continuously transforms to the helical state at zero magnetic field. For $B > \sqrt{-2t}$, it becomes fully polarized along the applied magnetic field.

Importantly, there is another stable solution that is not a global minimum of the free energy. This metastable mean-field solution is the skyrmion crystal phase. For the skyrmion crystal phase, the fourth order term M^4 is important. Expanding this term with respect to the order parameter $\boldsymbol{\Phi}$, we have

$$
M^4 = M_f^4 + 4M_f^2 \boldsymbol{\Phi} \cdot \boldsymbol{M}_f + 2\boldsymbol{\Phi}^2 M_f^2 + 4(\boldsymbol{M}_f \cdot \boldsymbol{\Phi})^2 + 4\boldsymbol{\Phi}^2 \boldsymbol{\Phi} \cdot \boldsymbol{M}_f + \boldsymbol{\Phi}^4.
\tag{A.26}
$$

Up to the quadratic term with $\boldsymbol{\Phi}$, the energy is minimized by superposition of any helical states. However, the cubic term results in a solution with triple helices. After the Fourier transform, we obtain

$$
\int dr^3 \boldsymbol{\Phi}^2 \boldsymbol{\Phi} \cdot \boldsymbol{M}_f = V \sum_{\mathbf{q}_1, \mathbf{q}_2, \mathbf{q}_3 \neq 0} (\boldsymbol{M}_f \cdot \boldsymbol{m}_{\mathbf{q}_1})(\boldsymbol{m}_{\mathbf{q}_2} \cdot \boldsymbol{m}_{\mathbf{q}_3})\delta(\mathbf{q}_1 + \mathbf{q}_2 + \mathbf{q}_3).
\tag{A.27}
$$

From Eqs. (A.22-A.24), we know that $|\mathbf{q}_i| = 1$ for all helical states in the limit of $t \to 0$. Hence, the cubic term stabilizes the coplanar magnetic order consisting of triple helices with $\mathbf{q}_1 + \mathbf{q}_2 + \mathbf{q}_3 = 0$. The trial solution is thus written as

$$
\boldsymbol{M}(\boldsymbol{r}) = M_f\hat{z} + \sum_{j=1}^{3}(\boldsymbol{m}_{\mathbf{q}_j} e^{-i\mathbf{q}_j \cdot \boldsymbol{r}} + \text{c.c.}),
\tag{A.28}
$$

where

$$\boldsymbol{m}_{\mathbf{q}_j} = \frac{\psi_j}{2}(\hat{a}_\perp + i\hat{b}_{q_j}),\tag{A.29}$$

with $\psi_j = |\psi_j|e^{i\phi_j}$ is a complex number. Here, we have used that all wave vectors $\mathbf{q}_j$ lie on the same plane, so we take an orthonormal vector to the plane $\hat{a}_\perp$ as the basis vector for all helices, while $\hat{b}_{q_j}$ is defined on the plane satisfying $\hat{a}_\perp \times \hat{b}_{q_j} = \mathbf{q}_j$. Using this trial solution, the dot product between magnetization vectors of each helical states is given by

$$\boldsymbol{m}_{q_j} \cdot \boldsymbol{m}_{q_{j'}} = \frac{\psi_j\psi_{j'}}{4}(\hat{a}_\perp + i\hat{b}_{q_j}) \cdot (\hat{a}_\perp + i\hat{b}_{q_{j'}}) = \frac{3\psi_j\psi_{j'}}{8},\tag{A.30}$$

where we have used identities $\hat{b}_{q_j} \cdot \hat{b}_{q_{j'}} = -\frac{1}{2}$ and $\hat{b}_{q_j} \cdot \hat{a}_\perp = 0$ for $j \neq j'$. Equation (A.27) is then simplified as

$$\frac{3V\psi_1\psi_2\psi_3}{16} \sum_j \boldsymbol{M}_f \cdot (\hat{a}_\perp + i\hat{b}_{q_j}) + \text{c.c.} = \frac{9V|\psi_1||\psi_2||\psi_3|}{8}(\boldsymbol{M}_f \cdot \hat{a}_\perp)\cos(\phi_1 + \phi_2 + \phi_3).\tag{A.31}$$

Therefore, the energy of the cubic term is minimized with $\hat{a}_\perp \parallel \boldsymbol{M}_f$ and $\cos(\phi_1 + \phi_2 + \phi_3) = -1$. It is also clear that the equality $|\psi_1| = |\psi_2| = |\psi_3|$ minimizes the energy for normalized magnetization vectors $\boldsymbol{M}$. The obtained solution indeed corresponds to the skyrmion crystal phase as shown in Fig 1.8(a). We should note that Eq. (A.28) is an approximate solution as higher order Fourier terms are not included.

A.5 Continuum limit of spin lattice model

In this section, we derive a free energy functional from a two-dimensional spin lattice model defined on a square lattice and triangular lattice. Our purpose is to compare the difference between square lattice and triangular lattice, although they become equivalent in the continuum limit. In addition, we also illustrate that a spin lattice model contains higher order spatial derivatives that are not included in the continuum limit.

For both square and triangular lattice systems, our Hamiltonian is written from Eq. (1.3) as

$$\begin{aligned} H &= \frac{S^2}{2} \sum_{\boldsymbol{r}} \left[\sum_{i=1}^{p} -J(\boldsymbol{m_r} \cdot \boldsymbol{m_{r+a\hat{\alpha}_i}} + \boldsymbol{m_r} \cdot \boldsymbol{m_{r-a\hat{\alpha}_i}}) + \boldsymbol{D}_i \cdot (\boldsymbol{m_r} \times \boldsymbol{m_{r+a\hat{\alpha}_i}} - \boldsymbol{m_r} \times \boldsymbol{m_{r-a\hat{\alpha}_i}}) \right] \\ &\quad -g\mu_B B_z S \sum_{\boldsymbol{r}} \boldsymbol{m_r} \cdot \hat{z}, \end{aligned}\tag{A.32}$$

where $\boldsymbol{m_r}$ is the unit vector parallel to the magnetic moment with magnitude S at site $\boldsymbol{r}$ with lattice constant a. The unit vectors connecting the nearest neighbor sites are depicted as $\hat{\alpha}_i$ with the number of inequivalent bonds $p = 2(3)$ for the square (triangular) lattice. The nearest-neighbor coupling includes the ferromagnetic exchange coupling $J > 0$ and the DM interaction $\boldsymbol{D}_i = \hat{\alpha}_i$ for chiral magnets from Eq. (2.3). The last term

represents the coupling with the external magnetic field, where g and μ_B denotes the g-factor and Bohr magneton, respectively.

In the continuum limit $a \ll 1$, we have

$$\boldsymbol{m}_{\boldsymbol{r}+a\hat{\alpha}_i} = \boldsymbol{m}(\boldsymbol{r}) + a\alpha_i^j \frac{\partial \boldsymbol{m}(\boldsymbol{r})}{\partial x_j} + \frac{1}{2}a^2 \alpha_i^j \alpha_i^k \frac{\partial^2 \boldsymbol{m}(\boldsymbol{r})}{\partial x_j \partial x_k} + \cdots, \tag{A.33}$$

where only the lowest order spatial derivative is included in the continuum limit, α_i^j is the j-th component of the vector $\hat{\alpha}_i$, and the magnetization vector $\boldsymbol{m}_{\boldsymbol{r}}$ becomes a vector field $\boldsymbol{m}(\boldsymbol{r})$. In addition, the energy functional of a two-dimensional system is given by

$$\mathcal{F} = \int dr^2 F(\boldsymbol{m}(\boldsymbol{r})). \tag{A.34}$$

Hence, we have to replace the summation with the integration as $\sum_{\boldsymbol{r}} \to \frac{\int dr^2}{\Omega}$ where Ω is the area of a commensurate unit cell of the underlying lattice.

A.5.1 Square lattice

In the square lattice, we have $\hat{\alpha}_1 = \hat{x}, \hat{\alpha}_2 = \hat{y}$. The exchange interaction is given as follows.

$$
\begin{aligned}
-\frac{J}{2}\sum_{i=1}^{p=2} \boldsymbol{m}_{\boldsymbol{r}} \cdot (\boldsymbol{m}_{\boldsymbol{r}+a\hat{\alpha}_i} + \boldsymbol{m}_{\boldsymbol{r}-a\hat{\alpha}_i}) &= -\frac{J}{2}\sum_{i=1}^{p=2} \boldsymbol{m} \cdot \left(2\boldsymbol{m} + a^2 \alpha_i^j \alpha_i^k \frac{\partial^2 \boldsymbol{m}}{\partial x_j \partial x_k}\right) \\
&= -\frac{J}{2}[4 - a^2 (\nabla \boldsymbol{m})^2], \tag{A.35}
\end{aligned}
$$

where we have used $\boldsymbol{m} \cdot \boldsymbol{m} = 1$ and $\alpha_i^j \alpha_i^k = \delta^{jk}$ in the last line. In comparison, the DM interaction has lower dimension in length, because the first order derivative does not vanish for antisymmetric interactions. It is obtained as

$$
\begin{aligned}
\frac{1}{2}\sum_{i=1}^{p=2} \boldsymbol{D}_i \cdot \boldsymbol{m}_{\boldsymbol{r}} \times (\boldsymbol{m}_{\boldsymbol{r}+a\hat{\alpha}_i} - \boldsymbol{m}_{\boldsymbol{r}-a\hat{\alpha}_i}) &= \sum_{i=1}^{p=2} \boldsymbol{D}_i \cdot \boldsymbol{m} \times a\alpha_i^j \frac{\partial \boldsymbol{m}}{\partial x_j} = a\sum_{i=1}^{p=2} \boldsymbol{D}_i \cdot \boldsymbol{m} \times \frac{\partial \boldsymbol{m}}{\partial x_i} \\
&= aD\left(\hat{x} \cdot \boldsymbol{m} \times \frac{\partial \boldsymbol{m}}{\partial x} + \hat{y} \cdot \boldsymbol{m} \times \frac{\partial \boldsymbol{m}}{\partial y}\right). \tag{A.36}
\end{aligned}
$$

In the second equality, we have used $\alpha_i^j = \delta_i^j$. Finally, the free energy functional is given by

$$
\begin{aligned}
\mathcal{F} &= \int \frac{dr^2}{a^2} \left[\frac{S^2}{2}a^2 J(\nabla \boldsymbol{m})^2 + S^2 aD\left(\hat{x} \cdot \boldsymbol{m} \times \frac{\partial \boldsymbol{m}}{\partial x} + \hat{y} \cdot \boldsymbol{m} \times \frac{\partial \boldsymbol{m}}{\partial y}\right) - g\mu_B BS\boldsymbol{m} \cdot \hat{z}\right] \\
&= \int dr^2 \left[\frac{\mathcal{J}}{2}(\nabla \boldsymbol{m})^2 - \mathcal{D}\boldsymbol{m} \cdot (\nabla \times \boldsymbol{m}) - h(\boldsymbol{m} \cdot \hat{z})\right], \tag{A.37}
\end{aligned}
$$

where $[\mathcal{J}, \mathcal{D}, h] = [S^2 J, \frac{S^2 D}{a}, \frac{g\mu_B B_z S}{a^2}]$ and $\Omega = a^2$ for the square lattice.

A.5.2   Triangular lattice

In the triangular lattice, each site has three pairs of nearest neighbors connected by $\hat{\alpha}_1 = (1,0), \hat{\alpha}_2 = (1/2, \sqrt{3}/2)$, and $\hat{\alpha}_3 = (1/2, -\sqrt{3}/2)$. Similarly to the case of the square lattice, the exchange interaction and the DM interaction are written as

$$
-\frac{J}{2} \sum_{i=1}^{p=3} \boldsymbol{m_r} \cdot (\boldsymbol{m_{r+a\hat{\alpha}_i}} + \boldsymbol{m_{r-a\hat{\alpha}_i}}) = -\frac{J}{2}\boldsymbol{m} \cdot \left(6\boldsymbol{m} + a^2(1 + 2 \times \frac{1}{4})\frac{\partial^2 \boldsymbol{m}}{\partial^2 x} + 2 \times \frac{3}{4}\frac{\partial^2 \boldsymbol{m}}{\partial^2 y} \right)
$$
$$
= -\frac{J}{2}\left[6 - \frac{3}{2}a^2(\nabla\boldsymbol{m})^2 \right], \tag{A.38}
$$

$$
\frac{1}{2}\sum_{i=1}^{p=3} \boldsymbol{D}_i \cdot \boldsymbol{m_r} \times (\boldsymbol{m_{r+a\hat{\alpha}_i}} - \boldsymbol{m_{r-a\hat{\alpha}_i}}) = \sum_{i=1}^{p=3} \boldsymbol{D}_i \cdot \boldsymbol{m} \times a\alpha_i^j \frac{\partial \boldsymbol{m}}{\partial x_j}
$$
$$
= a\boldsymbol{D}_1 \cdot \boldsymbol{m} \times \frac{\partial \boldsymbol{m}}{\partial x} + a\boldsymbol{D}_2 \cdot \boldsymbol{m} \times \left(\frac{1}{2}\frac{\partial \boldsymbol{m}}{\partial y} + \frac{\sqrt{3}}{2}\frac{\partial \boldsymbol{m}}{\partial y} \right)
$$
$$
+ \ a\boldsymbol{D}_2 \cdot \boldsymbol{m} \times \left(\frac{1}{2}\frac{\partial \boldsymbol{m}}{\partial y} - \frac{\sqrt{3}}{2}\frac{\partial \boldsymbol{m}}{\partial y} \right).
$$
$$
= \frac{3Da}{2}(\hat{x} \cdot \boldsymbol{m} \times \frac{\partial \boldsymbol{m}}{\partial x} + \hat{y} \cdot \boldsymbol{m} \times \frac{\partial \boldsymbol{m}}{\partial y}). \tag{A.39}
$$

In the triangular lattice, the unit area is given as $\Omega = \sqrt{3}/2a^2$. The energy functional is then obtained as

$$
\mathcal{F} \ = \ \int dr^2 \left[\frac{\mathcal{J}}{2}(\nabla\boldsymbol{m}) - \mathcal{D}\boldsymbol{m} \cdot (\nabla \times \boldsymbol{m}) - h(\boldsymbol{m} \cdot \hat{z}) \right], \tag{A.40}
$$

where $[\mathcal{J}, \mathcal{D}, h] = [\sqrt{3}S^2 J, \frac{\sqrt{3}S^2 D}{a}, \frac{2g\mu_B B_z S}{\sqrt{3}a^2}]$.

Now, we divide Eq. (A.40) by $\sqrt{3}$ and rescale all constants $[\mathcal{J}, \mathcal{D}, h]$ so that $\mathcal{J}$ becomes the same in Eqs. (A.37) and (A.40). We find that $[\mathcal{J}, \mathcal{D}, h] = [S^2 J, \frac{S^2 D}{a}, \frac{2g\mu_B B_z S}{3a^2}]$ for the triangular lattice. This indicates that the magnetic field B_z is effectively rescaled by $\frac{3}{2}$ in the triangular lattice in comparison to the square lattice.

A.6   Classical spin dynamics

In this section, we introduce the Landau-Lifshitz-Gilbert (LLG) equation, which is the equation of motion for classical spins with a phenomenological damping term, known as the Gilbert damping [286]. To obtain the atomistic LLG equation, we substitute the spin operators $\boldsymbol{S_r}$ in the spin lattice Hamiltonian by $S\boldsymbol{m_r}$, where $\boldsymbol{m_r}$ is a unit vector. After this substitution, the LLG equation describes the dynamics of classical spins as

$$
\frac{d\boldsymbol{m_r}}{dt} = -\frac{\gamma\boldsymbol{m_r}}{1 + \alpha^2} \times \left[\boldsymbol{H_r^{\text{eff}}} + \alpha\boldsymbol{m_r} \times \boldsymbol{H_r^{\text{eff}}} \right], \tag{A.41}
$$

where $\boldsymbol{H}_{\boldsymbol{r}}^{\text{eff}} = -[1/(\hbar\gamma S)]\partial H/\partial \boldsymbol{m}_{\boldsymbol{r}}$, $\gamma = g\mu_B/\hbar$ is the gyromagnetic ratio, and α is the Gilbert damping constant. Throughout this thesis we use $\alpha = 0.04$ unless otherwise stated. We also fix the temperature at $T = 0$ K, so thermal fluctuations are not included in Eq. (A.41). Time is measured in units of $\hbar/(JS)$. Assuming the exchange coupling $J = 1$ meV and $S = 1$, the time scale is in the order of 0.7 ps.

A.7 Derivation of edge twist and edge instability

A.7.1 Edge twist

Let us consider a one-dimensional ferromagnet with chiral modulations due to the Dzyaloshinskii-Moriya interaction by reviewing Ref. [101]. Assuming a one-dimensional spin chain along z axis under the magnetic field H applied along x axis, the classical ground state configuration of a helicoid is described by $\boldsymbol{M}/M_s = \boldsymbol{m} = (\cos\theta, \sin\theta, 0)$ where $M_s = |\boldsymbol{M}|$ is the saturation magnetization. Taking the lattice constant to be unity, the energy density is given by

$$
\begin{aligned}
E &= \int_{z_1}^{z_2} dz\, A\Big(\frac{d\boldsymbol{m}}{dz}\Big)^2 + D\hat{z}\cdot\Big(\boldsymbol{m}\times\frac{d\boldsymbol{m}}{dz}\Big) - \mu_0 H M_s \cos\theta \\
&= \int_{z_1}^{z_2} dz\, A\Big(\frac{d\theta}{dz}\Big)^2 - D\frac{d\theta}{dz} - \mu_0 H M_s \cos\theta,
\end{aligned}
\tag{A.42}
$$

where A is the exchange stiffness and D is the strength of the Dzyaloshinskii-Moriya interaction. In an infinite system, it forms a periodic array of helicoids with the zero-field helical wavelength $L_D = 4\pi A/D$, known as the chiral soliton lattice [132, 133, 326]. As the magnetic field is increased, the periodicity of helicoids continuously increases until the critical magnetic field $\pi^2 H_D/16$ with $H_D = D^2/2A\mu_0 M_s$ where it becomes fully polarized.

The property of the helical phase is strongly modified when a free boundary condition is introduced. Using the Variational principle, the change in the energy density at $\theta'(z) = \theta(z) + \epsilon\alpha(z)$ is given by

$$
\begin{aligned}
\delta E &= \epsilon\int_{z_1}^{z_2} dz\, \Big[2A\frac{d\alpha}{dz}\frac{d\theta}{dz} - D\frac{d\alpha}{dz} + \mu_0 H M_s \alpha \sin\theta\Big] \\
&= \epsilon\int_{z_1}^{z_2} dz\, \alpha\Big[-2A\frac{d^2\theta}{dz^2} + \mu_0 H M_s \sin\theta\Big] + \Big[\epsilon\alpha\Big(2A\frac{d\theta}{dz} - D\Big)\Big]_{z_1}^{z_2}. \quad\text{(A.43)}
\end{aligned}
$$

For the last equality, we have used the integration by parts. The energy density is minimized by $\theta(z)$ satisfying [100–102]

$$
\begin{aligned}
\frac{d^2\theta}{dz^2} &= \frac{\mu_0 H M_s \sin\theta}{2A} \quad \text{for } z_1 < z < z_2, \\
\frac{d\theta}{dz} &= \frac{D}{2A} \quad \text{for } z = z_1 \text{ or } z = z_2.
\end{aligned}
\tag{A.44}
$$

From the analytical solution of $\theta(z)$, it was shown that the periodicity of helicoid cannot change continuously in a confined system. Instead, the number of turns is quantized and changes with the magnetic field as a first order transition. Another point is that the second equation derived by the free boundary condition has an important implication that spin textures are twisted near edges at $D \neq 0$. As a result, the in-plane magnetization of thin film MnSi samples was not fully polarized even under the field greater than H_D due to the chiral modulation at boundaries [100]. Hence, the Dzyaloshinskii-Moriya interaction leads to the unique boundary condition that plays an important role in both surfaces and edges of thin film samples. It should be noted that this is a general property of magnetic systems without the inversion symmetry. The angle of twist depends on the form of the Dzyaloshinskii-Moriya interaction allowed by the symmetry of systems.

A.7.2   Edge instability

In this section, we review Ref. [105] to show the instability of twisted edge magnetizations in the presence of the Dzyaloshinskii-Moriya interaction. The free energy functional of a two-dimensional chiral magnet is given by

$$\mathcal{F} = \int dr^2 \Big[\sum_{i=1}^{3} A\Big(\frac{d\boldsymbol{m}}{dx_i}\Big)^2 + D\Big(\hat{x}\cdot\boldsymbol{m}\times\frac{d\boldsymbol{m}}{dx} + \hat{y}\cdot\boldsymbol{m}\times\frac{d\boldsymbol{m}}{dy}\Big) - Km_z^2 - \mu_0 H M_s m_z \Big], \quad \text{(A.45)}$$

where $\boldsymbol{m} = \boldsymbol{M}/M_s$ with $M_s = |\boldsymbol{M}|$ denoting the saturation magnetization, A is the exchange stiffness, D is the strength of the Dzyaloshinskii-Moriya interaction, and K is the magnetic anisotropy.

Using Eq. (A.45), we consider a semi-infinite system for $y \geq 0$ and periodic along x-axis in the ferromagnetic phase. In the presence of the Dzyaloshinskii-Moriya interaction, the edge magnetization at $y = 0$ is twisted along x-axis. Assuming the translational invariance in x-axis, the magnetization is described by $\boldsymbol{m} = (\sin\theta(y), 0, \cos\theta(y))$. Here, we introduce dimensionless variables using the zero-field helical wavelength $L_D = 4\pi A/D$ and the zero-anisotropy critical field $H_D = D^2/2A\mu_0 M_s$ [326]. The characteristic momentum Q, magnetic field h, and anisotropy κ are defined as

$$Q = \frac{2\pi}{L_D} = \frac{D}{2A}, \quad h = \frac{H}{H_D} = \frac{\mu_0 H M_s}{2AQ^2}, \quad \kappa = \frac{K}{AQ^2}. \quad \text{(A.46)}$$

Similarly, the unit of length, time, and energy are scaled as

$$\tilde{x} = xQ, \quad \tilde{y} = yQ, \quad \tilde{t} = \frac{t}{\gamma\mu_0 H_D}, \quad \tilde{\epsilon} = \frac{\epsilon}{\hbar/\gamma\mu_0 H_D}, \quad \text{(A.47)}$$

where $\gamma = g\mu_B/\hbar$ is the gyromagnetic ratio.

Analogously to the derivation of Eq. (A.44), the equation of motions for $\theta(\tilde{y})$ is written as

$$\begin{aligned}
\frac{d^2\theta}{d\tilde{y}^2} &= h\sin\theta + \frac{\kappa}{2}\sin 2\theta \quad \text{for } \tilde{y} > 0, \\
\frac{d\theta}{d\tilde{y}} &= 1 \quad \text{for } \tilde{y} = 0.
\end{aligned} \quad \text{(A.48)}$$

In the limit of $\tilde{y} \to \infty$, it is taken as $\theta(\tilde{y}) = 0$ and $\theta'(\tilde{y}) = 0$ so that the magnetization is aligned with the applied field in bulk. In addition, the second equation implies $\theta'(\tilde{y}) > 0$ and $-2\pi < \theta(\tilde{y}) \le 0$. Multiplying θ' to both sides, the first integral of Eq. (A.48) is obtained as

$$\frac{\theta'}{\sqrt{2h(1 - \cos\theta) + \kappa(1 - \cos\theta^2)}} = 1. \tag{A.49}$$

The above differential equation is solved by separation of variables. The obtained expression is

$$\frac{1}{\sqrt{h + \kappa}} \operatorname{arctanh} \sqrt{\frac{(h + \kappa)(\cos\theta + 1)}{2h + \kappa(\cos\theta + 1)}} = \tilde{y} - \tilde{y}_0, \tag{A.50}$$

where $\tilde{y}_0$ is an integration constant. In order to derive the inverse function $\theta(\tilde{y})$, it is rewritten as

$$
\begin{aligned}
\tanh^2\left[\sqrt{h + \kappa}\,(\tilde{y} - \tilde{y}_0)\right] &= \frac{(h + \kappa)(\cos\theta + 1)}{2h + \kappa(\cos\theta + 1)} = \frac{h + \kappa}{\frac{2h}{\cos\theta + 1} + \kappa} \\
&= \frac{1}{\frac{1}{h+\kappa}\left(\frac{h}{\cos^2\frac{\theta}{2}} - h\right) + 1} = \frac{1}{\frac{h}{h+\kappa}\tan^2\frac{\theta}{2} + 1}.
\end{aligned}
\tag{A.51}
$$

Using $\tanh^2 x = \frac{\sinh^2 x}{1 + \sinh^2 x}$, the final expression is obtained as [105]

$$\theta(\tilde{y}) = -\pi + 2\arctan\left[\sqrt{\frac{h}{h + \kappa}}\sinh(\sqrt{h + \kappa}\,(\tilde{y} - \tilde{y}_0))\right]. \tag{A.52}$$

From the boundary condition $\theta'(0) = 1$, the integration variable is given by

$$\tilde{y}_0 = -\frac{1}{\sqrt{\kappa + h}}\operatorname{arccosh}\left[\frac{h + \kappa + \sqrt{(h + \kappa)^2 - \kappa}}{\sqrt{h}}\right]. \tag{A.53}$$

The analytical solution in Eq. (A.52) is a monotonically increasing function with $\tilde{y}$. At the edge ($y = 0$), the magnetization is aligned to the negative x direction with an angle from z-axis increasing for smaller magnetic fields and anisotropies.

The magnon excitation of the ferromagnetic phase has a quadratic dispersion with the band gap $\Delta_b = h + \kappa$. In addition, the edge twist introduces an effective local potential, leading to magnonic states localized to edges. In order to study the magnonic bound states arising from the edge twist, we consider fluctuations from the saddle-point solution obtained in Eqs. (A.52) and (A.53). Following the standard procedure to construct an effective Bogoliubov–de Gennes Hamiltonian (see Section 1.1.3), we define a local basis:

$$
\begin{aligned}
\boldsymbol{e}_1 &= (0, 1, 0), \\
\boldsymbol{e}_2 &= (-\cos\theta, 0, \sin\theta), \\
\boldsymbol{e}_3 &= \boldsymbol{m} = (\sin\theta, 0, \cos\theta).
\end{aligned}
\tag{A.54}
$$

Employing the Holstein-Primakoff transformation, the normalized magnetization field is written as

$$\boldsymbol{m} = \boldsymbol{e}_3\sqrt{1 - 2|\psi|^2} + \boldsymbol{e}_+\psi + \boldsymbol{e}_-\psi^*, \tag{A.55}$$

where $\boldsymbol{e}_\pm = (\boldsymbol{e}_1 \pm i\boldsymbol{e}_2)/\sqrt{2}$. The magnon wave functions are represented by $\psi(\tilde{x}, \tilde{y}, \tilde{t})$ satisfying the translational invariance along x axis.

The spin wave Hamiltonian is constructed from the classical spin dynamics described by the Landau–Lifshitz equation. Here, the effect of damping is not included since we only need the precession around the classical spin ground state corresponding to magnon modes. It is given by

$$\frac{d\boldsymbol{m}}{dt} = -\gamma\boldsymbol{m} \times \mathbf{B}_F, \tag{A.56}$$

where $\mathbf{B}_F = -\frac{\partial\mathcal{F}}{\partial\boldsymbol{M}}$. Using the dimensionless physical units defined in Eqs. (A.46) and (A.47), we have

$$\frac{d\boldsymbol{m}}{d\tilde{t}} = \tilde{\nabla}^2\boldsymbol{m} - 2\tilde{\nabla} \times \boldsymbol{m} + h\hat{z} + \kappa m_z\hat{z}, \tag{A.57}$$

where $\tilde{\nabla}_{x/y} = \partial_{\tilde{x}/\tilde{y}}$ is a differential operator with respect to dimensionless coordinates. Substituting Eq. (A.55) and collecting only linear terms in ψ, it is written as

$$i\tau^z\partial_{\tilde{t}}\Psi = H\Psi, \tag{A.58}$$

where τ^i is the Pauli matrices and $\Psi = (\psi, \psi^*)^T$. In this spinor representation, the spin up/down state correspond to vector elements of $(\mp i\boldsymbol{e}_1 + \boldsymbol{e}_2)/\sqrt{2}$.

The Bogoliubov–de Gennes Hamiltonian is derived as [105]

$$H = H_0 + V, \tag{A.59}$$

with H_0 and $V = V(\tilde{y})$ denoting the bulk Hamiltonian and the edge potential due to the edge twist, respectively. After taking the Fourier transform in the x direction, they are given as

$$
\begin{aligned}
H_0 &= -\partial_{\tilde{y}}^2 + \tilde{q}_x^2 + \Delta_b, \\
V &= \tau_0\Big[-\theta'^2 + \theta' - \kappa\sin^2\theta\Big] + \tau_z 2\tilde{q}_x\sin\theta + \tau_x\Big[-\frac{1}{2}\theta'^2 + \theta' + \frac{\kappa}{2}\sin^2\theta\Big],
\end{aligned} \tag{A.60}
$$

where $\tilde{q}_x = q_x/Q$, τ_0 is the identity matrix, and $\Delta_b = h + \kappa$ corresponds to the bulk band gap of magnon spectrum. We have used the equality in Eq. (A.49) to obtain the above expression.

The magnon spectrum can be obtained numerically by solving Eq. (A.58). The eigenfunction satisfies

$$H\Phi = \tilde{\epsilon}(\tilde{q}_x)\tau_z\Phi \tag{A.61}$$

with $\Phi = (\phi_1, \phi_2)^T$ for normalized functions ϕ_1 and ϕ_2. The corresponding magnon wavefunction is given by $\psi(\tilde{q}_x, \tilde{y}, \tilde{t}) = \phi_1(\tilde{q}_x, \tilde{y})e^{i\tilde{\epsilon}(\tilde{q}_x)\tilde{t}} + \phi_2^*(\tilde{q}_x, \tilde{y})e^{-i\tilde{\epsilon}(\tilde{q}_x)\tilde{t}}$. Of particular
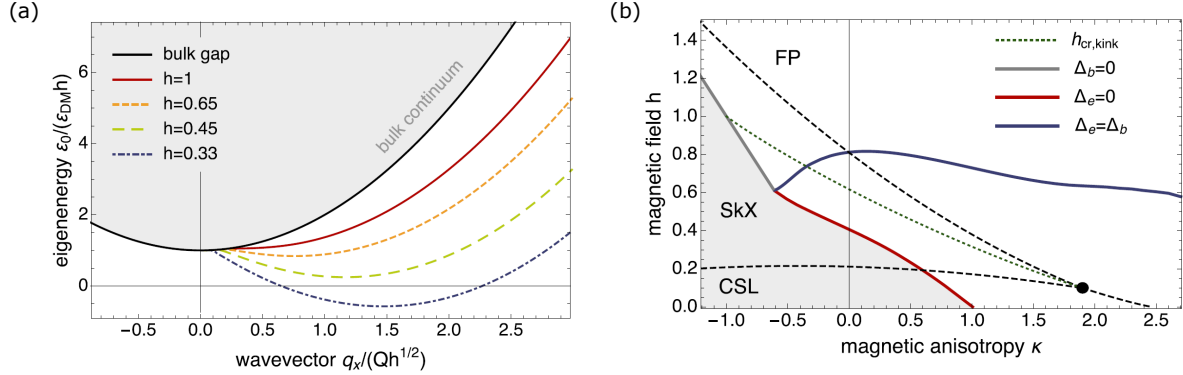
Figure A.2: **Edge instability below critical magnetic fields due to magnonic bound states at twisted edge magnetizations.** (a) Magnon energy dispersion $\tilde{\epsilon}(\tilde{q}_x) = \epsilon(\tilde{q}_x)/\epsilon_{\mathrm{DM}}$ of edge localized states with the lowest energy, obtained at $h =$ 1, 0.65, 0.45, 0.33 and $\kappa = 0$. The gray shaded area implies the bulk magnon bands with the rescaled bulk band gap ($\Delta_b/h = 1$). (b) Stability of the field-polarized state (FP) near the edge and in the bulk of samples. The black dashed line indicates the phase boundaries between the FP state, the skyrmion crystal (SkX), and the chiral soliton lattice (CSL) in the thermodynamic limit [311]. While the FP state is metastable in the white region, it becomes unstable in the gray shaded region. The red line indicates the critical fields for the local instability where the edge gap Δ_e becomes zero. On the gray solid line at $h = -\kappa$, the bulk energy gap closes, and the FP state becomes globally unstable. Below the blue line where $\Delta_e = \Delta_b$, there exists exponentially localized edge states with the energy $\Delta_e \leq \tilde{\epsilon}_e \leq \Delta_b$. Adapted from [105].

interest is bound states that are exponentially localized to edges. From Eq. (A.60), its asymptotic behavior in the limit of $\tilde{y} \to \infty$ is described by

$$\Phi(\tilde{y}) \sim \begin{pmatrix} c_1 e^{-\tilde{y}\sqrt{\Delta_b + \tilde{q}_x^2 - \tilde{\epsilon}(\tilde{q}_x)}} \\ c_2 e^{-\tilde{y}\sqrt{\Delta_b + \tilde{q}_x^2 + \tilde{\epsilon}(\tilde{q}_x)}} \end{pmatrix}, \tag{A.62}$$

with c_1 and c_2 being complex phases. Hence, edge localized magnon modes exist below the bulk continuum. It turns out there are many solutions for bound states with a different number of nodes in one-dimensional wave functions. In the following, we consider the lowest energy mode that is most strongly localized near the edge.

Figure A.2(a) shows the magnon spectrum of edge localized states at different magnetic fields and zero anisotropy $\kappa = 0$. The edge spectrum of bound states are highly anisotropic as it only allows positive values of $\tilde{q}_x$. Furthermore, their group velocity $\partial\epsilon/\partial q_x$ is almost always positive for large magnetic fields, implying that there is a preferred direction of propagation in magnonic edge states. Therefore, it is a chiral mode, although it is not a topologically protected edge state of Chern insulators. Instead of bulk topology, the chirality of edge states arises from the chiral edge twist, so the edge spectrum of the opposite edge is given by inverting the sign of $\tilde{q}_x$. Interestingly, the edge

spectrum is invariant with changing the sign of the Dzyaloshinskii-Moriya interaction in spite of the inverted in-plane components of edge magnetization.

Another important point is that the minimum energy of edge spectrum Δ_e becomes smaller at lower magnetic fields. In Ref. [105], the critical value was obtained as $h_c = 0.4067$ where the minimal value reaches zero energy at some momentum $q_x > 0$. In general, a negative energy of magnon spectrum implies the instability of underlying spin textures due to the magnon condensation. Hence, the critical magnetic field sets a lower bound for the metastable ferromagnetic phase. Below the critical field, it becomes locally unstable against creation of helical domains from edges as discussed in Section 1.3.4.

The stability of the ferromagnetic phase in the parameter space of (κ, h) is summarized in Fig. A.2(b). In two-dimensional systems, there exist three magnetic phases, known as the ferromagnetic phase, skyrmion crystal, and helical phase. The black dashed lines are the phase boundaries between them in the thermodynamic limit [311]. By adiabatically reducing the magnetic field at low temperatures, the ferromagnetic phase can persist beyond the phase boundary as a metastable state, indicated by the white regime. However, when the bulk/edge gap of magnon bands vanishes, it becomes unstable (gray regime). For $\kappa < -0.61$, the bulk band gap Δ_b vanishes at $\tilde{q}_x = 0$ and $h = -\kappa$ on the gray solid line, resulting in a global instability. In contrast, the ferromagnetic phase becomes locally unstable near edges for $\kappa > -0.61$ when the edge gap Δ_e vanishes on the red solid line.

A.8   Derivation of emergent electromagnetic field

Following Ref. [95], we derive the expressions for effective electromagnetic fields due to the noncoplanar spin structures. Let us consider a free electron model coupled to the magnetization:

$$i\hbar\frac{\partial \Psi}{\partial t} = \left[\frac{p^2}{2m_e} - g\boldsymbol{\sigma}\cdot\boldsymbol{m}(\boldsymbol{r},t)\right]\Psi, \tag{A.63}$$

where m_e is the electron mass, $\mathbf{p} = -i\hbar\nabla$ is the momentum, $\boldsymbol{\sigma}$ is the Pauli matrices, g is the coupling strength, and $\boldsymbol{m} = (\sin\theta\cos\phi, \sin\theta\sin\phi, \cos\theta)$ is the normalized magnetization. Assuming g to be sufficiently large and $\boldsymbol{m}$ to be a smooth function in space and time, the spin of conduction electrons is always parallel to $\boldsymbol{m}$.

Now, we perform the gauge transformation to rotate the spin quantization axis of conduction electrons along $\boldsymbol{m}$. By applying the rotation matrix to Ψ, a new wave function is given by

$$\Phi = U^\dagger(\boldsymbol{r},t)\Psi, \tag{A.64}$$

with

$$U = \exp\left(-i\frac{\theta}{2}\boldsymbol{\sigma}\cdot\boldsymbol{n}\right) = \cos\frac{\theta}{2}\sigma_0 - i\sin\frac{\theta}{2}(\boldsymbol{\sigma}\cdot\boldsymbol{n}), \tag{A.65}$$

where σ_0 is the identity matrix. The rotation axis $\boldsymbol{n}$ is defined as

$$\boldsymbol{n} = \frac{\hat{z}\times\boldsymbol{m}}{|\hat{z}\times\boldsymbol{m}|}. \tag{A.66}$$

We should note that the unitary matrix U satisfies the following identities for some vector field $\boldsymbol{\alpha}$.

$$U^\dagger(\boldsymbol{\sigma}\cdot\boldsymbol{\alpha})U = \left\{\cos\frac{\theta}{2}\sigma_0 + i\sin\frac{\theta}{2}(\boldsymbol{\sigma}\cdot\boldsymbol{n})\right\}(\boldsymbol{\sigma}\cdot\boldsymbol{\alpha})\left\{\cos\frac{\theta}{2}\sigma_0 - i\sin\frac{\theta}{2}(\boldsymbol{\sigma}\cdot\boldsymbol{n})\right\}$$
$$= \cos\theta(\boldsymbol{\sigma}\cdot\boldsymbol{\alpha}) + \sin\theta\left\{\boldsymbol{\sigma}\cdot(\boldsymbol{\alpha}\times\boldsymbol{n})\right\} + (1-\cos\theta)(\boldsymbol{\alpha}\cdot\boldsymbol{n})(\boldsymbol{\sigma}\cdot\boldsymbol{n}), \quad \text{(A.67)}$$

where the second line is obtained from $(\boldsymbol{\sigma}\cdot\boldsymbol{\alpha})(\boldsymbol{\sigma}\cdot\boldsymbol{n}) = \boldsymbol{\alpha}\cdot\boldsymbol{n} + i\boldsymbol{\sigma}\cdot(\boldsymbol{\alpha}\times\boldsymbol{n})$. From Eq. (A.67), the Schrödinger equation is rewritten as

$$i\hbar\frac{\partial\Phi}{\partial t} = \left[\frac{(\mathbf{p}+\frac{e}{c}\mathbf{A}^s)^2}{2m_e} - g\sigma_z - eV^s\right]\Phi, \quad \text{(A.68)}$$

where $e > 0$ is the elementary charge. Here, the gauge transformation transforms the coupling with the magnetization $\boldsymbol{m}$ to a vector potential $\mathbf{A}^s$ and V^s, which are given by [327]

$$\mathbf{A}^s = -\frac{i\hbar c}{e}U^\dagger\nabla U = \frac{\hbar c}{2e}\left\{\nabla\theta(\boldsymbol{\sigma}\cdot\boldsymbol{n}) - \sin\theta\nabla\phi\,\boldsymbol{\sigma}\cdot(\boldsymbol{n}\times\hat{z}) + \nabla\phi(1-\cos\theta)\sigma_z\right\},$$
$$V^s = \frac{i\hbar}{e}U^\dagger\partial_t U = -\frac{\hbar}{2e}\left\{\partial_t\theta(\boldsymbol{\sigma}\cdot\boldsymbol{n}) - \sin\theta\partial_t\phi\,\boldsymbol{\sigma}\cdot(\boldsymbol{n}\times\hat{z}) + \partial_t\phi(1-\cos\theta)\sigma_z\right\}. \text{(A.69)}$$

In the limit of $g \to \infty$, the ground state for the above equation has a fully polarized spin along the magnetization $\boldsymbol{m}$. Taking the vector potential and scalar potential as perturbations, the unperturbed Hamiltonian for a spin-up state is described by

$$H = \frac{(\mathbf{p}+\frac{e}{c}\mathbf{A}^s)^2}{2m_e} - g - eV^s, \quad \text{(A.70)}$$

with $\mathbf{A}^s = \frac{\hbar c}{2e}\nabla\phi(1-\cos\theta)$ and $V^s = -\frac{\hbar}{2e}\partial_t\phi(1-\cos\theta)$. Finally, the effective magnetic and electric fields are given by [173, 175]

$$B_z^s = \partial_x A_y^s - \partial_y A_x^s = \frac{\hbar c}{2e}\boldsymbol{m}\cdot(\partial_x\boldsymbol{m}\times\partial_y\boldsymbol{m}), \quad \text{(A.71)}$$

and

$$E_i^s = -\partial_i V^s - \frac{1}{c}\partial_t A_i^s = \frac{\hbar}{2e}\boldsymbol{m}\cdot(\partial_i\boldsymbol{m}\times\partial_t\boldsymbol{m}). \quad \text{(A.72)}$$

We have considered a simple continuum model to derive the emergent electromagnetic fields induced by noncoplanar magnetic textures. It should be noted that the equivalent result was obtained in a tight-binding model with spins ferromagnetically coupled to magnetization at each site by Hund's rule coupling [172, 178]. In the strong coupling limit, the hopping matrix of conduction electrons acquires an extra phase factor as the spin quantization axis of electrons rotates along the magnetization. This is in fact a geometrical phase that is equal to half the solid angle Ω subtended by three spins $\mathbf{S}_1$, $\mathbf{S}_2$, and $\mathbf{S}_3$ for a closed loop connecting them. Furthermore, it is proportional to a scalar spin chirality $\mathbf{S}_1\cdot(\mathbf{S}_2\times\mathbf{S}_2)$ for small Ω.
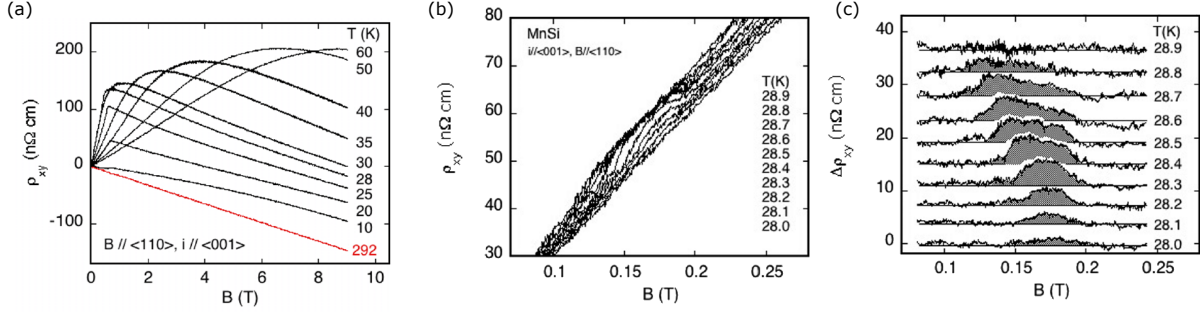
Figure A.3: **Topological Hall effect observed in a bulk sample of MnSi.** (a) Hall resistivity for single crystal MnSi. The magnetic field was applied along [110] direction, and the electric current was applied along [001] direction. (b) Hall resistivity near T_c where the skyrmion crystal phase is stable. (c) Additional Hall resistivity $\Delta\rho_{xy} = \rho_{xy}^T$ due to the topological Hall effect. Adapted from [135].

A.9 Topological Hall effect and Skyrmion Hall effect

The emergent gauge field arising from the non-zero scalar spin chirality results in the Hall motion of conduction electrons, known as the topological Hall effect. In the literatures, two different mechanisms were discussed for the topological Hall effect [179, 181]. When the periodicity of magnetic order is much longer than the underlying lattice structure, the topological Hall effect is characterized by the real space topological spin structures. Another possibility is that the topological Hall effect is associated with a nontrivial topological band structure in the reciprocal space, which could be realized by several inequivalent loops in a unit cell with a finite scalar spin chirality [177, 178]. In the following, we briefly review the experiments on the topological Hall effect due to the real space topological structures of magnetic skyrmions.

The Hall resistivity is generally written as [94, 95]

$$\rho_{xy} = \rho_{xy}^N + \rho_{xy}^A + \rho_{xy}^T = R_0 B + S_A \rho_{xx}^2 M + P R_0 B_z^s, \tag{A.73}$$

where ρ_{xy}^N is the normal Hall effect proportional to the Hall coefficient R_0 and ρ_{xy}^A is the anomalous Hall resistivity proportional to the magnetization M. Here, S_A denotes the coupling coefficient and $P(0 < P < 1)$ is the spin polarization ratio of conduction electrons. The contribution from the topological Hall effect is denoted as ρ_{xy}^T, which is proportional to the emergent magnetic field B_z^s. From Eq. (1.62), it is written as

$$B_z^s = \Psi_0 \rho(\boldsymbol{m}), \tag{A.74}$$

where $\Psi_0 = 2\pi\hbar c/e$ is the magnetic flux quantum, and the topological charge density $\rho(\boldsymbol{m})$ is given by

$$\rho(\boldsymbol{m}) = \frac{1}{4\pi}\boldsymbol{m} \cdot (\partial_x \boldsymbol{m} \times \partial_y \boldsymbol{m}). \tag{A.75}$$

Without the topological Hall effect, the Hall resistivity can be fitted well as a function of magnetic fields. Hence, we could estimate the contribution from the topological Hall
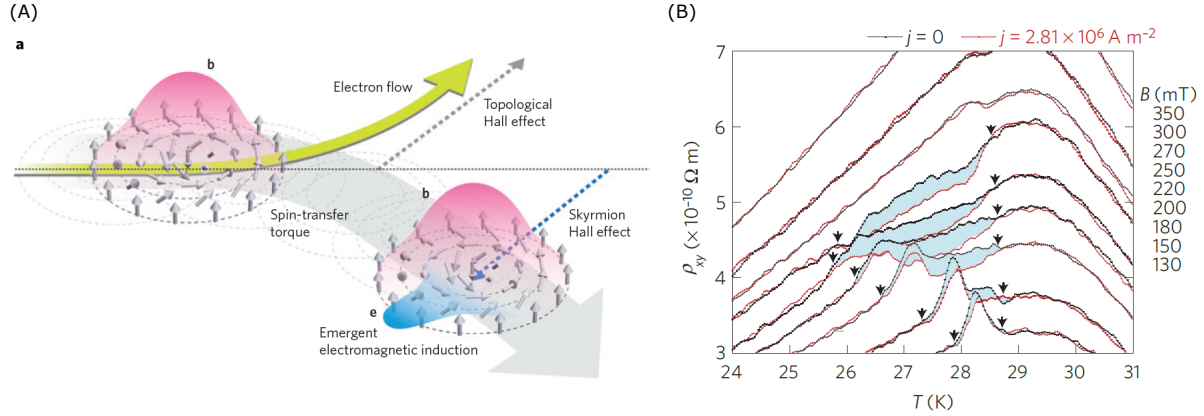
Figure A.4: **Skyrmion Hall effect and the emergent electromagnetic induction.**
(A) Schematic representation of topological Hall effect and skyrmion Hall effect. (B)
Hall resistivity ρ_{xy} as a function of temperatures in the skyrmion crystal phase with and
without applied d.c. current, measured in a single crystal of MnSi. (A) is adapted from
Ref. [94] and (B) is adapted from Ref. [328].

effect by deviations from fitted lines. This is illustrated in Fig. A.3, where an additional
contribution in the Hall resistivity was observed in MnSi near the critical temperature as
the skyrmion crystal phase was stabilized. Figure A.3(a) shows that the Hall resistivity is
linearly proportional to magnetic fields with a negative coefficient at room temperatures.
This is explained by the normal Hall effect. In contrast, $\Delta\rho_{xy}$ shown in Fig. A.3(c) has
a positive contribution, implying the negative topological charge of skyrmions. Further-
more, it was shown that the obtained value of $\Delta\rho_{xy}$ is in excellent agreement with the
estimated value of ρ_{xy}^T.

As a counterpart to the topological Hall effect, spin-polarized electric current can
drag skyrmions by the spin-transfer torque [175]. We should note that the manipulation
of spins using spin-transfer torque has been studied extensively in ferromagnetic domain
walls [329–332], which promises to be important for device applications such as race track
memory [260, 261]. In fact, the current-induced reversal of magnetization is already
implemented in commercially available MRAM devices [333].

Skyrmions can be considered as circulating spin currents from their vortexlike spin
structure. When they are driven by spin-polarized electric currents, the imbalance of
spin currents is generated. As a result, a Magnus force is exerted on skyrmions to deflect
their motion from the direction parallel to electric currents, known as the skyrmion Hall
effect (Fig. A.4(a)). The skyrmion Hall effect was first demonstrated in MnSi by rota-
tions of neutron scattering diffraction patterns under the application of a temperature
gradient and electric current parallel to each other [185]. Remarkably, it was found that
the threshold current density for the skyrmion motion is five orders of magnitude smaller
than that of the domain wall motion. Employing the classical spin dyna mics described
by the Landau-Lifshitz-Gilbert-Slonczewski equation [329], this was partly explained by
the particle nature of skyrmions that allows them to overcome the pinning effect from
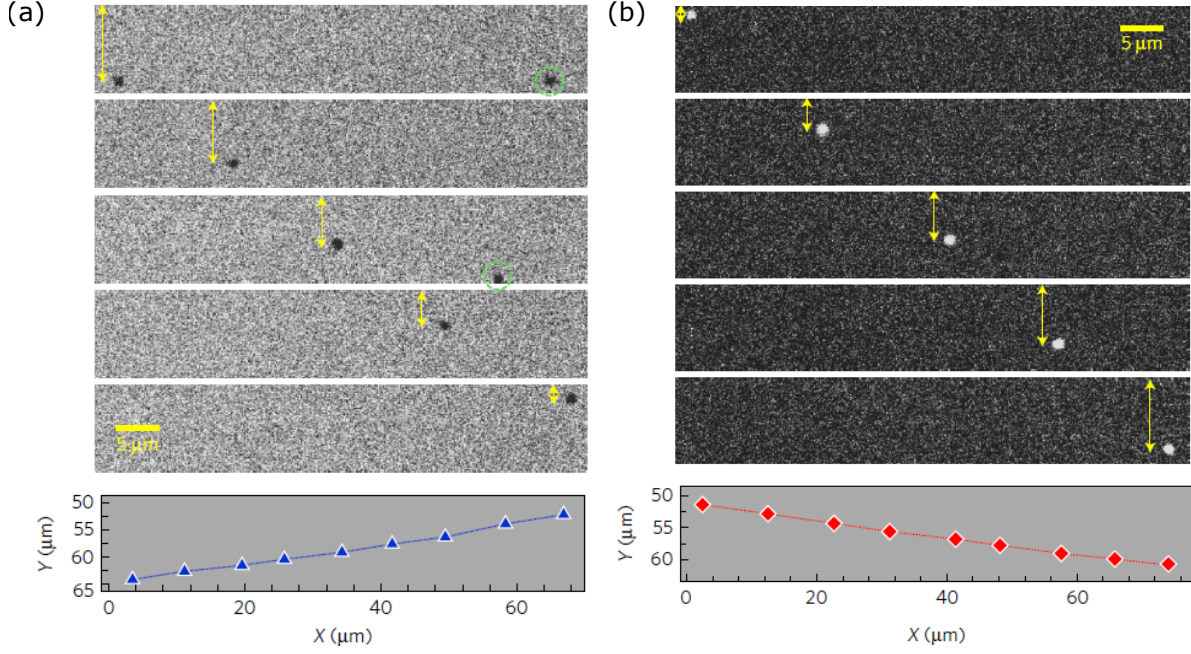
Figure A.5: **Direct imaging of skyrmion Hall effect under application of current pulses.** Snapshots and trajectory of skyrmion motion captured after injection of current pulses along the horizontal axis under (a) positive and (b) negative magnetic fields in the out-of-plane direction. The direction of transverse motion changes the sign as the topological charge of skyrmions is different in (a) ($Q = -1$) and (b) ($Q = +1$). Images were obtained by a polar magneto-optical Kerr effect microscope in multilayer systems consisting of $Ta/CoFeB/TaO_x$. Adapted from [334].

impurities [170]. Together with the stability due to the topological protection, the controlled motion by ultralow currents makes magnetic skyrmions attractive candidates for future information carriers [335].

Since a skyrmion induces a quantized magnetic flux, a moving skyrmion generates an emergent electric field following Faraday's laws of induction [328].

$$\mathbf{E}^s = -\mathbf{v}_d \times \mathbf{B}^s, \tag{A.76}$$

where $\mathbf{v}_d$ is the velocity of skyrmions and $\mathbf{B}^s$ is the emergent magnetic field. The effective electromagnetic induction effect generates extra electric currents transverse to the electric current, resulting in the suppression of the Hall resistivity ρ_{xy}. This is demonstrated in Fig.A.4(b), showing a decrease in the Hall resistivity by applying a electric current above the threshold values in the presence of skrymion crystals.

For further confirmation, the direct imaging of skyrmion motion is also possible. Employing *in-situ* Lorentz transmission electron microscopy, the skyrmion driven by electric currents was observed in FeGe near room temperature [336]. Similar observations were also reported in multilayer magnetic systems with the maximum speed exceeding 100 ms^{-1} [334, 337–339]. Figure A.5 shows snapshots of skyrmion motion under successive
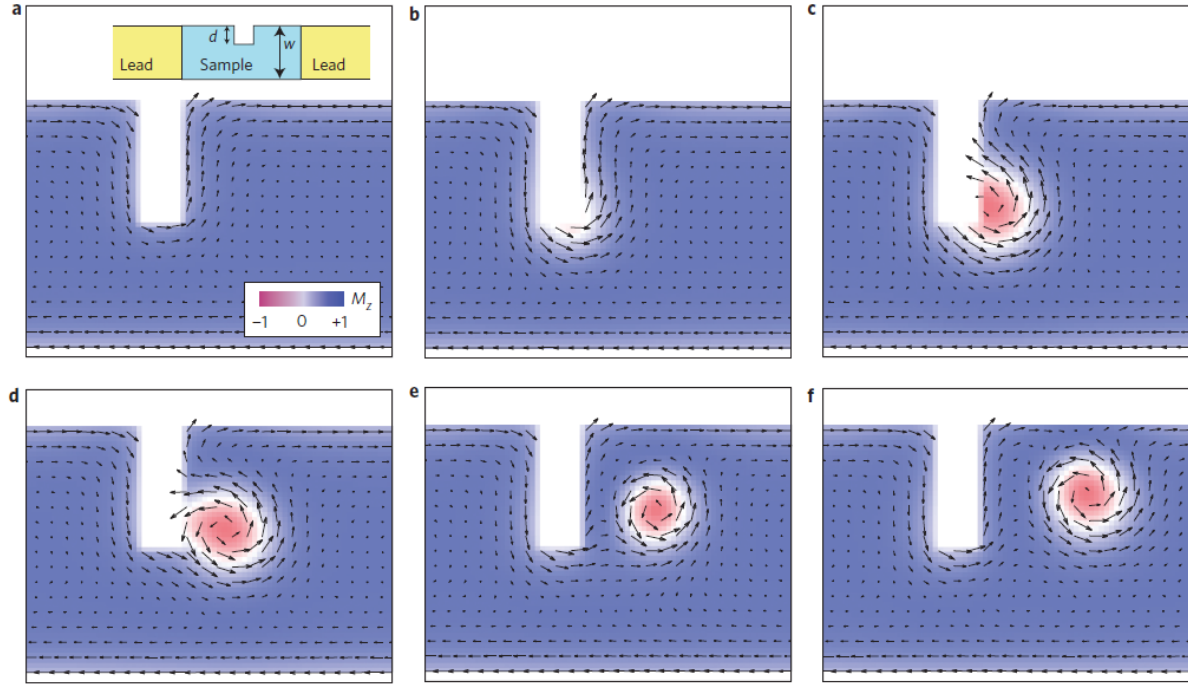
Figure A.6: **Nucleation process of skyrmions from notches with an applied electric current.** (a)-(f) Snapshots of spin configurations in a strip geometry with a rectangular notch, obtained by the Landau–Lifshitz–Gilbert simulation. The electric currents is applied in the horizontal axis. Adapted from [170].

applications of current pulses along the horizontal axis, using a polar magneto-optical Kerr effect microscope [334]. The trajectory of skyrmions indicates transverse motion due to the skyrmion Hall effect, which changes the sign for skyrmions with different topological charges.

The manipulation of magnetic textures with electric currents could be also used to nucleate skyrmions. For example, skyrmions could be converted from a ferromagnetic domain by pushing it into a wide nanowires [147, 340]. Another idea is to introduce a notch along the edge of a sample. In the numerical simulation shown in Fig. A.6, the continuous deformation of edge spin textures is observed under an electric current, resulting in formation of skyrmions. It can be explained from the fact that the topological charge is no longer quantized in a confined system, allowing a fractional topological charge. In comparison, the energy cost to create skyrmions in a bulk of samples is much higher, because many spins need to be simultaneously flipped. This process was also demonstrated experimentally by spin-polarized scanning tunneling microscopy and local heating of a sample [171, 252, 288, 341–343].

A.10   Thiele's approach for skyrmion motion

In this section, we introduce Thiele's approach to describe the skyrmion motion under microwave fields, following Ref. [290]. The main advantage of Thiele's approach is that we can obtain a simplified expression of driving forces exerted on single skyrmions, which can be used to derive the velocity of skyrmions [289]. A classical spin system under microwave fields can reach a time-periodic steady state in the presence of phenomenological damping constants. The Landau-Lifshitz-Gilbert (LLG) equation describes such classical spin dynamics (see Section A.6). In the following, we consider the LLG equation of isolated magnetic skyrmions defined on a square lattice under ac fields as shown in Fig. 4.1, where $\boldsymbol{m_r}(t)$ denotes a unit vector parallel to the magnetization at site $\boldsymbol{r}$.

Assuming that the velocity of skyrmion is much slower than the period of microwave field ω, the normalized magnetization $\boldsymbol{m_r}(t)$ can be separated into a slow part $\boldsymbol{m_{r,s}}(t)$ and a fast part $\boldsymbol{n_r}(t)$:

$$\boldsymbol{m_r}(t) = \boldsymbol{m_{r,s}}(t) + \boldsymbol{n_r}(t), \qquad (A.77)$$

where $\boldsymbol{n_r}(t+T) = \boldsymbol{n_r}(t)$ with $T = 2\pi/\omega$ denoting the period of driving field. Substituting $\boldsymbol{m_r}(t)$ into the LLG equation of Eq. (A.41) and taking the average over a period T, we obtain

$$\left\langle \frac{\partial \boldsymbol{m_{r,s}}}{\partial t} \right\rangle_T = -\gamma \langle \boldsymbol{m_r} \times \mathbf{H}_r^{\text{eff}} \rangle_T + \alpha \left\langle \boldsymbol{m_{r,s}} \times \frac{\partial \boldsymbol{m_{r,s}}}{\partial t} \right\rangle_T, \qquad (A.78)$$

where α is the Gilbert damping constant, γ is the gyromagnetic ratio, $\langle f \rangle_T = \frac{1}{T}\int_0^T f(t')dt'$, and $\mathbf{H}_r^{\text{eff}} = -[1/(\hbar\gamma S)]\partial H/\partial \boldsymbol{m_r}$ with H denoting the classical spin Hamiltonian. To derive this expression, we have used $\langle \boldsymbol{n_r} \rangle_T = \langle \partial_t \boldsymbol{n_r} \rangle_T = 0$, $\langle \boldsymbol{m_{r,s}} \times \partial_t \boldsymbol{n_r} \rangle_T \approx 0$, and $\langle \boldsymbol{n_r} \times \partial_t \boldsymbol{m_{r,s}} \rangle_T \approx 0$ from the assumption that $\boldsymbol{m_{r,s}}$ is almost constant over the period T. Denoting the velocity of skyrmion as $\boldsymbol{v_s}$, the slow part can be written as $\boldsymbol{m_{r,s}}(t) = \boldsymbol{m_s}(\boldsymbol{r} - \boldsymbol{v_s}t)$. The time derivative of $\boldsymbol{m_{r,s}}$ is then given by

$$\partial_t \boldsymbol{m_{r,s}} = \frac{\partial(\boldsymbol{r} - \boldsymbol{v_s}t)}{\partial t}\frac{\boldsymbol{m_{r,s}}}{\partial \boldsymbol{r}} = -(\boldsymbol{v_s} \cdot \nabla_r)\boldsymbol{m_{r,s}}. \qquad (A.79)$$

The time averaged expressions are approximately given as [290]

$$\langle \partial_t \boldsymbol{m_{r,s}} \rangle_T \approx -(\boldsymbol{v_s} \cdot \nabla_r)\boldsymbol{m_s}(\boldsymbol{r} - \boldsymbol{v_s}T/2), \qquad (A.80)$$

$$\langle \boldsymbol{m_{r,s}} \rangle_T \approx \boldsymbol{m_s}(\boldsymbol{r} - \boldsymbol{v_s}T/2). \qquad (A.81)$$

Hence, we obtain

$$\left\langle \frac{\partial \boldsymbol{m_{r,s}}}{\partial t} \right\rangle_T \approx -(\boldsymbol{v_s} \cdot \nabla_r)\tilde{\boldsymbol{m}}_{r,s}, \qquad (A.82)$$

where $\tilde{\boldsymbol{m}}_{r,s} = \langle \boldsymbol{m_{r,s}} \rangle_T$ is the time-averaged magnetization. Similarly, we have

$$\left\langle \boldsymbol{m_{r,s}} \times \frac{\partial \boldsymbol{m_{r,s}}}{\partial t} \right\rangle_T \approx \tilde{\boldsymbol{m}}_{r,s} \times (-\boldsymbol{v_s} \cdot \nabla_r)\tilde{\boldsymbol{m}}_{r,s}. \qquad (A.83)$$

Using the above expressions, Eq. (A.78) is rewritten as

$$(\boldsymbol{v}_s \cdot \nabla)\tilde{\boldsymbol{m}}_{r,s} = \gamma \left\langle \boldsymbol{m_r} \times \mathbf{H}_r^{\text{eff}} \right\rangle_T + \alpha \tilde{\boldsymbol{m}}_{r,s} \times (\boldsymbol{v}_s \cdot \nabla_r)\tilde{\boldsymbol{m}}_{r,s}. \tag{A.84}$$

In order to study the collective motion of skyrmions, we employ Thiele's approach and multiply both sides of Eq. (A.84) by $\int \tilde{\boldsymbol{m}}_s \cdot (\partial_r \tilde{\boldsymbol{m}}_s \times ...)dxdy$ for $i = x, y$ [289]. The left-hand side of Eq. (A.84) is obtained as

$$\begin{aligned}
\text{(LHS)} &= \int \tilde{\boldsymbol{m}}_{r,s} \cdot [\partial_i \tilde{\boldsymbol{m}}_{r,s} \times (\boldsymbol{v}_s \cdot \nabla_r)\tilde{\boldsymbol{m}}_{r,s}]dxdy \\
&= \int \tilde{\boldsymbol{m}}_{r,s} \cdot [\partial_i \tilde{\boldsymbol{m}}_{r,s} \times (v_{s,x}\partial_x + v_{s,y}\partial_y)\tilde{\boldsymbol{m}}_{r,s}]dxdy \\
&= -4\pi Q(\hat{z} \times \boldsymbol{v}_s)_i, \tag{A.85}
\end{aligned}$$

where $Q = 1/(4\pi) \int \tilde{\boldsymbol{m}}_s \cdot [\partial_x \tilde{\boldsymbol{m}}_s \times \partial_y \tilde{\boldsymbol{m}}_s]dxdy$ is an integer topological charge carried skyrmions as defined in Eq. (1.58). The second term on the right-hand side is given as

$$\begin{aligned}
&\alpha \int \tilde{\boldsymbol{m}}_{r,s} \cdot [\partial_i \tilde{\boldsymbol{m}}_{r,s} \times \{\tilde{\boldsymbol{m}}_{r,s} \times (\boldsymbol{v}_s \cdot \nabla_r)\tilde{\boldsymbol{m}}_{r,s}\}]dxdy \\
&= \alpha \int \tilde{\boldsymbol{m}}_{r,s} \cdot [(\partial_i \tilde{\boldsymbol{m}}_{r,s} \cdot (\boldsymbol{v}_s \cdot \nabla_r)\tilde{\boldsymbol{m}}_{r,s})\tilde{\boldsymbol{m}}_{r,s} - (\partial_i \tilde{\boldsymbol{m}}_{r,s} \cdot \tilde{\boldsymbol{m}}_{r,s})(\boldsymbol{v}_s \cdot \nabla_r)\tilde{\boldsymbol{m}}_{r,s}]dxdy \\
&= \alpha v_{s,j} \int (\partial_i \tilde{\boldsymbol{m}}_s \cdot \partial_j \tilde{\boldsymbol{m}}_s)dxdy = \alpha \eta \delta_{ij} v_{s,i}, \tag{A.86}
\end{aligned}$$

with $\eta \approx 4\pi$ for skyrmions. The last equality was obtained from $\partial_i(\tilde{\boldsymbol{m}}_{r,s} \cdot \tilde{\boldsymbol{m}}_{r,s}) = 2\partial_i \tilde{\boldsymbol{m}}_{r,s} \cdot \tilde{\boldsymbol{m}}_{r,s} = 0$. Finally, Eq. (A.84) is written in terms of the collective coordinate as

$$4\pi Q(\hat{z} \times \boldsymbol{v}_s) + \alpha \eta \boldsymbol{v}_s = \mathbf{F}, \tag{A.87}$$

where the net force exerted on the skyrmion is given by

$$\mathrm{F}_i = -\gamma \int \tilde{\boldsymbol{m}}_{r,s} \cdot \left[\partial_i \tilde{\boldsymbol{m}}_{r,s} \times \left\langle \boldsymbol{m_r} \times \mathbf{H}_r^{\text{eff}} \right\rangle_T \right]dxdy. \tag{A.88}$$

Finally, the velocity of skyrmion is given by

$$\begin{aligned}
v_{s,x} &= \frac{4\pi Q F_y + \alpha \eta F_x}{(4\pi Q)^2 + \alpha^2 \eta^2}, \\
v_{s,y} &= \frac{-4\pi Q F_x + \alpha \eta F_y}{(4\pi Q)^2 + \alpha^2 \eta^2}. \tag{A.89}
\end{aligned}$$

Ignoring small contributions proportional to the Gilbert damping coefficient, it is written as

$$(v_{s,x}, v_{s,y}) = \frac{(F_y, -F_x)}{4\pi Q}. \tag{A.90}$$

Therefore, we can obtain the analytical expression for skyrmion velocity by computing the total force $\mathbf{F}$ acting on skyrmions under microwave fields.

Appendix B

Floquet theory for classical spin systems

B.1 Introduction

B.1.1 Floquet Hamiltonian and kick operator

In this section, we introduce the theoretical basis of Floquet theory for quantum systems, including the Floquet Hamiltonian and kick operator. We refer to Ref. [285] for the content of this section. Let us consider a time-periodic Hamiltonian $\hat{H}(t+T) = \hat{H}(t)$ with a period T. Analogously to the Bloch theorem for spatially periodic Hamiltonians, the Floquet theorem guarantees the existence of Floquet states $|\psi_n(t)\rangle$ as a solution for the time-dependent Schrödinger equation [344]:

$$i\hbar\frac{d}{dt}|\psi(t)\rangle = \hat{H}(t)|\psi(t)\rangle,\tag{B.1}$$

with

$$|\psi_n(t)\rangle = |u_n(t)\rangle\,e^{-i\epsilon_n t/\hbar},\tag{B.2}$$

where ϵ_n and $|u_n(t)\rangle = |u_n(t+T)\rangle$ denotes the real quasienergy and Floquet mode, respectively. The Floquet states are eigenstates of the time-evolution operator $\hat{U}(t_2, t_1)$ over one period:

$$\hat{U}(t_0 + T, t_0)|\psi_n(t_0)\rangle = |\psi_n(t_0 + T)\rangle = e^{-i\epsilon_n T/\hbar}|\psi_n(t_0)\rangle.\tag{B.3}$$

We should note that the eigenvalue ϵ_n does not depend on t_0. The time evolution of Floquet states is described by $|\psi_n(t)\rangle = \hat{U}(t, t_0)|\psi_n(t_0)\rangle$. Conversely, we can write the time-evolution operator in terms of Floquet modes as

$$\hat{U}(t_2, t_1) = \sum_n e^{-i\epsilon_n(t_1 - t_2)}|u_n(t_2)\rangle\langle u_n(t_1)|.\tag{B.4}$$

Similarly to energy spectra of static systems, we consider the quasienergy spectrum to characterize time-periodic Hamiltonians. An important difference is that the quasienergy

spectrum is well-defined only up to modulo integer multiples of $\omega = 2\pi/T$, which gives the identical phase factor $e^{-i\epsilon_n T/\hbar}$ in Eq. (B.3). The quasienergy spectrum over the width of $\hbar\omega$ is often called a *Brillouin zone* in the energy space. Given ϵ_n and $|u_n(t)\rangle$ as one choice of quasienergy and Floquet mode, all the possible solutions are given as

$$\epsilon_{nm} = \epsilon_n + m\hbar\omega, \tag{B.5}$$

with m denoting integers and the corresponding Floquet mode is

$$|u_{nm}(t)\rangle = |u_n(t)\rangle \, e^{im\omega t}. \tag{B.6}$$

Substituting $|\psi_n(t)\rangle = |u_n(t)\rangle \, e^{-i\epsilon_n t/\hbar} = |u_{nm}(t)\rangle \, e^{-i\epsilon_{nm}t/\hbar}$ to the time-dependent Schrödigner equation of Eq. (B.1), we obtain

$$[\hat{H}(t) - i\hbar d_t] \, |u_{nm}(t)\rangle = \epsilon_{nm} \, |u_{nm}(t)\rangle \,. \tag{B.7}$$

The above equation is an eigenvalue problem defined in the extended Floquet Hilbert space $\mathcal{F} = \mathcal{H} \otimes \mathcal{L}_T$, where $\mathcal{H}$ is the original Hilbert space of $\hat{H}$ and $\mathcal{L}_T$ is the space of T-periodic time-dependent functions [344]. In the extended Floquet Hilbert space, the scalar product between two quantum states is defined as

$$\langle u|v\rangle_T = \frac{1}{T} \int_0^T dt' \, \langle u(t')|v(t')\rangle \,. \tag{B.8}$$

The quasienergy eigenvalue is also written as

$$\hat{Q} \, |u_{nm}(t)\rangle = \epsilon_{nm} \, |u_{nm}(t)\rangle \,, \tag{B.9}$$

with the quasienergy operator $\hat{Q} = \hat{H}(t) - i\hbar d_t$.

A complete set of orthogonal basis of $\mathcal{F}$ is constructed by [285]

$$|\alpha m(t)\rangle = |\alpha\rangle \, e^{im\omega t}, \tag{B.10}$$

where α is a complete set of orthogonal basis for $\hat{H}$ and m is integers. Using this basis, the matrix elements of $\hat{Q}$ is obtained as

$$\begin{aligned}
\langle \alpha'm'|\hat{Q}|\alpha m\rangle_T &= \frac{1}{T} \int_0^T dt \, e^{-im'\omega t} \, \langle \alpha'|\hat{H}(t) - i\hbar d_t|\alpha\rangle \, e^{im\omega t} \\
&= \langle \alpha'|\hat{H}_{m-m'}|\alpha\rangle + \delta_{m,m'}\delta_{\alpha,\alpha'}m\hbar\omega,
\end{aligned} \tag{B.11}$$

where $\hat{H}_m$ is the Fourier transform of the Hamiltonian $H(t)$, given as

$$\hat{H}_m = \frac{1}{T} \int_0^T dt \, e^{im\omega t} \hat{H}(t). \tag{B.12}$$

With respect to the Fourier mode index m, each block is represented by $\hat{Q}_{m'm} = \hat{H}_{m-m'} + \delta_{m'm}m\hbar\omega$ acting in the Hilbert space $\hat{H}$.

To compute the quasienergy spectrum, we need to block diagonalize the quasienergy operator $\hat{Q}$ with respect to the Fourier mode indices m, as shown below. The block diagonalized structure is represented as $\hat{Q}_m = \hat{H}_F + m\hbar\omega$, with $\hat{H}_F = \hat{H}_{m=0}$ defined below. Denoting a unitary operator $\hat{U}_F(t)$ that block diagonalize $\hat{Q}$, the quasienergy operator is evaluated as

$$\langle \alpha' m' | \hat{U}_F^\dagger \hat{Q} \hat{U}_F | \alpha m \rangle_T = \delta_{m,m'} \langle \alpha' | \hat{H}_F | \alpha \rangle + \delta_{m,m'} \delta_{\alpha,\alpha'} m\hbar\omega, \tag{B.13}$$

with

$$\hat{H}_F = \hat{U}_F^\dagger(t)\hat{H}(t)\hat{U}_F(t) - i\hbar\hat{U}_F^\dagger(t)d_t\hat{U}_F(t). \tag{B.14}$$

The time-independent Hamiltonian $\hat{H}_F$ is termed as an *effective Floquet Hamiltonian*, which can be diagonalized as

$$\hat{H}_F |\tilde{u}_n\rangle = \epsilon_n |\tilde{u}_n\rangle = \epsilon_n \sum_\alpha \gamma_{n\alpha} |\alpha\rangle, \tag{B.15}$$

with $\gamma_{n\alpha} = \langle \tilde{u}_n | \alpha \rangle$. We then obtain the Floquet modes and their quasienergies as

$$|u_{nm}(t)\rangle = \hat{U}_F(t) |\tilde{u}_n\rangle e^{im\omega t}, \tag{B.16}$$

$$\epsilon_{nm} = \epsilon_n + m\hbar\omega. \tag{B.17}$$

Therefore, we can solve time-periodic Hamiltonians by constructing the unitary operator $\hat{U}_F(t)$. Using $\hat{U}_F(t)$, we can obtain the effective Floquet Hamiltonian $\hat{H}_F$ and the quasienergy spectrum ϵ_{nm}. We should note that the derivation of $\hat{U}_F(t)$ is outlined in Appendix B.1.2. Furthermore, the time-evolution operator of Eq. (B.4) can be expressed in terms of $\hat{H}_F$ and $\hat{U}_F(t)$. Using the Floquet states $|u_{n0}(t)\rangle = \hat{U}_F(t) |\tilde{u}_n\rangle$ as a basis, we obtain [345]

$$\begin{aligned} \hat{U}(t_2, t_1) &= \sum_n e^{-i\epsilon_n(t_1-t_2)}\hat{U}_F(t_2) |\tilde{u}_n\rangle \langle \tilde{u}_n | \hat{U}_F^\dagger(t_1) \\ &= \hat{U}_F(t_2)e^{-i\hat{H}_F(t_1-t_2)}\hat{U}_F^\dagger(t_1), \end{aligned} \tag{B.18}$$

where we have used $\hat{H}_F = \sum_n \epsilon_n |\tilde{u}_n\rangle \langle \tilde{u}_n|$ for the last equality. The unitary operator $\hat{U}_F(t)$ can be expressed as

$$\hat{U}_F(t) = \exp\left(\hat{G}(t)\right), \tag{B.19}$$

where $\hat{G} = -\hat{G}^\dagger$ is an anti-hermitian operator. The hermitian operator $i\hat{G}$ is called the *kick operator* as it describes the time-evolution of Floquet states [346]. We should note that $\hat{G}(t+T) = \hat{G}(t)$ to preserve the periodicity in time.

B.1.2 High frequency expansion

In this section, we briefly outline the approximation scheme to compute a unitary operator $\hat{U}_F(t)$ that block diagonalize the quasienergy operator $\hat{Q}$ discussed in Appendix B.1.1.
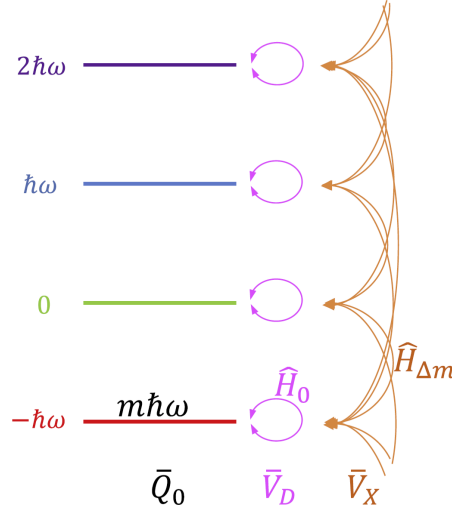
Figure B.1: **Schematic illustration of quasienergy spectrum in the perturbation theory.** The quasienergy operator is partitioned into $\hat{Q} = \hat{Q}_0 + \hat{V}_D + \hat{V}_x$, with $\hat{Q}_0$ denoting an unperturbed part as defined in the text. Adapted from [285].

The main idea is to expand $\hat{U}_F(t)$ perturbatively with $1/\omega$ in the limit of the large frequency $\omega = 2\pi/T$, hence known as the high frequency expansion. For the details of the calculation, we refer to Ref. [285].

Assuming that the frequency of driving is much larger than the energy scale of Hamiltonian $\hbar\omega \gg \hat{H}(t)$, we can separate the quasienergy operator of Eq. (B.11) as [285]

$$\hat{Q} = \hat{Q}_0 + \hat{V}_D + \hat{V}_x, \tag{B.20}$$

where each expression is given as

$$\hat{Q}_0 = -i\hbar d_t, \tag{B.21}$$

$$\hat{V}_D = \hat{H}_0, \tag{B.22}$$

$$\hat{V}_X(t) = \sum_{\Delta m \neq 0} e^{-i\Delta m \omega t} \hat{H}_{\Delta m}. \tag{B.23}$$

In the high frequency approximation, we take $\hat{Q}_0$ as an unperturbed part, where all quasienergies are degenerate with $\epsilon_{\alpha m}^{(0)} = \langle \alpha' m' | \hat{Q}_0 | \alpha m \rangle_T = m\hbar\omega$. The time-periodic Hamiltonian is taken as a perturbation $\hat{V}_D + \hat{V}_x$. While $\hat{V}_D$ maps a system within the same Fourier mode index m, $\hat{V}_X$ corresponds to a perturbation between different Fourier mode indices. The unperturbed quasienergy spectrum with perturbations from $\hat{V}_D$ and $\hat{V}_X$ is illustrated in Fig. B.1. The advantage of this method is that we can obtain a general expression of $\hat{U}_F(t)$ independent of the orthogonal basis $|\alpha m\rangle$.

To compute the unitary operator $\hat{U}_F(t)$ that bloch diagonalize $\hat{Q}$, we need to satisfy

$$\hat{U}_F^\dagger \hat{Q} \hat{U}_F = \hat{U}_F^\dagger [\hat{Q}_0 + \hat{V}_D + \hat{V}_X] \hat{U}_F = \hat{Q}_0 + \hat{W}_D, \tag{B.24}$$

where $\hat{W}_D$ is a bloch-diagonal operator. By solving Eq. (B.24) for each order of pertur-
bations, the perturbative expansion of $\hat{U}_F(t)$ is given as

$$\hat{U}_F(t) = \exp(\hat{G}), \tag{B.25}$$

$$\hat{G} = \sum_{\nu=1}^{\infty} G^{\nu}, \tag{B.26}$$

where the anti-unitary operator $\hat{G}$ is expanded in powers of $1/\omega$, whose expression was
obtained up to the second order in Ref. [285]. Depending on the desired accuracy of
calculations, we truncate the expansion up to higher orders to derive the approximate
expression for $\hat{U}_F(t) \approx \exp\left(\sum_{\nu=1}^{\nu'} \hat{G}^{\nu}\right)$. Here, we only present the result for the first
order term as it is sufficient for our calculations in Chapter 4. The expression for $\hat{G}^{(1)}$ is
given as [285]

$$\hat{G}^{(0)}(t) = 0, \tag{B.27}$$

$$\hat{G}^{(1)}(t) = -\sum_{m \neq 0} \frac{e^{im\omega t}}{m\hbar\omega} \hat{H}_{-m}, \tag{B.28}$$

with m denoting integers and $\hat{H}_m$ defined in Eq. (B.12).

Once a truncated series of $\hat{U}_F(t)$ is obtained, the corresponding Floquet Hamiltonian
can be computed by

$$H^F_{\alpha,\alpha'} = \langle\alpha'|\hat{H}_F|\alpha\rangle = \langle\alpha'0|\hat{U}_F^\dagger \hat{Q} \hat{U}_F|\alpha0\rangle_T. \tag{B.29}$$

The leading order terms were obtained as [285]

$$\hat{H}_F^{(0)} = \hat{H}_0, \tag{B.30}$$

$$\hat{H}_F^{(1)} = \sum_{m \neq 0} \frac{[\hat{H}_{-m}, \hat{H}_m]}{2m\hbar\omega}. \tag{B.31}$$

We should note that the equivalent expressions for the effective Floquet Hamiltonian have
been derived with different means such as the Floquet Magnus expansion [345–347].

B.2 Floquet theory on classical systems

In Appendix B.1, we have reviewed the Floquet theory applied to Schrödinger equations
under time-periodic drives. In the following sections of Appendix B, we provide a brief
review of Ref. [211], where the Floquet theory was extended to classical systems described
by equations of motion (EOM). Our purpose is to derive expressions of effective Floquet
Hamiltonians and kick operators for classical spin systems under laser fields. This section
provides a general strategy for applications of the Floquet theory to classical EOMs,
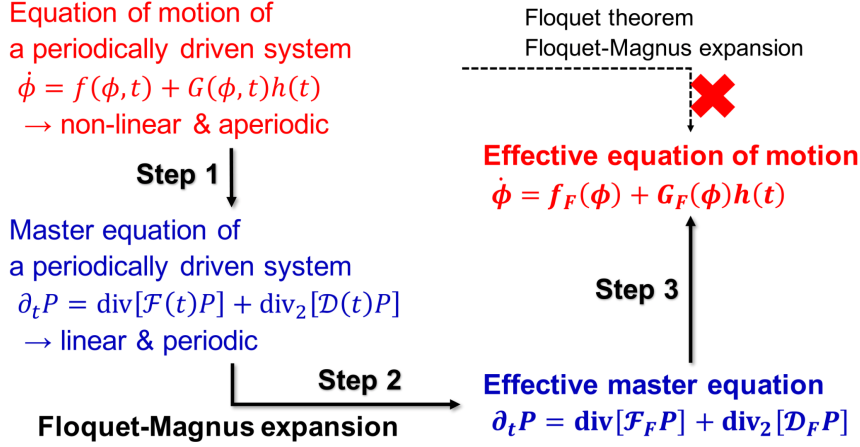followed by the application to classical spin systems in the next section.

Figure B.2: **Schematic illustration of Floquet theory applied to classical systems.** Each procedure is explained in the text. Adapted from [211].

The problem for the application to classical EOMs is that they are generally nonlinear equations. In addition, they may contain stochastic forces due to the thermal noise. Hence, we cannot use the Floquet theory developed for a linear equation. To overcome this problem, the main idea of Ref. [211] is to apply the high frequency expansion in the corresponding master equations instead of EOMs. Since the master equation is a linear equation describing the time evolution of probability density functions, we can apply the established result of the Floquet theory. Once the effective time-independent master equation is obtained by the Floquet expansion, we just need to derive the EOM corresponding to the effective master equation. The whole process is illustrated in Fig. B.2.

Let us consider the following generic equation of motion.

$$d_t \phi_{\boldsymbol{r},a}(t) = f_{\boldsymbol{r},a}[\phi(t),t] + \sum_{b=1}^{N_I} g_{\boldsymbol{r},ab}[\phi(t),t] h_{\boldsymbol{r},b}(t), \tag{B.32}$$

where $\phi(t) = [\vec{\phi}_{\boldsymbol{r}_1}(t), \vec{\phi}_{\boldsymbol{r}_2}(t), \ldots, \vec{\phi}_{\boldsymbol{r}_N}(t)]$ is a set of classical variables for N sites labeled by $\boldsymbol{r}$, each classical variable $\vec{\phi}_{\boldsymbol{r}}$ has N_I internal degrees of freedom denoted by the subscript a, $f_{\boldsymbol{r},a}[\phi(t),t]$ and $g_{\boldsymbol{r},ab}[\phi(t),t]$ respectively denotes a drift force and diffusion matrix, and $h_{\boldsymbol{r},a}(t)$ is a Gaussian random variable that satisfies

$$\langle h_a(t) \rangle = 0, \qquad \langle h_a(t) h_b(t') \rangle = 2D \delta_{ab} \delta(t-t'), \tag{B.33}$$

with D and $\langle \rangle$ denoting a diffusion constant and disorder average, respectively. We assume the time-periodic drift force $f_a(t) = f_a(t+T)$ and the diffusion matrix $g_{ab}(t) = g_{ab}(t+T)$.

Using the Stratonovich convention, the Fokker-Plank equation is obtained as a master equation of Eq. (B.32) [211] (Step 1 in Fig. B.2):

$$\frac{\partial P(\phi,t)}{\partial t} = \frac{\partial}{\partial \phi_i}[\mathcal{F}_i(\phi,t) P(\phi,t)] + \frac{\partial^2}{\partial \phi_i \phi_j}[\mathcal{D}_{ij}(\phi,t) P(\phi,t)], \tag{B.34}$$

with $P(\phi', t')$ representing the probability density for finding $\phi = \phi'$ at $t = t'$ in the whole parameter space of ϕ. Each expression is given as

$$\mathcal{F}_i(\phi, t) = -f_i(\phi, t) - Dg_{kl}(\phi, t)\frac{\partial g_{il}(\phi, t)}{\partial \phi_k}, \tag{B.35}$$

$$\mathcal{D}_{ij}(\phi, t) = Dg_{ik}(\phi, t)g_{kj}(\phi, t), \tag{B.36}$$

where i denotes all degrees of freedom of ϕ including N sites and N_I internal degree of freedoms. We note that $\mathcal{F}_i(t + T) = \mathcal{F}_i(t)$ and $\mathcal{D}_{ij}(\phi, T + t) = \mathcal{D}_{ij}(\phi, t)$ from the above equations. We define a Fokker-Plank operator $\mathcal{L}_t(P)$ as follows.

$$\mathcal{L}_t(P) = \text{div}[\mathcal{F}(t)P] + \text{div}_2[\mathcal{D}(t)P], \tag{B.37}$$

where $\text{div}[\mathcal{F}P] \equiv \partial_{\phi_i}[\mathcal{F}_i P]$ and $\text{div}_2[\mathcal{D}P] \equiv \partial_{\phi_i \phi_j}[\mathcal{D}_{ij}P]$. Using the Fokker-Plank operator $\mathcal{L}_t(P)$, we notice that the Fokker-Plank equation takes the same form as the Schrödinger equation:

$$i\partial_t P = H(t)P, \qquad \text{with } H(t) = i\mathcal{L}_t(P). \tag{B.38}$$

Since the Fokker-plank operator is periodic in time with $\mathcal{L}_{T+t} = \mathcal{L}_t$, we can apply the Floquet theory to describe the time-evolution of the probability density function $P(\phi, t) = U(t, 0)P(\phi, t = 0)$ (Step 2 in Fig. B.2).

From Eq. (B.18), the time-evolution operator is given by

$$U(t_2, t_1) = e^{g_F(t_2)}e^{(t_2 - t_1)\mathcal{L}_F}e^{-g_F(t_1)}, \tag{B.39}$$

where $\mathcal{L}_F = -iH_F$ is the effective Fokker-Plank operator obtained by the Floquet theory and $ig_F(t)$ is the kick operator satisfying $g_F(t+T) = g_F(t)$, which respectively represents a stroboscopic dynamics that develops over a long time and an instantaneous time-evolution at time t with small oscillations around the time-averaged solution. As discussed in Appendix B.1.2, the expressions for $\mathcal{L}_F$ and $g_F(t)$ can be obtained by the high frequency expansion. From Eqs. (B.28) and (B.31), we have [211]

$$\mathcal{L}_F = \sum_{m=0}^{\infty} \mathcal{L}_F^{(m)}, \qquad g_F = \sum_{m=0}^{\infty} g_F^{(m)}, \tag{B.40}$$

with the effective Fokker-Plank operator given as

$$\mathcal{L}_F^{(0)} = -iH_F^{(0)} = -iH_0 = \mathcal{L}_0, \tag{B.41}$$

$$\mathcal{L}_F^{(1)} = -iH_F^{(1)} = -i\sum_{m \neq 0}\frac{[H_{-m}, H_m]}{2m\omega}$$

$$= i\sum_{m \neq 0}\frac{[\mathcal{L}_{-m}, \mathcal{L}_m]}{2m\omega}, \tag{B.42}$$

and the kick operator given as

$$g_F^{(0)}(t) = 0, \tag{B.43}$$

$$g_F^{(1)}(t) = G^{(1)}(t) = -\sum_{m \neq 0} \frac{H_{-m} e^{im\omega t}}{m\omega}$$

$$= -i \sum_{m \neq 0} \frac{\mathcal{L}_{-m} e^{im\omega t}}{m\omega}, \tag{B.44}$$

where $\mathcal{L}_m = \frac{1}{T} \int_0^T dt \mathcal{L}_t e^{im\omega t}$ with the period $T = 2\pi/\omega$. Here, the commutator between the Fokker-Plank operators in Eq. (B.42) is interpreted as

$$[\mathcal{S}_1, \mathcal{S}_2](P) \equiv \mathcal{S}_1[\mathcal{S}_2(P)] - \mathcal{S}_2[\mathcal{S}_1(P)]. \tag{B.45}$$

If we are only interested in the long-time dynamics, we can ignore the kick operator and the master equation is described by

$$\partial_t P = \mathcal{L}_F P \approx \sum_{m=0}^{m_0} \mathcal{L}_F^{(m)} P, \tag{B.46}$$

which is truncated at m_0. As a final step, we need to derive the time-evolution of EOMs that are consistent with Eq. (B.39) (Step 3 in Fig. B.2).

Firstly, we consider the EOM corresponding to the effective Fokker-Plank equation of Eq. (B.46). The EOM corresponding to the kick operator is discussed afterwards. Here, we only consider the simplest case where the diffusion term $g_{\boldsymbol{r},ab}$ in Eq. (B.32) vanishes, which corresponds to the Landau-Lifshitz-Gilbert (LLG) equation at $T = 0$ K. Throughout this thesis, we do not discuss the finite temperature case, hence it is sufficient. For a more general case with diffusion terms, we refer to Ref. [211].

Assuming $\mathcal{D}_{ij} = 0$, the Fokker-Plank operator is given by

$$\mathcal{L}_t(P) = -\mathrm{div}[f(t)P]. \tag{B.47}$$

The Fourier mode of Fokker-Plank operator is then written as

$$\mathcal{L}_m = -\mathrm{div}(f_m P), \tag{B.48}$$

$$f_m = \frac{1}{T} \int_0^T dt \, f(t) e^{im\omega t}. \tag{B.49}$$

The commutation relation of the Fokker-Plank operator is obtained as [211]

$$[\mathcal{L}_m, \mathcal{L}_n](P) = \mathrm{div}[f_m \mathrm{div}(f_n P)] - \mathrm{div}[f_n \mathrm{div}(f_m P)]$$

$$= -\mathrm{div}[-[f_m, f_n]_{\mathrm{cl}} P], \tag{B.50}$$

where $\nabla_\phi \equiv (\partial/\partial_{\phi_1}, \partial/\partial_{\phi_2}, \dots)$ and the commutation relation is introduced as

$$[\vec{A}, \vec{B}]_{\mathrm{cl},j} = (\vec{A} \cdot \nabla_\phi) B_j - (\vec{B} \cdot \nabla_\phi) A_j = A_i \frac{\partial B_j}{\partial \phi_i} - B_i \frac{\partial A_j}{\partial \phi_i}, \tag{B.51}$$

where repeated indices imply the summation. The above commutation relation is known as the Lie braket in mathematics. The important point in Eq. (B.50) is that the Fokker-Plank operator is closed with respect to the commutator. Therefore, the effective Floquet EOM for Eq. (B.46) is described by the renormalized drift force f_F:

$$d_t\phi = f_F(\phi) = \sum_{\nu=0}^{\nu'} f_F^{(\nu)}(\phi),$$

(B.52)

with ν' indicating the truncated expansion. Up to the first order expansion, the effective drift force f_F is obtained from Eq. (B.42) as [211]

$$f_F^{(0)} = f_0,$$

(B.53)

$$f_F^{(1)} = i\sum_{m\neq 0} \frac{[f_{-m}, f_m]_{\mathrm{cl}}}{2m\omega}.$$

(B.54)

By solving Eq. (B.52), we can describe the long-time dynamics of classical systems under the time-periodic drives.

Secondly, we consider the EOM corresponding to the kick operator, which describes the short-time dynamics. Let us first consider the physical meaning of kick operators $g_F(s)$ for $s = t_1, t_2$. Without diffusion terms, Eq. (B.44) is written as

$$g_F^{(1)}(s)[P] = -i\sum_{m\neq 0} \frac{\mathcal{L}_{-m}e^{im\omega s}[P]}{m\omega} = -\frac{\mathrm{div}[f_{\mathrm{mic}}^{(1)}(\phi, s)P]}{\omega},$$

(B.55)

where

$$f_{\mathrm{mic}}^{(1)}(\phi, s) = -i\sum_{m\neq 0} \frac{f_{-m}e^{im\omega s}}{m}.$$

(B.56)

From Eq. (B.55), we see that $P(\phi, \tau) = \exp(\pm g_F(s))P_0(\phi)$ is formally a solution of the following master equation at $\tau = \frac{1}{\omega}$:

$$\frac{\partial P(\phi, \tau)}{\partial \tau} = \mp\mathrm{div}[f_{\mathrm{mic}}^{(1)}(\phi, s)P(\phi, \tau)],$$

$$P(\phi, \tau = 0) = P_0(\phi).$$

(B.57)

Treating $\mathcal{L}_{t,\mathrm{mic}}(P) = -\mathrm{div}[\pm f_{\mathrm{mic}}^{(1)}(\phi, s)P]$ as a Fokker-Plank operator for Eq. (B.57), the physical meaning of $\exp(g_F(s))$ can be interpreted as applications of the drift force $\pm f_{\mathrm{mic}}^{(1)}(\phi, s)$ from $\tau = 0$ to $\tau = \frac{1}{\omega}$, with τ denoting an auxiliary time for computing the kick operator. Assuming that the initial set of classical variables is denoted as ϕ_0, the corresponding equation of motion is obtained as [211]

$$\frac{\partial \phi_{\mathrm{kick}}}{\partial \tau} = \pm f_{\mathrm{mic}}^{(1)}(\phi_{\mathrm{kick}}, s),$$

$$\phi_{\mathrm{kick}}(\tau = 0) = \phi_0.$$

(B.58)

Thus, the kick operator maps from ϕ_0 to the solution of the above equation, written as $\phi_{\text{kick}}(\tau = \frac{1}{\omega})$.

As a summary, the full time-evolution of equations of motions in the high frequency expansion is described by the following procedures [211]. Starting from the initial configuration $\phi(t_1) = \phi_0$, we evaluate the time evolution operator $U(t_2, t_1)$ of Eq. (B.39) in three steps.

1. Substitute $-f_{\text{mic}}^{(1)}(\phi_0, t_1)$ to the right-hand side of Eq. (B.58) to solve the equation of motion for the initial kick operator. In the Euler method for $\omega \gg 1$, the approximate solution is given as

$$\phi_1 = \phi_0 - \frac{f_{\text{mic}}^{(1)}(\phi_0, t_1)}{\omega}. \tag{B.59}$$

2. Evaluate the effective Fokker-Plank operator for $t_2 - t_1$ in Eq. (B.52). The obtained solution is denoted as ϕ_2.

3. Substitute $f_{\text{mic}}^{(1)}(\phi_2, t_2)$ to the right-hand side of Eq. (B.58) to solve the equation of motion for the final kick operator. Using the Euler method for $\omega \gg 1$, the approximate solution is given as

$$\phi(t_2) = \phi_2 + \frac{f_{\text{mic}}^{(1)}(\phi_2, t_2)}{\omega}. \tag{B.60}$$

B.3   Application to classical spin systems

In this section, we apply the general formalism introduced in Appendix B.1 to classical spin systems. We refer to Ref. [211] for the content of this section. The equations of motion for classical spin systems correspond to the Landau-Lifshitz-Gilbert (LLG) equation introduced in Appendix A.6. Here, we only consider a case of $T = 0$ K, so there is no diffusion term. From Eq. (A.41), the drift force of the LLG equation is given as

$$\boldsymbol{f_r}(t) \quad = \quad -\frac{\gamma \boldsymbol{m_r}}{1 + \alpha^2} \times \left[\boldsymbol{H}_{\boldsymbol{r}}^{\text{eff}}(t) + \alpha \boldsymbol{m_r} \times \boldsymbol{H}_{\boldsymbol{r}}^{\text{eff}}(t) \right], \tag{B.61}$$

where $\boldsymbol{m_r}$ is a unit vector parallel to the magnetization at site $\boldsymbol{r}$, the microscopic magnetic field is depicted as $\boldsymbol{H}_{\boldsymbol{r}}^{\text{eff}}(t) = -[1/(\hbar\gamma S)]\partial H(t)/\partial \boldsymbol{m_r}$ with H denoting the classical spin Hamiltonian, and γ and α respectively denotes the gyromagnetic ratio and Gilbert damping constant.

With the time-periodic Hamiltonian $H(t + T) = H(t)$, the time-evolution of classical spins can be described by the Floquet theory. It is straightforward to compute $\boldsymbol{f}_{\text{mic},\boldsymbol{r}}^{(1)}(t)$, which is given from Eq. (B.56) as

$$\boldsymbol{f}_{\text{mic},\boldsymbol{r}}^{(1)}(t) = -\frac{\gamma \boldsymbol{m_r}}{1 + \alpha^2} \times \left[\boldsymbol{H}_{\text{mic},\boldsymbol{r}}^{(1)}(t) + \alpha \boldsymbol{m_r} \times \boldsymbol{H}_{\text{mic},\boldsymbol{r}}^{(1)}(t) \right], \tag{B.62}$$

with $\boldsymbol{H}_{\text{mic},\boldsymbol{r}}^{(1)}(t)$ given in Eq. (4.9). In contrast, we need to evaluate the commutation relation of $\boldsymbol{f_r}(t)$ for expressions of the effective drift force $\boldsymbol{f}_{F,\boldsymbol{r}}^{(1)}$ in Eq. (B.54). In the

following, we illustrate an efficient way to compute the commutation relation as discussed in Ref. [211].

We define the following operators:

$$L_{\boldsymbol{r},a} = -\epsilon_{abc} m_{\boldsymbol{r},b} \frac{\partial}{\partial m_{\boldsymbol{r},c}}, \tag{B.63}$$

$$K_{\boldsymbol{r},a} = \epsilon_{abc} L_{\boldsymbol{r},b} m_{\boldsymbol{r},c}, \tag{B.64}$$

$$N_{\boldsymbol{r},a} = L_{\boldsymbol{r},a} + \alpha K_{\boldsymbol{r},a}, \tag{B.65}$$

where ϵ_{abc} is the totally antisymmetric tensor of rank 3 and repeated indices imply the summation. Noting that $\boldsymbol{L}_{\boldsymbol{r}}$ is the angular momentum operator, we have the following commutation relations:

$$[L_{\boldsymbol{r},a}, L_{\boldsymbol{r}',b}] = \delta_{\boldsymbol{r},\boldsymbol{r}'} \epsilon_{abc} L_{\boldsymbol{r},c}, \tag{B.66}$$

$$[K_{\boldsymbol{r},a}, K_{\boldsymbol{r}',b}] = -\delta_{\boldsymbol{r},\boldsymbol{r}'} \epsilon_{abc} K_{\boldsymbol{r},c}, \tag{B.67}$$

$$[L_{\boldsymbol{r},a}, K_{\boldsymbol{r}',b}] = \delta_{\boldsymbol{r},\boldsymbol{r}'} \epsilon_{abc} L_{\boldsymbol{r},c}, \tag{B.68}$$

$$[N_{\boldsymbol{r},a}, N_{\boldsymbol{r}',b}] = \delta_{\boldsymbol{r},\boldsymbol{r}'} \Big(\epsilon_{abc} N_{\boldsymbol{r},c} + \alpha(N_{\boldsymbol{r},a} m_{\boldsymbol{r},b} - m_{\boldsymbol{r},a} N_{\boldsymbol{r},b}) \Big). \tag{B.69}$$

Now, we consider the commutation between Fokker-Plank operators $\mathcal{L}_A = -\sum_{\boldsymbol{r}}[\partial f_{\boldsymbol{r},A,a}/\partial m_{\boldsymbol{r},a}]$ and $\mathcal{L}_B = -\sum_{\boldsymbol{r}}[\partial f_{\boldsymbol{r},B,b}/\partial m_{\boldsymbol{r},b}]$, where

$$\boldsymbol{f}_{\boldsymbol{r},\gamma} = \frac{1}{T} \int_0^T dt\, \boldsymbol{f}_{\boldsymbol{r}}(t) e^{i\gamma\omega t}, \tag{B.70}$$

with integer $\gamma = A, B$. Using the identity

$$\frac{\partial}{\partial m_{\boldsymbol{r},a}}(\epsilon_{abc} m_{\boldsymbol{r},b} H^{\text{eff}}_{\boldsymbol{r},\gamma,c}) = -\epsilon_{abc} m_{\boldsymbol{r},a} \frac{\partial}{\partial m_b} H^{\text{eff}}_{\boldsymbol{r},\gamma,c} = \boldsymbol{L}_{\boldsymbol{r}} \cdot \boldsymbol{H}^{\text{eff}}_{\boldsymbol{r},\gamma}, \tag{B.71}$$

we can rewrite the Fokker-Plank operator as

$$\begin{aligned}
\mathcal{L}_\gamma &= \sum_{\boldsymbol{r}} \left(\boldsymbol{L}_{\boldsymbol{r}} \cdot \frac{\boldsymbol{H}^{\text{eff}}_{\boldsymbol{r},\gamma}}{1+\alpha^2} + \alpha \boldsymbol{K}_{\boldsymbol{r}} \cdot \frac{\boldsymbol{H}^{\text{eff}}_{\boldsymbol{r},\gamma}}{1+\alpha^2} \right) \\
&= \sum_{\boldsymbol{r}} \boldsymbol{N}_{\boldsymbol{r}} \cdot \overline{\boldsymbol{H}}_{\boldsymbol{r},\gamma},
\end{aligned} \tag{B.72}$$

where $\overline{\boldsymbol{H}}_{\boldsymbol{r},\gamma} = \frac{\gamma \boldsymbol{H}^{\text{eff}}_{\boldsymbol{r},\gamma}}{1+\alpha^2}$. The commutation of the Fokker-Plank operator is then derived as [211]

$$\begin{aligned}
[\mathcal{L}_A, \mathcal{L}_B] &= [\sum_{\boldsymbol{r}} \boldsymbol{N}_{\boldsymbol{r}} \cdot \overline{\boldsymbol{H}}_{\boldsymbol{r},A}, \sum_{\boldsymbol{r}'} \boldsymbol{N}_{\boldsymbol{r}'} \cdot \overline{\boldsymbol{H}}_{\boldsymbol{r}',B}] \\
&= \sum_{\boldsymbol{r}} \boldsymbol{N}_{\boldsymbol{r}} \cdot [\overline{\boldsymbol{H}}_{\boldsymbol{r},A}, \overline{\boldsymbol{H}}_{\boldsymbol{r},B}]_{\text{mag}},
\end{aligned} \tag{B.73}$$

where

$$
\begin{aligned}
[\overline{\boldsymbol{H}}_{\boldsymbol{r},A}, \overline{\boldsymbol{H}}_{\boldsymbol{r},B}]_{\mathrm{mag}} \;=\;& \overline{\boldsymbol{H}}_{\boldsymbol{r},A} \times \overline{\boldsymbol{H}}_{\boldsymbol{r},B} + \alpha \boldsymbol{m}_{\boldsymbol{r}} \times (\overline{\boldsymbol{H}}_{\boldsymbol{r},A} \times \overline{\boldsymbol{H}}_{\boldsymbol{r},B}) \\
&+ \sum_{\boldsymbol{r}'} \Big[(\overline{\boldsymbol{H}}_{\boldsymbol{r}',A} \cdot \boldsymbol{L}_{\boldsymbol{r}'})\overline{\boldsymbol{H}}_{\boldsymbol{r},B} - (\overline{\boldsymbol{H}}_{\boldsymbol{r}',B} \cdot \boldsymbol{L}_{\boldsymbol{r}'})\overline{\boldsymbol{H}}_{\boldsymbol{r},A}\Big] \\
&+ \sum_{\boldsymbol{r}'} \alpha \Big[(\boldsymbol{m}_{\boldsymbol{r}'} \cdot \overline{\boldsymbol{H}}_{\boldsymbol{r}',A} \times \boldsymbol{L}_{\boldsymbol{r}'})\overline{\boldsymbol{H}}_{\boldsymbol{r},B} - (\boldsymbol{m}_{\boldsymbol{r}'} \cdot \overline{\boldsymbol{H}}_{\boldsymbol{r}',B} \times \boldsymbol{L}_{\boldsymbol{r}'})\overline{\boldsymbol{H}}_{\boldsymbol{r},A}\Big]. \quad \text{(B.74)}
\end{aligned}
$$

Therefore, the effective drift force $\boldsymbol{f}_{F,\boldsymbol{r}}^{(1)}$ is simply given from Eq. (B.54) as

$$
\boldsymbol{f}_{F,\boldsymbol{r}}^{(1)} = -\frac{\gamma \boldsymbol{m}_{\boldsymbol{r}}}{1 + \alpha^2} \times \sum_{m \neq 0} \frac{i\gamma [\boldsymbol{H}_{\boldsymbol{r},-m}^{\mathrm{eff}}, \boldsymbol{H}_{\boldsymbol{r},m}^{\mathrm{eff}}]_{\mathrm{mag}}}{2m\omega(1 + \alpha^2)}. \tag{B.75}
$$

Finally, the effective drift force $\boldsymbol{f}_{F,\boldsymbol{r}}$ is obtained as

$$
\boldsymbol{f}_{F,\boldsymbol{r}} = \boldsymbol{f}_{\boldsymbol{r},0} + \boldsymbol{f}_{F,\boldsymbol{r}}^{(1)}. \tag{B.76}
$$

The corresponding effective LLG equation is given in Eq. (4.3).

Appendix C

Floquet theory for laser-driven skyrmions

C.1 Derivation of effective LLG equation and kicked operator

In this section, we derive the effective Landau-Lifshitz-Gilbert (LLG) equation and kicked operator of Cu_2OSeO_2 under electromagnetic fields of lasers, based on the Floquet formalism extended to classical spin systems [211] (see Appendix B). As discussed in Section 2.2.2, the electric polarization of Cu_2OSeO_2 takes different expressions depending on the direction of applied static magnetic fields $\mathbf{B}_0$. In the following, we compute $\boldsymbol{H}_F^{(1)}$ and $\boldsymbol{H}_{\mathrm{mic},\boldsymbol{r}}^{(1)}$ defined in Eqs. (4.4) and (4.9) for three cases with $\mathbf{B}_0 \parallel [001]$, $\mathbf{B}_0 \parallel [110]$, and $\mathbf{B}_0 \parallel [111]$, taking z-axis parallel to the applied magnetic field and x-axis along $[\bar{1}10]$ direction. The effective LLG equation is given by substituting $\boldsymbol{H}_F^{(1)}$ into Eq. (4.3). Similarly, the LLG equation corresponding to the kicked operator is given by substituting $\boldsymbol{H}_{\mathrm{mic},\boldsymbol{r}}^{(1)}$ into Eq. (4.8). The full time-evolution of classical spin systems under laser is then obtained by the combination of the kicked operator and effective LLG equation as described in Section 4.1.2.

For the calculation of the commutation relations defined in Eq. (B.74), we ignore small contributions proportional to the damping coefficient α. We have confirmed that it does not affect the result qualitatively by comparing the numerical solution of LLG equation and the time-evolution of spins computed by the Floquet theory, as shown in Fig. 4.4. We should note that the Fourier components of electromagnetic fields are written from Eqs. (4.14) and (4.15) as

$$\mathbf{E}_{\pm 1} = \frac{E_d}{2}(\pm i\cos\delta + \sin\delta, 1, 0), \qquad (C.1)$$

$$\mathbf{B}_{\pm 1} = \frac{B_d}{2}(1, \mp i\cos\delta - \sin\delta, 0), \qquad (C.2)$$

where $\mathbf{E}_m = \frac{1}{T}\int_0^T dt\, \mathbf{E}(t)e^{im\omega t}$ and $\mathbf{B}_m = \frac{1}{T}\int_0^T dt\, \mathbf{B}(t)e^{im\omega t}$ with $T = 2\pi/\omega$.

C.1.1   For $\mathbf{B}_0 \parallel [001]$

From Eq. (2.14), the electric polarization is given as

$$\mathbf{P_r} = \lambda\Big(- m_{r,z}m_{r,x}, m_{r,y}m_{r,z}, \frac{-m_{r,x}^2 + m_{r,y}^2}{2} \Big). \tag{C.3}$$

The time-dependent microscopic magnetic field of Eq. (4.1) is then written as

$$\boldsymbol{H_r}^{\mathrm{eff}}(t) = -\frac{\partial[H(t) - H_0]}{g\mu_B \partial \boldsymbol{m_r}} = \mathbf{B}(t) + \frac{\lambda}{g\mu_B}(-E_x m_{r,z}, E_y m_{r,z}, -E_x m_{r,x} + E_y m_{r,y}), \tag{C.4}$$

with $\mathbf{E}(t) = (E_x(t), E_y(t), 0)$ and $H_0 = \frac{1}{T}\int_0^T dt\, H(t)$. The Fourier component of the effective magnetic field is

$$\boldsymbol{H}_{r,\pm 1} = \mathbf{B}_{\pm 1} + \frac{\lambda}{g\mu_B}(-E_{x,\pm 1}m_{r,z}, E_{y,\pm 1}m_{r,z}, -E_{x,\pm 1}m_{r,x} + E_{y,\pm 1}m_{r,y}). \tag{C.5}$$

From Eq. (4.4), the effective magnetic field up to the first order expansion is obtained as

$$\begin{aligned}
\boldsymbol{H}_F^{(1)} &= \frac{i\gamma[\boldsymbol{H}_{r,-1}, \boldsymbol{H}_{r,+1}]_{\mathrm{mag}}}{(1+\alpha^2)\omega} \\
&= B_F\big\{ - 2\mathcal{E}_d m_{r,y} + 2\mathcal{E}_d^2 m_{r,x}m_{r,z}, -2\mathcal{E}_d m_{r,x} + 2\mathcal{E}_d^2 m_{r,y}m_{r,z}, \\
&\qquad 1 + \mathcal{E}_d^2(m_{r,x}^2 + m_{r,y}^2 - 3m_{r,z}^2)\big\}.
\end{aligned} \tag{C.6}$$

where $B_F = \frac{\gamma B_d^2 \cos\delta}{2(1+\alpha^2)\omega}$. Noting $\boldsymbol{H}_F^{(1)} = -\partial H_F^{(1)}/(g\mu_B \partial \boldsymbol{m_r})$, the first order term of the effective Floquet Hamiltonian is derived as

$$\begin{aligned}
H_F^{(1)} &= \sum_r \Big[- g\mu_B \mathbf{B}_F^{(1)} \cdot \boldsymbol{m_r} + 2g\mu_B B_F \mathcal{E}_d m_{r,x}m_{r,y}\Big], \\
\mathbf{B}_F^{(1)} &= B_F\big\{ 1 + \mathcal{E}_d^2(m_{r,x}^2 + m_{r,y}^2 - m_{r,z}^2)\big\}\,\hat{z}.
\end{aligned} \tag{C.7}$$

From Eq.(4.9), the microscopic field for the kicked operator is given by

$$\begin{aligned}
\boldsymbol{H}_{r,\mathrm{mic}}^{(1)}(t) &= -i(\boldsymbol{H}_{r,-1}e^{i\omega t} - \boldsymbol{H}_{r,+1}e^{-i\omega t}) \\
&= B_d\Big\{ \sin(\omega t) + \mathcal{E}_d m_{r,z}\cos(\omega t + \delta), \cos(\omega t + \delta) + \mathcal{E}_d m_{r,z}\sin(\omega t), \\
&\qquad \mathcal{E}_d m_{r,x}\cos(\omega t + \delta) + \mathcal{E}_d m_{r,y}\sin(\omega t)\Big\}.
\end{aligned} \tag{C.8}$$

C.1.2   For $\mathbf{B}_0 \parallel [110]$

From Eq. (2.14), the electric polarization is given as

$$\mathbf{P_r} = \lambda\Big(- m_{r,x}m_{r,y}, \frac{-m_{r,x}^2 + m_{r,z}^2}{2}, m_{r,y}m_{r,z} \Big). \tag{C.9}$$

The time-dependent microscopic magnetic field of Eq. (4.1) is then written as

$$\boldsymbol{H}_{\boldsymbol{r}}^{\text{eff}}(t) = -\frac{\partial[H(t) - H_0]}{g\mu_B \partial \boldsymbol{m}_{\boldsymbol{r}}} = \mathbf{B}(t) + \frac{\lambda}{g\mu_B}(-E_x m_{\boldsymbol{r},y} - E_y m_{\boldsymbol{r},x}, -E_x m_{\boldsymbol{r},x}, E_y m_{\boldsymbol{r},z}), \quad \text{(C.10)}$$

with $\mathbf{E}(t) = (E_x(t), E_y(t), 0)$ and $H_0 = \frac{1}{T}\int_0^T dt\, H(t)$. The Fourier component of the effective magnetic field is

$$\boldsymbol{H}_{\boldsymbol{r},\pm 1} = \mathbf{B}_{\pm 1} + \frac{\lambda}{g\mu_B}(-E_{x,\pm 1} m_{\boldsymbol{r},y} - E_{y,\pm 1} m_{\boldsymbol{r},x}, -E_{x,\pm 1} m_{\boldsymbol{r},x}, E_{y,\pm 1} m_{\boldsymbol{r},z}). \quad \text{(C.11)}$$

From Eq. (4.4), the effective magnetic field up to the first order expansion is obtained as

$$\boldsymbol{H}_F^{(1)} = \frac{i\gamma[\boldsymbol{H}_{\boldsymbol{r},-1}, \boldsymbol{H}_{\boldsymbol{r},+1}]_{\text{mag}}}{(1+\alpha^2)\omega}$$
$$= B_F\Big\{ -\mathcal{E}_d m_{\boldsymbol{r},z}(1 + 4\mathcal{E}_d m_{\boldsymbol{r},x}), 2\mathcal{E}_d^2 m_{\boldsymbol{r},y} m_{\boldsymbol{r},z}, 1 - \mathcal{E}_d m_{\boldsymbol{r},x} + \mathcal{E}_d^2(-2m_{\boldsymbol{r},x}^2 + m_{\boldsymbol{r},y}^2) \Big\}. \quad \text{(C.12)}$$

where $B_F = \frac{\gamma B_d^2 \cos\delta}{2(1+\alpha^2)\omega}$. Noting $\boldsymbol{H}_F^{(1)} = -\partial H_F^{(1)}/(g\mu_B \partial \boldsymbol{m}_{\boldsymbol{r}})$, the first order term of the effective Floquet Hamiltonian is derived as

$$H_F^{(1)} = \sum_{\boldsymbol{r}} \Big[-g\mu_B \mathbf{B}_F^{(1)} \cdot \boldsymbol{m}_{\boldsymbol{r}} + g\mu_B B_F \mathcal{E}_d m_{\boldsymbol{r},z} m_{\boldsymbol{r},x} \Big],$$
$$\mathbf{B}_F^{(1)} = B_F \big\{ 1 + \mathcal{E}_d^2(-2m_{\boldsymbol{r},x}^2 + m_{\boldsymbol{r},y}^2) \big\} \hat{z}. \quad \text{(C.13)}$$

From Eq.(4.9), the microscopic field for the kicked operator is given by

$$\boldsymbol{H}_{\boldsymbol{r},\text{mic}}^{(1)}(t) = -i(\boldsymbol{H}_{\boldsymbol{r},-1} e^{i\omega t} - \boldsymbol{H}_{\boldsymbol{r},+1} e^{-i\omega t})$$
$$= B_d\Big\{ (1 - \mathcal{E}_d m_{\boldsymbol{r},x})\sin(\omega t) + \mathcal{E}_d m_{\boldsymbol{r},y}\cos(\omega t + \delta), (1 + \mathcal{E}_d m_{\boldsymbol{r},x})\cos(\omega t + \delta),$$
$$\mathcal{E}_d m_{\boldsymbol{r},z}\sin(\omega t) \Big\}. \quad \text{(C.14)}$$

C.1.3 For $\mathbf{B}_0 \parallel [111]$

From Eq. (2.14), the electric polarization is given as

$$\mathbf{P}_{\boldsymbol{r}} = \lambda\Big(-\frac{m_{\boldsymbol{r},x}(\sqrt{2}m_{\boldsymbol{r},y} + m_{\boldsymbol{r},z})}{\sqrt{3}}, \frac{-m_{\boldsymbol{r},x}^2 + m_{\boldsymbol{r},y}(m_{\boldsymbol{r},y} - \sqrt{2}m_{\boldsymbol{r},z})}{\sqrt{6}}, -\frac{m_{\boldsymbol{r},x}^2 + m_{\boldsymbol{r},y}^2 - 2m_{\boldsymbol{r},z}^2}{2\sqrt{3}} \Big). \quad \text{(C.15)}$$

The time-dependent microscopic magnetic field of Eq. (4.1) is then written as

$$\boldsymbol{H}_{\boldsymbol{r}}^{\text{eff}}(t) = -\frac{\partial[H(t) - H_0]}{g\mu_B \partial \boldsymbol{m}_{\boldsymbol{r}}}$$
$$= \mathbf{B}(t) + \frac{\lambda}{g\mu_B\sqrt{3}}\Big\{ -\sqrt{2}(E_x m_{\boldsymbol{r},y} + E_y m_{\boldsymbol{r},x}) - (E_x m_{\boldsymbol{r},z}),$$
$$\sqrt{2}(-E_x m_{\boldsymbol{r},x} + E_y m_{\boldsymbol{r},y}) - (E_y m_{\boldsymbol{r},z}), -E_x m_{\boldsymbol{r},x} - E_y m_{\boldsymbol{r},y} \Big\}, \quad \text{(C.16)}$$

with $\mathbf{E}(t) = (E_x(t), E_y(t), 0)$ and $H_0 = \frac{1}{T}\int_0^T dt\, H(t)$. The Fourier component of the effective magnetic field is

$$\boldsymbol{H}_{\boldsymbol{r},\pm 1} = \mathbf{B}_{\pm 1} + \frac{\lambda}{g\mu_B\sqrt{3}}(-\sqrt{2}(E_{x,\pm 1}m_{\boldsymbol{r},y} + E_{y,\pm 1}m_{\boldsymbol{r},x}) - (E_{x,\pm 1}m_{\boldsymbol{r},z}),$$
$$\sqrt{2}(-E_{x,\pm 1}m_{\boldsymbol{r},x} + E_{y,\pm 1}m_{\boldsymbol{r},y}) - (E_{y,\pm 1}m_{\boldsymbol{r},z}), -E_{x,\pm 1}m_{\boldsymbol{r},x} - E_{y,\pm 1}m_{\boldsymbol{r},y}). \quad \text{(C.17)}$$

From Eq. (4.4), the effective magnetic field up to the first order expansion is obtained as

$$\boldsymbol{H}_F^{(1)} = \frac{i\gamma[\boldsymbol{H}_{\boldsymbol{r},-1}, \boldsymbol{H}_{\boldsymbol{r},+1}]_{\text{mag}}}{(1+\alpha^2)\omega}$$
$$= B_F\Big\{2\mathcal{E}_d^2 m_{\boldsymbol{r},x}(\sqrt{2}m_{\boldsymbol{r},y} - m_{\boldsymbol{r},z}), \sqrt{2}\mathcal{E}_d^2 m_{\boldsymbol{r},x}^2 - \mathcal{E}_d^2 m_{\boldsymbol{r},y}(\sqrt{2}m_{\boldsymbol{r},y} + 2m_{\boldsymbol{r},z}),$$
$$1 - \mathcal{E}_d^2(m_{\boldsymbol{r},x}^2 + m_{\boldsymbol{r},y}^2 - m_{\boldsymbol{r},z}^2)\Big\}. \quad \text{(C.18)}$$

where $B_F = \frac{\gamma B_d^2 \cos\delta}{2(1+\alpha^2)\omega}$. Noting $\boldsymbol{H}_F^{(1)} = -\partial H_F^{(1)}/(g\mu_B\partial\boldsymbol{m}_{\boldsymbol{r}})$, the first order term of the effective Floquet Hamiltonian is derived as

$$H_F^{(1)} = \sum_{\boldsymbol{r}}\Big[-g\mu_B\mathbf{B}_F^{(1)}\cdot\boldsymbol{m}_{\boldsymbol{r}}\Big],$$
$$\mathbf{B}_F^{(1)} = B_F\Big[\Big\{1 + \mathcal{E}_d^2\Big(-m_{\boldsymbol{r},x}^2 - m_{\boldsymbol{r},y}^2 + \frac{m_{\boldsymbol{r},z}^2}{3}\Big)\Big\}\hat{z} + \sqrt{2}\mathcal{E}_d^2(m_{\boldsymbol{r},x}^2 - \frac{m_{\boldsymbol{r},y}^2}{3})\hat{y}\Big]. \quad \text{(C.19)}$$

From Eq.(4.9), the microscopic field for the kicked operator is given by

$$\boldsymbol{H}_{\boldsymbol{r},\text{mic}}^{(1)}(t) = -i(\boldsymbol{H}_{\boldsymbol{r},-1}e^{i\omega t} - \boldsymbol{H}_{\boldsymbol{r},+1}e^{-i\omega t})$$
$$= \frac{B_d}{\sqrt{6}}\Big\{(\sqrt{6} - 2\mathcal{E}_d m_{\boldsymbol{r},x})\sin(\omega t) + \mathcal{E}_d(2m_{\boldsymbol{r},y} + \sqrt{2}m_{\boldsymbol{r},z})\cos(\omega t + \delta),$$
$$(\sqrt{6} + 2\mathcal{E}_d m_{\boldsymbol{r},x})\cos(\omega t + \delta) + \mathcal{E}_d(2m_{\boldsymbol{r},y} - \sqrt{2}m_{\boldsymbol{r},z})\sin(\omega t),$$
$$\sqrt{2}\mathcal{E}_d m_{\boldsymbol{r},x}\cos(\omega t + \delta) - \sqrt{2}\mathcal{E}_d m_{\boldsymbol{r},y}\sin(\omega t)\Big\}. \quad \text{(C.20)}$$

C.2   Spin precession mode using the Floquet theory

As shown in Eq. (4.20), the magnetization $\boldsymbol{m}_{\boldsymbol{r}}(t)$ can be partitioned into a fast part $\boldsymbol{n}_{\boldsymbol{r}}(t + T) = \boldsymbol{n}_{\boldsymbol{r}}(t)$ and a slow part $\boldsymbol{m}_{s,\boldsymbol{r}}(t)$, where $T = 2\pi/\omega$ denotes the period of electromagnetic fields from laser. In this section, we derive the analytical expression for the spin precession mode $\boldsymbol{n}_{\boldsymbol{r}}(t)$ under laser fields.

The full time-evolution of spins is described by $U(t_2, t_1)$ given in Eq. (B.39). As discussed in Section 4.1.2, $U(t_2, t_1)$ is evaluated by solving the three LLG equations in turn. Assuming $T \to 0$ and $\delta t \to 0$, the Euler's method yields a simple expression for

the time-evolution of $\boldsymbol{m_r}(t)$ from t_1 to $t_1 + \delta t$ as follows:

$$
\begin{aligned}
\delta \boldsymbol{m_r}(t_1) &= \boldsymbol{m_r}(t_1 + \delta t) - \boldsymbol{m_r}(t_1) = \boldsymbol{n_r}(t_1 + \delta t) - \boldsymbol{n_r}(t_1) + \boldsymbol{m}_{s,\boldsymbol{r}}(t_1 + \delta t) - \boldsymbol{m}_{s,\boldsymbol{r}}(t_1) \\
&= \frac{\boldsymbol{f}^{(1)}_{\mathrm{mic},\boldsymbol{r}}(t_1 + \delta t) - \boldsymbol{f}^{(1)}_{\mathrm{mic},\boldsymbol{r}}(t_1)}{\omega} + \boldsymbol{f}_{F,\boldsymbol{r}}\delta t + O(\omega^{-2}),
\end{aligned}
\tag{C.21}
$$

where $\boldsymbol{f}^{(1)}_{\mathrm{mic},\boldsymbol{r}}(t)$ and $\boldsymbol{f}_{F,\boldsymbol{r}}$ are defined in Eq. (B.62) and (B.76), respectively. Since the system is in the non-equilibrium steady state, the effective LLG equation of Eq. (4.3) should vanish on both sides. Hence, we have

$$
\boldsymbol{m}_{s,\boldsymbol{r}}(t_1 + \delta t) - \boldsymbol{m}_{s,\boldsymbol{r}}(t_1) = \boldsymbol{f}_F \delta t = 0.
\tag{C.22}
$$

Here, we should note that a change in spin textures due to the drift velocity of skyrmions is neglected. Therefore, the spin precession mode is obtained as

$$
\boldsymbol{n_r}(t) = \frac{\boldsymbol{f}^{(1)}_{\mathrm{mic}}(t)}{\omega} + O(\omega^{-2}).
\tag{C.23}
$$

C.3 Floquet magnon Hamiltonian

In this section, we illustrate how to derive the Floquet magnon Hamiltonian by performing the Holstein-Primakoff (HP) transformation (see Section 1.1.3) on the effective Floquet Hamiltonian $H_F^{(1)}$ (see Appendix C.1). For the static part of Hamiltonians H_0, the spin wave Hamiltonian is given as Eq. (1.10).

It is convenient to perform the HP transformation on the following general expressions. The cross term proportional to $\mathcal{E}_d$ is generally given as

$$
K_{ab} S_{\boldsymbol{r},a} S_{\boldsymbol{r},b} = K_{ab}\left\{ (\mathsf{S}_{\boldsymbol{r}}^{\alpha} \boldsymbol{e}_{\boldsymbol{r}}^{\alpha}) \cdot \hat{a} \right\}\left\{ (\mathsf{S}_{\boldsymbol{r}}^{\beta} \boldsymbol{e}_{\boldsymbol{r}}^{\beta}) \cdot \hat{b} \right\} = K_{ab} \sum_{\alpha,\beta} \mathsf{S}_{\boldsymbol{r}}^{\alpha} \mathsf{S}_{\boldsymbol{r}}^{\beta} L_{\boldsymbol{r}}^{\alpha a} L_{\boldsymbol{r}}^{\beta b},
\tag{C.24}
$$

with $a, b = x, y, z$ denoting the Cartesian coordinates and $\alpha = 1, 2, 3$ denoting the local orthogonal basis defined in Section 1.1.3. Here, we define a tensor $L_{\boldsymbol{r}}^{\alpha a}$ as

$$
L_{\boldsymbol{r}}^{\alpha a} = \boldsymbol{e}_{\boldsymbol{r}}^{\alpha} \cdot \hat{a}.
\tag{C.25}
$$

Only keeping the bilinear terms with respect to the magnon operators, we obtain

$$
\begin{aligned}
K_{ab} \sum_{\alpha,\beta} \mathsf{S}_{\boldsymbol{r}}^{\alpha} \mathsf{S}_{\boldsymbol{r}}^{\beta} L_{\boldsymbol{r}}^{\alpha a} L_{\boldsymbol{r}}^{\beta b} &= \frac{K_{ab}S}{2}\Big[\left\{ L_{\boldsymbol{r}}^{1a} L_{\boldsymbol{r}}^{1b} + i(L_{\boldsymbol{r}}^{1a} L_{\boldsymbol{r}}^{2b} + L_{\boldsymbol{r}}^{2a} L_{\boldsymbol{r}}^{1b}) - L_{\boldsymbol{r}}^{2a} L_{\boldsymbol{r}}^{2b} \right\} a_{\boldsymbol{r}}^{\dagger} a_{\boldsymbol{r}}^{\dagger} + \text{c.c.} \\
&\quad + \left\{ L_{\boldsymbol{r}}^{1a} L_{\boldsymbol{r}}^{1b} + L_{\boldsymbol{r}}^{2a} L_{\boldsymbol{r}}^{2b} - 2 L_{\boldsymbol{r}}^{3a} L_{\boldsymbol{r}}^{3b} \right\} (a_{\boldsymbol{r}}^{\dagger} a_{\boldsymbol{r}} + a_{\boldsymbol{r}} a_{\boldsymbol{r}}^{\dagger})\Big].
\end{aligned}
\tag{C.26}
$$

Similarly, terms proportional to $\mathcal{E}_d^2$ take the following form:

$$
N_{ab} S_{\boldsymbol{r},a}^2 S_{\boldsymbol{r},b} = N_{ab} \sum_{\alpha,\beta,\gamma} \mathsf{S}_{\boldsymbol{r}}^{\alpha} \mathsf{S}_{\boldsymbol{r}}^{\beta} \mathsf{S}_{\boldsymbol{r}}^{\gamma} L_{\boldsymbol{r}}^{\alpha a} L_{\boldsymbol{r}}^{\beta a} L_{\boldsymbol{r}}^{\gamma b}
\tag{C.27}
$$

Only keeping the bilinear terms with respect to the magnon operators again, we obtain

$$
N_{ab} \sum_{\alpha,\beta,\gamma} \mathsf{S}_{\boldsymbol{r}}^{\alpha} L_{\boldsymbol{r}}^{\alpha a} \mathsf{S}_{\boldsymbol{r}}^{\beta} L_{\boldsymbol{r}}^{\beta a} \mathsf{S}_{\boldsymbol{r}}^{\gamma} L_{\boldsymbol{r}}^{\gamma b} = \frac{N_{ab}S^2}{2}\Big[(L_{aab}^{113} + 2iL_{aab}^{123} - L_{aab}^{223})a_{\boldsymbol{r}}^{\dagger}a_{\boldsymbol{r}}^{\dagger} + \text{c.c.}
$$
$$
+ \;\; (L_{aab}^{113} + L_{aab}^{223} - 3L_{aab}^{333})(a_{\boldsymbol{r}}^{\dagger}a_{\boldsymbol{r}} + a_{\boldsymbol{r}}a_{\boldsymbol{r}}^{\dagger})\Big], \qquad \text{(C.28)}
$$

where we denote

$$
\begin{aligned}
L_{aab}^{113} &= 2L_{\boldsymbol{r}}^{1a} L_{\boldsymbol{r}}^{3a} L_{\boldsymbol{r}}^{1b} + (L_{\boldsymbol{r}}^{1a})^2 L_{\boldsymbol{r}}^{3b}, \\
L_{aab}^{223} &= 2L_{\boldsymbol{r}}^{2a} L_{\boldsymbol{r}}^{3a} L_{\boldsymbol{r}}^{2b} + (L_{\boldsymbol{r}}^{2a})^2 L_{\boldsymbol{r}}^{3b}, \\
L_{aab}^{333} &= (L_{\boldsymbol{r}}^{3a})^2 L_{\boldsymbol{r}}^{3b}, \\
L_{aab}^{123} &= L_{\boldsymbol{r}}^{1a} L_{\boldsymbol{r}}^{2a} L_{\boldsymbol{r}}^{3b} + L_{\boldsymbol{r}}^{3a} L_{\boldsymbol{r}}^{1a} L_{\boldsymbol{r}}^{2b} + L_{\boldsymbol{r}}^{2a} L_{\boldsymbol{r}}^{3a} L_{\boldsymbol{r}}^{1b}.
\end{aligned} \qquad \text{(C.29)}
$$

Using Eqs. (C.26) and (C.26), we can obtain the spin wave Hamiltonians for $H_F^{(1)}$. For $\mathbf{B}_0 \parallel [110]$, $H_F^{(1)}$ is rewritten from Eq. (C.13) as

$$
H_F^{(1)} = \sum_{\boldsymbol{r}} \Big[- g\mu_B B_F \boldsymbol{S}_{\boldsymbol{r}} \cdot \hat{z} + K_{zx} S_{\boldsymbol{r},z} S_{\boldsymbol{r},x} + N_{xz} S_{\boldsymbol{r},x}^2 S_{\boldsymbol{r},z} + N_{yz} S_{\boldsymbol{r},y}^2 S_{\boldsymbol{r},z} \Big], \qquad \text{(C.30)}
$$

with $K_{zx} = g\mu_B B_F \mathcal{E}_d$, $N_{xz} = 2g\mu_B B_F \mathcal{E}_d^2$, and $N_{yz} = -g\mu_B B_F \mathcal{E}_d^2$. Once the HP transformation is carried out, it is straightforward to obtain the Bogoliubov-de Gennes form of Floquet magnon Hamiltonian as demonstrated in Section 1.1.3.

Appendix D

Modern theory of polarization

D.1 Introduction

In classical electromagnetism, the electric dipole moment of a pair of opposite charges has a physically intuitive definition

$$\mathbf{p} = Q\boldsymbol{r}, \tag{D.1}$$

where Q is the magnitude of electric charge carried by each particle and $\boldsymbol{r}$ is the displacement vector from $-Q$ to $+Q$. It seems reasonable to generalize a definition of the macroscopic electric polarization for insulators as follows [86].

$$\mathbf{P} = \frac{1}{V_{\text{cell}}} \int_{\text{cell}} dr^3 \, \boldsymbol{r}\rho(\boldsymbol{r}), \tag{D.2}$$

where V_{cell} is a unit cell volume and $\rho(\boldsymbol{r})$ is the local (nuclear and electric) charge density. However, it turns out that this is not a correct definition. The main problem is that the integrand is not a cell-periodic function.

We can see this clearly in a simple picture of electric point charges, where the electric polarization is given by

$$\mathbf{P} = \frac{e}{V_{\text{cell}}} \sum_{j=1}^{2} Z_j \boldsymbol{r}_j, \tag{D.3}$$

with $Z_1 = +1$ and $Z_2 = -1$. The position of each charge is depicted as $\boldsymbol{r}_1$ and $\boldsymbol{r}_2$. Here, we are free to choose the origin such as $\{\boldsymbol{r}_1, \boldsymbol{r}_2\} = \{(0,0,0), (\frac{a}{2},0,0)\}$ or $\{\boldsymbol{r}_1, \boldsymbol{r}_2\} = \{(\frac{a}{2},0,0), (0,0,0)\}$ with lattice constant a. Depending on the choice of origin, the electric polarization becomes $\mathbf{P} = \pm\frac{e}{2A}\hat{x}$ with A being the area of unit cell projected to yz-plane. Thus, the electric polarization differs by $\Delta\mathbf{P} = \frac{e}{A}\hat{x}$ as we shift the origin. More generally, the origin of coordinates maybe shifted by any lattice vector $\mathbf{R}$. This leads to a difference in electric polarization

$$\Delta\mathbf{P} = \frac{e\mathbf{R}}{V_{\text{cell}}}. \tag{D.4}$$

Therefore, the definition of bulk polarization needs to satisfy this multivalued property but Eq. (D.2) does not.

Historically, the first important step towards the modern theory of polarization was made by Resta, who realized that only a change in the polarization is uniquely defined and experimentally observable [82]. Soon after that, the expression for the electric polarization was derived in terms of the Berry phase [82–86]

$$\mathbf{P} = \frac{-e}{(2\pi)^3} \int_{\mathrm{BZ}} \mathrm{tr}[\boldsymbol{\mathcal{A}}(\boldsymbol{k})]d\boldsymbol{k}, \tag{D.5}$$

where $\boldsymbol{\mathcal{A}}(\boldsymbol{k}) = i \langle u_{m,\boldsymbol{k}}|\nabla_{\boldsymbol{k}}|u_{n,\boldsymbol{k}}\rangle$ is the Berry connection of occupied bands [1, 7]. We should note that the gauge transformation $|\tilde{u}_{m,\boldsymbol{k}}\rangle = e^{i\theta_{\boldsymbol{k}}}|u_{m,\boldsymbol{k}}\rangle$ leads to

$$\begin{aligned}
\tilde{\mathbf{P}} &= \frac{-e}{(2\pi)^3} \int_{\mathrm{BZ}} \mathrm{tr}[\boldsymbol{\mathcal{A}}(\boldsymbol{k})]d\boldsymbol{k} + \frac{e}{(2\pi)^3} \int_{\mathrm{BZ}} \nabla\theta_{\boldsymbol{k}}d\boldsymbol{k} \\
&= \frac{-e}{(2\pi)^3} \int_{\mathrm{BZ}} \mathrm{tr}[\boldsymbol{\mathcal{A}}(\boldsymbol{k})]d\boldsymbol{k} + \frac{e\mathbf{R}}{V_{\mathrm{cell}}}.
\end{aligned} \tag{D.6}$$

Here, we have used a general form of gauge transformation $\theta_{\boldsymbol{k}} = \beta_{\boldsymbol{k}} + \mathbf{R} \cdot \boldsymbol{k}$ with $\beta_{\boldsymbol{k}}$ periodic in $\boldsymbol{k}$. We should also note that the integrand in Eq. (D.5) is cell-periodic as it can be also written in terms of the Wannier center (see Section 1.2.2).

It should be note that an equivalent result was derived by Thouless before the modern theory of polarization [302]. In this seminal work, he considered the quantized charge transport by adiabatically changing a Hamiltonian over a closed loop in the parameter space. For example, a simple example is to introduce a one-dimensional potential

$$V(x,t) = -V_0 \cos(2\pi x/a - \lambda), \tag{D.7}$$

where λ is adiabatically changed from $\lambda = 0$ to $\lambda = 2\pi$.

For large potential V_0, it is straightforward to see that this leads to a pumping of one electron by one lattice vector. Remarkably, the quantized charge transport is expected even if V_0 is small as long as the adiabatic condition is satisfied. Noting that $\frac{dP_x}{dt} = J_x$, the integral of the induced currents is given by

$$\begin{aligned}
\int_{t_i}^{t_f} dt\, J_x(t) &= \int_{t_i}^{t_f} dt\, \frac{dP_x}{d\lambda}\frac{d\lambda}{dt} = P_x(\lambda = 2\pi) - P_x(\lambda = 0) \\
&= -e \int_{-\pi}^{\pi} \frac{dk}{2\pi} \int_0^{2\pi} d\lambda\, \mathrm{tr}\Big(\partial_\lambda\mathcal{A}_k(k,\lambda) - \partial_k\mathcal{A}_\lambda(k,\lambda)\Big),
\end{aligned} \tag{D.8}$$

where $\mathcal{A}_{k/\lambda}(k,\lambda) = \langle u_{m,k}|\partial_{k/\lambda}|u_{n,k}\rangle$ for occupied states. The last equality is obtained by Eq. (D.5) and the Stokes theorem. An important observation in Eq. (D.8) is that the integral takes the form of the Chern number of a two-dimensional torus, so it is always quantized to be integers. Furthermore, the topological nature of quantized charge pumping is inherently related with chiral edge states in Quantum Hall states. In a finite system, the quantized charge transport is realized by pumping states on the left (right) edge above (below) the Fermi energy during one cycle [86]. If we replace the parameter space (k, λ) by (k_x, k_y), this corresponds to chiral edge states. Thus, it demonstrates the fundamental relationship between topological phases of matter and bulk electric polarization.

D.2 Multiband formulation of Wannier functions

In Section 1.2.2, we have introduced Wannier functions as the Fourier transform of Bloch functions that are smooth in the Brillouin zone. However, this is only possible for a rare case where there is no band touching with other bands. Practically, we need to construct Wannier functions from a group of bands that are isolated from other bands but may have band touchings among themselves. The main issue is that degenerate points in momentum space act as singularities in Fourier transforms, resulting in the loss of localization property in real space.

A simple solution is to apply a unitary transformation so that a new representation of Bloch functions $|\tilde{\psi}_{n,\boldsymbol{k}}\rangle$, not necessarily energy eigenstates, are smooth functions in the Brillouin zone [86].

$$|\tilde{\psi}_{n,\boldsymbol{k}}\rangle = \sum_{m=1}^{N} U_{mn}(\boldsymbol{k}) |\psi_{n,\boldsymbol{k}}\rangle, \tag{D.9}$$

where $U_{mn}(\boldsymbol{k})$ is a $N \times N$ unitary matrix with N denoting the number of bands. If this transformation is possible, we can construct well-localized Wannier functions from $|\tilde{\psi}_{n,\boldsymbol{k}}\rangle$. It is obvious that there is no unique choice of Wannier functions. In fact, there are infinitely many choices of a unitary matrix $U'_{mn}(\boldsymbol{k}) = U_{m\ell}(\boldsymbol{k})V_{\ell n}(\boldsymbol{k})$, given that $V_{\ell n}(\boldsymbol{k})$ is smoothly defined in k space.

Now, the question is how to find $|\tilde{\psi}_{n,\boldsymbol{k}}\rangle$ that can smooth out Bloch functions. In order to improve the smoothness of Bloch functions locally, we need to rotate a Bloch function at $\boldsymbol{k} + \delta\boldsymbol{k}$ to be optimally aligned with itself at $\boldsymbol{k}$. In a single band case, this implies that $\langle u_{n,\boldsymbol{k}}|u_{n,\boldsymbol{k}+\delta\boldsymbol{k}}\rangle$ is real and positive. In a multiband case, the inner product between Bloch functions $M_{mn}(\boldsymbol{k}, \boldsymbol{k} + \delta\boldsymbol{k}) = \langle u_{m,\boldsymbol{k}}|u_{n,\boldsymbol{k}+\delta\boldsymbol{k}}\rangle$ should be Hermitian and positive definite. This is achieved by employing the singular value decomposition $M(\boldsymbol{k}, \boldsymbol{k} + \delta\boldsymbol{k}) = UDV^{\dagger}$, where U and V are unitary and D is a diagonal matrix with real and positive elements. A new Bloch function is then given as $|\tilde{u}_{n,\boldsymbol{k}+\delta\boldsymbol{k}}\rangle = VU^{\dagger}|u_{n,\boldsymbol{k}+\delta\boldsymbol{k}}\rangle$, and a new inner product becomes $\tilde{M}(\boldsymbol{k}, \boldsymbol{k} + \delta\boldsymbol{k}) = UDU^{\dagger}$ that is Hermitian and positive definite. Usually, this procedure works well to obtain smoothly defined Bloch functions over the entire Brillouin zone.

While it is not possible to uniquely define Wannier functions, one of the special choices is called the maximally localized Wannier functions. They are defined as a Wannier function with a minimal quadratic spreading $\sum_{n=1}^{N}[\langle w_{n,0}|r^2|w_{n,0}\rangle - |\boldsymbol{r}_n|^2]$, where $\boldsymbol{r}_n = \langle w_{n,0}|\boldsymbol{r}|w_{n,0}\rangle$ is a Wannier center. They are the standard choice of Wannier functions in numerical packages following a general recipe of construction [348]. Also, they provide a natural choice for defining the bulk multipole moments as discussed in the following.

D.3 Maximally localized Wannier functions

For a multiband case, Wannier functions related by unitary transformations are equally valid as long as they are sufficiently localized. This implies that Wannier centers depend

on the choice of Wannier functions. A natural question is then what relations hold between Wannier centers and Berry phases. It is also related to the multiband formulation of bulk polarization. For isolated single bands, there is a direct correspondence between Wannier centers and Berry phases as shown below. From Eq. (1.43), the equality for a one-dimensional system with lattice constant a is derived as

$$r_n = \frac{a}{2\pi}\phi_n, \tag{D.10}$$

where r_n and ϕ_n are the Wannier center and Berry phase, respectively.

The answer to the above question is that Berry phases correspond to Wannier centers of maximally localized Wannier functions in one-dimensional systems [86]. To prove this, we first show that one-dimensional maximally localized Wannier functions are eigenstates of $P^{\mathrm{occ}} x P^{\mathrm{occ}}$, where P^{occ} is the projection operator to occupied states. The functional to be minimized for maximally localized Wannier functions can be rewritten as [348]

$$\Omega = \sum_n \left[\langle w_{n,0}|r^2|w_{n,0}\rangle - |\boldsymbol{r}_n|^2 \right] = \Omega_I + \tilde{\Omega}, \tag{D.11}$$

where

$$\Omega_I = \sum_n \left[\langle w_{n,0}|r^2|w_{n,0}\rangle - \sum_{m,\boldsymbol{R}} |\langle w_{m,\boldsymbol{R}}|\boldsymbol{r}|w_{n,0}\rangle|^2 \right],$$

$$\tilde{\Omega} = \sum_n \sum_{(m,\boldsymbol{R})\neq(n,0)} |\langle w_{m,\boldsymbol{R}}|\boldsymbol{r}|w_{n,0}\rangle|^2. \tag{D.12}$$

It is clear that the second functional is positive definite. The first functional is simplified by the projection operator $P^{\mathrm{occ}} = \sum_{n,\boldsymbol{R}} |w_{n,\boldsymbol{R}}\rangle \langle w_{n,\boldsymbol{R}}|$ and $Q = 1 - P^{\mathrm{occ}}$:

$$\Omega_I = \sum_n \left[\langle w_{n,0}|r^2|w_{n,0}\rangle - \sum_{m,\boldsymbol{R}} \langle w_{n,0}|\boldsymbol{r}|w_{m,\boldsymbol{R}}\rangle \langle w_{m,\boldsymbol{R}}|\boldsymbol{r}|w_{n,0}\rangle \right]$$

$$= \sum_n \sum_{i=x,y,z} \langle w_{n,0}|r_i Q r_i|w_{n,0}\rangle = \sum_{i=x,y,z} \mathrm{tr}_c[P^{\mathrm{occ}} r_i Q r_i]$$

$$= \sum_{i=x,y,z} \mathrm{tr}_c[(P^{\mathrm{occ}} r_i Q)(P^{\mathrm{occ}} r_i Q)^\dagger], \tag{D.13}$$

where tr_c denotes the trace per unit cell. For the last equality, we have used $(P^{\mathrm{occ}})^2 = P^{\mathrm{occ}}$ and $Q^2 = Q$. Thus, the first functional is also positive definite. More importantly, $P^{\mathrm{occ}} x Q$ commutes with the translation operator T_x:

$$T_x P^{\mathrm{occ}} x(1 - P^{\mathrm{occ}}) = T_x \sum_{\boldsymbol{R},n} \sum_{\boldsymbol{R}',m} |w_{n,\boldsymbol{R}}\rangle \langle w_{n,\boldsymbol{R}}| x \left(1 - |w_{m,\boldsymbol{R}'}\rangle \langle w_{m,\boldsymbol{R}'}| \right)$$

$$= \sum_{\boldsymbol{R},n} \sum_{\boldsymbol{R}',m} |w_{n,\boldsymbol{R}+a\hat{e}_x}\rangle \langle w_{n,\boldsymbol{R}+a\hat{e}_x}| (x+a) \left(1 - |w_{m,\boldsymbol{R}'+a\hat{e}_x}\rangle \langle w_{m,\boldsymbol{R}'+a\hat{e}_x}| \right) T_x$$

$$= P^{\mathrm{occ}} x(1 - P^{\mathrm{occ}}) T_x, \tag{D.14}$$

where the last equality is obtained by redefining $\boldsymbol{R}$ and $\boldsymbol{R}'$. Since $P^{\text{occ}}xQ$ has a well-defined eigenvalue for Bloch functions, the first functional Ω_I is gauge invariant and independent from choice of Wannier functions. Therefore, the total spreading functional Ω is minimized when $\tilde{\Omega} = 0$. This is satisfied if maximally localized Wannier functions are eigenstates of $P^{\text{occ}}xP^{\text{occ}}$ so that $\langle w_{m,\boldsymbol{R}}|x|w_{n,0}\rangle = x_n\delta_{m,n}\delta_{\boldsymbol{R},0}$. We should note that $P^{\text{occ}}xP^{\text{occ}}$, $P^{\text{occ}}yP^{\text{occ}}$, and $P^{\text{occ}}zP^{\text{occ}}$ do not commute with each other so the optimal choice is possible only in one-dimensional systems.

The remaining problem is the relationship between eigenvalues of $P^{\text{occ}}xP^{\text{occ}}$, which correspond to the Wannier centers of maximally localized Wannier functions, and Berry phases. In the following section, we resolve this issue by constructing the Wilson loop from $P^{\text{occ}}xP^{\text{occ}}$.

D.4 Wilson loop formalism

In periodic systems, the position operator is ill-defined as it does not commute with the translation operator. Instead, we could consider expectation values of another operator $e^{i\frac{2\pi}{L}\hat{x}}$, which commutes with the translation operator. With this approach, the expectation value of position operator was derived as [349]

$$\langle \hat{x}\rangle = \frac{L}{2\pi}\text{Im}\,\ln\langle\psi_0|e^{i\frac{2\pi}{L}\hat{x}}|\psi_0\rangle\,, \tag{D.15}$$

where L is the periodicity of one-dimensional systems and ψ_0 is the ground state.

Using Eq. (D.15) and following Ref. [80], we solve the eigenvalue problem of $P^{\text{occ}}xP^{\text{occ}}$. In this section, we focus on a one-dimensional system that contains N unit cells with N_{orb} orbitals per unit cell. The periodicity is given as $L = Na$ for lattice constant a. The position operator is introduced in the second quantized form:

$$e^{i\frac{2\pi}{L}\hat{x}} = \sum_{R,\alpha} c_{R,\alpha}^\dagger|0\rangle\,e^{-i\Delta_k(R+r_\alpha)}\langle 0|c_{R,\alpha}, \tag{D.16}$$

where $\Delta_k = \frac{2\pi}{L}$ and $c_{R,\alpha}^\dagger/c_{R,\alpha}$ is the creation/annihilation operator of the orbital labeled by $\alpha = 1, 2, .., N_{\text{orb}}$ inside the unit cell labeled by $R = 0, .., N-1$. The position of the orbital with respect to the fixed origin is depicted as r_α. We should note that the sign in the exponential needs to be changed in this approach. The discrete Fourier transform is defined as

$$c_{R,\alpha} = \frac{1}{\sqrt{N}}\sum_k e^{-ik(R+r_\alpha)}c_{k,\alpha},$$

$$c_{k,\alpha} = \frac{1}{\sqrt{N}}\sum_R e^{ik(R+r_\alpha)}c_{R,\alpha}, \tag{D.17}$$

where $k = m\Delta_k$ for $m = 0, \ldots, N-1$. In order to represent the cell-periodic part of

Bloch functions, they satisfy

$$
\begin{aligned}
c_{R+N,\alpha} &= c_{R,\alpha}, \\
c_{k+G,\alpha} &= e^{iGr_\alpha} c_{k,\alpha},
\end{aligned}
\tag{D.18}
$$

with G being a reciprocal lattice vector. After performing the Fourier transform, the position operator is given by

$$
\hat{x} = \sum_{k,\alpha} c^\dagger_{k+\Delta_k,\alpha} |0\rangle \langle 0| c_{k,\alpha}.
\tag{D.19}
$$

Now, we construct the projection operator. The second quantized Hamiltonian is generally written as

$$
H = \sum_k c^\dagger_{k,\alpha} h^{\alpha\beta}(k) c_{k,\beta},
\tag{D.20}
$$

which is diagonalized as

$$
h^{\alpha\beta}(k) = \sum_n [u_{n,k}]^\alpha \epsilon_{n,k} [u^*_{n,k}]^\beta,
\tag{D.21}
$$

where $[u_{n,k}]^\alpha$ is the αth component of the eigenstate $|u_{n,k}\rangle$. The Hamiltonian is then rewritten as

$$
H = \sum_{n,k} \gamma^\dagger_{n,k} \epsilon_{n,k} \gamma_{n,k},
\tag{D.22}
$$

with $\gamma_{n,k} = \sum_\alpha [u^*_{n,k}]^\alpha c_{k,\alpha}$ representing energy eigenstates of the Bloch Hamiltonian. To choose the periodic gauge $\gamma_{n,k+G} = \gamma_{n,k}$, we impose $[u_{n,k+G}]^\alpha = [V(G)]^{\alpha\beta} [u_{n,k}]^\beta$ where $[V^{-1}(G)]^{\alpha\beta} = e^{-iGr_\alpha} \delta_{\alpha,\beta}$. The projection operator for occupied states are then written as

$$
p^{\mathrm{occ}} = \sum_{n=1}^{N_{\mathrm{occ}}} \sum_k \gamma^\dagger_{n,k} |0\rangle \langle 0| \gamma_{n,k}.
\tag{D.23}
$$

We now proceed to diagonalize the position operator projected into the subspace of occupied bands. It is simplified as

$$
\begin{aligned}
p^{\mathrm{occ}} e^{i\frac{2\pi}{L}\hat{x}} p^{\mathrm{occ}} &= \sum_{n,k} \sum_{n',k'} \gamma^\dagger_{n,k} |0\rangle \left(\sum_{q,\alpha} \langle 0| \gamma_{n,k} c^\dagger_{q+\Delta_q,\alpha} |0\rangle \langle 0| c_{q,\alpha} \gamma^\dagger_{n',k'} |0\rangle \right) \langle 0| \gamma_{n',k'} \\
&= \sum_{m,n}^{N_{\mathrm{occ}}} \sum_k \gamma^\dagger_{m,k} |0\rangle \langle u_{m,k+\Delta_k} | u_{n,k}\rangle \langle 0| \gamma_{n,k},
\end{aligned}
\tag{D.24}
$$

with $\langle u_{m,k} | u_{n,q}\rangle = \sum_\alpha [u^*_{m,k}]^\alpha [u_{n,q}]^\alpha$. It should be noted that the orthogonality relation does not hold between Bloch functions at different k points. For the last equality, we have used $\langle 0| \gamma_{n,k} c^\dagger_{q,\alpha} |0\rangle = [u^*_{n,k}]^\alpha \delta_{k,q}$.

The overlapping matrix $M_k^{mn} = \langle u_{m,k+\Delta_k} | u_{n,k}\rangle$ is not unitary but becomes unitary in the thermodynamic limit. Employing the singular value decomposition of $M_k = UDV^\dagger$

with D being a positive diagonal matrix, the non-unitary part of M_k results in diagonal elements in D that are less than 1. Hence, we replace the non-unitary overlapping matrix M_k with a unitary matrix $\mathcal{M}_k = UV^\dagger$, which becomes exact in the thermodynamic limit. To diagonalize the projected position operator, let us write the eigenvalue problem:

$$(p^{\text{occ}} e^{i\frac{2\pi}{L}\hat{x}} p^{\text{occ}}) |\psi^j\rangle = E^j |\psi^j\rangle . \tag{D.25}$$

In the subspace of occupied states spanned by $\gamma_{n,k} |0\rangle$, the eigenstate $|\psi^j\rangle$ is represented as $\{v_{k_1}, \ldots, v_{k_N}\}^j$ for $j = 1, \ldots, N_{\text{occ}}$, where $|v_{k_i}^j\rangle$ is a vector spanned over occupied states at $k_i = \Delta_k(i-1)$ with $i = 1, \ldots, N$. The matrix elements of Eq. (D.25) are then given as

$$\begin{pmatrix} 0 & 0 & \ldots & 0 & \mathcal{M}_{k_N} \\ \mathcal{M}_{k_1} & 0 & \ldots & 0 & 0 \\ 0 & \mathcal{M}_{k_2} & \ldots & 0 & 0 \\ \vdots & \vdots & \ldots & \vdots & \vdots \\ 0 & 0 & \ldots & \mathcal{M}_{k_{N-1}} & 0 \end{pmatrix} \begin{pmatrix} v_{k_1} \\ v_{k_2} \\ \vdots \\ \vdots \\ v_{k_N} \end{pmatrix}^j = E^j \begin{pmatrix} v_{k_1} \\ v_{k_2} \\ \vdots \\ \vdots \\ v_{k_N} \end{pmatrix}^j . \tag{D.26}$$

After repeated operations of $p^{\text{occ}} e^{i\frac{2\pi}{L}\hat{x}} p^{\text{occ}}$ for N times, each component of $|\psi^j\rangle$ maps to itself. The corresponding unitary operator for this closed loop is called the Wilson loop, which is defined as

$$W_{k_f \leftarrow k_i} = \mathcal{M}_{k_f - \Delta_k} \mathcal{M}_{k_f - 2\Delta_k} \ldots \mathcal{M}_{k_i + \Delta_k} \mathcal{M}_{k_i}, \tag{D.27}$$

where the subscript k_i/k_f labels the starting/ending point of a loop. For each component of $|\psi^j\rangle$, we obtain

$$W_{k + \frac{2\pi}{a} \leftarrow k} |v_k^j\rangle = (E^j)^N |v_k^j\rangle , \tag{D.28}$$

with the subscript k denoting the starting point of the Wilson loop. The eigenstate $|v_k^j\rangle$ depends on k but not for the eigenvalue $(E^j)^N$. Since the Wilson loop is unitary, its eigenvalue is a phase factor. In fact, it is equivalent to parallel transport of occupied states, so the eigenvalues are equal to the Berry phases of occupied states:

$$(E^j)^N = e^{i\phi^j}. \tag{D.29}$$

It is easy to check that Wilson loop is written in terms of the Berry connection in the thermodynamic limit. Taking the limit of $\Delta_k \to 0$, the overlapping matrix is expanded as

$$\begin{aligned} M_k^{mn} &= \langle u_{m,k+\Delta_k} | u_{n,k} \rangle = \langle u_{m,k} | u_{n,k} \rangle + \Delta_k \langle \partial_k u_{m,k} | u_{n,k} \rangle \\ &= \delta_{mn} - \Delta_k \langle u_{m,k} | \partial_k u_{n,k} \rangle , \end{aligned} \tag{D.30}$$

where we have used $\partial_k \langle u_{m,k}|u_{n,k}\rangle = 0$. Noting that $\mathcal{A}^{mn}(k) = i\langle u_{m,k}|\partial_k u_{n,k}\rangle$ is the Berry connection, the Wilson loop is expressed as

$$
\begin{aligned}
W_{k+\frac{2\pi}{a}\leftarrow k} &= \lim_{N\to\infty}\prod_{n=1}^{N}\mathcal{M}_{k+\frac{2\pi}{a}-n\Delta_k} = \lim_{N\to\infty}\prod_{n=1}^{N}\left[I + i\Delta_k\mathcal{A}(k+\frac{2\pi}{a}-n\Delta_k)\right] \\
&= \exp\left[i\int_{k}^{k+\frac{2\pi}{a}}\mathcal{A}(k)dk\right].
\end{aligned}
\tag{D.31}
$$

From Eq. (D.29), there are N possible solutions for the eigenvalue of $p^{\mathrm{occ}}e^{i\frac{2\pi}{L}\hat{x}}p^{\mathrm{occ}}$.

$$
E^{j,R} = \exp\left(i\frac{\phi^j + 2\pi R}{N}\right),
\tag{D.32}
$$

for $R = 0,\ldots,N-1$. The eigenstates of $p^{\mathrm{occ}}e^{i\frac{2\pi}{L}\hat{x}}p^{\mathrm{occ}}$ is then obtained as

$$
|\psi_R^j\rangle = \frac{1}{\sqrt{N}}\sum_{n=1}^{N_{\mathrm{occ}}}\sum_{k}[v_k^j]^n e^{-ikR}\gamma_{n,k}^{\dagger}|0\rangle.
\tag{D.33}
$$

From Section D.3, we know that $|\psi_R^j\rangle$ are maximally localized Wannier functions. As discussed in Section 1.2.2, each eigenvalue of Eq. (D.32) represents the center of Wannier function that is exponentially localized in each unit cell labeled by R. Hence, the expectation value of $p^{\mathrm{occ}}e^{i\frac{2\pi}{L}\hat{x}}p^{\mathrm{occ}}$ is also given as

$$
\langle\psi_0^j|e^{i\frac{2\pi}{L}\hat{x}}|\psi_0^j\rangle = e^{i\frac{2\pi}{L}\nu^j},
\tag{D.34}
$$

with ν^j denoting the Wannier center. Finally, we derive the relation between the Wannier center of maximally localized Wannier functions and Berry phases from Eqs. (D.32) and (D.34).

$$
\nu^j = \frac{a}{2\pi}\phi^j.
\tag{D.35}
$$

Using Eq. (D.35), the expectation value of position operator in one-dimensional systems is given by

$$
\tilde{r} = \sum_j \nu^j = \frac{a}{2\pi}\int_{k}^{k+\frac{2\pi}{a}}\mathrm{tr}[\mathcal{A}(k)]dk.
\tag{D.36}
$$

For higher-dimensional systems, the expectation value of the position operator in the x-axis is defined equivalently by treating Bloch wave functions as one-dimensional systems with parameters (k_y, k_z) [79, 80]:

$$
\tilde{r}_x = \frac{a^2}{(2\pi)^2}\int dk_y dk_z \sum_j \nu_x^j(k_y, k_z) = \frac{a^3}{(2\pi)^3}\int_{\mathrm{BZ}}dk^3\mathrm{tr}[\mathcal{A}_x(\boldsymbol{k})],
\tag{D.37}
$$

where $\nu_x^j(k_y, k_z)$ is the eigenvalue of the Wilson loop $W_{x,\boldsymbol{k}} = W_{(k_x+\frac{2\pi}{a},k_y,k_z)\leftarrow(k_x,k_y,k_z)}$. Hence, we obtain Eq. (1.44).

Appendix E

Calculation of magnonic multipole moment

E.1 Wilson loop in magnonic systems

In this section, we introduce the Wilson loop formalism adapted for magnonic wave functions. In parallel with the definition of Wilson loops in electronic systems discussed in Appendix D.3, the Wilson loop in magnonic systems is defined as the parallel transport of the lowest energy magnon eigenstates. Only the difference from electronic systems is that we need to use the paraunitary inner product of Eq. (5.2) whenever the inner product of magnonic wave functions are computed. Throughout Appendix E, we take the lattice constant to be unity. The content of Appendix E was published in Ref. [212].

Using the orthogonal basis for magnon bands defined in Section 5.1.1, we introduce the Wilson loop $W_{x,\boldsymbol{k}}$ of the lowest M magnon bands in two-dimensional systems as

$$W_{x,(k_x,k_y)} = \mathcal{M}_{(k_x+(N_k-1)\Delta_k,k_y)}\mathcal{M}_{(k_x+(N_k-2)\Delta_k,k_y)} \ldots \mathcal{M}_{(k_x,k_y)} \,, \tag{E.1}$$

where $\Delta_k = 2\pi/N_k$ and $\mathcal{M}_{(k_x,k_y)}$ is the unitary part of the overlapping matrix

$$[M_{(k_x,k_y)}]^{mn} = \langle u^m_{(\Delta_k+k_x,k_y)}|u^n_{(k_x,k_y)}\rangle_{\text{para}} \,, \tag{E.2}$$

with the band index $m, n = 1, \ldots, M$ and the subscript indicating the paraunitary inner product of Eq. (5.2). We take the periodic gauge across the Brillouin zone, i.e. $|u^n_{\boldsymbol{k}+\mathbf{G}}\rangle = |u^n_{\boldsymbol{k}}\rangle$ with $\mathbf{G}$ denoting a reciprocal lattice vector. The singular value decomposition is used for extracting the unitary part $\mathcal{M}_{(k_x,k_y)}$, which becomes exact in the thermodynamic limit. Here, we should note that the paraunitary inner product is necessary to ensure that the Wilson loop becomes unitary in the thermodynamic limit. The eigenvalue of a Wilson loop is given as

$$W_{x,\boldsymbol{k}}\,|\nu^j_{x,\boldsymbol{k}}\rangle = e^{i2\pi\nu^j_x(k_y)}\,|\nu^j_{x,\boldsymbol{k}}\rangle \,, \tag{E.3}$$

where $j = 1, \ldots, M$ and $\nu^j_x(k_y)$ are the Wannier centers. We should note that the eigenstates $|\nu^j_{x,\boldsymbol{k}}\rangle$ depend on both k_x and k_y although the Wannier centers $\nu^j_x(k_y)$ only depend on k_y.

Treating k_y as a parameter, one-dimensional Wannier functions along x-axis are given as

$$|\Psi^j_{R_x,k_y}\rangle = \frac{1}{\sqrt{N_k}} \sum_{n=1}^{M} \sum_{k_x} [\nu^j_{x,\boldsymbol{k}}]^n e^{-ik_x R_x} T_{\boldsymbol{k}} v_n \,, \tag{E.4}$$

where $[\nu^j_{x,\boldsymbol{k}}]^n$ is the nth element of $|\nu^j_{x,\boldsymbol{k}}\rangle$ and the Wannier function $|\Psi^j_{R_x,k_y}\rangle$ is exponentially localized along x-axis with a unit cell labeled by $R_x \in \{0, 1, 2, \ldots\}$. Since the Wannier functions in Eq. (E.4) are labeled by a real space index R_x and a momentum space index k_y, they are called hybrid Wannier functions. They form a complete orthogonal set, i.e.,

$$\langle \Psi^j_{R_x,k_y} | \Psi^{j'}_{R'_x,k'_y} \rangle_{\text{para}} = \delta_{R_x,R'_x} \delta_{k_y,k'_y} \delta_{j,j'} \,. \tag{E.5}$$

Since the Wannier center $\nu^j_x(k_y)$ is the expectation value of the position operator $\hat{x}$ (see Section 1.2.2), we have

$$\nu^j_x(k_y) = \langle \Psi^j_{0,k_y} | \hat{x} | \Psi^j_{0,k_y} \rangle_{\text{para}} \mod 1 \,. \tag{E.6}$$

In order to ensure that the Wannier centers obtained using Eq. (E.3) and Eq. (E.6) are consistent, the origin for the eigenvalues of $\hat{x}$ must coincide with the origin defined via the Wilson loop, which corresponds to the site within the magnetic unit cell where it has purely real elements for all eigenstates.

In electronic systems, the Wilson loop is written in terms of the Berry connection in the thermodynamic limit (see Eq. (D.31)). The same relationship also holds in magnonic systems. In the thermodynamic limit, we have

$$\begin{aligned}
[\mathcal{M}_{\boldsymbol{k}}]^{mn} &= \xi v_m^T (T_{\boldsymbol{k}}^\dagger + \Delta_k \partial_{k_x} T_{\boldsymbol{k}}^\dagger) \Sigma T_{\boldsymbol{k}} v_n \\
&= \delta_{mn} - \Delta_k \xi v_m^T T_{\boldsymbol{k}}^\dagger \Sigma \partial_{k_x} T_{\boldsymbol{k}} v_n \\
&= \delta_{mn} + i \Delta_k \mathcal{A}_x^{mn}(\boldsymbol{k}) \,,
\end{aligned} \tag{E.7}$$

where $\mathcal{A}_x^{mn}(\boldsymbol{k})$ is the Berry connection for magnons given as Eq. (5.3). From Eq. (E.7), the Wilson loop is derived in the thermodynamic limit as

$$\begin{aligned}
W_{x,\boldsymbol{k}} &= \lim_{N_k \to \infty} \prod_{\ell=0}^{N_k-1} [I + i\Delta_k \mathcal{A}_x(k_x + \ell\Delta_k, k_y)] \\
&= \exp\left[i \int_0^{2\pi} \mathcal{A}_x(\boldsymbol{k}) \, dk_x\right] \,.
\end{aligned} \tag{E.8}$$

Analogously to Eq. (1.45), the magnonic polarization along the x-axis is given by the summation of Wannier centers:

$$p_x = \frac{1}{N_k} \sum_{k_y} \sum_{j=1}^{M} \nu^j_x(k_y) \mod 1 \,. \tag{E.9}$$

Similarly, the total bulk polarization along the y-axis is given by

$$p_y = \frac{1}{N_k} \sum_{k_x} \sum_{j=1}^{M} \nu_y^j(k_x) \bmod 1 \,. \tag{E.10}$$

In the continuum limit, we obtain Eqs. (5.11) and (5.12).

E.2 Nested Wilson loop in magnonic systems

In this section, we introduce the nested Wilson loop for magnonic systems. Given a gapped Wannier spectrum $\nu_x(k_y)$ that contains M bands, we define a subspace of Wannier bands as $\nu_x^+ \in [0, \frac{1}{2})$ and $\nu_x^- \in [-\frac{1}{2}, 0)$. To construct the nested Wilson loop, we need to introduce a Wannier band basis:

$$|\omega_{x,\boldsymbol{k}}^j\rangle = \sum_{n=1}^{M} [\nu_{x,\boldsymbol{k}}^j]^n T_{\boldsymbol{k}} v_n \,, \tag{E.11}$$

where $j = 1, \ldots, M_W$ with $M_W = M/2$ is the number of bands that belong to the Wannier sector $\nu_x^{\pm}$ and $[\nu_{x,\boldsymbol{k}}^j]^n$ is the n-th matrix element of eigenstates of the Wilson loop defined in Eq. (E.3). Similarly to the Wilson loop, the nested Wilson loop $\tilde{W}_{y,\boldsymbol{k}}^{\nu_x^{\pm}}$ for magnonic systems is defined as

$$
\begin{aligned}
[\tilde{W}_{y,\boldsymbol{k}}^{\nu_x^{\pm}}]^{j,j'} ={}& \langle \omega_{x,(k_x,k_y+2\pi)}^j | \omega_{x,(k_x,k_y+(N_k-1)\Delta_k)}^r \rangle_{\mathrm{para}} \\
&\times \langle \omega_{x,(k_x,k_y+(N_k-1)\Delta_k)}^r | \ldots | \omega_{x,(k_x,k_y+\Delta_k)}^t \rangle_{\mathrm{para}} \\
&\times \langle \omega_{x,(k_x,k_y+\Delta_k)}^t | \omega_{x,(k_x,k_y)}^{j'} \rangle_{\mathrm{para}} \,,
\end{aligned}
\tag{E.12}
$$

where the paraunitary matrix is inserted as defined in Eq. (5.2) to ensure the orthogonality relations in the Wannier band basis. Diagonalizing the nested Wilson loop, we obtain

$$\tilde{W}_{y,\boldsymbol{k}}^{\nu_x^{\pm}} | \nu_{y,\boldsymbol{k}}^{\nu_x^{\pm},p} \rangle = e^{i2\pi \nu_y^{\nu_x^{\pm},p}(k_x)} | \nu_{y,\boldsymbol{k}}^{\nu_x^{\pm},p} \rangle \,, \tag{E.13}$$

where $\nu_y^{\nu_x^{\pm},p}$ is the Wannier center along the y axis evaluated in the Wannier sector $\nu_x^{\pm}$ and $p = 1, \ldots, M_W$. Alternatively, the eigenvalues of the nested Wilson loop can be written as

$$\nu_y^{\nu_x^{\pm},p}(k_x) = \langle \Phi_{0,k_x}^{\nu_x^{\pm},p} | \hat{y} | \Phi_{0,k_x}^{\nu_x^{\pm},p} \rangle_{\mathrm{para}} \bmod 1 \,, \tag{E.14}$$

with

$$|\Phi_{R_y,k_x}^{\nu_x^{\pm},p}\rangle = \frac{1}{\sqrt{N_k}} \sum_{k_y} \sum_{j=1}^{M_W} [\nu_{y,\boldsymbol{k}}^{\nu_x^{\pm},p}]^j e^{-ik_y R_y} | \omega_{x,(k_x,k_y)}^j \rangle \,, \tag{E.15}$$

where $R_y \in \{0, 1, 2, \ldots\}$ labels the unit cells along the y-axis and $[\nu_{y,\mathbf{k}}^{\nu_x^{\pm}, p}]^j$ is the j-th element of $|\nu_{y,\mathbf{k}}^{\nu_x^{\pm}, p}\rangle$. The total Wannier sector polarization is

$$p_y^{\nu_x^{\pm}} = \frac{1}{N_k} \sum_{k_x} \sum_{p=1}^{M_W} \nu_y^{\nu_x^{\pm}, p}(k_x) \bmod 1 \,, \tag{E.16}$$

and similarly

$$p_x^{\nu_y^{\pm}} = \frac{1}{N_k} \sum_{k_y} \sum_{p=1}^{M_W} \nu_x^{\nu_y^{\pm}, p}(k_y) \bmod 1 \,. \tag{E.17}$$

In the continuum limit, we obtain Eqs. (5.15) and (5.16).

E.3   Edge polarization in strip geometry

In this section, we define the magnonic polarization in a strip geometry. For example, we consider a system with boundaries that is periodic along x-axis and open along y-axis. Treating it as a one-dimensional periodic system, the Wilson loop along x-axis is given by

$$W_{x,k_x} = \mathcal{M}_{k_x + (N_k - 1)\Delta_k} \mathcal{M}_{k_x + (N_k - 2)\Delta_k} \ldots \mathcal{M}_{k_x} \,, \tag{E.18}$$

where $\Delta_k = 2\pi / N_k$ and

$$[\mathcal{M}_{k_x}]^{mn} = \langle u_{\Delta_k + k_x}^m | u_{k_x}^n \rangle_{\text{para}} \,, \tag{E.19}$$

with $m, n = 1, \ldots, M'$. Here, the number of magnon bands is typically given by $M' = M \times N_y$ where N_y is the number of unit cells in the y-axis and M is the number of the bulk magnon bands. After diagonalizing the Wilson loop, we have

$$W_{x,k_x} |\nu_{x,k_x}^j\rangle = e^{i2\pi\nu_x^j} |\nu_{x,k_x}^j\rangle \,, \tag{E.20}$$

where $j = 1, \ldots M'$ and ν_x^j are the Wannier centers. The hybrid Wannier functions along the x-axis are then given by

$$|\Psi_{R_x}^j\rangle = \frac{1}{\sqrt{N_k}} \sum_{n=1}^{M'} \sum_{k_x} [\nu_{x,k_x}^j]^n e^{-ik_x R_x} T_{k_x} v_n \,, \tag{E.21}$$

where $R_x \in \{0, 1, 2, \ldots\}$ is the lattice vector labeling the unit cells along the x-axis and $[\nu_{x,k_x}^j]^n$ is the n-th element of $|\nu_{x,k_x}^j\rangle$. The magnonic polarization within each unit cell is given by

$$p_x(R_y) = \sum_{j=1}^{M'} \nu_x^j \rho^j(R_y) \,, \tag{E.22}$$

where $\rho^j(R_y)$ is the probability density of the hybrid Wannier function within the unit cell labeled by $R_y \in \{0, 1, \ldots, N_y - 1\}$.

E.4 Symmetry constraints

In this section, we discuss the symmetry constraint and quantization of a magnonic quadrupole moment in the presence of $C_{2x}\mathcal{T}$, $C_{2y}\mathcal{T}$, and C_{2z}, where C_{2i} depicts the two-fold rotation about i-axis for $i = x, y, z$ and $\mathcal{T}$ is the time-reversal symmetry. Following Ref. [80], we consider the symmetry operation $C_{2y}\mathcal{T}$ on the Wilson loop. Two degenerate states at $\boldsymbol{k}$ transformed by $C_{2y}\mathcal{T}$ are related by the unitary sewing matrix

$$
\begin{aligned}
B^{mn}_{C_{2y}\mathcal{T},\boldsymbol{k}} &= \langle u^m_{(k_x,-k_y)}| \hat{C}_{2y}K |u^n_{(k_x,k_y)}\rangle_{\text{para}} \\
&= \xi v^T_m T^\dagger_{(k_x,-k_y)}\hat{C}_{2y}K\Sigma T_{(k_x,k_y)}v_n \,,
\end{aligned}
\tag{E.23}
$$

where K is the complex conjugation operator and $\hat{C}_{2y}$ is the unitary operator representation of C_{2y}. From $\hat{C}_{2y}K |u^n_{(k_x,k_y)}\rangle = |u^m_{(k_x,-k_y)}\rangle B^{mn}_{C_{2y}\mathcal{T},\boldsymbol{k}}$, we have

$$
|u^{n*}_{(k_x,k_y)}\rangle = \hat{C}^\dagger_{2y} |u^m_{(k_x,-k_y)}\rangle B^{mn}_{C_{2y}\mathcal{T},\boldsymbol{k}} \,.
\tag{E.24}
$$

Taking the complex conjugate of both sides and noting that $[\Sigma, \hat{C}_{2y}] = [\Sigma, K] = 0$, the symmetry transformation of a overlapping matrix $M_{(k_x,k_y)}$ is obtained as

$$
\begin{aligned}
M^{mn}_{(k_x,k_y)} &= \langle u^m_{(k_x+\Delta_k,k_y)}|u^n_{(k_x,k_y)}\rangle_{\text{para}} \\
&= [B^T_{C_{2y}\mathcal{T},(k_x+\Delta_k,k_y)} \langle u^*_{(k_x+\Delta_k,-k_y)}|\hat{C}^*_{2y}\hat{C}^T_{2y}|u^*_{(k_x,-k_y)}\rangle_{\text{para}} B^*_{C_{2y}\mathcal{T},(k_x,k_y)}]^{mn} \,.
\end{aligned}
\tag{E.25}
$$

Since $B_{C_{2y}\mathcal{T},\boldsymbol{k}}$ is unitary, the symmetry transformation of the Wilson loop is given by

$$
W_{x,(k_x,k_y)} = B^T_{C_{2y}\mathcal{T},(k_x,k_y)}W^*_{x,(k_x,-k_y)}B^*_{C_{2y}\mathcal{T},(k_x,k_y)} \,.
\tag{E.26}
$$

Given $W_{x,\boldsymbol{k}} |\nu^j_{\boldsymbol{k}}\rangle = e^{i2\pi\nu^j_x(k_y)} |\nu^j_{\boldsymbol{k}}\rangle$, we obtain

$$
\begin{aligned}
W_{x,\boldsymbol{k}}B^T_{C_{2y}\mathcal{T},\boldsymbol{k}} |\nu^j_{\boldsymbol{k}}\rangle &= B^T_{C_{2y}\mathcal{T},\boldsymbol{k}}W^*_{x,(k_x,-k_y)} |\nu^j_{\boldsymbol{k}}\rangle \\
&= e^{-i2\pi\nu^j_x(-k_y)}B^T_{C_{2y}\mathcal{T},\boldsymbol{k}} |\nu^j_{\boldsymbol{k}}\rangle \,.
\end{aligned}
\tag{E.27}
$$

This implies that $B^T_{C_{2y}\mathcal{T},\boldsymbol{k}} |\nu^j_{\boldsymbol{k}}\rangle$ is also an eigenstate of the Wilson loop. The eigenvalues of symmetry related eigenstates are given by

$$
\nu^j_x(k_y) \overset{C_{2y}\mathcal{T}}{=} -\nu^j_x(-k_y) \bmod 1 \,.
\tag{E.28}
$$

Likewise, the Wannier center in the y axis is constrained by

$$
\nu^j_y(k_x) \overset{C_{2x}\mathcal{T}}{=} -\nu^j_y(-k_x) \bmod 1 \,.
\tag{E.29}
$$

From Eqs. (E.28) and (E.29), Wannier centers of $C_{2x}\mathcal{T}$ and $C_{2y}\mathcal{T}$ symmetric systems are guaranteed to be $\nu_{x/y} = 0, \frac{1}{2}$ or a pair of eigenvalues satisfying $\nu^1_{x/y}(k_{y/x}) = -\nu^2_{x/y}(-k_{y/x})$.

We should note that the same result is obtained by C_{2z} symmetry [80] and by replacing rotational symmetries C_{2x} and C_{2y} with reflection symmetries M_x and M_y, which conserves spin textures of Néel skyrmions. The symmetry constraints also leads to the quantization of p_x and p_y to be either 0 or $\frac{1}{2}$.

Similarly, the symmetry related eigenvalues of the nested Wilson loop are given as

$$\nu_x^{\nu_y,j}(k_y) \overset{C_{2y}\mathcal{T}}{=} -\nu_x^{\nu_y,j}(-k_y) \bmod 1 \,, \tag{E.30}$$

$$\nu_y^{\nu_x,j}(k_x) \overset{C_{2x}\mathcal{T}}{=} -\nu_y^{\nu_x,j}(-k_x) \bmod 1 \,. \tag{E.31}$$

Hence, the Wannier sector polarization is quantized to be 0 or $\frac{1}{2}$. In addition, the C_{2z} symmetry relates the Wannier centers from different Wannier sectors via

$$\nu_x^{\nu_y,j}(k_y) \overset{C_{2z}}{=} -\nu_x^{-\nu_y,j}(-k_y) \bmod 1 \,, \tag{E.32}$$

$$\nu_y^{\nu_x,j}(k_x) \overset{C_{2z}}{=} -\nu_y^{-\nu_x,j}(-k_x) \bmod 1 \,. \tag{E.33}$$

From the above two equations, the Wannier sector polarizations of different Wannier sectors are identified as

$$p_x^{\nu_y} = -p_x^{-\nu_y} \bmod 1 \,, \tag{E.34}$$

$$p_y^{\nu_x} = -p_y^{-\nu_x} \bmod 1 \,. \tag{E.35}$$

Finally, the bulk quadrupole moment of Eq. (5.19) is given by

$$q_{xy} = p_y^{\nu_x^+} p_x^{\nu_y^+} + p_y^{\nu_x^-} p_x^{\nu_y^-} = 2p_y^{\nu_x^-} p_x^{\nu_y^-}$$

$$= 0 \text{ or } \frac{1}{2} \bmod 1 \,. \tag{E.36}$$

Bibliography

[1] M. V. Berry, Proc. Roy. Soc. Lond. A **392**, 45 (1984).

[2] R. Shindou, R. Matsumoto, S. Murakami, and J.-i. Ohe, Phys. Rev. B **87**, 174427 (2013).

[3] K. v. Klitzing, G. Dorda, and M. Pepper, Phys. Rev. Lett. **45**, 494 (1980).

[4] F. D. M. Haldane, Rev. Mod. Phys. **89**, 040502 (2017).

[5] R. B. Laughlin, Phys. Rev. B **23**, 5632 (1981).

[6] D. J. Thouless, M. Kohmoto, M. P. Nightingale, and M. den Nijs, Phys. Rev. Lett. **49**, 405 (1982).

[7] J. Zak, Phys. Rev. Lett. **62**, 2747 (1989).

[8] B. Simon, Phys. Rev. Lett. **51**, 2167 (1983).

[9] M. Nakahara, *Geometry, Topology and Physics, Second Edition* (Institute of Physics Publishing, Bristol, 2003).

[10] Y. Hatsugai, Phys. Rev. B **48**, 11851 (1993).

[11] Y. Hatsugai, Phys. Rev. Lett. **71**, 3697 (1993).

[12] R. Jackiw and C. Rebbi, Phys. Rev. D **13**, 3398 (1976).

[13] W. P. Su, J. R. Schrieffer, and A. J. Heeger, Phys. Rev. Lett. **42**, 1698 (1979).

[14] W. P. Su and J. R. Schrieffer, Phys. Rev. Lett. **46**, 738 (1981).

[15] B. I. Halperin, Phys. Rev. B **25**, 2185 (1982).

[16] M. Z. Hasan and C. L. Kane, Rev. Mod. Phys. **82**, 3045 (2010).

[17] J. E. Moore, Nature **464**, 194 (2010).

[18] X.-L. Qi and S.-C. Zhang, Rev. Mod. Phys. **83**, 1057 (2011).

[19] S. Murakami, N. Nagaosa, and S.-C. Zhang, Science **301**, 1348 (2003).

[20] S. Murakami, N. Nagaosa, and S.-C. Zhang, Phys. Rev. Lett. **93**, 156804 (2004).

[21] J. Sinova, D. Culcer, Q. Niu, N. A. Sinitsyn, T. Jungwirth, and A. H. MacDonald, Phys. Rev. Lett. **92**, 126603 (2004).

[22] C. L. Kane and E. J. Mele, Phys. Rev. Lett. **95**, 226801 (2005).

[23] C. L. Kane and E. J. Mele, Phys. Rev. Lett. **95**, 146802 (2005).

[24] F. D. M. Haldane, Phys. Rev. Lett. **61**, 2015 (1988).

[25] A. V. Chumak, V. I. Vasyuchka, A. A. Serga, and B. Hillebrands, Nat. Phys. **11**, 453 (2015).

[26] M. Krawczyk and D. Grundler, J. Phys. Condens. Matter **26**, 123202 (2014).

[27] L. Zhang, J. Ren, J.-S. Wang, and B. Li, Phys. Rev. B **87**, 144101 (2013).

[28] X. S. Wang, H. W. Zhang, and X. R. Wang, Phys. Rev. Appl. **9**, 024029 (2018).

[29] H. Katsura, N. Nagaosa, and P. A. Lee, Phys. Rev. Lett. **104**, 066403 (2010).

[30] Y. Onose, T. Ideue, H. Katsura, Y. Shiomi, N. Nagaosa, and Y. Tokura, Science **329**, 297 (2010).

[31] R. Matsumoto and S. Murakami, Phys. Rev. B **84**, 184406 (2011).

[32] R. Matsumoto and S. Murakami, Phys. Rev. Lett. **106**, 197202 (2011).

[33] R. Matsumoto, R. Shindou, and S. Murakami, Phys. Rev. B **89**, 054420 (2014).

[34] S. Fujimoto, Phys. Rev. Lett. **103**, 047203 (2009).

[35] I. Dzyaloshinsky, J Phys Chem Solids **4**, 241 (1958).

[36] T. Moriya, Phys. Rev. **120**, 91 (1960).

[37] H. Katsura, N. Nagaosa, and A. V. Balatsky, Phys. Rev. Lett. **95**, 057205 (2005).

[38] A. Mook, J. Henk, and I. Mertig, Phys. Rev. B **90**, 024412 (2014).

[39] R. Chisnell, J. S. Helton, D. E. Freedman, D. K. Singh, R. I. Bewley, D. G. Nocera, and Y. S. Lee, Phys. Rev. Lett. **115**, 147201 (2015).

[40] S. A. Owerre, J. Phys. Condens. Matter **28**, 386001 (2016).

[41] A. Mook, J. Henk, and I. Mertig, Phys. Rev. B **94**, 174444 (2016).

[42] E. Iacocca and O. Heinonen, Phys. Rev. Applied **8**, 034015 (2017).

[43] S. K. Kim, H. Ochoa, R. Zarzuela, and Y. Tserkovnyak, Phys. Rev. Lett. **117**, 227201 (2016).

[44] A. L. Chernyshev and P. A. Maksimov, Phys. Rev. Lett. **117**, 187203 (2016).

[45] X. S. Wang, Y. Su, and X. R. Wang, Phys. Rev. B **95**, 014435 (2017).

[46] A. Rückriegel, A. Brataas, and R. A. Duine, Phys. Rev. B **97**, 081106 (2018).

[47] S. A. Owerre, Phys. Rev. B **95**, 014422 (2017).

[48] S. A. Owerre, J. Appl. Phys. **121**, 223904 (2017).

[49] X. Wan, A. M. Turner, A. Vishwanath, and S. Y. Savrasov, Phys. Rev. B **83**, 205101 (2011).

[50] S. M. Young, S. Zaheer, J. C. Y. Teo, C. L. Kane, E. J. Mele, and A. M. Rappe, Phys. Rev. Lett. **108**, 140405 (2012).

[51] N. P. Armitage, E. J. Mele, and A. Vishwanath, Rev. Mod. Phys. **90**, 015001 (2018).

[52] J. Fransson, A. M. Black-Schaffer, and A. V. Balatsky, Phys. Rev. B **94**, 075401 (2016).

[53] F.-Y. Li, Y.-D. Li, Y. B. Kim, L. Balents, Y. Yu, and G. Chen, Nat. Commun. **7**, 1 (2016).

[54] A. Mook, J. Henk, and I. Mertig, Phys. Rev. Lett. **117**, 157204 (2016).

[55] Y. Su and X. R. Wang, Phys. Rev. B **96**, 104437 (2017).

[56] S.-K. Jian and W. Nie, Phys. Rev. B **97**, 115162 (2018).

[57] A. Mook, J. Henk, and I. Mertig, Phys. Rev. B **95**, 014418 (2017).

[58] K. Li, C. Li, J. Hu, Y. Li, and C. Fang, Phys. Rev. Lett. **119**, 247202 (2017).

[59] S. A. Owerre, Sci. Rep. **7**, 6931 (2017).

[60] K. Hwang, N. Trivedi, and M. Randeria, Phys. Rev. Lett. **125**, 047203 (2020).

[61] C. Gong, L. Li, Z. Li, H. Ji, A. Stern, Y. Xia, T. Cao, W. Bao, C. Wang, Y. Wang, Z. Q. Qiu, R. J. Cava, S. G. Louie, J. Xia, and X. Zhang, Nature **546**, 265 (2017).

[62] B. Huang, G. Clark, E. Navarro-Moratalla, D. R. Klein, R. Cheng, K. L. Seyler, D. Zhong, E. Schmidgall, M. A. McGuire, D. H. Cobden, W. Yao, D. Xiao, P. Jarillo-Herrero, and X. Xu, Nature **546**, 270 (2017).

[63] S. S. Pershoguba, S. Banerjee, J. C. Lashley, J. Park, H. Ågren, G. Aeppli, and A. V. Balatsky, Phys. Rev. X **8**, 011010 (2018).

[64] S. Bao, J. Wang, W. Wang, Z. Cai, S. Li, Z. Ma, D. Wang, K. Ran, Z.-Y. Dong, D. L. Abernathy, S.-L. Yu, X. Wan, J.-X. Li, and J. Wen, Nat. Commun. **9**, 2591 (2018).

[65] B. Yuan, I. Khait, G.-J. Shu, F. C. Chou, M. B. Stone, J. P. Clancy, A. Paramekanti, and Y.-J. Kim, Phys. Rev. X **10**, 011062 (2020).

[66] Y. Aharonov and A. Casher, Phys. Rev. Lett. **53**, 319 (1984).

[67] K. Nakata, J. Klinovaja, and D. Loss, Phys. Rev. B **95**, 125429 (2017).

[68] K. Nakata, S. K. Kim, J. Klinovaja, and D. Loss, Phys. Rev. B **96**, 224414 (2017).

[69] H. Kondo, Y. Akagi, and H. Katsura, Phys. Rev. B **99**, 041110 (2019).

[70] H. Kondo, Y. Akagi, and H. Katsura, Phys. Rev. B **100**, 144401 (2019).

[71] N. Okuma, Phys. Rev. Lett. **119**, 107205 (2017).

[72] T. Holstein and H. Primakoff, Phys. Rev. **58**, 1098 (1940).

[73] J. T. Haraldsen and R. S. Fishman, J. Phys. Condens. Matter **21**, 216001 (2009).

[74] M. Sato and Y. Ando, Rep. Prog. Phys. **80**, 076501 (2017).

[75] S. A. Díaz, J. Klinovaja, and D. Loss, Phys. Rev. Lett. **122**, 187203 (2019).

[76] S. A. Díaz, T. Hirosawa, J. Klinovaja, and D. Loss, Phys. Rev. Research **2**, 013231 (2020).

[77] J. H. P. Colpa, Physica A **93**, 327 (1978).

[78] M. Kohmoto, Ann Phys (N Y) **160**, 343 (1985).

[79] W. A. Benalcazar, B. A. Bernevig, and T. L. Hughes, Science **357**, 61 (2017).

[80] W. A. Benalcazar, B. A. Bernevig, and T. L. Hughes, Phys. Rev. B **96**, 245115 (2017).

[81] F. Schindler, A. M. Cook, M. G. Vergniory, Z. Wang, S. S. P. Parkin, B. A. Bernevig, and T. Neupert, Sci. Adv. **4**, eaat0346 (2018).

[82] R. Resta, Ferroelectrics **136**, 51 (1992).

[83] R. D. King-Smith and D. Vanderbilt, Phys. Rev. B **47**, 1651 (1993).

[84] D. Vanderbilt and R. D. King-Smith, Phys. Rev. B **48**, 4442 (1993).

[85] R. Resta, Rev. Mod. Phys. **66**, 899 (1994).

[86] D. Vanderbilt, *Berry Phases in Electronic Structure Theory: Electric Polarization, Orbital Magnetization and Topological Insulators* (Cambridge University Press, 2018).

[87] J. D. Jackson, *Classical Electrodynamics*, 3rd ed. (Wiley, New York, 1998).

[88] T. Kariyado, T. Morimoto, and Y. Hatsugai, Phys. Rev. Lett. **120**, 247202 (2018).

[89] H. Araki, T. Mizoguchi, and Y. Hatsugai, Phys. Rev. Research **2**, 012009 (2020).

[90] H. Wakao, T. Yoshida, H. Araki, T. Mizoguchi, and Y. Hatsugai, Phys. Rev. B **101**, 094107 (2020).

[91] M. Serra-Garcia, V. Peri, R. Süsstrunk, O. R. Bilal, T. Larsen, L. G. Villanueva, and S. D. Huber, Nature **555**, 342 (2018).

[92] C. W. Peterson, W. A. Benalcazar, T. L. Hughes, and G. Bahl, Nature **555**, 346 (2018).

[93] S. Mittal, V. V. Orre, G. Zhu, M. A. Gorlach, A. Poddubny, and M. Hafezi, Nat. Photonics **13**, 692 (2019).

[94] N. Nagaosa and Y. Tokura, Nat. Nanotechnol. **8**, 899 (2013).

[95] S. Seki and M. Mochizuki, *Skyrmions in Magnetic Materials*, SpringerBriefs in Physics (Springer International Publishing, 2016).

[96] A. Fert, N. Reyren, and V. Cros, Nat. Rev. Mater. **2**, 1 (2017).

[97] N. Kanazawa, S. Seki, and Y. Tokura, Adv. Mater. **29**, 1603227 (2017).

[98] K. Everschor-Sitte, J. Masell, R. M. Reeve, and M. Kläui, J. Appl. Phys. **124**, 240901 (2018).

[99] C. Back, V. Cros, H. Ebert, K. Everschor-Sitte, A. Fert, M. Garst, T. Ma, S. Mankovsky, T. L. Monchesky, M. Mostovoy, N. Nagaosa, S. S. P. Parkin, C. Pfleiderer, N. Reyren, A. Rosch, Y. Taguchi, Y. Tokura, K. v. Bergmann, and J. Zang, J. Phys. D **53**, 363001 (2020).

[100] M. N. Wilson, E. A. Karhu, D. P. Lake, A. S. Quigley, S. Meynell, A. N. Bogdanov, H. Fritzsche, U. K. Rößler, and T. L. Monchesky, Phys. Rev. B **88**, 214420 (2013).

[101] S. Rohart and A. Thiaville, Phys. Rev. B **88**, 184422 (2013).

[102] S. A. Meynell, M. N. Wilson, H. Fritzsche, A. N. Bogdanov, and T. L. Monchesky, Phys. Rev. B **90**, 014406 (2014).

[103] K. M. D. Hals and K. Everschor-Sitte, Phys. Rev. Lett. **119**, 127203 (2017).

[104] H. Du, R. Che, L. Kong, X. Zhao, C. Jin, C. Wang, J. Yang, W. Ning, R. Li, C. Jin, X. Chen, J. Zang, Y. Zhang, and M. Tian, Nat. Commun. **6**, 8504 (2015).

[105] J. Müller, A. Rosch, and M. Garst, New J. Phys. **18**, 065006 (2016).

[106] S. A. Díaz, T. Hirosawa, D. Loss, and C. Psaroudaki, Nano Lett. **20**, 6556 (2020).

[107] T. H. R. Skyrme and B. F. J. Schonland, Proc. Roy. Soc. Lond. A **260**, 127 (1961).

[108] T. H. R. Skyrme, Nuclear Physics **31**, 556 (1962).

[109] E. Witten, Nucl Phys B **160**, 57 (1979).

[110] G. S. Adkins, C. R. Nappi, and E. Witten, Nucl Phys B **228**, 552 (1983).

[111] Y. Togawa, T. Koyama, K. Takayanagi, S. Mori, Y. Kousaka, J. Akimitsu, S. Nishihara, K. Inoue, A. S. Ovchinnikov, and J. Kishine, Phys. Rev. Lett. **108**, 107202 (2012).

[112] M. M. Salomaa and G. E. Volovik, Rev. Mod. Phys. **59**, 533 (1987).

[113] C. Bäuerle, Y. M. Bunkov, S. N. Fisher, H. Godfrin, and G. R. Pickett, Nature **382**, 332 (1996).

[114] P. M. Walmsley and A. I. Golov, Phys. Rev. Lett. **109**, 215301 (2012).

[115] S. L. Sondhi, A. Karlhede, S. A. Kivelson, and E. H. Rezayi, Phys. Rev. B **47**, 16419 (1993).

[116] A. Schmeller, J. P. Eisenstein, L. N. Pfeiffer, and K. W. West, Phys. Rev. Lett. **75**, 4290 (1995).

[117] L. Brey, H. A. Fertig, R. Côté, and A. H. MacDonald, Phys. Rev. Lett. **75**, 2562 (1995).

[118] A. H. MacDonald, H. A. Fertig, and L. Brey, Phys. Rev. Lett. **76**, 2153 (1996).

[119] M. Abolfath, J. J. Palacios, H. A. Fertig, S. M. Girvin, and A. H. MacDonald, Phys. Rev. B **56**, 6795 (1997).

[120] D. C. Wright and N. D. Mermin, Rev. Mod. Phys. **61**, 385 (1989).

[121] A. N. Bogdanov, U. K. Rößler, and A. A. Shestakov, Phys. Rev. E **67**, 016602 (2003).

[122] J.-i. Fukuda and S. Žumer, Nat. Commun. **2**, 246 (2011).

[123] P. J. Ackerman, T. Boyle, and I. I. Smalyukh, Nat. Commun. **8**, 673 (2017).

[124] T.-L. Ho, Phys. Rev. Lett. **81**, 742 (1998).

[125] U. Al Khawaja and H. Stoof, Nature **411**, 918 (2001).

[126] R. A. Battye, N. R. Cooper, and P. M. Sutcliffe, Phys. Rev. Lett. **88**, 080401 (2002).

[127] L. S. Leslie, A. Hansen, K. C. Wright, B. M. Deutsch, and N. P. Bigelow, Phys. Rev. Lett. **103**, 250401 (2009).

[128] J.-y. Choi, W. J. Kwon, and Y.-i. Shin, Phys. Rev. Lett. **108**, 035301 (2012).

[129] A. Bogdanov and D. Yablonsky, Sov. Phys. JETP, **68**, 101 (1989).

[130] A. Bogdanov and A. Hubert, J. Magn. Magn. Mater. **138**, 255 (1994).

[131] U. K. Rößler, A. N. Bogdanov, and C. Pfleiderer, Nature **442**, 797 (2006).

[132] I. E. Dzyaloshinskii, Sov. Phys. JETP **19**, 960 (1964).

[133] I. E. Dzyaloshinskii, Sov. Phys. JETP **20**, 223 (1964).

[134] S. Mühlbauer, B. Binz, F. Jonietz, C. Pfleiderer, A. Rosch, A. Neubauer, R. Georgii, and P. Böni, Science **323**, 915 (2009).

[135] A. Neubauer, C. Pfleiderer, B. Binz, A. Rosch, R. Ritz, P. G. Niklowitz, and P. Böni, Phys. Rev. Lett. **102**, 186602 (2009).

[136] X. Z. Yu, Y. Onose, N. Kanazawa, J. H. Park, J. H. Han, Y. Matsui, N. Nagaosa, and Y. Tokura, Nature **465**, 901 (2010).

[137] W. Münzer, A. Neubauer, T. Adams, S. Mühlbauer, C. Franz, F. Jonietz, R. Georgii, P. Böni, B. Pedersen, M. Schmidt, A. Rosch, and C. Pfleiderer, Phys. Rev. B **81**, 041203 (2010).

[138] D. Morikawa, K. Shibata, N. Kanazawa, X. Z. Yu, and Y. Tokura, Phys. Rev. B **88**, 024408 (2013).

[139] P. Milde, D. Köhler, J. Seidel, L. M. Eng, A. Bauer, A. Chacon, J. Kindervater, S. Mühlbauer, C. Pfleiderer, S. Buhrandt, C. Schütte, and A. Rosch, Science **340**, 1076 (2013).

[140] X. Z. Yu, N. Kanazawa, Y. Onose, K. Kimoto, W. Z. Zhang, S. Ishiwata, Y. Matsui, and Y. Tokura, Nat. Mater. **10**, 106 (2011).

[141] S.-Z. Lin, C. Reichhardt, C. D. Batista, and A. Saxena, Phys. Rev. Lett. **110**, 207202 (2013).

[142] S. Seki, X. Z. Yu, S. Ishiwata, and Y. Tokura, Science **336**, 198 (2012).

[143] S. Seki, S. Ishiwata, and Y. Tokura, Phys. Rev. B **86**, 060403 (2012).

[144] I. Kézsmárki, S. Bordács, P. Milde, E. Neuber, L. M. Eng, J. S. White, H. M. Rønnow, C. D. Dewhurst, M. Mochizuki, K. Yanai, H. Nakamura, D. Ehlers, V. Tsurkan, and A. Loidl, Nat. Mater. **14**, 1116 (2015).

[145] A. Fert, V. Cros, and J. Sampaio, Nat. Nanotechnol. **8**, 152 (2013).

[146] G. Chen, A. Mascaraque, A. T. N'Diaye, and A. K. Schmid, Appl. Phys. Lett. **106**, 242404 (2015).

[147] W. Jiang, P. Upadhyaya, W. Zhang, G. Yu, M. B. Jungfleisch, F. Y. Fradin, J. E. Pearson, Y. Tserkovnyak, K. L. Wang, O. Heinonen, S. G. E. t. Velthuis, and A. Hoffmann, Science **349**, 283 (2015).

[148] S. Woo, K. Litzius, B. Krüger, M.-Y. Im, L. Caretta, K. Richter, M. Mann, A. Krone, R. M. Reeve, M. Weigand, P. Agrawal, I. Lemesh, M.-A. Mawass, P. Fischer, M. Kläui, and G. S. D. Beach, Nat. Mater. **15**, 501 (2016).

[149] C. Moreau-Luchaire, C. Moutafis, N. Reyren, J. Sampaio, C. a. F. Vaz, N. Van Horne, K. Bouzehouane, K. Garcia, C. Deranlot, P. Warnicke, P. Wohlhüter, J.-M. George, M. Weigand, J. Raabe, V. Cros, and A. Fert, Nat. Nanotechnol. **11**, 444 (2016).

[150] A. Soumyanarayanan, M. Raju, A. L. Gonzalez Oyarce, A. K. C. Tan, M.-Y. Im, A. P. Petrović, P. Ho, K. H. Khoo, M. Tran, C. K. Gan, F. Ernult, and C. Panagopoulos, Nat. Mater. **16**, 898 (2017).

[151] M. Bode, M. Heide, K. von Bergmann, P. Ferriani, S. Heinze, G. Bihlmayer, A. Kubetzka, O. Pietzsch, S. Blügel, and R. Wiesendanger, Nature **447**, 190 (2007).

[152] S. Heinze, K. von Bergmann, M. Menzel, J. Brede, A. Kubetzka, R. Wiesendanger, G. Bihlmayer, and S. Blügel, Nat. Phys. **7**, 713 (2011).

[153] A. K. Nayak, V. Kumar, T. Ma, P. Werner, E. Pippel, R. Sahoo, F. Damay, U. K. Rößler, C. Felser, and S. S. P. Parkin, Nature **548**, 561 (2017).

[154] Y. S. Lin, P. J. Grundy, and E. A. Giess, Appl. Phys. Lett. **23**, 485 (1973).

[155] T. Garel and S. Doniach, Phys. Rev. B **26**, 325 (1982).

[156] M. Ezawa, Phys. Rev. Lett. **105**, 197202 (2010).

[157] X. Yu, M. Mostovoy, Y. Tokunaga, W. Zhang, K. Kimoto, Y. Matsui, Y. Kaneko, N. Nagaosa, and Y. Tokura, Proc. Natl. Acad. Sci. U.S.A. **109**, 8856 (2012).

[158] N. Nagaosa, X. Z. Yu, and Y. Tokura, Philos. Trans. Royal Soc. A **370**, 5806 (2012).

[159] T. Okubo, S. Chung, and H. Kawamura, Phys. Rev. Lett. **108**, 017206 (2012).

[160] A. O. Leonov and M. Mostovoy, Nat. Commun. **6**, 8275 (2015).

[161] S. Hayami, R. Ozawa, and Y. Motome, Phys. Rev. B **95**, 224424 (2017).

[162] T. Kurumaji, T. Nakajima, M. Hirschberger, A. Kikkawa, Y. Yamasaki, H. Sagayama, H. Nakao, Y. Taguchi, T.-h. Arima, and Y. Tokura, Science **365**, 914 (2019).

[163] B. Berg and M. Lüscher, Nucl Phys B **190**, 412 (1981).

[164] S. Buhrandt and L. Fritz, Phys. Rev. B **88**, 195137 (2013).

[165] S. D. Yi, S. Onoda, N. Nagaosa, and J. H. Han, Phys. Rev. B **80**, 054416 (2009).

[166] R. F. L. Evans, W. J. Fan, P. Chureemart, T. A. Ostler, M. O. A. Ellis, and R. W. Chantrell, J. Phys. Condens. Matter **26**, 103202 (2014).

[167] A. O. Leonov, Y. Togawa, T. L. Monchesky, A. N. Bogdanov, J. Kishine, Y. Kousaka, M. Miyagawa, T. Koyama, J. Akimitsu, T. Koyama, K. Harada, S. Mori, D. McGrouther, R. Lamb, M. Krajnak, S. McVitie, R. L. Stamps, and K. Inoue, Phys. Rev. Lett. **117**, 087202 (2016).

[168] D. Song, Z.-A. Li, J. Caron, A. Kovács, H. Tian, C. Jin, H. Du, M. Tian, J. Li, J. Zhu, and R. E. Dunin-Borkowski, Phys. Rev. Lett. **120**, 167204 (2018).

[169] F. N. Rybakov, A. B. Borisov, and A. N. Bogdanov, Phys. Rev. B **87**, 094424 (2013).

[170] J. Iwasaki, M. Mochizuki, and N. Nagaosa, Nat. Nanotechnol. **8**, 742 (2013).

[171] J. Sampaio, V. Cros, S. Rohart, A. Thiaville, and A. Fert, Nat. Nanotechnol. **8**, 839 (2013).

[172] P. W. Anderson and H. Hasegawa, Phys. Rev. **100**, 675 (1955).

[173] G. E. Volovik, J. Phys. C **20**, L83 (1987).

[174] N. Nagaosa and Y. Tokura, Physica Scripta **2012**, 014020 (2012).

[175] J. Zang, M. Mostovoy, J. H. Han, and N. Nagaosa, Phys. Rev. Lett. **107**, 136804 (2011).

[176] J. Ye, Y. B. Kim, A. J. Millis, B. I. Shraiman, P. Majumdar, and Z. Tešanović, Phys. Rev. Lett. **83**, 3737 (1999).

[177] K. Ohgushi, S. Murakami, and N. Nagaosa, Phys. Rev. B **62**, R6065 (2000).

[178] Y. Taguchi, Y. Oohara, H. Yoshizawa, N. Nagaosa, and Y. Tokura, Science **291**, 2573 (2001).

[179] M. Onoda, G. Tatara, and N. Nagaosa, J. Phys. Soc. Japan **73**, 2624 (2004).

[180] P. Bruno, V. K. Dugaev, and M. Taillefumier, Phys. Rev. Lett. **93**, 096806 (2004).

[181] N. Nagaosa, J. Phys. Soc. Japan **75**, 042001 (2006).

[182] B. Binz and A. Vishwanath, Physica B Condens. Matter **403**, 1336 (2008).

[183] M. Lee, W. Kang, Y. Onose, Y. Tokura, and N. P. Ong, Phys. Rev. Lett. **102**, 186601 (2009).

[184] Y. Li, N. Kanazawa, X. Z. Yu, A. Tsukazaki, M. Kawasaki, M. Ichikawa, X. F. Jin, F. Kagawa, and Y. Tokura, Phys. Rev. Lett. **110**, 117202 (2013).

[185] F. Jonietz, S. Mühlbauer, C. Pfleiderer, A. Neubauer, W. Münzer, A. Bauer, T. Adams, R. Georgii, P. Böni, R. A. Duine, K. Everschor, M. Garst, and A. Rosch, Science **330**, 1648 (2010).

[186] X. Z. Yu, N. Kanazawa, W. Z. Zhang, T. Nagai, T. Hara, K. Kimoto, Y. Matsui, Y. Onose, and Y. Tokura, Nat. Commun. **3**, 988 (2012).

[187] J. Iwasaki, M. Mochizuki, and N. Nagaosa, Nat. Commun. **4**, 1463 (2013).

[188] M. Garst, J. Waizner, and D. Grundler, J. Phys. D **50**, 293002 (2017).

[189] Y. Onose, Y. Okamura, S. Seki, S. Ishiwata, and Y. Tokura, Phys. Rev. Lett. **109**, 037603 (2012).

[190] C. Schütte and M. Garst, Phys. Rev. B **90**, 094423 (2014).

[191] M. Mochizuki and S. Seki, J. Phys. Condens. Matter **27**, 503001 (2015).

[192] O. Petrova and O. Tchernyshyov, Phys. Rev. B **84**, 214433 (2011).

[193] M. Mochizuki, Phys. Rev. Lett. **108**, 017601 (2012).

[194] T. Schwarze, J. Waizner, M. Garst, A. Bauer, I. Stasinopoulos, H. Berger, C. Pfleiderer, and D. Grundler, Nat. Mater. **14**, 478 (2015).

[195] A. Pimenov, A. A. Mukhin, V. Y. Ivanov, V. D. Travkin, A. M. Balbashov, and A. Loidl, Nat. Phys. **2**, 97 (2006).

[196] M. Mochizuki and S. Seki, Phys. Rev. B **87**, 134403 (2013).

[197] M. Mochizuki, Phys. Rev. Lett. **114**, 197203 (2015).

[198] Y. Okamura, F. Kagawa, M. Mochizuki, M. Kubota, S. Seki, S. Ishiwata, M. Kawasaki, Y. Onose, and Y. Tokura, Nat. Commun. **4**, 2391 (2013).

[199] Y. Okamura, F. Kagawa, S. Seki, M. Kubota, M. Kawasaki, and Y. Tokura, Phys. Rev. Lett. **114**, 197202 (2015).

[200] J. Iwasaki, A. J. Beekman, and N. Nagaosa, Phys. Rev. B **89**, 064412 (2014).

[201] S.-Z. Lin, C. D. Batista, and A. Saxena, Phys. Rev. B **89**, 024415 (2014).

[202] M. Ezawa, Phys. Rev. B **83**, 100408 (2011).

[203] V. E. Demidov, S. Urazhdin, and S. O. Demokritov, Nat. Mater. **9**, 984 (2010).

[204] F. Macià, F. C. Hoppensteadt, and A. D. Kent, Nanotechnology **25**, 045303 (2014).

[205] A. Pushp, T. Phung, C. Rettner, B. P. Hughes, S.-H. Yang, L. Thomas, and S. S. P. Parkin, Nat. Phys. **9**, 505 (2013).

[206] S. Wintz, V. Tiberkevich, M. Weigand, J. Raabe, J. Lindner, A. Erbe, A. Slavin, and J. Fassbender, Nat. Nanotechnol. **11**, 948 (2016).

[207] C. Behncke, C. F. Adolff, N. Lenzing, M. Hänze, B. Schulte, M. Weigand, G. Schütz, and G. Meier, Communications Physics **1**, 1 (2018).

[208] A. Roldán-Molina, M. J. Santander, A. S. Nunez, and J. Fernández-Rossier, Phys. Rev. B **92**, 245436 (2015).

[209] A. Roldán-Molina, A. S. Nunez, and J. Fernández-Rossier, New J. Phys. **18**, 045015 (2016).

[210] J. Waizner, *Spin wave excitations in magnetic helices and skyrmion lattices*, Ph.D. thesis, Universität zu Köln (2016).

[211] S. Higashikawa, H. Fujita, and M. Sato, arXiv:1810.01103 [cond-mat] (2018).

[212] T. Hirosawa, S. A. Díaz, J. Klinovaja, and D. Loss, Phys. Rev. Lett. **125**, 207204 (2020).

[213] C. Bradley and A. Cracknell, *The mathematical theory of symmetry in solids: Representation theory for point groups and space groups*, EBSCO ebook academic collection (OUP Oxford, 2010).

[214] I. A. Ado, A. Qaiumzadeh, A. Brataas, and M. Titov, Phys. Rev. B **101**, 161403 (2020).

[215] J. Goss, "Symmetry Operations and Character Tables," Retrived from the following website. https://www.staff.ncl.ac.uk/j.p.goss/symmetry/index.html.

[216] C. Pappas, E. Lelièvre-Berna, P. Falus, P. M. Bentley, E. Moskvin, S. Grigoriev, P. Fouquet, and B. Farago, Phys. Rev. Lett. **102**, 197202 (2009).

[217] C. Pfleiderer, T. Adams, A. Bauer, W. Biberacher, B. Binz, F. Birkelbach, P. Böni, C. Franz, R. Georgii, M. Janoschek, F. Jonietz, T. Keller, R. Ritz, S. Mühlbauer, W. Münzer, A. Neubauer, B. Pedersen, and A. Rosch, J. Phys. Condens. Matter **22**, 164207 (2010).

[218] T. Adams, S. Mühlbauer, C. Pfleiderer, F. Jonietz, A. Bauer, A. Neubauer, R. Georgii, P. Böni, U. Keiderling, K. Everschor, M. Garst, and A. Rosch, Phys. Rev. Lett. **107**, 217206 (2011).

[219] A. Tonomura, X. Yu, K. Yanagisawa, T. Matsuda, Y. Onose, N. Kanazawa, H. S. Park, and Y. Tokura, Nano Lett. **12**, 1673 (2012).

[220] S. X. Huang and C. L. Chien, Phys. Rev. Lett. **108**, 267201 (2012).

[221] D. McGrouther, R. J. Lamb, M. Krajnak, S. McFadzean, S. McVitie, R. L. Stamps, A. O. Leonov, A. N. Bogdanov, and Y. Togawa, New J. Phys. **18**, 095004 (2016).

[222] M. Belesi, I. Rousochatzakis, M. Abid, U. K. Rößler, H. Berger, and J.-P. Ansermet, Phys. Rev. B **85**, 224413 (2012).

[223] J. S. White, I. Levatić, A. A. Omrani, N. Egetenmeyer, K. Prša, I. Živković, J. L. Gavilano, J. Kohlbrecher, M. Bartkowiak, H. Berger, and H. M. Rønnow, J. Phys. Condens. Matter **24**, 432201 (2012).

[224] E. Ruff, S. Widmann, P. Lunkenheimer, V. Tsurkan, S. Bordács, I. Kézsmárki, and A. Loidl, Sci. Adv. **1**, e1500916 (2015).

[225] A. Fert and P. M. Levy, Phys. Rev. Lett. **44**, 1538 (1980).

[226] C. Thessieu, C. Pfleiderer, A. N. Stepanov, and J. Flouquet, J. Phys. Condens. Matter **9**, 6677 (1997).

[227] K. Koyama, T. Goto, T. Kanomata, and R. Note, Phys. Rev. B **62**, 986 (2000).

[228] D. Lamago, R. Georgii, C. Pfleiderer, and P. Böni, Physica B Condens. Matter **385-386**, 385 (2006).

[229] W. Xie, S. Thimmaiah, J. Lamsal, J. Liu, T. W. Heitmann, D. Quirinale, A. I. Goldman, V. Pecharsky, and G. J. Miller, Inorganic Chemistry **52**, 9399 (2013).

[230] G. C. Loh and C. K. Gan, AIP Advances **7**, 056412 (2017).

[231] Y. Ishikawa and M. Arai, J. Phys. Soc. Japan **53**, 2726 (1984).

[232] Y. Tokunaga, X. Z. Yu, J. S. White, H. M. Rønnow, D. Morikawa, Y. Taguchi, and Y. Tokura, Nat. Commun. **6**, 7638 (2015).

[233] K. Shibata, X. Z. Yu, T. Hara, D. Morikawa, N. Kanazawa, K. Kimoto, S. Ishiwata, Y. Matsui, and Y. Tokura, Nat. Nanotechnol. **8**, 723 (2013).

[234] H. Schmid, Ferroelectrics **162**, 317 (1994).

[235] P. Curie, Journal de physique théorique et appliquée **3**, 393 (1894).

[236] T.-h. Arima, J. Phys. Soc. Japan **80**, 052001 (2011).

[237] I. Dzyaloshinskii, Sov. Phys. JETP **10**, 628 (1959).

[238] D. Astrov, Sov. Phys. JETP **11**, 708 (1960).

[239] V. J. Folen, G. T. Rado, and E. W. Stalder, Phys. Rev. Lett. **6**, 607 (1961).

[240] T. Kimura, T. Goto, H. Shintani, K. Ishizaka, T. Arima, and Y. Tokura, Nature **426**, 55 (2003).

[241] I. A. Sergienko and E. Dagotto, Phys. Rev. B **73**, 094434 (2006).

[242] M. Kenzelmann, A. B. Harris, S. Jonas, C. Broholm, J. Schefer, S. B. Kim, C. L. Zhang, S.-W. Cheong, O. P. Vajk, and J. W. Lynn, Phys. Rev. Lett. **95**, 087206 (2005).

[243] M. Mostovoy, Phys. Rev. Lett. **96**, 067601 (2006).

[244] J. Kanamori, J Phys Chem Solids **10**, 87 (1959).

[245] P. W. Anderson, Phys. Rev. **79**, 350 (1950).

[246] M. Mochizuki, N. Furukawa, and N. Nagaosa, Phys. Rev. Lett. **105**, 037205 (2010).

[247] C. Jia, S. Onoda, N. Nagaosa, and J. H. Han, Phys. Rev. B **74**, 224444 (2006).

[248] C. Jia, S. Onoda, N. Nagaosa, and J. H. Han, Phys. Rev. B **76**, 144424 (2007).

[249] T.-h. Arima, J. Phys. Soc. Japan **76**, 073702 (2007).

[250] Y.-H. Liu, Y.-Q. Li, and J. H. Han, Phys. Rev. B **87**, 100402 (2013).

[251] J. S. White, K. Prša, P. Huang, A. A. Omrani, I. Živković, M. Bartkowiak, H. Berger, A. Magrez, J. L. Gavilano, G. Nagy, J. Zang, and H. M. Rønnow, Phys. Rev. Lett. **113**, 107203 (2014).

[252] N. Romming, C. Hanneken, M. Menzel, J. E. Bickel, B. Wolter, K. v. Bergmann, A. Kubetzka, and R. Wiesendanger, Science **341**, 636 (2013).

[253] H. Nakamura, R. Ikeno, G. Motoyama, T. Kohara, Y. Kajinami, and Y. Tabata, J Phys Conf Ser **145**, 012077 (2009).

[254] H. Imamura, P. Bruno, and Y. Utsumi, Phys. Rev. B **69**, 121303 (2004).

[255] M. A. Ruderman and C. Kittel, Phys. Rev. **96**, 99 (1954).

[256] T. Kasuya, Prog. Theor. Phys. **16**, 45 (1956).

[257] K. Yosida, Phys. Rev. **106**, 893 (1957).

[258] A. H. MacDonald, S. M. Girvin, and D. Yoshioka, Phys. Rev. B **37**, 9753 (1988).

[259] J. Torrejon, J. Kim, J. Sinha, S. Mitani, M. Hayashi, M. Yamanouchi, and H. Ohno, Nat. Commun. **5**, 4655 (2014).

[260] S. S. P. Parkin, M. Hayashi, and L. Thomas, Science **320**, 190 (2008).

[261] S. Parkin and S.-H. Yang, Nat. Nanotechnol. **10**, 195 (2015).

[262] T. Graf, C. Felser, and S. S. P. Parkin, Prog. Solid. State Ch. **39**, 1 (2011).

[263] C. Felser, L. Wollmann, S. Chadov, G. H. Fecher, and S. S. P. Parkin, APL Mater. **3**, 041518 (2015).

[264] H. Y. Kwon, K. M. Bu, Y. Z. Wu, and C. Won, J. Magn. Magn. Mater. **324**, 2171 (2012).

[265] S. Seki, M. Garst, J. Waizner, R. Takagi, N. D. Khanh, Y. Okamura, K. Kondou, F. Kagawa, Y. Otani, and Y. Tokura, Nat. Commun. **11**, 1 (2020).

[266] A. Brataas, Y. Tserkovnyak, G. E. W. Bauer, and B. I. Halperin, Phys. Rev. B **66**, 060404 (2002).

[267] C. Du, T. v. d. Sar, T. X. Zhou, P. Upadhyaya, F. Casola, H. Zhang, M. C. Onbasli, C. A. Ross, R. L. Walsworth, Y. Tserkovnyak, and A. Yacoby, Science **357**, 195 (2017).

[268] J. Jersch, V. E. Demidov, H. Fuchs, K. Rott, P. Krzysteczko, J. Münchenberger, G. Reiss, and S. O. Demokritov, Appl. Phys. Lett. **97**, 152502 (2010).

[269] A. Kirilyuk, A. V. Kimel, and T. Rasing, Rev. Mod. Phys. **82**, 2731 (2010).

[270] S. A. Owerre, J. Phys. Commun. **1**, 021002 (2017).

[271] E. Beaurepaire, J.-C. Merle, A. Daunois, and J.-Y. Bigot, Phys. Rev. Lett. **76**, 4250 (1996).

[272] A. V. Kimel, A. Kirilyuk, P. A. Usachev, R. V. Pisarev, A. M. Balbashov, and T. Rasing, Nature **435**, 655 (2005).

[273] T. Kampfrath, A. Sell, G. Klatt, A. Pashkin, S. Mährlein, T. Dekorsy, M. Wolf, M. Fiebig, A. Leitenstorfer, and R. Huber, Nat. Photonics **5**, 31 (2011).

[274] S. Takayoshi, M. Sato, and T. Oka, Phys. Rev. B **90**, 214413 (2014).

[275] S. Takayoshi, H. Aoki, and T. Oka, Phys. Rev. B **90**, 085150 (2014).

[276] M. Sato, S. Takayoshi, and T. Oka, Phys. Rev. Lett. **117**, 147202 (2016).

[277] T. Oka and S. Kitamura, Annu. Rev. Condens. Matter Phys. **10**, 387 (2019).

[278] T. Oka and H. Aoki, Phys. Rev. B **79**, 081406 (2009).

[279] J. W. McIver, B. Schulte, F.-U. Stein, T. Matsuyama, G. Jotzu, G. Meier, and A. Cavalleri, Nat. Phys. **16**, 38 (2020).

[280] J. Cayssol, B. Dóra, F. Simon, and R. Moessner, Phys Status Solidi Rapid Res Lett **7**, 101 (2013).

[281] S. A. Owerre, Ann Phys (N Y) **399**, 93 (2018).

[282] S. A. Owerre, Sci. Rep. **8**, 4431 (2018).

[283] K. Nakata, S. K. Kim, and S. Takayoshi, Phys. Rev. B **100**, 014421 (2019).

[284] M. Elyasi, K. Sato, and G. E. W. Bauer, Phys. Rev. B **99**, 134402 (2019).

[285] A. Eckardt and E. Anisimovas, New J. Phys. **17**, 093039 (2015).

[286] T. L. Gilbert, IEEE Transactions on Magnetics **40**, 3443 (2004), conference Name: IEEE Transactions on Magnetics.

[287] Y. Aharonov and D. Bohm, Phys. Rev. **115**, 485 (1959).

[288] H. Fujita and M. Sato, Phys. Rev. B **95**, 054421 (2017).

[289] A. A. Thiele, Phys. Rev. Lett. **30**, 230 (1973).

[290] W. Wang, M. Beg, B. Zhang, W. Kuch, and H. Fangohr, Phys. Rev. B **92**, 020403 (2015).

[291] J. A. Fülöp, S. Tzortzakis, and T. Kampfrath, Adv. Opt. Mater. **8**, 1900681 (2020).

[292] R. B. Versteeg, I. Vergara, S. D. Schäfer, D. Bischoff, A. Aqeel, T. T. M. Palstra, M. Grüninger, and P. H. M. van Loosdrecht, Phys. Rev. B **94**, 094409 (2016).

[293] M. Ikka, A. Takeuchi, and M. Mochizuki, Phys. Rev. B **98**, 184428 (2018).

[294] H. Y. Yuan, X. S. Wang, M.-H. Yung, and X. R. Wang, Phys. Rev. B **99**, 014428 (2019).

[295] X. Ni, M. Weiner, A. Alù, and A. B. Khanikaev, Nat. Mater. **18**, 113 (2019).

[296] H. Fan, B. Xia, L. Tong, S. Zheng, and D. Yu, Phys. Rev. Lett. **122**, 204301 (2019).

[297] H. Xue, Y. Yang, F. Gao, Y. Chong, and B. Zhang, Nat. Mater. **18**, 108 (2019).

[298] B.-Y. Xie, H.-F. Wang, H.-X. Wang, X.-Y. Zhu, J.-H. Jiang, M.-H. Lu, and Y.-F. Chen, Phys. Rev. B **98**, 205147 (2018).

[299] X.-D. Chen, W.-M. Deng, F.-L. Shi, F.-L. Zhao, M. Chen, and J.-W. Dong, Phys. Rev. Lett. **122**, 233902 (2019).

[300] B.-Y. Xie, G.-X. Su, H.-F. Wang, H. Su, X.-P. Shen, P. Zhan, M.-H. Lu, Z.-L. Wang, and Y.-F. Chen, Phys. Rev. Lett. **122**, 233903 (2019).

[301] A. Sil and A. K. Ghosh, J. Phys. Condens. Matter **32**, 205601 (2020).

[302] D. J. Thouless, Phys. Rev. B **27**, 6083 (1983).

[303] H. Watanabe and M. Oshikawa, Phys. Rev. X **8**, 021065 (2018).

[304] R. Jackiw and J. R. Schrieffer, Nucl Phys B **190**, 253 (1981).

[305] J.-H. Park, G. Yang, J. Klinovaja, P. Stano, and D. Loss, Phys. Rev. B **94**, 075416 (2016).

[306] M. Thakurathi, J. Klinovaja, and D. Loss, Phys. Rev. B **98**, 245404 (2018).

[307] M. Pletyukhov, D. M. Kennes, J. Klinovaja, D. Loss, and H. Schoeller, Phys. Rev. B **101**, 161106 (2020).

[308] M. Pletyukhov, D. M. Kennes, J. Klinovaja, D. Loss, and H. Schoeller, Phys. Rev. B **101**, 165304 (2020).

[309] C. W. Peterson, T. Li, W. A. Benalcazar, T. L. Hughes, and G. Bahl, Science **368**, 1114 (2020).

[310] A. Mook, J. Klinovaja, and D. Loss, Phys. Rev. Research **2**, 033491 (2020).

[311] M. N. Wilson, A. B. Butenko, A. N. Bogdanov, and T. L. Monchesky, Phys. Rev. B **89**, 094411 (2014).

[312] C. M. Purser, V. P. Bhallamudi, F. Guo, M. R. Page, Q. Guo, G. D. Fuchs, and P. C. Hammel, Appl. Phys. Lett. **116**, 202401 (2020).

[313] H. Huebl, C. W. Zollitsch, J. Lotze, F. Hocke, M. Greifenstein, A. Marx, R. Gross, and S. T. B. Goennenwein, Phys. Rev. Lett. **111**, 127003 (2013).

[314] Y. Tabuchi, S. Ishino, A. Noguchi, T. Ishikawa, R. Yamazaki, K. Usami, and Y. Nakamura, Science **349**, 405 (2015).

[315] Y. Li, T. Polakovic, Y.-L. Wang, J. Xu, S. Lendinez, Z. Zhang, J. Ding, T. Khaire, H. Saglam, R. Divan, J. Pearson, W.-K. Kwok, Z. Xiao, V. Novosad, A. Hoffmann, and W. Zhang, Phys. Rev. Lett. **123**, 107701 (2019).

[316] J. Jena, B. Göbel, T. Hirosawa, S. A. Dìaz, T.Hinokihara, V. Kumar, I. Mertig, C. Felser, D. Loss, and S. Parkin, "Observation of fractional spin textures and bulk-boundary correspondence", submitted to Nature.

[317] J. Jena, B. Göbel, T. Ma, V. Kumar, R. Saha, I. Mertig, C. Felser, and S. S. P. Parkin, Nat. Commun. **11**, 1115 (2020).

[318] L. Peng, R. Takagi, W. Koshibae, K. Shibata, K. Nakajima, T.-h. Arima, N. Nagaosa, S. Seki, X. Yu, and Y. Tokura, Nat. Nanotechnol. , 1 (2020).

[319] A. Altland and B. D. Simons, *Condensed Matter Field Theory*, 2nd ed. (Cambridge University Press, Cambridge, 2010).

[320] P. W. Anderson, Phys. Rev. **115**, 2 (1959).

[321] J. B. Goodenough, Phys. Rev. **100**, 564 (1955).

[322] B. D. Cullity and C. D. Graham, *Introduction to Magnetic Materials*, 2nd ed. (Wiley New Jersey, 2008).

[323] M. Sasaki and F. Matsubara, J. Phys. Soc. Japan **77**, 024004 (2008).

[324] P. Bak and M. H. Jensen, J. Phys. C **13**, L881 (1980).

[325] Y. A. Izyumov, Soviet Physics Uspekhi **27**, 845 (1984).

[326] Y. Togawa, Y. Kousaka, K. Inoue, and J.-i. Kishine, J. Phys. Soc. Japan **85**, 112001 (2016).

[327] G. Tatara, H. Kohno, and J. Shibata, Phys. Rep. **468**, 213 (2008).

[328] T. Schulz, R. Ritz, A. Bauer, M. Halder, M. Wagner, C. Franz, C. Pfleiderer, K. Everschor, M. Garst, and A. Rosch, Nat. Phys. **8**, 301 (2012).

[329] J. C. Slonczewski, J. Magn. Magn. Mater. **159**, L1 (1996).

[330] L. Berger, Phys. Rev. B **54**, 9353 (1996).

[331] M. Tsoi, R. E. Fontana, and S. S. P. Parkin, Appl. Phys. Lett. **83**, 2617 (2003).

[332] J. Grollier, P. Boulenc, V. Cros, A. Hamzić, A. Vaurès, A. Fert, and G. Faini, Appl. Phys. Lett. **83**, 509 (2003).

[333] A. V. Khvalkovskiy, D. Apalkov, S. Watts, R. Chepulskii, R. S. Beach, A. Ong, X. Tang, A. Driskill-Smith, W. H. Butler, P. B. Visscher, D. Lottis, E. Chen, V. Nikitin, and M. Krounbi, J. Phys. D **46**, 074001 (2013).

[334] W. Jiang, X. Zhang, G. Yu, W. Zhang, X. Wang, M. Benjamin Jungfleisch, J. E. Pearson, X. Cheng, O. Heinonen, K. L. Wang, Y. Zhou, A. Hoffmann, and S. G. E. te Velthuis, Nat. Phys. **13**, 162 (2017).

[335] G. Yu, P. Upadhyaya, Q. Shao, H. Wu, G. Yin, X. Li, C. He, W. Jiang, X. Han, P. K. Amiri, and K. L. Wang, Nano Lett. **17**, 261 (2017).

[336] X. Z. Yu, N. Kanazawa, W. Z. Zhang, T. Nagai, T. Hara, K. Kimoto, Y. Matsui, Y. Onose, and Y. Tokura, Nat. Commun. **3**, 988 (2012).

[337] S. Woo, K. Litzius, B. Krüger, M.-Y. Im, L. Caretta, K. Richter, M. Mann, A. Krone, R. M. Reeve, M. Weigand, P. Agrawal, I. Lemesh, M.-A. Mawass, P. Fischer, M. Kläui, and G. S. D. Beach, Nat. Mater. **15**, 501 (2016).

[338] K. Litzius, I. Lemesh, B. Krüger, P. Bassirian, L. Caretta, K. Richter, F. Büttner, K. Sato, O. A. Tretiakov, J. Förster, R. M. Reeve, M. Weigand, I. Bykova, H. Stoll, G. Schütz, G. S. D. Beach, and M. Kläui, Nat. Phys. **13**, 170 (2017).

[339] S. Woo, K. M. Song, X. Zhang, Y. Zhou, M. Ezawa, X. Liu, S. Finizio, J. Raabe, N. J. Lee, S.-I. Kim, S.-Y. Park, Y. Kim, J.-Y. Kim, D. Lee, O. Lee, J. W. Choi, B.-C. Min, H. C. Koo, and J. Chang, Nat. Commun. **9**, 959 (2018).

[340] Y. Zhou and M. Ezawa, Nat. Commun. **5**, 1 (2014).

[341] M. Finazzi, M. Savoini, A. R. Khorsand, A. Tsukamoto, A. Itoh, L. Duò, A. Kirilyuk, T. Rasing, and M. Ezawa, Phys. Rev. Lett. **110**, 177205 (2013).

[342] W. Koshibae and N. Nagaosa, Nat. Commun. **5**, 5148 (2014).

[343] G. Berruto, I. Madan, Y. Murooka, G. M. Vanacore, E. Pomarico, J. Rajeswari, R. Lamb, P. Huang, A. J. Kruchkov, Y. Togawa, T. LaGrange, D. McGrouther, H. M. Rønnow, and F. Carbone, Phys. Rev. Lett. **120**, 117201 (2018).

[344] J. H. Shirley, Phys. Rev. **138**, B979 (1965).

[345] S. Rahav, I. Gilary, and S. Fishman, Phys. Rev. A **68**, 013820 (2003).

[346] N. Goldman and J. Dalibard, Phys. Rev. X **4**, 031027 (2014).

[347] A. P. Itin and M. I. Katsnelson, Phys. Rev. Lett. **115**, 075301 (2015).

[348] N. Marzari and D. Vanderbilt, Phys. Rev. B **56**, 12847 (1997).

[349] R. Resta, Phys. Rev. Lett. **80**, 1800 (1998).